Numerical studies of entanglement dynamics in open spin systems

Guillermo Javier Preisser Beltrán

Université de Strasbourg

UNIVERSITÉ DE STRASBOURG

EDSC École Doctorale des Sciences Chimiques

ÉCOLE DOCTORALE DES SCIENCES CHIMIQUES

Centre Européen des Sciences Quantiques (CESQ)

THÈSE présentée par :

Guillermo Javier PREISSER BELTRÁN

soutenue le : **15 septembre 2023**

pour obtenir le grade de : **Docteur de l'Université de Strasbourg**

Discipline/ Spécialité : Physique

Numerical Studies of Entanglement Dynamics in Open Spin Systems

THÈSE dirigée par :

Dr. SCHACHENMAYER Johannes	Chargé de recherche, CNRS

RAPPORTEURS :

Dr. SAFAVI-NANI Arghavan	Professeur, University of Amsterdam
Dr. GENES Claudiu	Professeur, Max Planck Institute for the Science of Light

AUTRES MEMBRES DU JURY :

Dr. MANFREDI Giovanni	Directeur de recherches, CNRS

Résumé : L'étude des capacités de simulation quantique à plusieurs corps à l'aide de méthodes classiques est un domaine d'étude pertinent et passionnant. Avec les capacités avancées des simulateurs quantiques, il devient crucial d'explorer les limites des méthodes classiques de simulation quantique dans la poursuite de l'obtention d'un avantage quantique.

L'objectif central de cette thèse est de développer une compréhension théorique plus approfondie de la dynamique de l'entropie d'intrication dans les systèmes de spins ouverts, et d'étudier les implications en termes de simulation classique de systèmes de spins ouverts à plusieurs corps par des méthodes de réseaux de tenseurs. Deux résultats principaux sont présentés dans cette thèse. L'une est une étude de la dynamique de croissance de l'intrication de l'opérateur dans une chaîne de spin ouverte avec déphasage, qui présente une croissance logarithmique à long terme. Une telle croissance logarithmique permet une simulation pendant de longues périodes avec la méthode Matrix Product Density Operator, et une compréhension analytique complète de l'effet en est dérivée. La seconde est une comparaison approfondie entre l'enchevêtrement d'opérateur et l'enchevêtrement de trajectoire où nous avons constaté que, dans la plupart des cas, l'enchevêtrement de trajectoire présente une croissance plus rapide pendant de longues périodes, ce qui rend l'approche de l'opérateur de densité de produit matriciel fondamentalement plus efficace qu'un dénouement de trajectoire quantique où chaque trajectoire est représentée comme un état de produit matriciel.

Mots-clés : Intrication quantique, Systèmes Quantiques Ouverts, Etats de Produits Matrices, Dynamique Quantique à Plusieurs Corps, Trajectoires Quantiques.

Abstract: The investigation of quantum many-body simulation capabilities using classical methods is a pertinent and exciting field of study. With the advancing capabilities of quantum simulators, it becomes crucial to explore the limits of classical methods for quantum simulation in the pursuit of achieving quantum advantage**.**

The central aim of this thesis to develop a deeper theoretical understanding of entanglement entropy dynamics in open spin systems, and study the implications in terms of the classical simulation of many-body open spin systems through tensor network methods. There are two main results presented in this thesis. One is a study of Operator Entanglement growth dynamics in an open spin-chain with dephasing, which is found to exhibit a logarithmic growth at long times. Such logarithmic growth enables simulation for long times with the Matrix Product Density Operator method, and a full analytical understanding of the effect is derived. The second one is a thorough comparison between Operator Entanglement and Trajectory Entanglement where we found that, in most cases, Trajectory Entanglement exhibits a faster growth for long times, making the Matrix Product Density Operator approach fundamentally more efficient than a quantum trajectory unravel where each trajectory is represented as a Matrix Product State.

Keywords: Entanglement, Open Quantum Systems, Matrix Product States, Many-body quantum dynamics, Quantum Trajectories.

"The final mystery is oneself. When one has weighed the sun in the balance, and measured the steps of the moon, and mapped out the seven heavens star by star, there still remains oneself. Who can calculate the orbit of his own soul?"
— Oscar Wilde, De Profundis

To my family and friends,
who always supported and believed in me

Acknowledgments

Here I want to thank all the people who made this work possible. Every friend, professor and family member who taught me something and help me to get where I am now. While it be just too difficult to name each and every one of them, there are some people that deserve a special recognition.

First of all I want to thank my advisor Johannes Schachenmayer, whose support and guidance over the past three-and-a-half years were invaluable. I know I made it difficult at times and there are definitely things that I wish I could have done better. Nevertheless, I will always be grateful for giving me the opportunity to do a PhD and explore a field as fascinating as it is quantum physics. The numerical techniques and physics concepts imparted during my doctoral studies provided profound insights into the understanding of quantum many-body systems.

I also want to give special thanks to David Wellnitz, who was fundamental for the realization of the work presented in this thesis. Thank you for always being there to help me and answer with such clarity to any of the doubts that I had. It is honestly impressive the way you approach to problems and –at least in most cases– how you are able to solve them with such an apparent easiness.

I am grateful for all the current and former members of the group, whose assistance and camaraderie made my time in Strasbourg a truly enjoyable experience. A heartfelt thank you to Guido P., Sven, Vineesha, Francesco, Tatiana, Guido M., Tanul, Ruben, and David H.

A special acknowledgment goes to the individuals I had the opportunity to collaborate with on research projects: Jérôme Dubail, Vincenzo Alba, Thomas Botzung, and David Wellnitz. I am privileged to have learned from you and appreciate your contributions to our joint projects.

I also thank Nataliia Voievoda from the QUSTEC program for her excellent support and for assisting me in navigating French bureaucracy. Her role was critical in facilitating my secondment at the University of Ljubljana, where I had the chance to work with Tomaž Prosen, to whom I am also grateful.

Because life is not all about physics, I want to express my gratitude to the friends and great people I met during my time in Strasbourg and Ljubljana. Léa Clavel and Jérémy De Barros, your friendship enriched my experience, and it was through you that I managed to speak (more or less) French. You were were great colocs and it was actually quite a fun experience to spend the pandemic with you. Thanks to Lamijah, Chuy, Sonya, Emily and Manuel, whose friendship I deeply appreciate. Whether it was just hangout, having a beer, or talk about music or cinema, it was great to spend some time together and I feel happy and privileged

that I have met you.

Thanks to my fellow Mexicans and physicists friends, Jonathan and Andrés, who inspire me and motivate me to keep going.

Finalmente, quiero agradecer a mi familia. En particular, a mi padre Alain, a mi madre Rosa y a mi abuela Silvia. Gracias por todo su apoyo durante mis estudios y durante toda mi vida. Quiero agradecer también a mis hermanos Alain y Raúl, y a toda mi familia en Ensenada.

Thank you all/Gracias.

Resumé de la Thèse en Français

Introduction

Le concept d'intrication a été introduit pour la première fois par Erwin Schrödinger en 1935 comme moyen de décrire des corrélations non locales entre des particules qui semblaient violer la physique classique. Ces corrélations ont été discutées pour la première fois dans l'article fondateur d'Einstein, Podolsky et Rosen intitulé "*Can Quantum-Mechanical Description of Physical Reality Be Considered Complete ?*"[1]. Dans cet article, Einstein, Podolsky et Rosen ont présenté une expérience de pensée qui impliquait une situation où deux particules étaient corrélées de telle manière que la mesure de l'état d'une particule déterminerait instantanément l'état de l'autre, quelle que soit leur distance. Cet article a conduit à une série de discussions, qui n'ont pas permis d'avancer ou de comprendre de manière significative la nature de ce phénomène. Du moins pas avant 1964, lorsque John Bell a fourni ce que l'on appelle maintenant le théorème de Bell, qui ouvre la possibilité de tester expérimentalement la nature de l'intrication. Cela a conduit à une série d'expériences, notamment John Clauser et Stuart Freedman en 1964[2], et Alain Aspect en 1982 [3], pour lesquels ils ont remporté le prix Nobel de physique (avec Anton Zeillinger) en 2022 .

En plus de fournir des informations précieuses sur le fonctionnement de la nature, il a également été démontré que l'intrication joue un rôle crucial dans de nombreuses applications liées aux protocoles et technologies quantiques, telles que l'informatique quantique [4–6], la cryptographie quantique[7, 8] et la téléportation quantique [9]. De manière cruciale, l'intrication joue également un rôle fondamental dans la possibilité de simuler classiquement des systèmes quantiques. Le lien entre l'intrication et la simulation classique des systèmes quantiques peut être fait via le concept de Matrix Product States (MPS). Un MPS est une décomposition d'un vecteur d'état à plusieurs corps en un produit de matrices $\chi \times \chi$ (où les entrées des matrices sont des kets locaux) [10–13]. De manière analogue aux MPS pour les états purs, une décomposition en produit matriciel de la matrice de densité peut également être définie, connue sous le nom d'opérateur de densité de produit de matrice de densité (MPDO). L'efficacité d'une telle décomposition est déterminée principalement par la quantité de ce que l'on appelle «Operator Entanglement» (OE). Les développements récents, en particulier dans les expériences avec des atomes ultra-froids, ont rendu accessible le concept de simulation quantique analogique [14]. Le but de telles expériences est de simuler la dynamique quantique dans une expérience, de mieux comprendre les régimes où les simulations sur

les ordinateurs classiques échouent. La question de la croissance de l'intrication (des opérateurs) est donc un axe de recherche fondamental. L'objectif de cette thèse est de faire progresser notre compréhension de la croissance de l'intrication (opérateur) dans les systèmes quantiques ouverts à plusieurs corps.

Dans la suite de ce résumé, je fournirai un bref résumé des résultats obtenus dans cette thèse. Je vais d'abord présenter les concepts, modèles et techniques numériques les plus importants employés dans ce travail. Ensuite, je présenterai les deux résultats principaux de cette thèse. L'un des travaux est une comparaison de l'OE et d'une autre forme de calcul de l'entropie d'intrication, que nous appellerons «Trajectory Entanglement» (TE) et l'autre est une étude sur la croissance de l'intrication des opérateurs logarithmiques.

Méthodes numériques pour les systèmes de spin quantiques ouverts

Tous les scénarios physiques sur lesquels nous nous concentrons dans cette thèse impliquent des modèles de spin de dynamique quantique à plusieurs corps en présence de dissipation. Nous modélisons cette dynamique à l'aide des équations principales de Lindblad, qui sont données par

$$\frac{d}{dt}\hat{\rho} = -\mathrm{i}[\hat{H}, \hat{\rho}] + \sum_{\eta} \mathcal{D}[\hat{L}_\eta]\hat{\rho}, \tag{1}$$

$\hat{\rho}$ désigne une matrice de densité à plusieurs corps pour un système spin 1/2 particules. La première partie régit la dynamique hamiltonienne cohérente, la seconde la dissipation. Ici, nos canaux dissipatifs sont donnés par des superopérateurs

$$\mathcal{D}[\hat{L}_\eta]\hat{\rho} = \hat{L}_\eta \hat{\rho} \hat{L}_\eta^\dagger - \frac{1}{2}\{\hat{L}_\eta^\dagger \hat{L}_\eta, \hat{\rho}\}, \tag{2}$$

Les systèmes considérés dans cette thèse étaient des chaînes 1D spin-1/2 XXZ avec l'hamiltonien

$$\hat{H} = \frac{1}{4}\sum_i \big[- J(\hat{\sigma}_i^x \hat{\sigma}_{i+1}^x + \hat{\sigma}_i^y \hat{\sigma}_{i+1}^y) + J_z \hat{\sigma}_i^z \hat{\sigma}_{i+1}^z \big], \tag{3}$$

ici, $\hat{\sigma}$ sont des matrices de Pauli standard. L'hamiltonien présente une physique d'échange de spin (au taux J) et des interactions spin-spin (avec une tase J_z).

Nous avons considéré deux types de dissipation. L'une est l'émission/absorption spontanée, définie respectivement par les deux opérateurs de saut pour le spin i :

$$\hat{L_i^+} = \sqrt{\gamma_+}\hat{\sigma}_i^+, \quad \hat{L_i^-} = \sqrt{\gamma_-}\hat{\sigma}_i^-. \tag{4}$$

Ce type de bruit est particulièrement important lorsque les niveaux de spin sont réalisés à l'aide de niveaux atomiques dans des expériences d'atomes ultrafroids [15]. L'autre type de dissipation que nous avons considéré est le déphasage, qui est un autre type de bruit typique dans les systèmes à atomes froids, par

ex. lorsque des spins sont réalisés avec des bosons durs. Cela peut être considéré comme une perte de relation de phase définie entre les deux états de spin [16]. Dans l'équation maîtresse, cela est exprimé par les opérateurs de saut locaux

$$\hat{L}_i^z = \sqrt{\gamma_z}\hat{\sigma}_i^z. \tag{5}$$

Ici, il est important de remarquer que pour le déphasage, l'aimantation est conservée. Une conséquence directe de cela est une surprenante croissance logarithmique à long terme de l'intrication des opérateurs, qui était l'une des principales découvertes surprenantes de ma thèse (voir publication : [17]).

Matrix Product States et Intrication Quantique

Les états de produits matriciels (MPS) sont devenus des outils puissants dans l'étude des systèmes quantiques à plusieurs corps. Introduit à l'origine comme un cadre pour simuler efficacement des systèmes quantiques unidimensionnels, le MPS a depuis révolutionné notre compréhension de l'intrication et de son rôle dans la simulation classique des systèmes quantiques.

Dans les systèmes quantiques à plusieurs corps, représenter avec précision l'état du système devient de plus en plus difficile à mesure que le nombre de particules et la dimension du système augmentent. Traditionnellement, pour représenter un état quantique, il faut stocker un grand nombre de nombres complexes, nécessitant une quantité exponentielle de mémoire et de ressources de calcul. Par exemple, dans un système avec N particules et chaque particule ayant d niveaux, le nombre de nombres complexes requis croît comme d^N, rendant les simulations exactes pratiquement impossibles pour les systèmes à grande échelle.

Les états de produits matriciels fournissent une solution élégante à ce problème en utilisant une représentation compacte qui capture les caractéristiques essentielles de l'état quantique. Au lieu de stocker la fonction d'onde entière, MPS représente l'état comme un produit de matrices, de dimensions $\chi \times \chi$ (où les entrées des matrices sont des kets locaux). Dans une telle représentation, l'entropie bipartite d'intrication de von Neumann S est bornée par $\max[S] = \log_2$. Par conséquent, pour représenter un état physique $|\psi(t)\rangle$ avec une entropie d'intrication $S(t)$ comme un MPS, la taille de la matrice (ou 'dimension de la liaison') doit croître d'au moins $\chi \propto 2^{S(t)}$ avec le temps. Par exemple, une évolution où S augmente linéairement dans le temps peut donc être considérée comme difficile en calcul [18].

En tronquant la quantité maximale d'entropie d'intrication, MPS fournit une approximation de l'état réel du système, en conservant les informations les plus pertinentes tout en éliminant les détails moins significatifs. Heureusement, il convient de noter que pour un large éventail de problèmes, tels que la dynamique proche de l'équilibre, les basses énergies et les courtes échelles de temps, il s'avère que seule une quantité modeste d'intrication est suffisante pour obtenir une simulation exacte. Dans ces cas, la dimension de liaison χ de la représentation de l'état du produit matriciel peut rester relativement petite, ce qui rend la simulation traitable par calcul.

De manière analogue aux MPS pour les états purs, une forme d'opérateur de densité de produit matriciel (MPDO) de la matrice de densité $\hat{\rho}$ peut également être définie. Une forme MPO permet d'exprimer facilement la matrice de densité sous la forme d'une décomposition de Schmidt entre une gauche et une bloc droit. L'entropie bipartite de cette décomposition est donnée par la « operator space entanglement entropy » ou simplement « operator entanglement » (OE). L'OE indique l'efficacité d'une représentation MPDO. Il peut être facilement calculé numériquement [19–23] et se prête à un traitement analytique [24–26]. Nous soulignons que, malgré son nom, OE n'est pas nécessairement lié à une véritable intrication quantique entre des blocs de spins distincts lorsque $\hat{\rho}$ est un état mixte.

Dans les chapitres 3 et 6 le MPS et la méthode MPDO sont présentés plus en détail. En particulier, l'utilisation de MPOD pour simuler la dynamique OE dans un système de chaîne de spin XXZ sera l'un des sujets majeurs de cette thèse.

Trajectoires quantiques et intrication quantique

Alternativement à l'approche MPDO, la matrice de densité peut être non uniquement décomposé en un mélange statistique d'états purs [voir Fig. 1 pour un croquis]. Chaque état pur peut alors être exprimé sous la forme d'un MPS, et l'efficacité d'une telle représentation est déterminée par les entropies d'intrication bipartite dans les états individuels. Pour calculer le temps évolution, les trajectoires à l'état pur peuvent être stochastiquement évolué avec une technique connue sous le nom de Monte-Carlo quantique méthode de la fonction d'onde ou trajectoires quantiques (QT) [27–29].

Cette approche a été appliquée avec succès dans de nombreuses simulations avec MPS [30, 31]. Nous le notons QT+MPS, et l'entropie bipartite moyenne des trajectoires « intrication de trajectoire » (TE). En général, en raison de l'espace d'état local plus petit, une approche QT + MPS semble favorable par rapport à un MPDO, en particulier pour les calculs où seuls de petits nombres de trajectoires sont nécessaires pour la convergence statistique (par exemple pour calcul de l'évolution d'observables locales simples). Cependant, une mise à l'échelle d'entropie réduite pourrait rendre l'approche MPDO fondamentalement plus efficace car elle peut considérablement assouplir les exigences sur les dimensions de liaison χ. L'un des travaux majeurs de cette thèse est une comparaison détaillée entre les deux méthodes.

Dans la section 5, nous approfondirons les détails des trajectoires quantiques et l'utilisation des trajectoires quantiques pour simuler l'évolution temporelle des systèmes quantiques. Plus particulièrement, une grande partie de notre attention sera concentrée sur la question de la croissance de TE.

Résultat principal (i) – Comparaison détaillée : Operator Entanglement vs. Trajectory Entanglement

L'un des principaux résultats de cette thèse est une comparaison approfondie entre la méthode QT + MPS et MPDO. En particulier, nous comparons la croissance

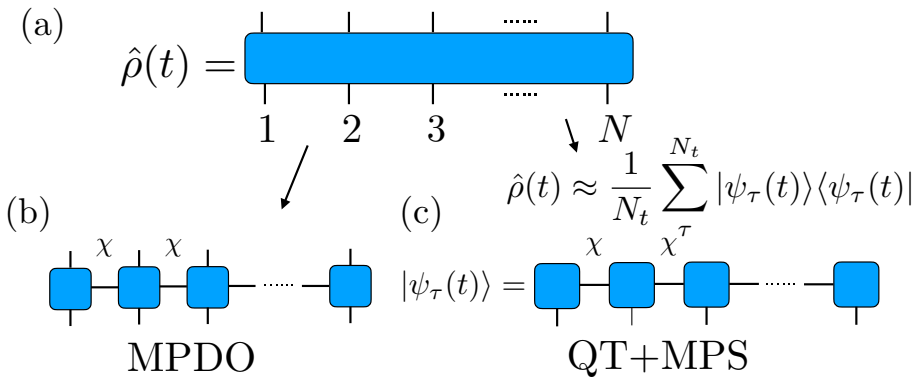

Figure 1: *Opérator Densité Produit Matriciel vs. Trajectoires Quantiques + Matrix Product States* — Schémas de différentes approches numériques pour simuler la dynamique des équations maîtresse

OE avec la croissance TE pour notre modèle de spin et pour les deux types de dissipation : émission/absorption spontanée et déphasage (voir Figs. 2 et 3 pour quelques comparatifs cruciaux résultats).

Dans le cas de l'émission/absorption spontanée, sur la Fig.2(a) pour MPDO on remarque un comportement de "montée et descente" qui peut s'expliquer par une dominance initiale de l'hamiltonien hermitien à $t \ll \gamma^-1$. Aux instants $t \geq \gamma^-1$ la cohérence initiale est détruite par la dissipation et l'OE diminue jusqu'à atteindre une valeur nulle. Pour QT+MPS, sur la Fig.2(b), la situation est différente ; plutôt que de voir un schéma de montée et de descente, ce que nous remarquons, c'est que, dans le cas d'une émission/absorption spontanée élevée, après la montée initiale, la valeur de TE atteint un plateau. Pour le cas de γ intermédiaire ou bas ceci est encore plus défavorable puisqu'on ne constate qu'une croissance continue de TE, ce qui complique sévèrement la possibilité d'une simulation à long terme. Pour le cas du déphasage, sur la Fig.3, pour le cas du MPDO, nous voyons d'abord le comportement "montée et descente" mais ensuite, de manière surprenante, nous remarquons une croissance logarithmique lente. Un tel comportement est expliqué plus en détail dans la section suivante. Or, dans le cas de QT+MPS, on observe une croissance très prononcée du TE, atteignant les valeurs maximales de , sans aucun signe de ralentissement.

En conclusion principale, ces résultats impliquent étonnamment que bien que l'approche MPDO semble initialement moins favorable par rapport à QT + MPS, en raison d'espaces d'états locaux réduits, à des temps plus longs, la méthode MPDO peut avoir des avantages fondamentaux. Ceci est une conséquence des différents comportements de mise à l'échelle de OE et TE à long terme. Outre l'avantage évident en termes de mise à l'échelle de l'entropie, il existe d'autres points en faveur de MPDO, tels que l'invariance translationnelle et une plus grande taille de pas de temps convergent, ce qui en fait l'approche la plus pratique dans la plupart des scénarios. La comparaison a été résumée dans un long article qui à été publiée sur *Phys. Rev. A* ***108****, 012616* [32]).

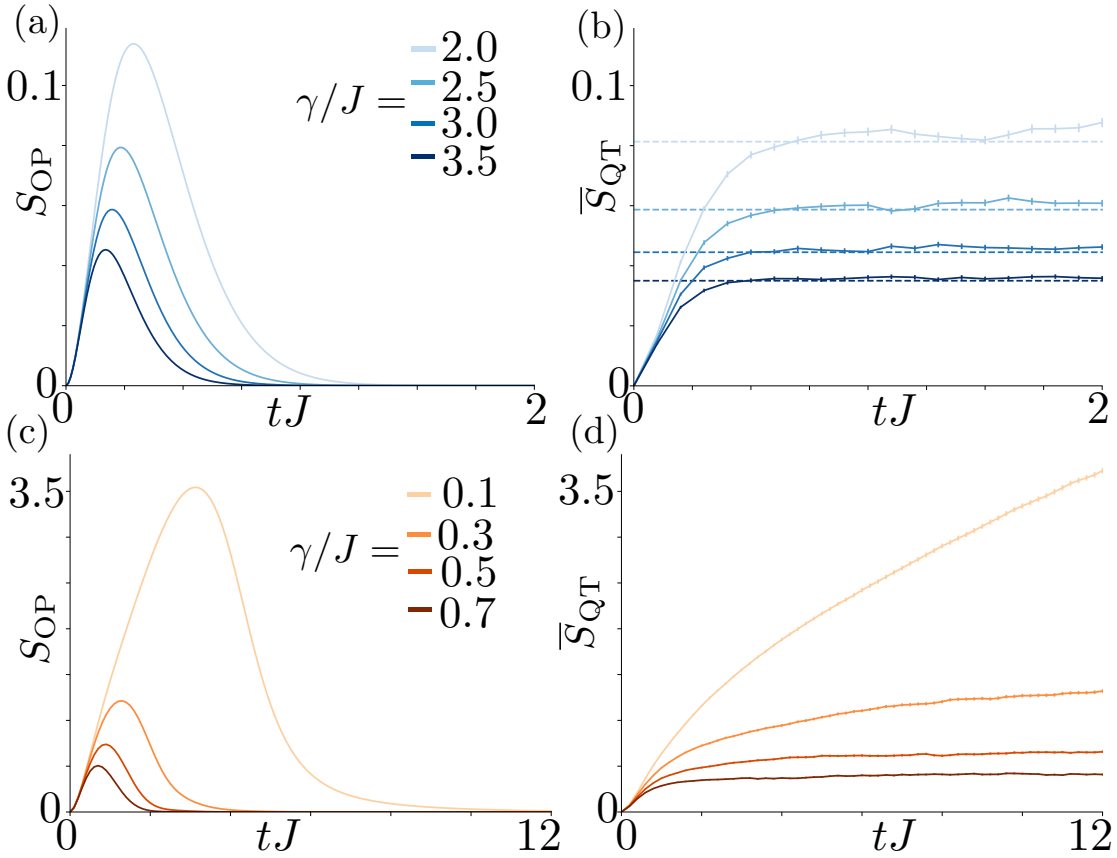

Figure 2: *MPDO vs QT+MPS en présence d'émission/absorption spontanée élevée et intermédiaire* — Évolution dans le temps de S_{OP} (a/c) et S_{QT} (b/d); Dans les deux cas, S_{OP} présente un comportement clairement ascendant et descendant. (b) Pour une émission/absorption spontanée élevée (taux $\gamma/J = 2.0, 2.5, 3.0, 3.5$) S_{QT} atteint rapidement une constante plateau (les lignes pointillées horizontales indiquent une estimation analytique). (d) En cas d'émission/absorption spontanée intermédiaire (taux $\gamma/J = 0.1, 0.3, 0.5, 0.7$) S_{QT} suit une augmentation continue qui diminue avec l'augmentation de γ jusqu'à atteindre un plateau autour des valeurs de $\gamma/J \geq 0.5$ [Pour MPDO: $N = \infty$; pour QT+MPS: $N = 40$; (b) $N_t = 2000$; (d) $N_t = 500$]

Résultat principal (ii) – Croissance de l'intrication d'opérateur logarithmique

Un autre résultat majeur de cette thèse est lié à la recherche d'une logarithmique de l'intrication des opérateurs aux temps longs.

Comme mentionné précédemment, dans le cas du déphasage, pour l'hamiltonien XXZ et l'état de Neél initial polarisé dans la direction $\hat{z}$, après une montée et une descente initiales, on remarque une augmentation logarithmique. Utilisation d'une combinaison de simulations MPO pour des chaînes d'infinies longueur et arguments analytiques valables pour un fort déphasage nous avons démontré que

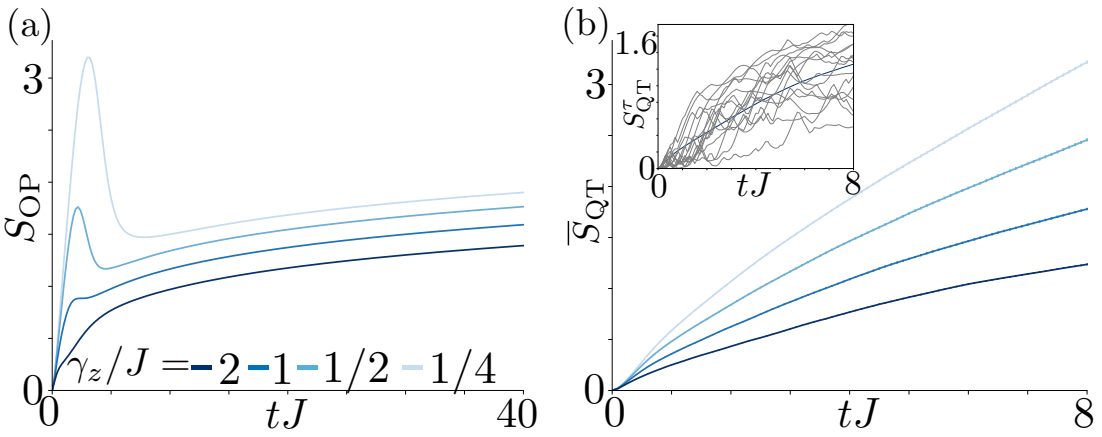

Figure 3: *MPDO vs QT+MPS en présence de déphasage* — Évolution temporelle des entropies pour $\gamma_z/J = 0.25, 0.5, 1, 2$ (lignes bleues solides, couleur du clair au foncé). (a) Montée et descente, et croissance logarithmique universelle à long terme de S_{OP} (Voir Fig. 4 pour plus de détails). (b) En revanche, S_{QT} croît régulièrement dans les simulations QT+MPS. [Pour MPDO: $N = \infty$, $\chi = 512$; pour QT+MPS: $\chi = 256$, $N_t = 400$]

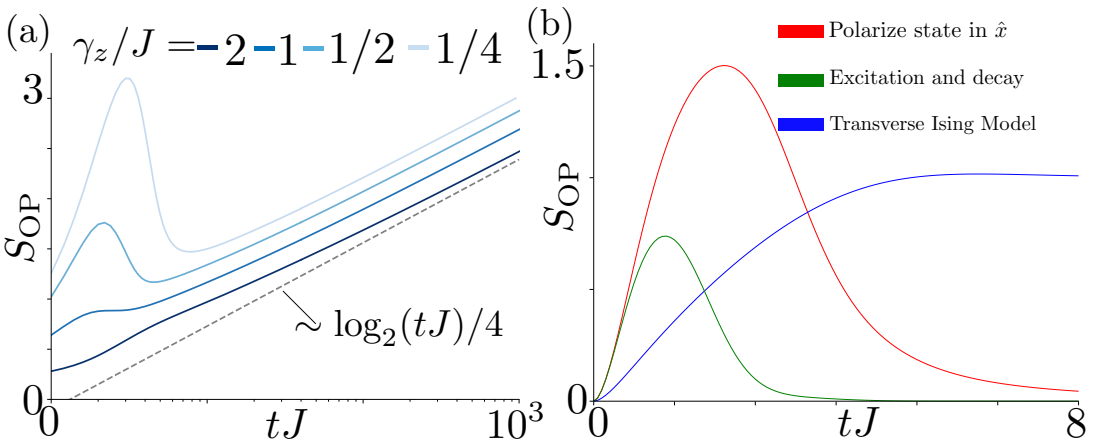

Figure 4: *La montée et la descente et la lente remontée de l'intrication de l'opérateur sous déphasage* — (a) Évolution temporelle des entropies pour $\gamma_z/J = 0.25, 0.5, 1, 2$ (blue solid lines, color from light to dark). The OE shows a logarithmic growth. (b) Breaking cases: In order give an idea of the mechanism that generates the logarithmic growth we give a series of examples that break the conservation of magnetisation and prevent the logarithmic growth from appearing.[For MPDO: $N = \infty$, $\chi = 512$; for QT+MPS: $\chi = 256$, $N_t = 400$]

cette croissance est inhérente à une loi de conservation $U(1)$.

Dans la Fig. 4, nous voyons d'abord qu'il s'agit en effet d'une croissance logarithmique, plus précisément à long terme, elle croît universellement comme $\frac{1}{4}\log(t)$. En revanche, sur la figure 4 (b), nous montrons comment, pour les scénarios qui cassent la conservation de l'aimantation, la croissance logarithmique se décompose également.

Les principales réalisations ont été : *i*) le développement d'un code numérique qui permet de simuler efficacement notre équation maîtresse pour un système infini (en exploitant l'invariance translationnelle du problème) ; et *ii*) Le développement d'une compréhension analytique complète de la croissance logarithmique universelle. Ce dernier pourrait être atteint dans une nouvelle théorie des perturbations, où la dynamique du système pourrait être mappée à des processus classiques efficaces pour les matrices de densité diagonales.

Conclusion générale

Cette thèse a conduit au développement de nouvelles techniques de simulation numérique basées sur la MPS pour simuler la dynamique quantique ouverte à plusieurs corps de modèles de spin-1/2. Avec ces codes, deux nouvelles idées principales ont été produites : Dans un premier travail, la thèse a réalisé une comparaison approfondie entre QT+MPS et MPDO. Nous avons montré des avantages significatifs pour la méthode MPDO. Dans le deuxième travail, nous expliquons l'augmentation logarithmique de l'OE dans une chaîne de spin XXZ avec déphasage. Nous avons pu expliquer ce comportement et démontrer que la croissance est inhérente à une loi de conservation $U(1)$.

Dans l'ensemble, cette thèse a contribué à une amélioration significative de notre compréhension de la croissance de l'intrication dans les systèmes quantiques ouverts à plusieurs corps. Cela sera crucial pour comprendre et modéliser les futures expériences de simulation quantique analogique, en particulier dans les systèmes avec des atomes ultrafroids.

Bibliography

[1] A. Einstein, B. Podolsky, and N. Rosen. Can Quantum-Mechanical Description of Physical Reality Be Considered Complete? *Phys. Rev.*, 47(10):777–780, May 1935.

[2] Stuart J. Freedman and John F. Clauser. Experimental Test of Local Hidden-Variable Theories. *Phys. Rev. Lett.*, 28(14):938–941, April 1972.

[3] Alain Aspect, Philippe Grangier, and Gérard Roger. Experimental Realization of Einstein-Podolsky-Rosen-Bohm Gedankenexperiment: A New Violation of Bell's Inequalities. *Phys. Rev. Lett.*, 49(2):91–94, July 1982.

[4] T. M. Graham, Y. Song, J. Scott, C. Poole, L. Phuttitarn, K. Jooya, P. Eichler, X. Jiang, A. Marra, B. Grinkemeyer, M. Kwon, M. Ebert, J. Cherek, M. T. Lichtman, M. Gillette, J. Gilbert, D. Bowman, T. Ballance, C. Campbell, E. D. Dahl, O. Crawford, N. S. Blunt, B. Rogers, T. Noel, and M. Saffman. Multi-qubit entanglement and algorithms on a neutral-atom quantum computer. *Nature*, 604:457–462, April 2022.

[5] Artur Ekert and Richard Jozsa. Quantum algorithms: entanglement–enhanced information processing. *Philosophical Transactions of the Royal Society of London. Series A: Mathematical, Physical and Engineering Sciences*, 356(1743):1769–1782, 1998.

[6] Ryszard Horodecki, Paweł Horodecki, Michał Horodecki, and Karol Horodecki. Quantum entanglement. *Rev. Mod. Phys.*, 81(2):865–942, June 2009.

[7] Thomas Jennewein, Christoph Simon, Gregor Weihs, Harald Weinfurter, and Anton Zeilinger. Quantum Cryptography with Entangled Photons. *Phys. Rev. Lett.*, 84(20):4729–4732, May 2000.

[8] Artur K. Ekert. Quantum cryptography based on Bell's theorem. *Phys. Rev. Lett.*, 67(6):661–663, August 1991.

[9] S. Pirandola, J. Eisert, C. Weedbrook, A. Furusawa, and S. L. Braunstein. Advances in quantum teleportation. *Nat. Photonics*, 9:641–652, October 2015.

[10] Guifré Vidal. Efficient Simulation of One-Dimensional Quantum Many-Body Systems. *Phys. Rev. Lett.*, 93(4):040502, July 2004.

[11] F. Verstraete, V. Murg, and J. I. Cirac. Matrix product states, projected entangled pair states, and variational renormalization group methods for quantum spin systems. *Adv. Phys.*, 57(2):143–224, March 2008.

[12] Ulrich Schollwöck. The density-matrix renormalization group in the age of matrix product states. *Ann. Phys.*, 326(1):96–192, January 2011.

[13] Sebastian Paeckel, Thomas Köhler, Andreas Swoboda, Salvatore R. Manmana, Ulrich Schollwöck, and Claudius Hubig. Time-evolution methods for matrix-product states. *Ann. Phys.*, 411:167998, December 2019.

[14] Andrew J. Daley, Immanuel Bloch, Christian Kokail, Stuart Flannigan, Natalie Pearson, Matthias Troyer, and Peter Zoller. Practical quantum advantage in quantum simulation. *Nature*, 607:667–676, July 2022.

[15] M. Morgado and S. Whitlock. Quantum simulation and computing with Rydberg-interacting qubits. *AVS Quantum Sci.*, 3(2), June 2021.

[16] H. Pichler, A. J. Daley, and P. Zoller. Nonequilibrium dynamics of bosonic atoms in optical lattices: Decoherence of many-body states due to spontaneous emission. *Phys. Rev. A*, 82(6):063605, December 2010.

[17] D. Wellnitz, G. Preisser, V. Alba, J. Dubail, and J. Schachenmayer. Rise and Fall, and Slow Rise Again, of Operator Entanglement under Dephasing. *Phys. Rev. Lett.*, 129(17):170401, October 2022.

[18] Norbert Schuch, Michael M. Wolf, Frank Verstraete, and J. Ignacio Cirac. Entropy Scaling and Simulability by Matrix Product States. *Phys. Rev. Lett.*, 100(3):030504, January 2008.

[19] Tomaž Prosen and Iztok Pižorn. Operator space entanglement entropy in a transverse Ising chain. *Phys. Rev. A*, 76(3):032316, September 2007.

[20] Tianci Zhou and David J. Luitz. Operator entanglement entropy of the time evolution operator in chaotic systems. *Phys. Rev. B*, 95(9):094206, March 2017.

[21] V. Alba, J. Dubail, and M. Medenjak. Operator Entanglement in Interacting Integrable Quantum Systems: The Case of the Rule 54 Chain. *Phys. Rev. Lett.*, 122(25):250603, June 2019.

[22] Kyungjoo Noh, Liang Jiang, and Bill Fefferman. Efficient classical simulation of noisy random quantum circuits in one dimension. *Quantum*, 4:318, September 2020.

[23] Tibor Rakovszky, C. W. von Keyserlingk, and Frank Pollmann. Dissipation-assisted operator evolution method for capturing hydrodynamic transport. *arXiv*, April 2020.

[24] J. Dubail. Entanglement scaling of operators: a conformal field theory approach, with a glimpse of simulability of long-time dynamics in 1 + 1d. *J. Phys. A: Math. Theor.*, 50(23):234001, May 2017.

[25] Bruno Bertini, Pavel Kos, and Tomaž Prosen. Operator Entanglement in Local Quantum Circuits I: Chaotic Dual-Unitary Circuits. *SciPost Phys.*, 8(4):067, April 2020.

[26] Bruno Bertini, Pavel Kos, and Tomaž Prosen. Operator Entanglement in Local Quantum Circuits II: Solitons in Chains of Qubits. *SciPost Phys.*, 8(4):068, April 2020.

[27] Jean Dalibard, Yvan Castin, and Klaus Mølmer. Wave-function approach to dissipative processes in quantum optics. *Phys. Rev. Lett.*, 68(5):580–583, February 1992.

[28] R. Dum, P. Zoller, and H. Ritsch. Monte Carlo simulation of the atomic master equation for spontaneous emission. *Phys. Rev. A*, 45(7):4879–4887, April 1992.

[29] Howard Carmichael. *An Open Systems Approach to Quantum Optics.* Springer, Berlin, Germany, 1993.

[30] Hendrik Weimer, Augustine Kshetrimayum, and Román Orús. Simulation methods for open quantum many-body systems. *Rev. Mod. Phys.*, 93(1):015008, March 2021.

[31] Andrew J. Daley. Quantum trajectories and open many-body quantum systems. *Adv. Phys.*, 63(2):77–149, March 2014.

[32] Guillermo Preisser, David Wellnitz, Thomas Botzung, and Johannes Schachenmayer. Comparing bipartite entropy growth in open-system matrix product simulation methods, March 2023. [Online; accessed 6. Jun. 2023].

Contents

Chapter 1

Introduction

The concept of entanglement was first introduced by Erwin Schrödinger in 1935 as a method to describe non-local correlations between particles that seemed to violate classical physics. These correlations were initially discussed in the seminal paper by Einstein, Podolsky, and Rosen titled "*Can Quantum-Mechanical Description of Physical Reality Be Considered Complete?*"[1]. In this paper, Einstein, Podolsky, and Rosen presented a thought experiment involving two particles correlated such that measuring the state of one particle would instantaneously determine the state of the other, irrespective of the distance between them. This paper sparked a series of discussions that initially did not yield significant advancement or understanding of this phenomenon. This changed in 1964 when John Bell formulated what is now known as Bell's Theorem, which opened up the possibility of experimentally testing the nature of entanglement. This led to a series of experiments, most notably those conducted by John Clauser and Stuart Freedman in 1964[2], and Alain Aspect in 1982 [3]. Aspect, along with Anton Zeillinger, was awarded the Nobel Prize in Physics in 2022 for his work on this subject.

Entanglement, in addition to providing valuable insights into the workings of nature, has been proven to be integral to many applications in quantum protocols and technologies, such as quantum computing [4–6], quantum cryptography[7, 8], and quantum teleportation [9]. Significantly, entanglement also underpins the feasibility of classically simulating quantum systems. This connection is encapsulated in the concept of Matrix Product States (MPS), which represents a decomposition of a many-body state vector into a product of $\chi \times \chi$ matrices (with the matrix entries being local kets) [10–13]. Analogous to MPS for pure states, a matrix product decomposition of the density matrix, known as density matrix product density operator, can also be defined [14–18]. The efficiency of such a decomposition is largely determined by the extent of 'operator entanglement'. Recent advancements, particularly in experiments with ultracold atoms, have brought the concept of analogue quantum simulation within reach [19]. The aim of these experiments is to simulate quantum dynamics experimentally, shedding light on scenarios where classical computer simulations falter. Hence, research into (operator) entanglement growth is a fundamental area of exploration. The objective of this thesis is to enhance our understanding of (operator) entanglement growth in

open quantum many-body systems.

In the following sections of this introduction, I will provide a concise overview of the results presented in this thesis. The initial section introduces Open Quantum Systems and Dissipation, followed by a discussion on Matrix Product States and Entanglement, which form the foundational concepts for the numerical studies within this thesis. We then delve into Quantum Trajectories represented as Matrix Product States, a crucial numerical tool leveraged in this work. We also introduce Trajectory Entanglement as a measure of entanglement entropy in Quantum Trajectories. Lastly, we encapsulate the primary findings of this thesis.

1.1 Open Quantum Systems

Within the domain of quantum mechanics, an open quantum system refers to any system that interacts with an external environment. Unlike isolated quantum systems, open quantum systems experience energy, matter, or information exchange with their surroundings. Accounting for every detail of these interactions and providing a comprehensive description of the environment would render most computational dynamics intractable.

Owing to the complexity of open quantum systems, it is necessary to utilize a series of approximations. The most notable among these is the Markov approximation, which presumes that the environment is memoryless [20]. This suggests that the time evolution of a system can be described solely by its current state, using a Markovian master equation. The well-known Lindblad master equation is an example of such a Markovian master equation, encapsulating both the unitary evolution, dictated by the Hamiltonian, and the non-unitary evolution emerging from interactions with the environment, represented by the Lindblad operators.

Various methods have been developed to handle open quantum systems under the Markov approximation. One method we will emphasize is quantum trajectories, a stochastic approach to analyzing system evolution [21]. Furthermore, multiple methods have been devised to manage open systems with Matrix Product States [22]. Chapter 2 introduces the most important methods used in this thesis.

1.2 Matrix Product States and Entanglement

Matrix Product States (MPS) have emerged as invaluable tools in the exploration of quantum many-body systems. Initially introduced as an efficient simulation framework for one-dimensional quantum systems, MPS have since radically transformed our understanding of entanglement and its implications for the classical simulation of quantum systems [23–25].

In quantum many-body systems, the representation of the system's state becomes increasingly challenging with the growth of the number of particles and the dimensionality of the system. Conventionally, the representation of a quantum state necessitates storing a large number of complex numbers, requiring an ex-

ponentially large quantity of memory and computational resources. For instance, in a system with N particles, each with d levels, the required number of complex numbers expands as d^N, making exact simulations for large-scale systems practically unfeasible.

MPS propose a clever solution to this problem through a compact representation that encapsulates the essential attributes of the quantum state. Instead of storing the entire wavefunction, MPS depict the state as a product of matrices with dimensions $\chi \times \chi$ (where the entries of the matrices are local kets). In such a representation, the bipartite von Neumann entanglement entropy S is bounded by $\max[S] = \log_2$. Therefore, to represent a physical state $|\psi(t)\rangle$ with entanglement entropy $S(t)$ as an MPS, the matrix size (or 'bond dimension') must grow at least as $\chi \propto 2^{S(t)}$ over time. For instance, an evolution where S increases linearly over time can hence be regarded as computationally challenging [26].

By truncating the entanglement entropy, MPS provide an approximation to the system's true state, preserving the most pertinent information while disregarding less critical details. Interestingly, for a broad range of problems such as near-equilibrium dynamics, low energies, and short timescales, a modest amount of entanglement is often sufficient to enable an accurate simulation. In these cases, the bond dimension χ of the MPS representation can remain relatively small, thereby making the simulation computationally manageable.

In parallel with MPSs for pure states, a matrix product density operator (MPDO) form of the density matrix $\hat{\rho}$ can also be defined. An MPDO form allows the easy expression of the density matrix as a Schmidt decomposition between a left and a right block. The bipartite entropy of this decomposition is given by the 'operator space entanglement entropy' or simply 'operator entanglement' (OE). The OE indicates the efficiency of an MPDO representation. It can be readily computed numerically [27–31] and is amenable to analytical treatment [32–34]. It's worth noting that, despite its name, OE does not necessarily denote genuine quantum entanglement between distinct blocks of spins when $\hat{\rho}$ is a mixed state.

Chapters 6 and 3 present the MPS and MPDO methods in greater detail, with a particular emphasis on their application to simulate many-body spin systems.

1.3 Quantum Trajectories and Entanglement

Alternatively to the MPDO approach, the density matrix can be non-uniquely decomposed into a statistical mixture of pure states, as illustrated in Fig. 1. Each pure state can then be represented as an MPS, and the efficiency of such a representation is determined by the bipartite entanglement entropies in the individual states. To compute the time evolution of these states, they can be stochastically evolved using a technique known as the Quantum Monte Carlo wavefunction method or Quantum Trajectories (QT) [35–37].

This approach has been successfully applied in numerous MPS simulations [18, 38]. We refer to this as the QT+MPS method, and define the average bipartite entropy of the trajectories as 'Trajectory Entanglement' (TE). Importantly, similar to OE, TE does not necessarily relate to genuine entanglement between distinct

blocks of spins, but should rather be interpreted as a measure of the efficiency of the QT+MPS method for simulating a system.

A significant portion of this thesis is dedicated to a detailed comparison between the MPDO and the QT+MPS methods. Our results show considerable advantages for the MPDO method. Nevertheless, QT+MPS remains a very useful technique that, by providing access to individual trajectories constituting the density matrix ensemble, can reveal crucial insights into the properties of the system.

1.4 Overview of Results

This thesis advances the theoretical understanding of entanglement entropy dynamics in open spin systems and investigates the practical implications of these insights for simulating many-body open spin systems using tensor network methods.

Chapter 2 presents an overview of the open quantum systems theory, introducing key concepts including the Lindblad equation, which governs the system's dynamics in the presence of an environment. This chapter also explores Quantum Trajectories, offering a numerical alternative for deriving system dynamics by introducing dissipation through a Monte Carlo process.

In Chapter 3, we delve into Matrix Product States (MPS), providing a comprehensive overview of the technique and its application in the evolution of quantum many-body systems. Towards the chapter's end, we introduce the XXZ model, which serves as the main model used in this thesis. We execute simulations to understand this system's general properties and discuss essential aspects to consider when employing MPS methods for such model simulations.

Chapter 4 offers a more detailed discussion on entanglement entropy, examining various metrics for its quantification. We place particular emphasis on the area law.

Subsequently, Chapter 5 combines quantum trajectories with MPS into the QT+MPS method. This technique proposes an alternative to density matrix simulations for open quantum many-body systems. Additionally, we explore how trajectories can shed light on conserved quantities in an open system.

Chapter 6 pivots the focus to the theory of matrix product density operators (MPDO), underlining the feasibility of simulating infinite translationally invariant systems. We introduce the Operator Entanglement (OE) and examine how conserved quantities influence its behavior in the context of open systems.

Chapters 7 and 8 unveil the two major findings of this thesis. First, we study an XXZ spin chain, introducing dephasing as a form of dissipation, and observe a 'rise and fall' pattern succeeded by logarithmic growth in the OE dynamics. We offer an in-depth analytical understanding of the OE dynamics in this scenario. Our second substantial work entails a meticulous comparison between the QT+MPS and MPDO techniques for simulating open spin systems, highlighting significant advantages of the MPDO method.

Finally, Chapter 9 recaps the work presented, underlines its most significant implications, and outlines potential future research directions.

Bibliography

[1] A. Einstein, B. Podolsky, and N. Rosen. Can Quantum-Mechanical Description of Physical Reality Be Considered Complete? *Phys. Rev.*, 47(10):777–780, May 1935.

[2] Stuart J. Freedman and John F. Clauser. Experimental Test of Local Hidden-Variable Theories. *Phys. Rev. Lett.*, 28(14):938–941, April 1972.

[3] Alain Aspect, Philippe Grangier, and Gérard Roger. Experimental Realization of Einstein-Podolsky-Rosen-Bohm Gedankenexperiment: A New Violation of Bell's Inequalities. *Phys. Rev. Lett.*, 49(2):91–94, July 1982.

[4] T. M. Graham, Y. Song, J. Scott, C. Poole, L. Phuttitarn, K. Jooya, P. Eichler, X. Jiang, A. Marra, B. Grinkemeyer, M. Kwon, M. Ebert, J. Cherek, M. T. Lichtman, M. Gillette, J. Gilbert, D. Bowman, T. Ballance, C. Campbell, E. D. Dahl, O. Crawford, N. S. Blunt, B. Rogers, T. Noel, and M. Saffman. Multi-qubit entanglement and algorithms on a neutral-atom quantum computer. *Nature*, 604:457–462, April 2022.

[5] Artur Ekert and Richard Jozsa. Quantum algorithms: entanglement–enhanced information processing. *Philosophical Transactions of the Royal Society of London. Series A: Mathematical, Physical and Engineering Sciences*, 356(1743):1769–1782, 1998.

[6] Ryszard Horodecki, Paweł Horodecki, Michał Horodecki, and Karol Horodecki. Quantum entanglement. *Rev. Mod. Phys.*, 81(2):865–942, June 2009.

[7] Thomas Jennewein, Christoph Simon, Gregor Weihs, Harald Weinfurter, and Anton Zeilinger. Quantum Cryptography with Entangled Photons. *Phys. Rev. Lett.*, 84(20):4729–4732, May 2000.

[8] Artur K. Ekert. Quantum cryptography based on Bell's theorem. *Phys. Rev. Lett.*, 67(6):661–663, August 1991.

[9] S. Pirandola, J. Eisert, C. Weedbrook, A. Furusawa, and S. L. Braunstein. Advances in quantum teleportation. *Nat. Photonics*, 9:641–652, October 2015.

[10] Guifré Vidal. Efficient Simulation of One-Dimensional Quantum Many-Body Systems. *Phys. Rev. Lett.*, 93(4):040502, July 2004.

[11] F. Verstraete, V. Murg, and J. I. Cirac. Matrix product states, projected entangled pair states, and variational renormalization group methods for quantum spin systems. *Adv. Phys.*, 57(2):143–224, March 2008.

[12] Ulrich Schollwöck. The density-matrix renormalization group in the age of matrix product states. *Ann. Phys.*, 326(1):96–192, January 2011.

[13] Sebastian Paeckel, Thomas Köhler, Andreas Swoboda, Salvatore R. Manmana, Ulrich Schollwöck, and Claudius Hubig. Time-evolution methods for matrix-product states. *Ann. Phys.*, 411:167998, December 2019.

[14] Michael Zwolak and Guifré Vidal. Mixed-State Dynamics in One-Dimensional Quantum Lattice Systems: A Time-Dependent Superoperator Renormalization Algorithm. *Phys. Rev. Lett.*, 93(20):207205, November 2004.

[15] R. Orús and G. Vidal. Infinite time-evolving block decimation algorithm beyond unitary evolution. *Phys. Rev. B*, 78(15):155117, October 2008.

[16] A. H. Werner, D. Jaschke, P. Silvi, M. Kliesch, T. Calarco, J. Eisert, and S. Montangero. Positive Tensor Network Approach for Simulating Open Quantum Many-Body Systems. *Phys. Rev. Lett.*, 116(23):237201, June 2016.

[17] Jiří Guth Jarkovský, András Molnár, Norbert Schuch, and J. Ignacio Cirac. Efficient Description of Many-Body Systems with Matrix Product Density Operators. *PRX Quantum*, 1(1):010304, September 2020.

[18] Hendrik Weimer, Augustine Kshetrimayum, and Román Orús. Simulation methods for open quantum many-body systems. *Rev. Mod. Phys.*, 93(1):015008, March 2021.

[19] Andrew J. Daley, Immanuel Bloch, Christian Kokail, Stuart Flannigan, Natalie Pearson, Matthias Troyer, and Peter Zoller. Practical quantum advantage in quantum simulation. *Nature*, 607:667–676, July 2022.

[20] C. W. Gardiner and P. Zoller. *Quantum noise*. Springer, 1991.

[21] Andrew J. Daley. Quantum trajectories and open many-body quantum systems. *Adv. Phys.*, 63(2):77–149, Mar 2014.

[22] Hendrik Weimer, Augustine Kshetrimayum, and Román Orús. Simulation methods for open quantum many-body systems. *Rev. Mod. Phys.*, 93(1):015008, March 2021.

[23] Guifré Vidal. Efficient Simulation of One-Dimensional Quantum Many-Body Systems. *Phys. Rev. Lett.*, 93(4):040502, Jul 2004.

[24] Steven R. White. Density matrix formulation for quantum renormalization groups. *Phys. Rev. Lett.*, 69(19):2863–2866, November 1992.

[25] Ulrich Schollwöck. The density-matrix renormalization group in the age of matrix product states. *Ann. Phys.*, 326(1):96–192, Jan 2011.

[26] Norbert Schuch, Michael M. Wolf, Frank Verstraete, and J. Ignacio Cirac. Entropy Scaling and Simulability by Matrix Product States. *Phys. Rev. Lett.*, 100(3):030504, January 2008.

[27] Tomaž Prosen and Iztok Pižorn. Operator space entanglement entropy in a transverse Ising chain. *Phys. Rev. A*, 76(3):032316, September 2007.

[28] Tianci Zhou and David J. Luitz. Operator entanglement entropy of the time evolution operator in chaotic systems. *Phys. Rev. B*, 95(9):094206, March 2017.

[29] V. Alba, J. Dubail, and M. Medenjak. Operator Entanglement in Interacting Integrable Quantum Systems: The Case of the Rule 54 Chain. *Phys. Rev. Lett.*, 122(25):250603, June 2019.

[30] Kyungjoo Noh, Liang Jiang, and Bill Fefferman. Efficient classical simulation of noisy random quantum circuits in one dimension. *Quantum*, 4:318, September 2020.

[31] Tibor Rakovszky, C. W. von Keyserlingk, and Frank Pollmann. Dissipation-assisted operator evolution method for capturing hydrodynamic transport. *arXiv*, April 2020.

[32] J. Dubail. Entanglement scaling of operators: a conformal field theory approach, with a glimpse of simulability of long-time dynamics in 1 + 1d. *J. Phys. A: Math. Theor.*, 50(23):234001, May 2017.

[33] Bruno Bertini, Pavel Kos, and Tomaž Prosen. Operator Entanglement in Local Quantum Circuits I: Chaotic Dual-Unitary Circuits. *SciPost Phys.*, 8(4):067, April 2020.

[34] Bruno Bertini, Pavel Kos, and Tomaž Prosen. Operator Entanglement in Local Quantum Circuits II: Solitons in Chains of Qubits. *SciPost Phys.*, 8(4):068, April 2020.

[35] Jean Dalibard, Yvan Castin, and Klaus Mølmer. Wave-function approach to dissipative processes in quantum optics. *Phys. Rev. Lett.*, 68(5):580–583, February 1992.

[36] R. Dum, P. Zoller, and H. Ritsch. Monte Carlo simulation of the atomic master equation for spontaneous emission. *Phys. Rev. A*, 45(7):4879–4887, April 1992.

[37] Howard Carmichael. *An Open Systems Approach to Quantum Optics*. Springer, Berlin, Germany, 1993.

[38] Andrew J. Daley. Quantum trajectories and open many-body quantum systems. *Adv. Phys.*, 63(2):77–149, March 2014.

Chapter 2

Open Quantum Systems

Traditionally in quantum mechanics, the study of isolated systems has provided us with profound insights into the fundamental nature of matter and energy. However, in reality, quantum systems rarely exist in perfect isolation. They are constantly subjected to interactions and entanglements with their surroundings. Such a system, which interacts with its environment, is defined as an open quantum system [1, 2]. In the context of open quantum systems, the environment is often referred to as a "bath" or "reservoir". This bath can comprise various degrees of freedom, such as photons, phonons, or other environmental particles, depending on the specific physical system under study.

Open quantum systems encompass a wide array of phenomena that arise when quantum entities, like atoms, molecules, or solid-state systems, interact with their environment. These interactions lead to intriguing phenomena such as decoherence and dissipation, which profoundly impact the behavior and properties of the quantum system. The understanding and control of these phenomena are crucial for fully harnessing the potential of quantum technologies and exploring the boundary between quantum and classical realms.

More specifically, in the context of this thesis, one central question we address is how the environment impacts the simulatability of many-body quantum systems. In other words, how does dissipation influence the growth of entanglement entropy in the dynamics of many-body quantum systems? Answering this question is complex and requires considering various factors, such as the model used to represent the interaction with the environment, the simulation method applied to the system, the type of dissipation, as well as the initial state and the Hamiltonian used for its evolution. To make the first steps towards a satisfying answer, a basic understanding of open quantum systems is indispensable.

In this chapter, we will provide an overview of open quantum systems theory. We will primarily focus on the density matrix, which is the mathematical construct that describes the system under environmental influence, and we will aim to understand and derive the Lindblad Master equation, which dictates the evolution of the density matrix. Finally, we will introduce Quantum Trajectories, which play a significant role in the work presented in this thesis.

2.1 The Density Matrix

The density matrix, also known as the density operator, is a fundamental mathematical construct in quantum mechanics that enables a statistical description of quantum states. Unlike the wavefunction, which represents the complete information of a quantum system, the density matrix incorporates both pure states and mixed states, accounting for uncertainties arising from environmental interactions, measurement uncertainties, or partial knowledge of the system. Every density operator for a system is a positive semi-definite, Hermitian operator of trace one acting on the Hilbert space of the system and generally can be expressed as [3, 4]

$$\hat{\rho} = \sum_j p_j \left|\psi_j\right\rangle \left\langle\psi_j\right|, \tag{2.1}$$

where $0 \leq p_j \leq 1$ and $\sum_j p_j = 1$. In order to know if a density matrix corresponds a pure state one can verify the following properties. A density operator represents a pure state if and only if:

- It can be written as an outer product of a state vector $|\psi\rangle$ with itself, that is, $\hat{\rho} = |\psi\rangle \langle\psi|$.
- It is idempotent, that is $\hat{\rho} = \hat{\rho}^2$.
- It has purity one, that is $\mathrm{tr}(\rho^2) = 1$

Regarding operations such as expected values, this will be simply be done by $\mathrm{tr}(\hat{\rho}\hat{A})$, which can be easily seen from

$$\left\langle \hat{A} \right\rangle = \sum_j p_j \left\langle\psi_j\right| \hat{A} \left|\psi_j\right\rangle = \sum_j p_j \mathrm{tr}(\left|\psi_j\right\rangle \left\langle\psi_j\right| \hat{A}) = \mathrm{tr}\left(\sum_j p_j \left|\psi_j\right\rangle \left\langle\psi_j\right| \hat{A} \right) = \mathrm{tr}(\hat{\rho}\hat{A}). \tag{2.2}$$

In the case for close systems the evolution of the density matrix is given by the von Neumann equation

$$\partial_t \hat{\rho} = -\mathrm{i}\big[\hat{H}, \hat{\rho}\big] \tag{2.3}$$

where $\hat{H}$ is the system's Hamiltonian. For the case of open quantum systems, where there is dissipation present, one has to resort to the Lindblad Master Equation.

It is also important to mention that, given that the Pauli matrices provide a basis for 2×2 self-adjoint matrices, it is possible to write any arbitrary state for a qubit in the form

$$\hat{\rho} = \frac{1}{2}(\hat{I} + \mathbf{a} \cdot \hat{\boldsymbol{\sigma}}) \tag{2.4}$$

The coefficient $\boldsymbol{a}$ is named the Bloch vector and can be calculated as the expectation value of the Pauli matrices.

$$\boldsymbol{a} = \mathrm{tr}(\hat{\rho}\hat{\boldsymbol{\sigma}}) = \langle \hat{\boldsymbol{\sigma}} \rangle \tag{2.5}$$

Points with $|\boldsymbol{a}| = 1$ represent pure states, while mixed states are represented by points in the interior. This is known as the Bloch sphere picture of qubit state space.

2.2 The Lindblad Master Equation

The Lindblad master equation is a mathematical description used in quantum mechanics to model how open quantum systems evolve over time. It is named after the physicist Goran Lindblad, who developed this equation in the 1970s. It is given by

$$\partial_t \hat{\rho} = -\mathrm{i}\big[\hat{H}, \hat{\rho}\big] + \sum_i \gamma_i \Big(2\hat{C}_i \hat{\rho} \hat{C}_i^\dagger - \hat{C}_i^\dagger \hat{C}_i \hat{\rho} - \hat{\rho} \hat{C}_i^\dagger C_i\Big), \tag{2.6}$$

where H is the system's Hamiltonian, describing the unitary aspects of the dynamics, and $\hat{C}_i$ are a set of jump operators describing the dissipative part of the dynamics and γ_i are the corresponding dissipation rates. The jump operators describe how the environment acts on the system, and must ultimately be determined from microscopic models of the system-environment dynamics.

In order to derivate the Lindblad equation we will start by introducing two of the main approximations which will be essential in order to capture the loss of information and irreversible evolution of an open quantum system: the Born and the Markov approximations.

Born Approximation: The Born approximation assumes that the system-environment interaction is weak. This means that the system's influence on the environment and vice versa is relatively small. It allows us to treat the system-environment interaction as a perturbation and simplify the calculations.

Markov Approximation: The Markov approximation assumes that the system and the environment quickly reach a state of equilibrium, or at least a quasi-steady state. In other words, the environment forgets its past interactions with the system very rapidly. This approximation simplifies the mathematics by allowing us to ignore the memory of the environment and treat the system's evolution as memoryless.

In order to describe the dynamics of the system and the bath we use the Hamiltonian

$$\hat{H} = \hat{H}_S + \hat{H}_B + \hat{H}_{SB}, \tag{2.7}$$

where H_S is the system's Hamiltonian, H_B is the bath's Hamiltonian and H_{SB} is the system-bath interaction.

While it is possible to describe the dynamics of the entire system (including the bath and the interaction), let's call it $\hat{\Omega}$, through a Liouville equation $\partial_t \hat{\Omega} = -\mathrm{i}\big[\hat{H}, \hat{\Omega}\big]$. Given that this equation contains an infinite number of degrees of freedom, is impossible to solve analytically except in very particular cases. So, making use of the approximations previously stated, we are going to be able to ignore the degrees of freedom of the bath and arrive to an equation of the density matrix of the system only, by tracing over the bath, $\hat{\rho} = \mathrm{tr}_B(\hat{\Omega})$. For convenient we will change to the interaction picture, defined by the unitary transformation $\tilde{\hat{M}} = \hat{U}_0 \hat{M} \hat{U}_O^\dagger$, where $\hat{M}$ is an arbitrary operator and $\hat{U}_0 = e^{i(\hat{H}_S + \hat{H}_B)}$. It is easy to note that the Liouville equation becomes

$$\partial_t \tilde{\hat{\Omega}} = -\mathrm{i}\big[\tilde{\hat{H}}_{BS}, \tilde{\hat{\Omega}}\big] \tag{2.8}$$

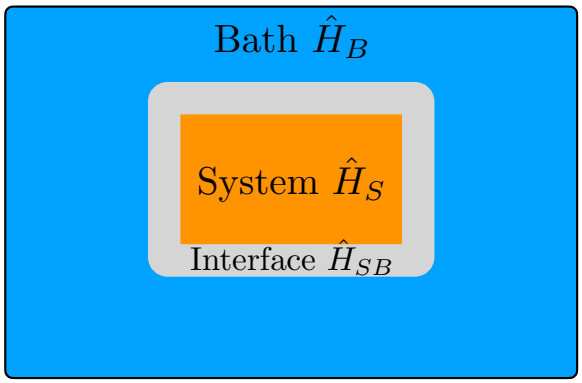

Figure 2.1: Bipartition between system and bath

Making use of the explicit time-dependence of the Hamiltonian, we can integrate directly

$$\tilde{\hat{\Omega}}(t) = \tilde{\hat{\Omega}}(0) - \mathrm{i}\int_0^t dt'[\tilde{\hat{H}}_{BS}(t'), \tilde{\hat{\Omega}}(t')]. \tag{2.9}$$

This implicit equation for can be substituted back into the Liouville equation to obtain an exact differo-integral equation

$$\partial_t\tilde{\hat{\Omega}}(t) = -\mathrm{i}[\tilde{\hat{H}}_{BS}, \tilde{\hat{\Omega}}(0)] - \mathrm{i}\int_0^t dt'[\tilde{\hat{H}}_{BS}(t), [\tilde{\hat{H}}_{BS}(t'), \tilde{\hat{\Omega}}(t')]]. \tag{2.10}$$

We proceed with the derivation by assuming the interaction is initiated at $t = 0$, and at that time there are no correlations between the system and the bath. This allows to express our initial state in the form $\hat{\Omega}(0) = \hat{\rho}(0) \otimes \hat{R}_0$, where R_0 is the density operator of the bath initially.

We proceed by tracing over the bath degrees of freedom of the integral, which yields

$$\partial_t\tilde{\hat{\rho}}(t) = -\mathrm{i}\int_0^t dt'\mathrm{tr}_R\Big\{[\tilde{\hat{H}}_{BS}(t), [\tilde{\hat{H}}_{BS}(t'), \tilde{\hat{\Omega}}(t')]]\Big\}. \tag{2.11}$$

This equation is exact for the dynamics of the density matrix, however there is the problem that it also requires the full knowledge of the dynamics of the bath degrees of freedom. It is here where we will make use of the **Born approximation**, which rests on the largeness of the bath and the fact that the coupling is weak, which would lead to an effective evolution of the system only, with the bath acting only in form of dissipation. This allows to factorize the density matrix at all times as $\tilde{\hat{\Omega}}(t) = \tilde{\hat{\rho}}(t) \otimes \hat{R}_0$. The master equation then becomes

$$\partial_t\tilde{\hat{\rho}}(t) = -\mathrm{i}\int_0^t dt'\mathrm{tr}_R\Big\{[\tilde{\hat{H}}_{BS}(t), [\tilde{\hat{H}}_{BS}(t'), \hat{\rho}(t') \otimes \hat{R}_0]]\Big\}. \tag{2.12}$$

A final assumption, which makes it easier to solve is the **Markov approximation**, in which we assume that the time derivative of the density matrix depends only on its current state, and not on its past. This can be justified considering fast bath dynamics, wherein correlations within the bath are lost extremely quickly, and amounts to replacing $\hat{\rho}(t') \to \hat{\rho}(t)$

$$\partial_t \tilde{\hat{\rho}}(t) = -\mathrm{i} \int_0^t dt' \mathrm{tr}_R \Big\{ [\tilde{\hat{H}}_{BS}(t), [\tilde{\hat{H}}_{BS}(t'), \tilde{\hat{\rho}}(t) \otimes \hat{R}_0]] \Big\}. \tag{2.13}$$

If the interaction Hamiltonian is assumed to have the form

$$\hat{H}_{BS} = \sum_i \hat{\alpha}_i \hat{\Gamma}_i \tag{2.14}$$

for system operators $\hat{\alpha}_i$ and bath operators $\hat{\Gamma}_i$, then $\tilde{\hat{H}}_{BS} = \tilde{\hat{\alpha}}_i \tilde{\hat{\Gamma}}_i$. The master equation becomes

$$\partial_t \tilde{\hat{\rho}}(t) = -\mathrm{i} \int_0^t dt' \mathrm{tr}_R \Big\{ [\tilde{\hat{\alpha}}_i(t) \tilde{\hat{\Gamma}}_i(t), [\tilde{\hat{\alpha}}_j(t') \tilde{\hat{\Gamma}}_i(t'), \hat{\rho}(t) \otimes \hat{R}_0]] \Big\}. \tag{2.15}$$

which can be expanded as

$$\begin{aligned} \partial_t \tilde{\hat{\rho}}(t) = -\mathrm{i} \int_0^t dt' [& (\tilde{\hat{\alpha}}_i(t) \tilde{\hat{\alpha}}_j(t') \tilde{\hat{\rho}}(t) - \tilde{\hat{\alpha}}_i(t) \tilde{\hat{\rho}}(t) \tilde{\hat{\alpha}}_j(t')) \langle \tilde{\hat{\Gamma}}_i(t) \tilde{\hat{\Gamma}}_j(t') \rangle \\ & + (\tilde{\hat{\rho}}(t) \tilde{\hat{\alpha}}_j(t') \tilde{\hat{\alpha}}_i(t) - \tilde{\hat{\alpha}}_j(t') \tilde{\hat{\rho}}(t) \tilde{\hat{\alpha}}_i(t)) \langle \tilde{\hat{\Gamma}}_j(t') \tilde{\hat{\Gamma}}_i(t) \rangle)] \end{aligned} \tag{2.16}$$

The expectation values are with respect to the bath degrees of freedom.Assuming rapid decay of these correlations (ideally $\langle \tilde{\hat{\Gamma}}_i(t) \tilde{\hat{\Gamma}}_j(t') \rangle \propto \delta(t - t')$), which is part the Markov approximation, the form of the Lindblad equation (8.3) is achieved.

2.3 Vectorization of the Density Matrix

Now we will introduce a vectorization of the density matrix and Lindblad master equation (8.3). While right now it won't seem of much use such representation will be of great help when we apply tensor network methods for the simulation of the (vectorized) density operator. We start by considering the density operator as a $D \times D$ matrix, where D is the dimension of the Hilbert space (i.e. dim $\mathcal{H} = d^N$ where N is the number of sites and d the number of levels of the system), and we want to express it as a D^2 dimension vector in the form

$$\vec{\rho} = \sum_{n=1}^{D^2} c_n \hat{e}_n. \tag{2.17}$$

Here, the role of basis vectors is done by matrices, which we now call basis operators. Under such decomposition the vector space spanned by the density matrices has a well-defined scalar product defined by the trace, i.e. $\vec{\rho_1} \cdot \vec{\rho_2} = \mathrm{tr}(\vec{\rho_1} \vec{\rho_2})$. Under such scalar product the basis operators then have to fulfill the condition $\mathrm{tr}(\hat{\sigma}_i \hat{\sigma}_j) = \delta_{i,j}$. Considering a two-level system, one could initially opt for a traditional basis $\hat{e}_1 = |0\rangle\langle 0|, \hat{e}_2 |0\rangle\langle 1|, \hat{e}_3 = |1\rangle\langle 0|, \hat{e}_4 = |1\rangle\langle 1|$, however a more convenient choice – through which one avoids the use of complex numbers for the

coefficients which is computationally more expensive – are the Gell-Mann matrices [5]. For two-level systems they are related to the Pauli matrices as

$$\hat{e}_1 = \frac{1}{\sqrt{2}}\mathbb{1} \quad \hat{e}_2 = \frac{1}{\sqrt{2}}\hat{\sigma}^x$$
$$\hat{e}_3 = \frac{1}{\sqrt{2}}\hat{\sigma}^y \quad \hat{e}_4 = \frac{1}{\sqrt{2}}\hat{\sigma}^z. \tag{2.18}$$

Using this basis one is able to express the vectorized density matrix in a similar form as in (2.4), where the coefficients c_n will be simply the projection of ρ under each basis vector $c_n = \mathrm{tr}(\hat{e}_n\vec{\rho})$.

As for the Lindblad equation, its vectorized form will be expressed as

$$\partial_t\vec{\rho} = \mathcal{L}\vec{\rho}. \tag{2.19}$$

We call $\mathcal{L}$ the Liouvillian super-operator, since is an operator acting on operators. The Liouvillian super-operator will be given by a $D^2 \times D^2$ matrix. Here it can be convenient to clarify how does the superoperator $\mathcal{L}$ acts on the vectorized density matrix. Some important points to take into account are the following:

- A left multiplication of the matrix $\hat{\rho}$ by an $D \times D$ matrix $\hat{A}$, i.e. $\hat{A}\hat{\rho}$, is equivalent to an operation on $\vec{\rho}$ by the $D^2 \times D^2$ matrix $\hat{I} \otimes \hat{A}$, where $\hat{I}$ is the $D \times D$ identity matrix.

- Similarly, a right multiplication of the matrix $\hat{\rho}$ by an $D \times D$ matrix B, i.e. $\hat{\rho}B$, is equivalent to an operation on the vector $\vec{\rho}$ by the $D^2 \times D^2$ matrix $\hat{B}^T \otimes \hat{I}$. Here T denotes the transpose of the matrix.

- Finally, a combination of left and right matrices multiplication, $\hat{A}\hat{\rho}\hat{B}$, is equivalent to an operation on the vector $\vec{\rho}$ by the $D^2 \times D^2$ matrix $\hat{B}^T \otimes \hat{A}$.

Going back to differential equation (2.19), in which the solution is given by

$$\vec{\rho}(t) = e^{\mathcal{L}t}\vec{\rho}(0). \tag{2.20}$$

The operation of the super-operator $e^{\mathcal{L}t}$ on the density matrix could be understood as a repetitive operations of the super-operator $\mathcal{L}$ as in the Taylor expansion:

$$e^{\mathcal{L}t}\vec{\rho} \equiv \sum_k \frac{1}{k!}\mathcal{L}\vec{\rho}t^k = \vec{\rho} + \mathcal{L}\vec{\rho}t + \frac{1}{2}\mathcal{L}^2\vec{\rho}t^2 + \dots \tag{2.21}$$

Typically, the resulting dynamics of the system observables (expectation values and other correlation functions) $c(t)$ will have the analytical form of sum of decaying oscillations [6]

$$c(t) = \sum_m d_m e^{\lambda_m t}. \tag{2.22}$$

Here, λ_m are the exponential coefficients and d_m are the associated amplitudes, both can be complex. We may divide λ_m into its real and imaginary parts, $\lambda_m = -\alpha_m + \mathrm{i}\omega_m$, with α_m as the decay rates and ω_m as the oscillation frequencies.

The coefficients λ_m are the eigenvalues of the super-operator $\mathcal{L}$, obtained by the eigenvalue equation:

$$\mathcal{L}\vec{\sigma}_m = \lambda_m \vec{\sigma}_m \tag{2.23}$$

These eigenvalues can be used for the analysis of the Liouvillian super-operator dynamics. However to solve the equation exactly an obtain an exact value for the coefficients λ_m and the amplitudes d_m can be challenging, so one normally recurs to numerical methods, such as quantum trajectories.

2.4 Quantum Trajectories

Quantum trajectory techniques, developed in Quantum Optics in the early 1990s [7–11], serve as means of numerically simulating dissipative dynamics. These techniques can be applied to any system where the time evolution of the density operator is described via a master equation (in Lindblad form).

The essential idea of quantum trajectories is to treat the evolution of a quantum system as a stochastic process. This approach accounts for the random nature of measurements and the inherent fluctuations in quantum dynamics. Unlike traditional methods that solve the master equation either analytically or numerically, quantum trajectories offer a probabilistic description of the system's evolution. This is achieved by considering individual stochastic realizations, or "trajectories."

Initially, the advantage of the quantum trajectory lies in propagating state vectors of a size smaller than the portion of the Hilbert space one would typically use in the case of density matrix propagation. To illustrate, for a state with a Hilbert space dimension of $\dim(\mathcal{H}) = d^N$, the corresponding density matrix would rely on a Hilbert space of dimension $\dim(\mathcal{H}) = d^{2N}$. However, a significant downside of this method is the need to collect many samples to minimize statistical errors. Therefore, for the method to be efficient, it's crucial that the number of samples required remains smaller than the size of the Hilbert space [12].

2.4.1 Wave Function Unravelling

Essentially what we want to achieve through the quantum trajectory method is an approximation of density operator $\hat{\rho}$ of the form

$$\hat{\rho}(t) \approx \frac{1}{N_t} \sum_{\tau=1}^{N_t} |\psi_\tau(t)\rangle \langle\psi_\tau(t)| , \tag{2.24}$$

where each trajectory $|\psi_\tau\rangle$ evolves stochastically with a non-hermitian Hamiltonian

$$\hat{H} = \hat{H}_s - \tfrac{i\hbar}{2} \sum_m \gamma_m \hat{C}_m^\dagger \hat{C}_m. \tag{2.25}$$

Here it is important to remark that since the Hamiltonian is non-hermitian, it will not conserve probability. Just as with the master equation (8.3), the $\hat{C}_m$

are the jump operators which will introduce the dissipation, and γ_m are the correspondent dissipation rates. The simplest form of the quantum trajectory method involves expanding the master equation to first order in a time step δt, and was first described in this form by Dalibard et al. [9] and Dum et al. [11].The process though which trajectory evolves $|\psi_\tau(t)\rangle \to |\psi_\tau(t+\delta t\rangle$ can be summarized in two steps

(a) Calculate $|\psi_\tau(t+\delta t)\rangle$. For small δt we get up to first order expansion

$$|\psi_\tau(t+\delta t)\rangle = (1 - \frac{i\hat{H}\delta t}{\hbar})\,|\psi_\tau(t)\rangle \tag{2.26}$$

Since $\hat{H}$ is non-hermitian $|\phi^1(t+\delta t)\rangle$ is not normalized. Thus,

$$\langle\psi_\tau(t+\delta t)|\psi_\tau(t+\delta t)\rangle = \langle\psi_\tau|\,(1 + \frac{i\hat{H}^\dagger\delta t}{\hbar})(1 - \frac{i\hat{H}\delta t}{\hbar})\,|\psi_\tau(t)\rangle \tag{2.27}$$

$$\equiv 1 - \delta p \tag{2.28}$$

$$\delta p = \delta t \frac{i}{\hbar}\,\langle\psi_\tau(t)|\,\hat{H} - \hat{H}^\dagger\,|\psi_\tau(t)\rangle \equiv \sum_m \delta p_m, \tag{2.29}$$

where

$$\delta p_m \equiv \delta t\,\langle\psi_\tau(t)|\,\gamma_m \hat{C}_m^\dagger \hat{C}_m\,|\psi_\tau(t)\rangle \geq 0. \tag{2.30}$$

While one can always adjust δt such that $\delta p \ll 1$, one can notice already how the high rate of dissipation γ_m will imply the need of using a smaller time-step δt. In this particular case we'll have a scaling of time-step $\delta t \approx 1/\sum_m \gamma_m$. On section 5.1, we will see how this becomes even more problematic when one tries to apply the method to many-body systems.

(b) The second step corresponds to a **gedanken experiment** of a measurement process, in which we consider the possibility of a quantum jump. To decide whether a quantum jump has occurred, we define a random number ϵ uniformly distributed between zero and one and compare it to δp. Two cases may arise:

1. $\epsilon \geq \delta p$

   This will be the large majority of the cases, since $\delta p \ll 1$. In this case, there is no quantum jump and the state evolves as

   $$|\psi_\tau(t+\delta t\rangle = \frac{|\psi_\tau(t+\delta t)\rangle}{\sqrt{1-\delta p}}. \tag{2.31}$$

2. $\epsilon < \delta p$ A quantum jump occurs to one of the state $\hat{C}_m\,|\phi(t)\rangle$ according to the relative probability among the various possible types of jumps, $\Pi_m = \frac{\delta p_m}{\delta p}$ (notice that $\sum_m \Pi_m = 1$). So

   $$|\psi_\tau(t+\delta t)\rangle = \frac{\sqrt{\gamma_m}\hat{C}_m\,|\psi_\tau(t)\rangle}{\sqrt{\frac{\delta p_m}{\delta t}}} \tag{2.32}$$

In order to demonstrate the equivalence between the stochastic propagation and the master equation, we do a statistical average of the trajectory evolution through a time-step and see if we recover the master equation. We start considering density operator

$$\hat{\sigma}(t) = |\psi(t)\rangle \langle\psi(t)| \tag{2.33}$$

Repeating the previous procedure, the propagation of this density operator in a given step is:

$$\overline{\hat{\sigma}}(t+\delta t) = (1-\delta p)\frac{|\psi_\tau(t+\delta t)\rangle}{\sqrt{1-\delta p}}\frac{\langle\psi_\tau(t+\delta t)|}{\sqrt{1-\delta p}} + \delta p \sum_m \Pi_m \frac{\hat{C}_m |\psi(t)\rangle}{\sqrt{\frac{\delta p_m}{\delta t}}}\frac{\langle\psi(t)|\hat{C}_m^\dagger}{\sqrt{\frac{\delta p_m}{\delta t}}} \tag{2.34}$$

This can be expressed as

$$\begin{aligned}\overline{\hat{\sigma}}(t+\delta t) =& \Big[1 - \frac{i\delta t}{\hbar}(\hat{H}_s - \frac{i\hbar}{2}\sum_m \gamma_m \hat{C}_m^\dagger \hat{C}_m)\Big] |\psi_\tau(t+\delta t)\rangle \langle\psi_\tau(t+\delta t)| \\ & \Big[1 + \frac{i\delta t}{\hbar}(\hat{H}_s + \frac{i\hbar}{2}\sum_m \gamma_m \hat{C}_m^\dagger \hat{C}_m)\Big] + \delta t \sum_m \gamma_m \hat{C}_m |\psi\rangle \langle\psi]| \hat{C}_m^\dagger\end{aligned} \tag{2.35}$$

And finally one arrives to

$$\overline{\hat{\sigma}}(t+\delta t) = \hat{\sigma}(t) + \frac{i\delta t}{\hbar}\Big[\hat{\sigma}(\hat{H}_s + \frac{i\hbar}{2}\sum_m \gamma_m \hat{C}_m^\dagger \hat{C}_m) - (\hat{H}_s - \frac{i\hbar}{2}\sum_m \gamma_m \hat{C}_m^\dagger \hat{C}_m)\hat{\sigma}\Big] \tag{2.36}$$

$$\begin{aligned}&+ \delta t \sum_m \gamma_m \hat{C}_m \hat{\sigma} \hat{C}_m^\dagger \\ &= \hat{\sigma} + \frac{i\delta t}{\hbar}[\hat{H}_S, \hat{\sigma}] + \delta t \sum_m \frac{1}{2}\gamma_m \Big[2\hat{C}_m \hat{\sigma} \hat{C}_m^\dagger - \hat{C}_m^\dagger \hat{C}_m \hat{\sigma} - \hat{\sigma}\hat{C}_m^\dagger \hat{C}_m\Big]\end{aligned} \tag{2.37}$$

which holds whether $\sigma(t)$ corresponds to a pure state or to a mixed state. In this way, we see that taking a stochastic average over trajectories is equivalent to the master Eq. (8.3).

Of course normally one is interested in computing mean values of interesting observables. Here, for each trajectory, we get $\langle\psi_\tau(t)|\hat{A}|\psi_\tau\rangle$ for many solutions $|\psi_\tau(t)\rangle$, thus

$$\langle\hat{A}\rangle_{N_t} = \sum_{\tau=1}^{N_t} \frac{1}{N_t} \langle\psi_\tau(t)|\hat{A}|\psi_\tau(t)\rangle \tag{2.38}$$

and $\left\langle\hat{A}\right\rangle_{N_\tau} \to \left\langle\hat{A}\right\rangle$ as $N_t \to \infty$.

One can also compute the correspondent standard deviation of the observable obtained through trajectories as

$$\sigma_A = \sqrt{\frac{1}{N_t - 1}\sum_\tau \left(\left\langle\hat{A}\right\rangle_\tau - \left\langle\hat{A}\right\rangle_{N_t}\right)^2}. \tag{2.39}$$

Then as error bars one simply use the sample standard error of the mean, $\epsilon_r = \langle A \rangle_{N_t} / \sqrt{N_t}$.

An alternative implementation can offer a slight improvement to the quantum trajectory method. Instead of drawing a random number at every time step, we can draw a random number once and evolve the state for one or more time steps without normalization [13]. The evolution continues until the square of the norm of the state drops below a predefined threshold ϵ. This process can be summarized as follows:

1. Draw a random number $\epsilon \in [0, 1)$.
2. Evolve the initial state $|\psi\rangle$ according to effective Hamiltonian (2.25).
3. If the square of the norm drops below ϵ, perform quantum jump according to Eq. (2.32).
4. Continue with step 1.

It's important to remark that, in this variation of the method, to get accurate results at the moment of computing the value of an observable, it's necessary to normalise the state. In practice what one does is simply to create a copy of the state during the simulation and normalize that copy and calculate the observable, so one does not affect the Monte-Carlo process of the trajectory evolution.

2.4.2 Quantum Trajectory simulation for the lossy mode of a cavity

Lastly, in order to have a better grasp of how the method works, we will look at a simple example. Consider the mode of a cavity with initially 10 photons ($|\psi(t = 0)\rangle = |10\rangle$). The dynamics of the state are given by Hamiltonian

$$\hat{H} = \omega \hat{a}^\dagger \hat{a} - \tfrac{i\kappa}{2} \hat{a}^\dagger \hat{a}. \tag{2.40}$$

In this particular case we can easily identify the jump operator as $\hat{C} = \hat{a}$. As we see from Fig. 2.2, most we simply evolve with Hamiltonian (2.40) and normalize, just as it is expressed in Eq. (2.31). However in certain cases it will happen that $\epsilon < \delta p$ and one would apply one of the jump operators according to Eq. (2.32), which one can see in Fig.2.2, which in that particular case translate into the loss of a photon in one of the modes. Averaging a large number of trajectories one can reproduce the results that one would obtain by exactly solving the master equation. As far as how many trajectories are needed it depends mostly on the standard deviation of the observable one intends to simulate, since for an accurate mean one needs a number of trajectories $Nt \gg \sigma_A^2 / \langle A \rangle^2$ [14].

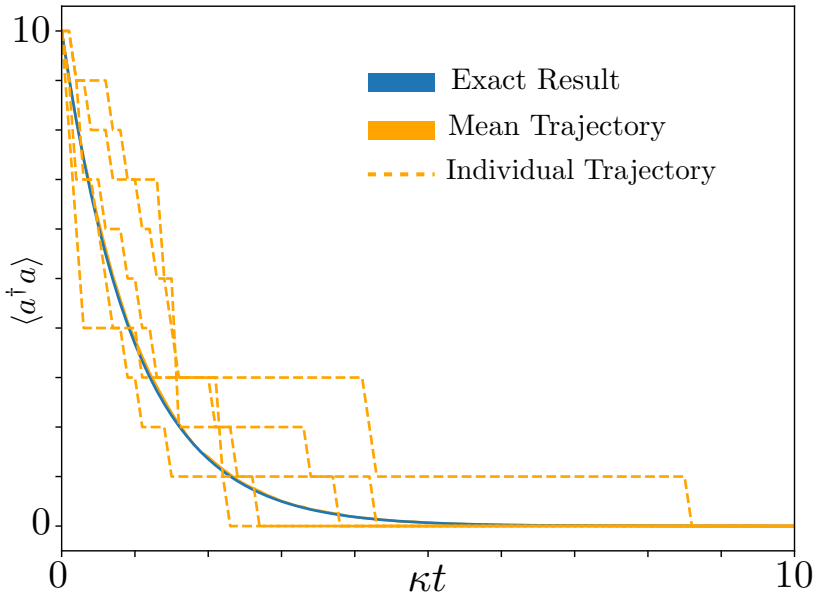

Figure 2.2: *Quantum Trajectory Dynamics* — Example of the trajectory dynamics of the mode cavity with losses initial in a state with 10 photons. One can notice how the exact results for the mean number of photos $\langle a^\dagger a \rangle$ matches for the trajectory average and the exact result $[N_t = 500, \kappa = 1]$.

Bibliography

[1] Ulrich Weiss. *Quantum Dissipative Systems | Series in Modern Condensed Matter Physics*, volume 13. World Scientific Publishing Company, Singapore, March 2008.

[2] Heinz-Peter Breuer, Francesco Petruccione, Heinz-Peter Breuer, and Francesco Petruccione. *The Theory of Open Quantum Systems*. Oxford University Press, Oxford, England, UK, June 2002.

[3] U. Fano. Description of States in Quantum Mechanics by Density Matrix and Operator Techniques. *Rev. Mod. Phys.*, 29(1):74–93, January 1957.

[4] Brian C. Hall. Systems and Subsystems, Multiple Particles. In *Quantum Theory for Mathematicians*, pages 419–440. Springer, New York, NY, New York, NY, USA, April 2013.

[5] Reinhold A. Bertlmann and Philipp Krammer. Bloch vectors for qudits. *J. Phys. A: Math. Theor.*, 41(23):235303, May 2008.

[6] Morag Am-Shallem, Amikam Levy, Ido Schaefer, and Ronnie Kosloff. Three approaches for representing Lindblad dynamics by a matrix-vector notation. *arXiv*, October 2015.

[7] Howard Carmichael. *An Open Systems Approach to Quantum Optics*. Springer, Berlin, Germany, 1993.

[8] M. B. Plenio and P. L. Knight. The quantum-jump approach to dissipative dynamics in quantum optics. *Rev. Mod. Phys.*, 70(1):101–144, January 1998.

[9] Jean Dalibard, Yvan Castin, and Klaus Mølmer. Wave-function approach to dissipative processes in quantum optics. *Phys. Rev. Lett.*, 68(5):580–583, February 1992.

[10] Klaus Mølmer, Yvan Castin, and Jean Dalibard. Monte Carlo wave-function method in quantum optics. *J. Opt. Soc. Am. B, JOSAB*, 10(3):524–538, March 1993.

[11] R. Dum, P. Zoller, and H. Ritsch. Monte Carlo simulation of the atomic master equation for spontaneous emission. *Phys. Rev. A*, 45(7):4879–4887, April 1992.

[12] Andrew J. Daley. Quantum trajectories and open many-body quantum systems. *Adv. Phys.*, 63(2):77–149, March 2014.

[13] Andrew J. Daley. Quantum trajectories and open many-body quantum systems. *Adv. Phys.*, 63(2):77–149, Mar 2014.

[14] William H Press, Saul A Teukolsky, William T Vetterling, and Brian P Flannery. *The Art of Scientific Computing*. Cambridge University Press, 1992.

Chapter 3

Matrix Product States

Quantum many-body systems present significant challenges for theoretical understanding and numerical simulations. The exponential growth of the Hilbert space with the number of particles makes it computationally intractable to describe the behavior and dynamics of these systems accurately. In pursuit of efficient and precise representations, Matrix Product States (MPS) have emerged as a powerful tool combining mathematical elegance and practical utility.

The concept of MPS originated from the Density Matrix Renormalization Group (DMRG) method introduced by Steven R. White in 1992 [1, 2]. White's groundbreaking work revolutionized the field of numerical simulations of quantum many-body systems, providing a powerful approach for studying one-dimensional systems with exceptional accuracy and efficiency [3, 4].

Though developed independently from DMRG, the connection with MPS quickly became evident. In a significant breakthrough, Ostlund and Rommer [5] established a crucial link between the block-growth step of the infinite-system DMRG and the matrix form inherent to MPS. Their pivotal insight revealed that the block-growth step – a central component of the infinite-system DMRG algorithm – could be naturally expressed as a matrix, mirroring the structure adopted by MPS. A further significant advancement occurred when researchers realized that DMRG naturally yields quantum states in the form of MPS [6]. This MPS formalism, rooted in tensor network representations, enabled a deeper understanding of the underlying structures and entanglement properties captured by the DMRG method.

Despite its significance, this development was not widely recognized until around 2004, when a notable shift occurred. It was then that Cirac, Verstraete, Vidal, and their collaborators began systematically exploring the immense potential of MPS. This exploration led to the discovery of various extensions and advancements in DMRG methodology, which were not readily apparent or expressible within the traditional DMRG framework. A non-exhaustive list of these works is included here [7–14].

MPS offer a compact and flexible representation of quantum states, allowing for efficient numerical calculations while preserving the essential features of the original system. They are particularly effective in capturing the entanglement structure and in describing low-energy states of one-dimensional systems, making

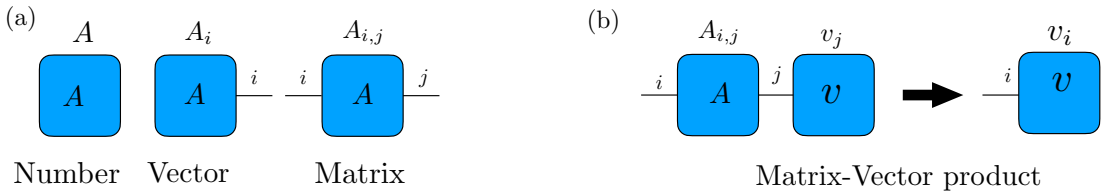

Figure 3.1: MPS diagrammatic notation

them a powerful tool for studying condensed matter physics, quantum information theory, and related fields.

In this chapter, our primary focus will be on establishing a solid foundation in MPS, understanding their applications, and exploring their advantages in simulating one-dimensional quantum many-body systems. We will begin by delving into the basics of notation to provide a clear understanding of the language and framework used in MPS representations. Building upon this foundation, we will explore the pivotal role played by the Singular Value Decomposition (SVD) in MPS simulations. As we progress, our attention will shift to the crucial algorithms employed for MPS evolution, such as the Time-Evolving Block Decimation (TEBD), which is instrumental in simulating the dynamics of MPS systems. To conclude, we will present a series of numerical simulations that offer insights into the method and its applications.

3.1 Introduction to Matrix Product States

To become acquainted with MPS techniques, it is advantageous to first familiarize oneself with the diagrammatic notation. This notation serves as a fundamental tool for expressing key concepts related to MPS, enabling a deeper understanding of the underlying ideas. Figure 3.1(a) illustrates how the number of 'legs' in the diagram corresponds to the dimensionality of the corresponding array. For a scalar, whether real or complex, a 'leg-less' square suffices. Adding a leg represents a vector, while two legs represent a matrix, and so on. This intuitive representation allows one to quickly grasp the dimensionality of the array. In Fig. 3.1(b), one can also observe how operations between different tensors are represented in the diagrammatic notation. When two tensors are multiplied together, and they share a common index, that index is contracted in the diagram. This contraction signifies the summation over that index.

Having established the basics of the notation, let us now delve into a more concrete explanation of why MPS are necessary. Conventionally, a quantum many-body state is expressed in the following form:

$$|\psi\rangle = \sum_{i_1=1}^{d}, \sum_{i_2=1}^{d}, \cdots, \sum_{i_N=1}^{d} c_{i_1,i_2,\ldots,i_N} |i_1\rangle \otimes |i_2\rangle \otimes \cdots \otimes |i_N\rangle \,. \tag{3.1}$$

Here, N represents the number of particles, and d denotes the number of levels or dimensions of the system. However, a significant challenge arises with such

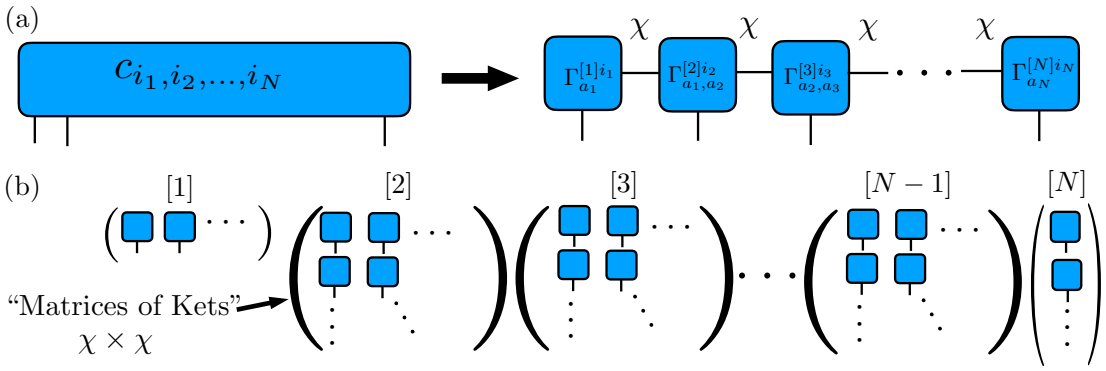

Figure 3.2: *MPS general idea: Express the state as a product of tensors*— (a) We start with a quantum state represented by an N-dimensional tensor, where the coefficients are fully captured and we aim to achieve a more efficient representation, we express the state as a product of lower-dimensional tensors. (b) The tensors can be visualized as matrices where the entries are ket vectors, and the dimensions of such matrices is limited by, what we will refer to as, a bond dimension χ, capturing some of the entanglement, reducing the complexity and enabling tractable computations

representations: the number of complex numbers required to represent the state, also known as the dimension of the Hilbert space, scales exponentially with the number of particles and levels as d^N.

A very rough approximation would be to consider a product state, often referred to as a mean-field approximation, given by:

$$|\psi\rangle \approx \sum_{i_1=1}^{d}, \sum_{i_2=1}^{d}, \cdots, \sum_{i_N=1}^{d} c_{i_1}^{[1]} c_{i_2}^{[2]}, \ldots, c_{i_N}^{[N]} \, |i_1\rangle \otimes |i_2\rangle \otimes \cdots \otimes |i_N\rangle \,, \tag{3.2}$$

In this case, only dN complex numbers would be required to represent the state. However, such an approximation cannot capture the entanglement present in quantum many-body systems and would therefore be highly inaccurate in a large number of cases. To obtain a more accurate representation that properly accounts for entanglement, we turn to MPS. The idea behind MPS can be summarized schematically in Fig 3.2. By expressing the coefficients $c_{i_1,i_2,\cdots,i_N}$ as a product of N matrices $\Gamma^{[n]}$, where the entries of such matrices are ket vectors, we can capture some of the entanglement present in the system. The parameter χ, known as the bond dimension, imposes an upper limit on the dimension of these matrices. The MPS representation, then, aims to represent the quantum state $|\psi\rangle$ in the form [8]:

$$c_{i_1,i_2,\cdots,i_N} = \sum_{a_1,a_2,\ldots,a_{N-1}}^{\chi} \Gamma_{a_1}^{[1]i_1} \Gamma_{a_1,a_2}^{[2]i_2} \Gamma_{a_2,a_3}^{[3]i_3} \cdots \Gamma_{a_{N-1}}^{[N]i_N}. \tag{3.3}$$

While there are some other details to consider, particularly regarding the canonical form representation, for now let's just see at what would we gain by representing the state in such way. Particularly one can see that the total number of com-

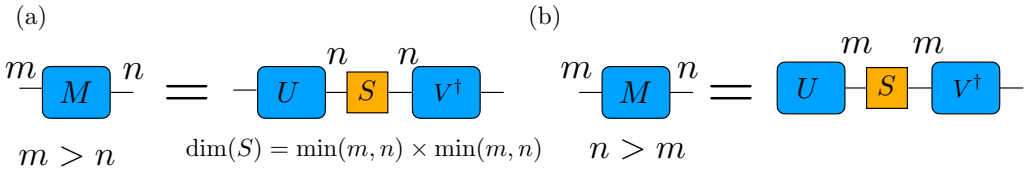

Figure 3.3: SVD Decomposition

plex numbers in the truncated MPS is $\sim d\chi^2(N-2) + 2\chi d$. That is to say, a decomposition which grows only linearly with N, rather than exponentially, for fixed bond dimension. This fact alone should be motivation enough to pursue such decomposition and see how can we arrive at such representation.

In the upcoming sections, we will provide a step-by-step explanation of these ideas, unravelling the key techniques used in MPS. Particularly we would see how arrive at such decomposition for a generic quantum state, how do we perform evolution of the quantum state in this representation and how do we evaluate its efficiency. We will begin by exploring one of the most fundamental techniques to achieve the MPS form: Singular Value Decomposition.

3.1.1 Singular Value Decomposition (SVD) and Schmidt Decomposition

The Singular Value Decomposition (SVD) decomposition represents a matrix as a product of three essential components: a unitary matrix, a diagonal matrix of singular values, and another unitary matrix. This factorization provides a unique representation that captures the intrinsic characteristics of the matrix, allowing for efficient analysis and manipulation.

In the context of MPS, the SVD plays a dual role. On one hand, it facilitates the efficient storage and manipulation of tensors by decomposing them into a product of smaller tensors. This factorization allows for truncation of, what later will known as the bond dimensions, leading to a controlled approximation of the quantum state while preserving the most important features.

Having an arbitrary matrix M of dimensions $(m \times n)$, the SVD guarantees a decomposition of the following form

$$M = USV^\dagger \tag{3.4}$$

where

- U is of dimension $(m\times \min(m,n))$ and has orthonormal columns (the left singular vectors), i.e. $U^\dagger U = I$; if $m \leq n$ this implies that it is unitary, and also $UU^\dagger = I$.

- S is of dimension $(\min(m,n)\times \min(m,n))$, diagonal with real non-negative entries $S_{aa} = \lambda_a$. These are the so-called singular values. The number r of non-zero singular values is the (Schmidt) rank of M. In the following, we assume descending order: $\lambda_1 \geq \lambda_2 \geq \cdots \geq \lambda_r > 0$.

- $V^\dagger$ is of dimension $(\min(m,n) \times n)$ and has orthonormal rows (the right singular vectors), i.e. $V^\dagger V = I$. If $m \geq n$ this implies that it is unitary, and also $VV^\dagger = I$.

We will now employ the SVD to obtain the Schmidt decomposition, a pivotal factorization that will be extensively utilized throughout this thesis.

We start by considering the state of a bipartite system $|\psi\rangle \in \mathcal{H}_A \bigotimes \mathcal{H}_B$. Any such state can be written as

$$|\psi\rangle = \sum_{ij}^{d} c_{i,j} |ij\rangle , \tag{3.5}$$

where $|ij\rangle$ is just the tensor product between $|i\rangle_A \bigotimes |j\rangle_B$, where $|i\rangle_{\mathrm{A}}$ and $|j\rangle_{\mathrm{B}}$ are orthonormal bases of A and B which, in this particular case, both of them have dimension d. Here one can read the coefficients c_{ij} as entries of a matrix c. Doing a SVD decomposition on such matrix one obtains

$$c_{i,j} = \sum_{\alpha}^{d} u_{i,\alpha} s_{\alpha,\alpha} v^*_{\alpha,j} \tag{3.6}$$

In a more general case where the dimensions of system A and B are different, the index α would run until min(dim(A),dim(B)). Reconstructing the state $|\psi\rangle$ in terms of the SVD decomposed coefficient c, one obtains

$$|\psi\rangle = \sum_{ij}^{d} \sum_{\alpha}^{d} u_{i,\alpha} s_{\alpha,\alpha} v^*_{\alpha,j} \left|i^A\right\rangle \left|j^B\right\rangle \tag{3.7}$$

$$= \sum_{\alpha=1}^{d} \left(\sum_{i} u_{i\alpha} \left|i^A\right\rangle \right) \lambda_\alpha \left(\sum_{j} v^*_{ja} \left|j^B\right\rangle \right) \tag{3.8}$$

$$= \sum_{\alpha}^{d} \lambda_\alpha \left|\psi^A_\alpha\right\rangle \left|\psi^B_\alpha\right]\rangle . \tag{3.9}$$

We will refer to the decomposition of the state in the form of (3.9) as the *Schmidt decomposition.*

It's easy to see how when $d = 1$ we will have a (classical) product state, and when $d > 1$, it is an entangled state.

3.1.2 Maximum Bond Dimension χ and Von Neumann Entropy

Given its connection with entanglement, here it may result convenient to introduce the Von Neumann Entropy (VNE), which is given by

$$S_{\mathrm{vN}} \equiv -\mathrm{tr}\rho_A \log_2 \rho_A, \tag{3.10}$$

where $\rho_A = \mathrm{tr}_B \rho$. The VNE (or entanglement entropy) is considered as the standard measure of entanglement [15] and its exploration will be discussed in

greater detail in subsequent chapters. In the present context we will use the VNE as a crucial foundation for introducing one of the key concepts of MPS: approximating the state by truncating the number of Schmidt coefficients. This truncation enables more efficient numerical simulations, making it an essential technique within the framework of MPS.

We start by calculating the correspondent density matrix $\hat{\rho}$ of $|\psi\rangle$

$$\hat{\rho} = \sum_{i',j'} c^*_{i',j'} \sum_{i,j} c_{i,j} \, |ij\rangle \, \langle i'j'| \tag{3.11}$$

We can obtain the density matrix ρ_A, by tracing over the second subsystem

$$\hat{\rho}_A = \sum_n \langle n| \, \rho \, |n\rangle_2 \,, \quad \hat{\rho}_A = \sum_{i',i'} \sum_n c^*_{i',i'} \sum_n c^*_{i',n} c_{i,n} \, |i\rangle \, \langle i'| \,, \tag{3.12}$$

once again we do a SVD decomposition, now on both c

$$\hat{\rho}_A = \sum_{i',i'} \sum_n \sum_\alpha u^*_{i,\alpha} s_{\alpha,\alpha} v_{\alpha,n} \sum_\beta u_{i',\beta} s_{\beta,\beta} v^*_{\beta,n} \, |i\rangle \, \langle i'| \tag{3.13}$$

Here we used the property $\sum_n v_{\alpha,n} v^*_{\beta,n} = \delta_{\beta,\alpha}$, which comes form the fact we are dealing with unitary matrices. In a more explicit way we have

$$\hat{U}^\dagger \hat{U} = \sum_{i,j} \sum_{i',j'} u^*_{i,j} u_{i',j'} \, |j\rangle \, \langle i|i'\rangle \, \langle j'| = \hat{I} \tag{3.14}$$

$$= \sum_{i,j} \sum_{j'} u^*_{i,j} u_{i,j'} \, |j\rangle \, \langle j'| = \hat{I} \tag{3.15}$$

$$= \sum_j u^*_{i,j} u_{i,j'} = \delta_{j,j'} \tag{3.16}$$

Continuing the calculation of $\hat{\rho}_A$ we obtain

$$\rho_A = \sum_{i',i'} \sum_\alpha u^*_{i,\alpha} (s_{\alpha,\alpha})^2 u_{i',\alpha} \, |i\rangle \, \langle i'| \tag{3.17}$$

$$= \sum_\alpha (\lambda_\alpha)^2 \, |\phi_\alpha\rangle \, \langle \phi_\alpha| \tag{3.18}$$

Where we used the property $\sum_n u_{\alpha,n} u^*_{\beta,n} = \delta_{\beta,\alpha}$.

Remarkably, the SVD diagonalizes the reduced density matrix, facilitating the calculation of the VNE as

$$S_{\text{vN}}(\rho_A) = -\sum_\alpha^r (\lambda_\alpha)^2 \log_2[(\lambda_\alpha)^2] \tag{3.19}$$

For (3.19) the maximum possible value of entanglement is given by $\max[S_{\text{vN}}] = \log_2(r)$. However, and this is where one of the key approximations of MPS comes in, if instead of keeping all singular values, we just keep the χ largest ones, we are able to impose an upper limit in terms of entanglement entropy given by

$$\max[S_{\text{vN}}] = \log_2(\chi). \tag{3.20}$$

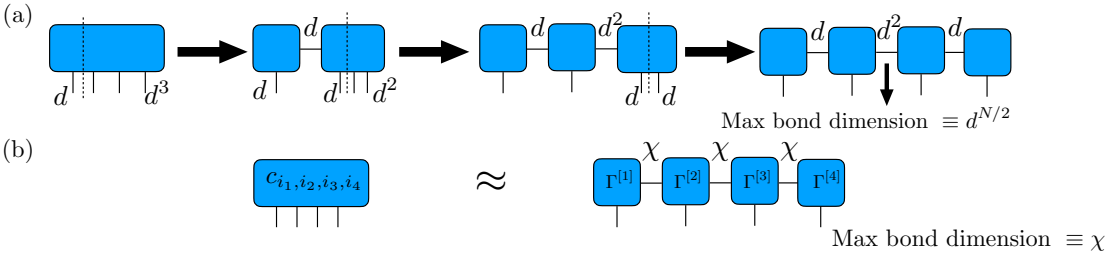

Figure 3.4: *SVD and maximum value of bond dimension* — (a) By applying a singular value decomposition through all sites, one will eventually have a maximum bond dimension of $d^{N/2}$ at the center bond. There is not really advantage of these since the number of complex terms to describe the state still scales exponentially $\sim d^{N/2}$. (b) For the MPS decomposition to be efficient we truncate the number of terms after each SVD, keeping the most relevant χ terms.

The bond dimension, which throughout this work we'll refer to as χ, serves as an upper limit for the dimension of the matrices within the MPS. As seen in Fig. 3.4 to impose a dimension constraint allows us to efficiently approximate quantum states while controlling the computational resources required.

3.2 MPS decomposition and the canonical form

By now we have understanding of one of the main techniques and key points about MPS, now comes the real question: how do we pass from a general state of the form of Eq. (3.1), to express the coefficients in the MPS form as depicted in Eq. (3.3). We now only want any representation of a product of the matrices but rather, taking into account that the matrices $\gamma^{[n]}$ are not uniquely defined, we want to achieve a representation in which the tensors fulfill certain orthogonality conditions (see Fig. 3.5), leading to the so-called canonical form. We say that an MPS is in its canonical form when, on each bond, there is an index α related to the Schmidt decomposition of $|\psi\rangle$. While this was previously achieved with two sites this in Eq. (3.9) for two sites, we want to arrive to a general result for N sites. This will be achieved through a series of Schmidt decompositions of the quantum state and the introduction of a set of diagonal tensors λ. Starting with a generic N-body wave function with coefficients $c_{i_1,i_2,\cdots,i_N}$ we do a bipartition between site 1, and the rest $2,\cdots,N$ sites, imposing an upper limit in the dimension of the common index a_1. Initially one obtains a decomposition of the form $|\psi\rangle = \sum_{a_1}^{\chi} \lambda_{a_1}^{[1]} \left|\psi_{a_1}^{[1]}\right\rangle \left|\psi_{a_1}^{[2,\cdots,N]}\right\rangle$ Expanding $\left|\psi^{[1]}\right\rangle$ in the local basis one obtains

$$|\psi\rangle = \sum_{i_1,a_1=1}^{d,\chi} \Gamma_{a_1}^{[1]i_1} \lambda_{a_1}^{[1]} |i_1\rangle \left|\psi_{a_1}^{[2,\ldots,N]}\right\rangle \tag{3.21}$$

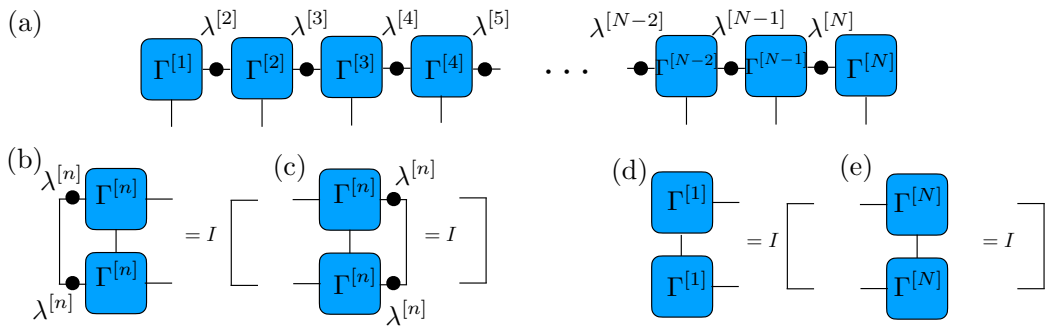

Figure 3.5: *Canonical decomposition of MPS and orthogonality conditions* — (a) The canonical form allows for a MPS represented with the set of tensors $\{\Gamma\lambda\}$, this form allows to fulfill orthonormal conditions. (b/c) Proper contraction of physical and bond indices. (d/e) At the edges the contraction will occur with physical indices only.

From there one can proceed to express $\left|\psi_{a_1}^{[2,\cdots,N]}\right\rangle$ in the basis of the second site

$$\left|\psi_{a_1}^{[2,\cdots,N]}\right\rangle = \sum_{i_2} |i_2\rangle \left|\phi_{i_2,a_1}^{[3,\cdots,N]}\right\rangle \tag{3.22}$$

Writing each state $\left|\phi_{i_2,a_1}^{[3,\cdots,N]}\right\rangle$ in terms of at most χ $\left|\psi^{[3,\cdots,N]}\right\rangle$ and the correspondent $\lambda_{a_2}^{[2]}$ coefficients we have:

$$\left|\phi_{i_2,a_1}^{[3,\cdots,N]}\right\rangle = \sum_{a_2}^{\chi} \Gamma_{a_1,a_2}^{[2]} \lambda_{a_2}^{[2]} \left|\psi^{[3,\cdots,N]}\right\rangle \tag{3.23}$$

Substituting in (3.21) we get

$$|\psi\rangle = \sum_{i_1,i_2,a_1,a_2} \Gamma_{a_1}^{[1]i_1} \lambda_{a_1}^{[1]} \Gamma_{a_1,a_2}^{21]i_2} \lambda_{a_2}^{[2]} |i_1\rangle |i_2\rangle \left|\psi^{[3,\cdots,N]}\right\rangle \tag{3.24}$$

Repeating the steps going through the rest of the sites one eventually one can express the state as

$$|\psi\rangle = \sum_{\{i_n\}} \sum_{\{a_n\}}^{\chi} \prod_n \Gamma_{a_n a_{n+1}}^{[n]\,i_n} \lambda_{a_n}^{[n]} \bigotimes_n |i_n\rangle \,. \tag{3.25}$$

Let's look at what we have achieved by expressed out state in the canonical form. Physically we can see every $\lambda^{[n]}$ as the set unique Schmidt values of the decomposition of the whole state as

$$|\psi\rangle = \sum_i^{\chi} \lambda_i \left|\psi^L\right\rangle \left|\psi^R\right\rangle \tag{3.26}$$

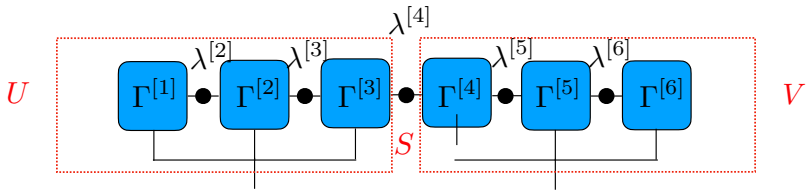

Figure 3.6: *Canonical form as a Schmidt decomposition* — The orthogonality conditions of the canonical form ensure that the matrices U and V are unitary. The entries $\lambda^{[n]}$ are then the singular values for this decomposition.

Here the diagonal matrix λ contains the decreasingly ordered Schmidt coefficients ($\lambda_1 \geq \lambda_2 \geq \cdots \geq \lambda_\chi \geq 0$) and α labels the Schmidt vectors, which form orthonormal sets, $\left|\psi^L\right\rangle$ (matrix U) $\left|\psi^R\right\rangle$ (matrix V) fulfilling the condition

$$\left\langle \psi_i^{L/R} \middle| \psi_j^{L/R} \right\rangle = \delta_{ij}. \tag{3.27}$$

This orthogonality property ensures that setting the smallest entries $\{\lambda\}$ to zero during the truncation corresponds to throwing away the least important contributions [16]. A schematic representation can be seen in Fig. 3.5.

It is worth nothing that we start from the left-most state to arrive to the canonical form, one could also have achieved the canonical form starting from the right. For our interests it's enough to achieve such form, and explain some of the advantages that the decomposition brings. Particularly the canonical decomposition makes the calculation of expectation values straightforward. When one wants to calculate the expectation value of certain operator on site i in a many-body system, normally one would have to apply the operator $\hat{I}_1 \otimes \hat{I}_2 \otimes \cdots \otimes \hat{I}_{i-1} \otimes \hat{O}_i \otimes \hat{I}_{i+1} \otimes \cdots \otimes \hat{I}_N$. This would imply dealing with an array of dimension $d^N \times d^N$ which ends up being computationally expensive. On the other hand, the MPS approach is very straightforward. We consider a tensor correspondent to the operator $\hat{O}_i$ which we apply and then we apply the complex conjugate of the state. After that the canonical form allows to contract the indices and end up with the correspondent expectation value. This process is represented in Fig. 3.7.

One could also compute expectation values for observables involving more sites for example $\hat{O}_1 \otimes \hat{O}_3$, for which is the process is essentially the same. Only in cases where a two (or more sites) operator cannot be expressed as an external product (i.e increases entanglement entropy in one of the bonds), as can it happen with the application of evolution two-site operators then certain conditions regarding the orthogonality of the MPS have to be taken into account. This will be discussed with detail on Section 3.4.

3.3 Conserved quantities

Before we go into the details about how to actually perform the time-evolution in a MPS, it is important to get acquainted with the concept of conserved quantities and its implementation to speed-up MPS calculations. For a more detailed description with emphasis on some of the more mathematical aspects one can also

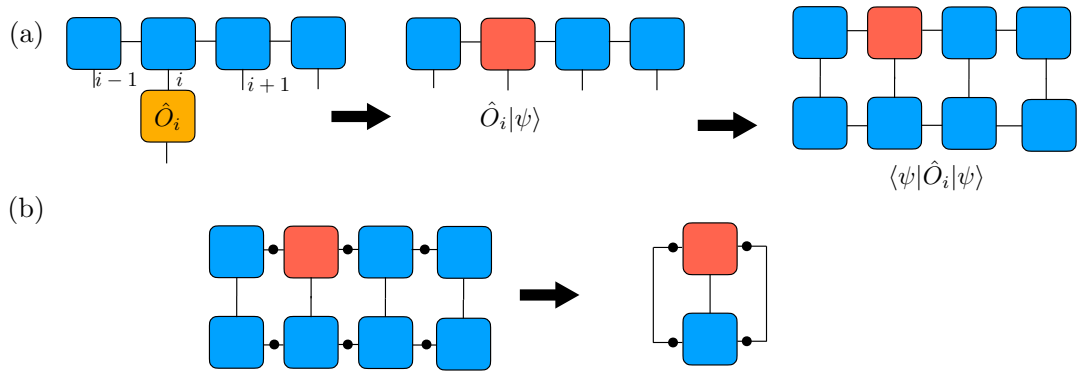

Figure 3.7: *Calculating Expectation Values* — Schematic representation of calculating expectation values with MPS. (a) Within the MPS framework one acts with a local tensor correspondent to the operator of the site one wants calculate the expectation value, and then simply acts with the complex conjugate of the state. (b) Making use of the canonical form, the procedure of contracting the indices is straightforward.

see Ref. [17]. As for something more focused in the details regarding the implementation in the numerical simulations via the ITensor library, see Ref. [18]. In this thesis conservation laws will be used regularly, particularly in the Chapters 7 and 8 to speed up calculations.

One example that we will focus and one can frequently encounter in the case of spin systems is the conservation of total magnetization, defined as $S^z = \sum_i \sigma_i^z$. When magnetization is conserved the through all times there is a defined conserved quantity M, which means that through all times, one can express $S^z |\psi(t)\rangle = M |\psi(t)\rangle$. This is not to say that there cannot be changes in the spin configurations in the chain, is just that such changes cannot break the total value M. In practice to gain numerical advantage from this fact, one assigns to each site a quantum number. For the case of magnetization, one would assign either $+1$ or -1. Just like with sites, it is also possible to assign a quantum number to the inner indices, in doing so, one establishes a *flow*, in which the condition $\chi_{\text{in}} = \chi_{\text{out}} + i_{\text{out}}$ must be fulfilled. By doing so, the tensors $\Gamma^{[n]}$ become block-sparse with blocks associated to the different possible quantum numbers, as indicated in Fig. 3.8.

3.4 Time Evolving Block Decimation

We now want to know how to perform the dynamics simulation. Particularly, given the MPS framework that we have presented so far, we want to know how do we pass from state $|\psi(t)\rangle$ to state $|\psi(t+dt)\rangle$. One initially could think about creating a tensor which corresponds to the operator $e^{-i\hat{H}dt}$ and apply it to the state as shown in Fig. 3.9(a). However this, although possible, would be highly inefficient. The main problem with this approach is by evolving all sites at once there is also an increase in all bond dimensions. In a many-body system, just to

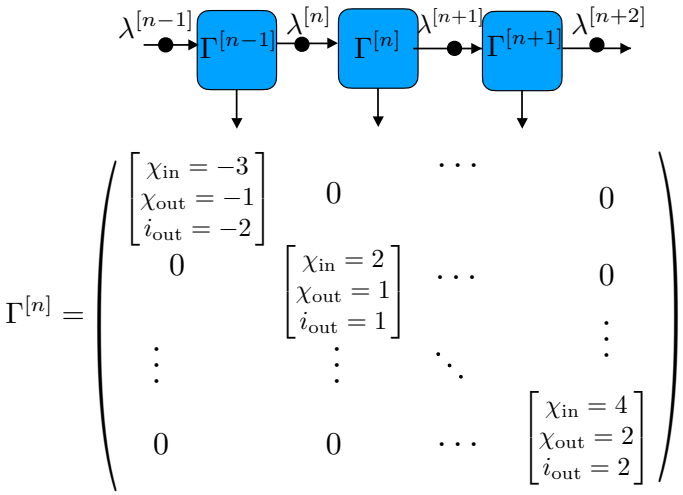

Figure 3.8: *Quantum Number Conservation* — The top indicates the "flow" of quantum numbers. Number conservation requires that incoming and outgoing indices add up to the same number. The matrix below indicates the resulting block-sparse structure of $\Gamma^{[n]}$.

store this intermediate state becomes computationally expensive.

An alternative to this is the time evolving black decimation (TEBD) algorithm. This algorithm relies on the Trotter decomposition of the time evolution operator into local two-site operators [16]. Having previously presented how to apply 2-site operators (see Fig. 3.11), now it's a matter of how to accurately apply such operators to perform the evolution in the system.

We start by expressing the Hamiltonian of two site gates

$$\hat{H} = \sum_i \hat{H}_{i,i+1} \tag{3.28}$$

$$e^{-i\sum_{j=1}^{N}\hat{H}_j t} = \prod_{j=1}^{N} e^{-i\hat{H}_j t} + \mathcal{O}^{N^2 t^2} \tag{3.29}$$

Then one can write the time evolution operator as a product of two site operators

$$\exp(-i\hat{H}dt) = \exp\left[-i\left(\sum_l \hat{H}_{j,j+1}\right)\right] \tag{3.30}$$

$$= \prod_l \exp\Big[-i\hat{H}_{l,l+1}dt\Big] + \mathcal{O}(dt^2) \tag{3.31}$$

where the remainder $\sim \mathcal{O}(dt^2)$ is given by the Baker-Campbell-Hausdorff formula. Passing the two-gates through all sites of the MPS, in what is known as a sweep, one evolves the state from t to $t + dt$. We have to remember, that due to the fact that the terms $\hat{H}_{j,j+1}$ don't, in general, commute, the simple sweep given is Eq. (3.31) is only accurate up to first order in the time step, and would thus require

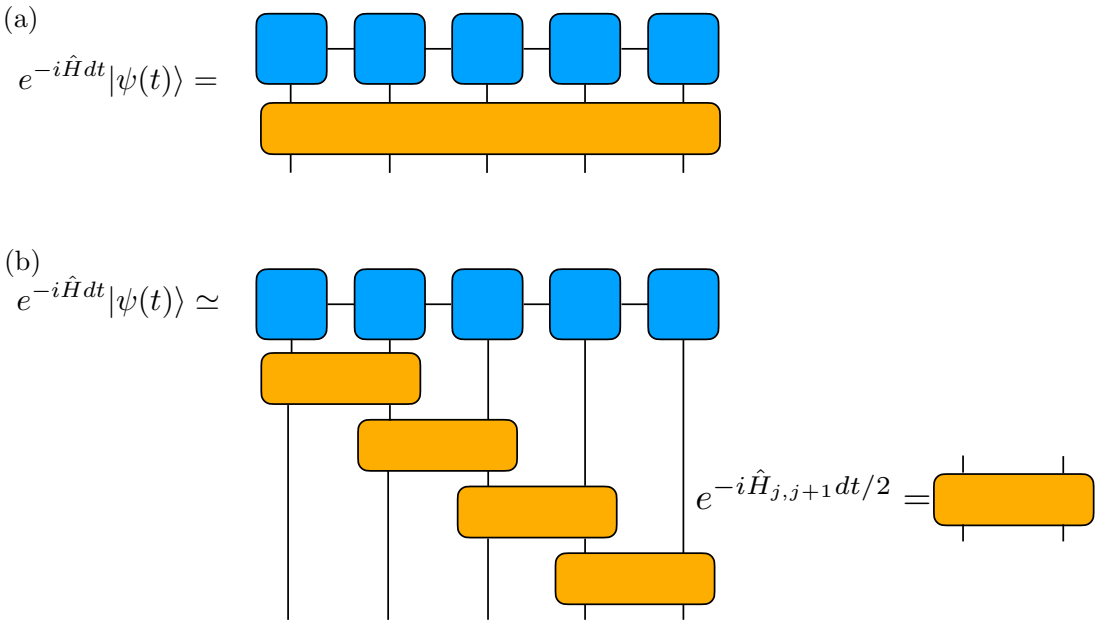

Figure 3.9: *MPS evolution* — (a) It is possible to evolve all sites at once, acting with the evolution operator as one N-site gate, however this has complications mainly due the fact that, by doing that, the dimension of all bonds increase at once, making the intermediate state during the evolution hard to storage. (b) A more convenient approach is the trotter evolution, in which one applies a series of two-site gates, individually increasing the bonds between each site, which then one can truncate.

very small time steps. There are several higher order methods that have been introduced. In this thesis we will rely mostly in 2nd and 4th order methods. The 2nd order method that we use in this thesis is RL, where R is a sweep to the right direction starting from site 1, and L which is a sweep in the left direction starting from the end-site. Explicitly the evolution can be expressed as

$$\exp(-i\hat{H}dt) = \prod_{l=1}^{N-1} \exp\Big[-i\hat{H}_{l,l+1}dt/2\Big] \prod_{l=N-1}^{1} \exp\Big[-i\hat{H}_{l,l+1}dt/2\Big]. \tag{3.32}$$

Note how the Hamiltonian in each of the two-site evolution operators is multiplied by a factor of $1/2$ due to the fact that we apply two sweeps to evolve through one time-step. A schematic representation of the 2nd order trotter evolution can be seen in Fig. 3.10. For the 4th order evolution we apply a series of sweeps of the form *RLR(-2L)RRRRLRLLLL(-2R)LRL*. Here the Hamiltonian on each of the R and L two-site gates will be multiplied by a factor factor of $1/12$, while the gates *(-2R)* and *(-2L)* are multiplied by a factor of $-1/6$. Note how the total product of the exponentials then adds to one time-step. For a comprehensive derivation of the 4th-order trotter evolution and the errors involved one can refer to [19].

It is convenient to clarify the process that involves applying each of the trotter gates. Particularly we want to focus on conserving the orthogonality conditions after the application of each of the trotter evolution two-site gates we

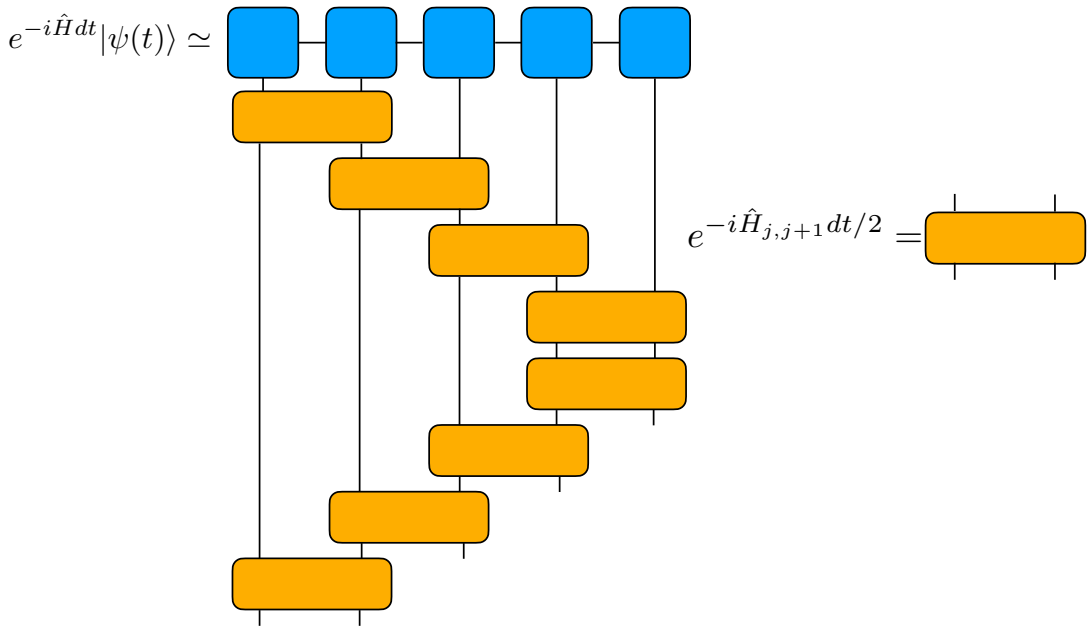

Figure 3.10: *Second order trotter evolution* — Schematic representation of the second order trotter evolution. Since we apply each gate twice we need to multiply the Hamiltonian in the evolution operator by a factor of 1/2.

want to make sure that the orthogonality condition is fulfilled. Also, unlike the single-site gates, it is important to mention that the application of a two-site gate can increase the bond dimension between the sites that it is applied it. We present a detailed scheme on Fig. 3.11 of the application of evolution operator $\hat{U}_{i,i+1} = \exp(-i\hat{H}_{i,i+1}dt)$. What it is important to highlight about the process is the application of inverse tensors $\lambda^{[i/i+1]}$ in order to ensure the canonical form, and also the fact that the unitary evolution it what ultimately allows to fulfill the orthogonality condition. In the case of open systems when one deals with non-unitary evolution a different approach will be employed.

To have a more concrete idea about how the Trotter decomposition works, let's apply a 2nd order decomposition to a disordered Heisenberg model

$$\hat{H} = -J \sum_{i=1}^{N-1} \hat{\sigma}_i \cdot \hat{\sigma}_{\mathbf{i+1}} + \sum_{i=1}^{N} h_i \hat{\sigma}_i^z \tag{3.33}$$

Considering it is a second-order decomposition, we apply the two-site gate $\hat{U}_{j,j+1} = e^{-i\hat{H}_{j,j+1}dt/2}$ twice. This allows us to achieve a total evolution of the form:

$$\hat{U} \approx \hat{U}_{1,2}, \hat{U}_{2,3} \ldots \hat{U}_{N-1,N} \hat{U}_{N,N-1} \ldots \hat{U}_{2,1}, \tag{3.34}$$

as depicted in Figure 3.10. However, it is important to note that when combining two-site and one-site gates in the Hamiltonian (3.33), the one-site gates will only act once on the boundary sites 1 and N, unlike the middle sites.

This can be easily fixed defining the two-site evolution Hamiltonian in the

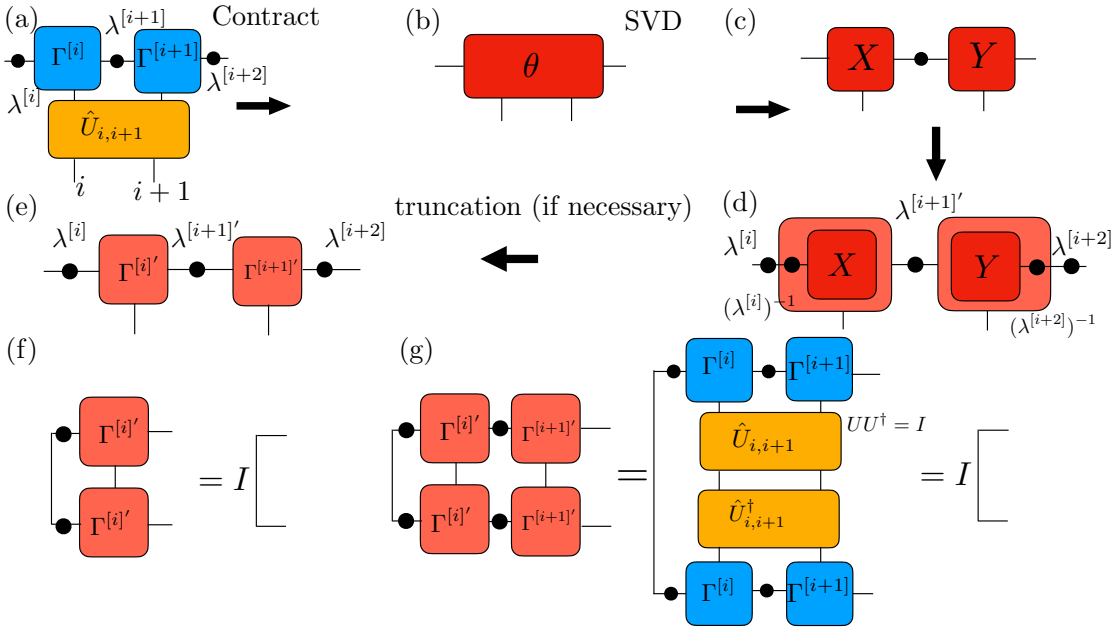

Figure 3.11: *Application of two-site gates and canonical form*— (a) One acts first with the evolution operator $\hat{U}_{1,2}$ on tensors $\Gamma^{[i]}$ and $\Gamma^{[i+1]}$. (b) This will give as a result a tensor θ in which we could apply a SVD decomposition obtaining new tensors X and Y. Such Tensors don't necessarily are expressed in the same local basis as $\Gamma^{[1]}$ and $\Gamma^{[2]}$. (d) We introduce $\lambda^{[1]}$ back into the tensor network by multiplying X and Y with the inverse of the Schmidt coefficients $(\lambda^{[1]})^{-1}$. (e) We obtain the updated tensors $\Gamma^{[1]}$, $\Gamma^{[2]}$, and $\lambda^{[2]}$. If necessary a truncation will be applied on new bond $\lambda^{[i+1]}$.(f) The orthogonality at site i is fulfilled due to the unitarity of the singular value decomposition. (g) At site $i+1$ the orthogonality is fulfilled due to the unitarity of the evolution operator.

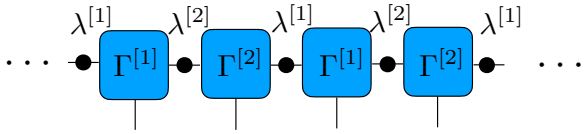

Figure 3.12: *Infinite MPS* — Taking advantage of the translational invariance of the system by n sites, we want to reduce its MPS representation by n sites, here $n = 2$.

following way: For the first two sites, $1, 2$ we'll have

$$\hat{H}_{1,2} = -J\hat{\sigma}_1 \cdot \hat{\sigma}_2 + h_1\hat{\sigma}_1^z + \frac{h_2}{2}\hat{\sigma}_2^z, \tag{3.35}$$

while for the center sites ($i = 2, \ldots, N-1$) we'll have

$$\hat{H}_{i,i+1} = -J\hat{\sigma}_i \cdot \hat{\sigma}_{i+1} + \frac{h_i}{2}\hat{\sigma}_i^z + \frac{h_{i+1}}{2}\hat{\sigma}_{i+1}^z, \tag{3.36}$$

finally for sites $N-1, N$

$$\hat{H}_{N-1,N} = -J\hat{\sigma}_{N-1} \cdot \hat{\sigma}_N + h_{N-1}\hat{\sigma}_{N-1}^z + \frac{h_N}{2}\hat{\sigma}_N^z \tag{3.37}$$

3.4.1 Infinite MPS

While MPS methods can be effective simulating large systems 1D systems as long entanglement entropy is low, there is still a computational cost that is roughly proportional to the size of the lattice which prevents increasing the size indefinitely. However, in the case of systems which are invariant under translations there is a way around it, and one can make the cost independent of the system of size. Starting from a translationally invariant state $|\psi\rangle$ it is possible to do a translationally invariant MPS representation of such state. This allows the possibility in simulating the dynamics of the system storing only one of the translationally invariant subsystems instead of an entire, infinitely long, chain. This is schematically represented in Fig. 3.12, which is translationally invariant by two sites. The two-site invariance allows to connect tensor $\Gamma^{[2]}$ with tensor $\lambda^{[1]}$. Then, using only two tensors $\Gamma^{[1/2]}$ and two tensors $\lambda^{[1/2]}$ it is possible to simulate the whole (infinite) system. We first present the unitary version, following closely the procedure shown in Ref. [20].

Starting with a infinite array of sites, i, in 1D described by an initial state $|\psi\rangle$ and a nearest neighbors interaction Hamiltonian

$$\hat{H} = \sum_i \hat{h}_{i,i+1}, \tag{3.38}$$

where both $\hat{H}$ and $|\psi\rangle$ are translationally invariant by $n = 2$ sites. The goal is to do a evolution of the whole (infinite) system.

$$|\psi(t)\rangle = \exp(-i\hat{H}t)\,|\psi(t=0)\rangle \tag{3.39}$$

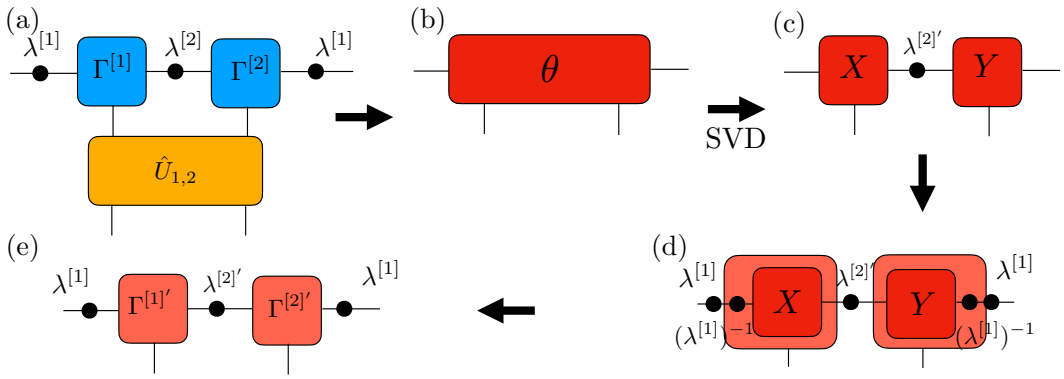

Figure 3.13: *Application of evolution operator on infinite MPS* — Considering a 2-site invariant system the process of applying the gates closely resembles the case for the finite-site, in we also use a Schmidt decomposition (a) One acts first with the evolution operator $\hat{U}_{1,2}$ on tensors $\Gamma^{[1]}$ and $\Gamma^{[2]}$. (b) This will give as a result a tensor θ in which we could apply a SVD decomposition obtaining new tensors X and Y. Such Tensors don't necessarily are expressed in the same local basis as $\Gamma^{[1]}$ and $\Gamma^{[2]}$. (c) We introduce $\lambda^{[1]}$ back into the tensor network by multiplying X and Y with the inverse of the Schmidt coefficients $(\lambda^{[1]})^{-1}$. (d) We obtain the updated tensors $\Gamma^{[1]}$, $\Gamma^{[2]}$, and $\lambda^{[2]}$. Just like the finite case it's easy to see that the unitary of the operator $\hat{U}_{1,2}$ ensures orthogonality.

We can proceed by doing trotter decomposition of the evolution operator $\exp(-i\hat{H}t)$ dividing the evolution in two parts

$$\hat{U}_{1,2} = \bigotimes_{2i,2i+1} \hat{U} \tag{3.40}$$

and

$$\hat{U}_{2,1} = \bigotimes_{2i-1,2i} \hat{U} \tag{3.41}$$

Even though we will partially break the translationally invariance by applying the gates, we can initially represent the whole MPS using 4 tensors which we denominate

$$\begin{aligned} \Gamma^{[2r]} &= \Gamma^{[1]} & \lambda^{[2r]} &= \lambda^{[1]} \\ \Gamma^{[2r+1]} &= \Gamma^{[2]} & \lambda^{[2r+1]} &= \lambda^{[2]} \end{aligned} \tag{3.42}$$

For a finite case of N sites, the simulation of the time evolution is achieved by updating the MPS so as to account for the repeated application of gates $\hat{U}_{12}$ and $\hat{U}_{21}$ on $|\psi\rangle$. But for $N = \infty$, the action of the gates preserve the invariance of the evolved state under shifts by two sites, and only tensors $\Gamma^{[1]}, \Gamma^{[2]}, \lambda^{[1]}$ and $\lambda^{[1]}$ are need to be updated – a task that is achieved through simple matrix manipulations, as depicted in Fig. 3.13, where - just like we did in the case of finite systems - a key step is the insertion of the matrices $\lambda^{[1]}$ and $\lambda^{[2}$ to maintain the canonical form. Given the hermitian evolution, one can assure that the new sites $\Gamma^{[1]'}$ and $\Gamma^{[2]'}$ by the same form we show in Fig. 3.11 (d/e). In order to account for the whole evolution one would also act with evolution operator $\hat{U}_{2,1}$ on a similar

way, repeating the application of gates according to the chosen trotter order and method.

Using this approach, the gain in terms of efficiency is notable, whereas for N sites the TEBD algorithm requires $\mathcal{O}(nd\chi^2)$ space to store an MPS and $\mathcal{O}(nd^3\chi^3)$ time to simulate a small evolution $\exp(-iHdt)$, for $N = \infty$ sites the iTEBD requires computational space and time that scale just as $O(d^2\chi^2)$ and $O(d^3\chi^3)$.

3.5 Simulation Examples

To finalize we will present a series of simulations of many-body quantum systems using MPS methods. This will have the main purpose of getting acquainted with essentials of the MPS technique, and start exploring some of the many-body models that will be studied throughout this thesis. Most of the simulation will involve non-equilibrium dynamics. A prominent and frequently employed protocol in our study is the quantum quench [21–28]. This protocol involves initiating an isolated system at $t = 0$ in a specific pure state $|\psi_0\rangle$, often chosen as the ground state of a quantum many-body Hamiltonian $\hat{H}_0$. Subsequently, for $t > 0$, the system undergoes unitary dynamics governed by a different Hamiltonian $\hat{H}$, wherein a parameter of the Hamiltonian is abruptly altered at $t = 0$. Such method will be used constantly and it will be particularly useful to study the growth of entanglement entropy in subsequent chapters.

All the simulations presented here will be with finite systems. The simulation of (infinitely) translationally invariant is possible, but given that the approach for open and closed systems is similar, we will present the infinite MPS approach when we explain Matrix Product Density Operators and Operator Entanglement in Chapter 6.

3.5.1 XXZ Model

Throughout this thesis we will frequently consider a 1D spin-1/2 XXZ chain with Hamiltonian ($\hbar \equiv 1$ throughout this paper)

$$\hat{H}_{XXZ} = \frac{1}{4}\sum_{i}^{N-1}\left[-J(\hat{\sigma}_i^x\hat{\sigma}_{i+1}^x + \hat{\sigma}_i^y\hat{\sigma}_{i+1}^y) + J_z\hat{\sigma}_i^z\hat{\sigma}_{i+1}^z\right], \tag{3.43}$$

Here, N is the number of spins, $\hat{\sigma}_i^{x,y,z}$ denote standard Pauli matrices defined in a local basis $|\downarrow,\uparrow\rangle_i$, J is the nearest neighbor spin-coupling strength, and J_z is the ZZ spin-spin interaction. For finite system size calculations we consider open boundary conditions.

Using Jordan-Wigner transformation [29], It is possible to rewrite the spin variables as fermionic variables. Hamiltonian (7.3) then is expressed as

$$\hat{H}_{XXZ} = \sum_{i}\left[-\frac{J}{2}(\hat{\sigma}_i^+\hat{\sigma}_{i+1}^- + \hat{\sigma}_i^-\hat{\sigma}_{i+1}^+) + \frac{J_z}{4}\hat{\sigma}_i^z\hat{\sigma}_{i+1}^z\right]. \tag{3.44}$$

$$\hat{H} = \sum_i [-\frac{J}{2}(\hat{\sigma}_i^+ \hat{\sigma}_{i+1}^- + \hat{\sigma}_i^- \hat{\sigma}_{i+1}^+) + \frac{J_z}{4}\hat{\sigma}_i^z \hat{\sigma}_{i+1}^z$$

hopping terms ZZ spin-spin interaction

$$(i) \quad e^{-iJdt(\hat{\sigma}_i^+ \hat{\sigma}_{i+1}^- + \hat{\sigma}_i^- \hat{\sigma}_{i+1}^+)} |\uparrow_i\downarrow_{i+1}\rangle \approx |\uparrow_i\downarrow_{i+1}\rangle - iJdt|\downarrow_i\uparrow_{i+1}\rangle$$

$$(ii) \quad e^{-iJdt(\hat{\sigma}_i^z \hat{\sigma}_{i+1}^z)} |\uparrow_i\downarrow_{i+1}\rangle \approx |\uparrow_i\downarrow_{i+1}\rangle + iJdt|\uparrow_i\downarrow_{i+1}\rangle$$

Figure 3.14: *Effects of XXZ Hamiltonian* – The effects that the XXZ Hamiltonian will have in the state (here for simplicity we choose a two-site Néel state), are the following: (i) For the case of hopping terms, that will simply add an additional probability amplitude in which will flip the correspondent spin terms i and $i+1$ from up and down to down and up (and viceversa). (ii) For the case of the spin-spin interaction, in the case the spins i and $i+1$ are pointing in opposite directions (up-down, down-up) it will simply add probability amplitude with an additional minus sign.

Writing the Hamiltonian in this manner will make some of the underlying physics more evident and will help to see why XXZ serves as a valuable framework for studying non-equilibrium dynamics. As one can see in Fig. 3.14, it's clear that the first terms, which we'll denominate hopping terms, if they act on $|\uparrow\downarrow\rangle$ we'll create super superpositions where the two spins will exchange places (same with state $|\downarrow\uparrow\rangle$). While the third them, which we denominate spin-spin interaction, will introduce an extra-minus sign when there is an up-down/down-up configuration. This hints at one of the fundamental properties of the XXZ Hamiltonian: the conservation of the total magnetization. This means that $|\psi\rangle$ stays an eigenoperator of $\hat{S}^z$ in the sense that $\hat{S}^z |\psi(t)\rangle = M |\psi(t)\rangle$ at all times, where $\hat{S}^z = \sum_n \hat{\sigma}_n^z$ (for the Néel state, $M = 0$). The behaviour of the site and total magnetization of the system, using a Néel state can be seen in Fig. 3.15

An essential condition in all the simulations that we perform with MPS methods will be the convergence in bond dimension χ. To illustrate the importance of this we can see Fig. 3.16. In Fig. 3.16 (a) we perform a quantum quench with Hamiltonian (7.3) on an Néel state, and measure entanglement entropy, S_{vN} in the center of the chain, where we notice a linear growth, until it reaches the limit established by the bond dimension. In case the bond dimension is equal or higher the maximum value of bond dimension the spin chain can have, that is to say $\chi_{\max} = d^{N/2}$, the linear growth will persist until it saturates to its maximum value $S_{\text{vN}} = \log_2(\chi_{\max}) = N/2$. [30]. This linear growth was first pointed out by Calabrese and Cardy [31] and has been encountered in numerous numerical studies on quenched non-equilibrium system [21, 22, 31–34]. We will elaborate on such behavior in later sections, but for our purposes now we want to focus on how the bond dimension χ limits the maximum value of Entanglement Entropy and

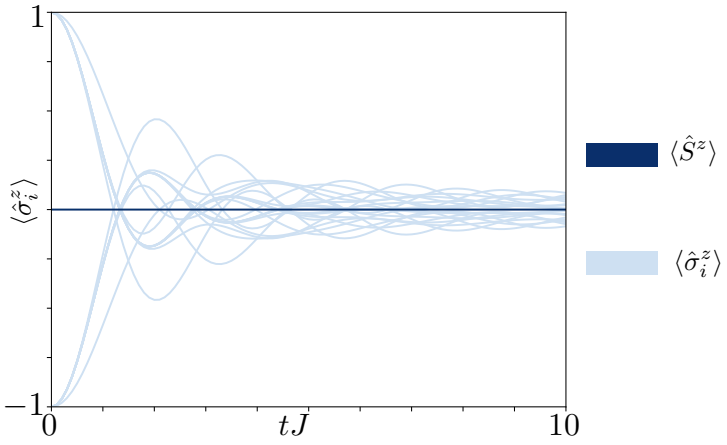

Figure 3.15: *Magnetization Conservation* — Time evolution of $\langle \sigma^z \rangle$ for every site (light blue), and in dark blue we see the value of $\langle \hat{S}_i^z \rangle$, using a Néel state as initial state. The hopping terms, while they create new configurations in the spin chain, such configurations always constrained by the conservation of total magnetization. [$N = 20$, $dt = 0.1, J_z = 1$, $\chi = 512$]

how this affects the accuracy of the simulations. Specifically, what we see is that $\max[S] = \log_2(\chi)$, which is consistent with the analytical results. By trying with larger and larger bond dimensions we can see until which point in time the values for entanglement entropy match, i.e. until which time the results are converged in bond dimension. In Fig. 3.16(b) we look at the time evolution of $\langle \sigma_z \rangle$ for different values of bond dimension to see how this affects the observables and its very clear how this affects strongly the results. By looking at extreme cases $\chi = 4$ and $\chi = 256$ one can notice a great contrast. Examining the behavior of $\langle \sigma_z \rangle$ we notice a tendency for $\langle \sigma_z \rangle$ to go to zero as the system evolves.

In most of the simulations the Néel state will be used as an initial state, partly because we are are interested in entanglement entropy growth dynamics for which the Néel state, under the XXZ Hamiltonian dynamics, turns out to be an ideal choice. To see this more clearly one can use other initial states in order to gain some intuition and context about the effects of XXZ Hamiltonian in other settings. In Fig. 3.17 we try different initial states under a XXZ quantum quench, plotting also the evolution of the Néel state as reference. First we try with several random up/down configurations, in which we notice a lesser growth. This is easy to see in the sense that in random up/down configurations there will be sites with same arrows pairs ($|\uparrow\uparrow\rangle, |\downarrow\downarrow\rangle$), in which the XXZ Hamiltonian will have no effect and thus will not contribute to the entanglement entropy growth. Other of the configurations is the so-called wall state which is half spins up, followed by half spins down.

Previously, we stated that the at the center of the chain, value of S_{vN} is the highest, where performing a quantum quench it reaches a maximum value of $S_{textvN} = N/2$. This maximum value of bond dimension can be simply seeing by doing a series of SVD's decomposition from one extreme of the chain to another (see Fig. 3.4). This effect can be seen explicitly in Fig. 3.18, where we measure

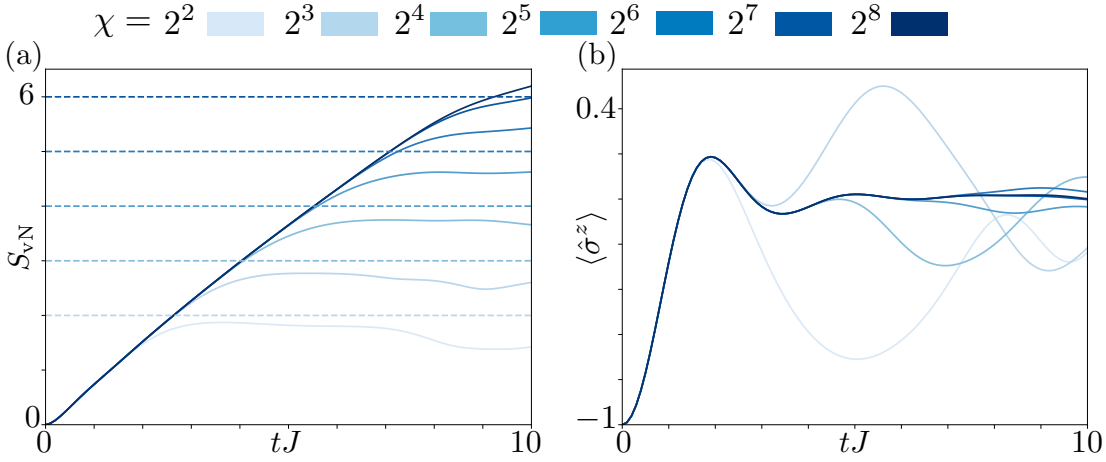

Figure 3.16: *Bond Dimension χ and Observables* — (a) Time evolution of entanglement entropy on site $N/2$ for different values of $\chi = 4, 8, 16, 33, 64, 128, 256$. The maximum value of S_{vN} at the center site is limited by $\log_2(\chi)$. The results are converged with a value of $\chi = 256$ until times $tJ \approx 7$. (b) Time evolution of $\exp(\hat{\sigma}^z)$ on site $N/2$ varying bond dimension χ. Since the results are only converged up to times $tJ \approx 7$, anything after that time may not be accurate. In fact, the results for converged and non-converged observables can diverge significantly, as can be seen by comparing the values for $\chi = 4$ and $\chi = 256$. [$N = 20$, $dt = 0.1, J_z = 1$]

S_{vN} at different bonds. As expected the highest value is at the center of the chain, (in our code first bond is left most, so middle bond is actually N/2 +1), and we see that equivalent bipartitions give the same value of S_{vN}, and so one has the same value for bond 2 and N, 3 and $N-1$, and so on.

Given that we are interested in exploring the limits of the MPS methods for simulation of quantum many-body, we normally would focus on the value of S_{vN} at the center bond, so in fact throughout this thesis, unless differently noted we always refer to the entanglement entropy as the value at the center bond. More concretely, $S_{\mathrm{vN}} \equiv S_{\mathrm{vN}}^{(N/2)}$

Lastly we will explore the effect of parameter J_z correspondent to the ZZ spin interaction. In Fig.3.19(a) we see how by increasing the ZZ spin-spin interaction there is also increase in the entanglement entropy. This of course implies an increasingly difficulty in simulating many-body spin systems in the XXZ model the larger J_z is. In Fig. 3.19(b), we see a that as one increases the ZZ spin-spin interaction one sees a quicker reduction on the oscillations of the value of $\langle\sigma_z\rangle$.

3.5.2 Transverse Field Ising Model

We now will try with a slightly different model, the so called Transverse Field Ising Model (TFIM), which is described with Hamiltonian

$$\hat{H}_{\mathrm{transverse}} = \frac{1}{4}\sum_i J\hat{\sigma}_i^x\sigma_{i+1}^x + \frac{h_z}{2}\sum_i \hat{\sigma}_i^z. \tag{3.45}$$

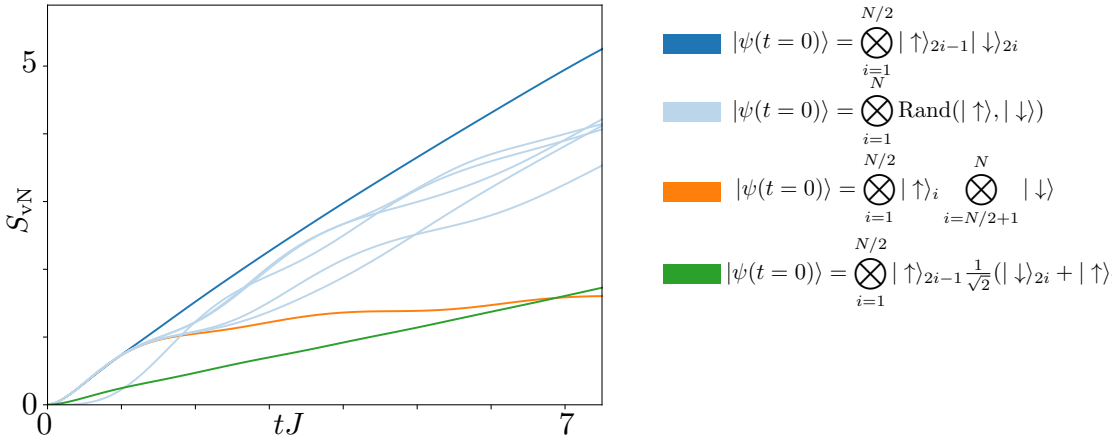

Figure 3.17: *Initial State and Entanglement Entropy Growth* — Time evolution of entanglement entropy using different initial states. One can notice that the largest growth rate occurs with the Néel state (dark blue). We also produce evolution starting from several random initial up/down configurations (light blue) , a wall-state (orange line) with a product state of an up and a polarised state in the $\hat{x}$ direction (green line). [$N = 20$, $dt = 0.1$, $\chi = 256$,$J_z = 1$]

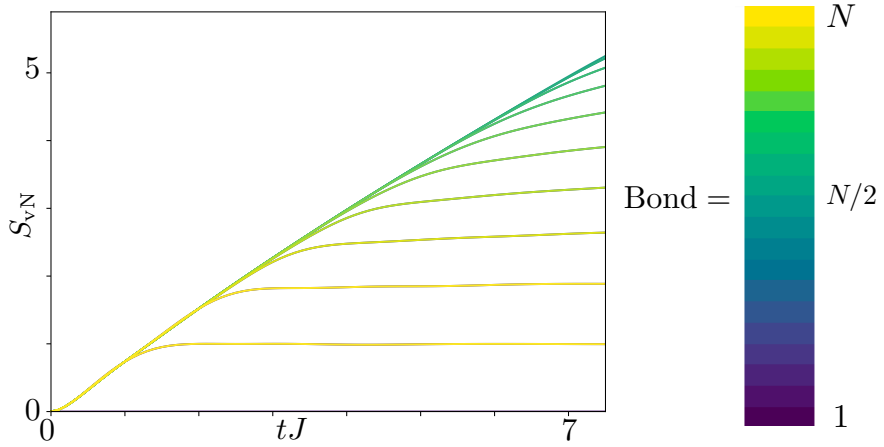

Figure 3.18: *Entanglement Entropy and Bipartition Site* — (a) Time evolution of entanglement entropies, measured at different bonds. As expected, the highest value of S_{vN} is at the center of the chain. The values of equivalent bipartitions are the same and thus superimposed on the plot. [$N = 20$, $dt = 0.1$, $\chi = 256$, $J_z = 1$]

Here, J is a nearest neighbor coupling for the spins, and h_z is another coupling coefficient that determines the relative strength of the external field compared to the nearest neighbor interaction.

The TFIM, unlike the XXZ model, does not conserve total magnetization, but rather the quantity is conserved is parity. While right now this may seem to not have much relevance, it will be important to be acquainted with such properties of the system, since in Chapter 7 we will see how conserved quantities play a fundamental role in understanding entanglement entropies in open spin systems,

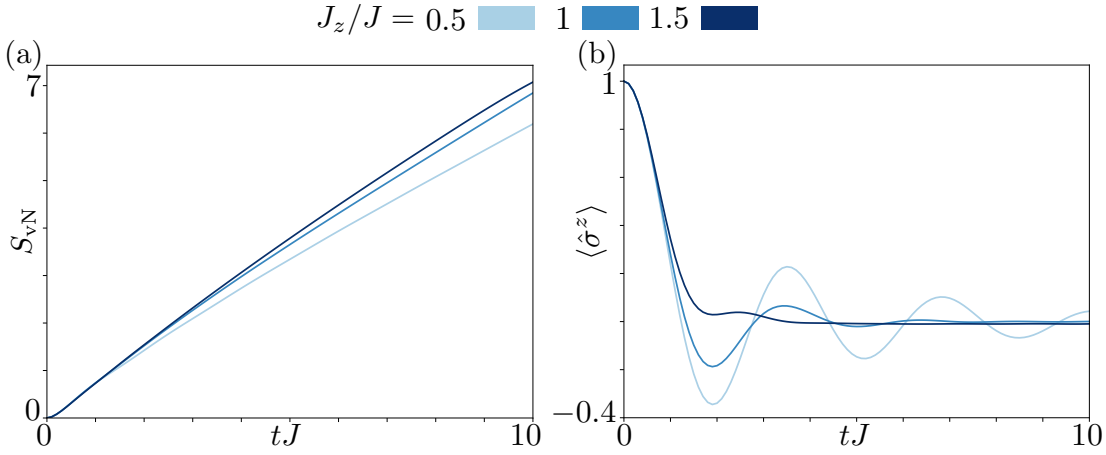

Figure 3.19: *Effect of ZZ spin-spin interaction* — (a) Time evolution of entanglement entropy for diffent values of $J_z/J = 0.5, 1, 1.5$. We notice an increase of S_{vN} as one increases J_z/J. (b) Time evolution of $\langle\sigma_z\rangle$ in the middle site for different values of $J_z/J = 0.5, 1, 1.5$. Particularly we see how by increasing the value of J_z/J there is much quicker reduction on the oscillation amplitude of $\langle\sigma_z\rangle$ as the system evolves [$N = 20$, $dt = 0.1$, $\chi = 512$].

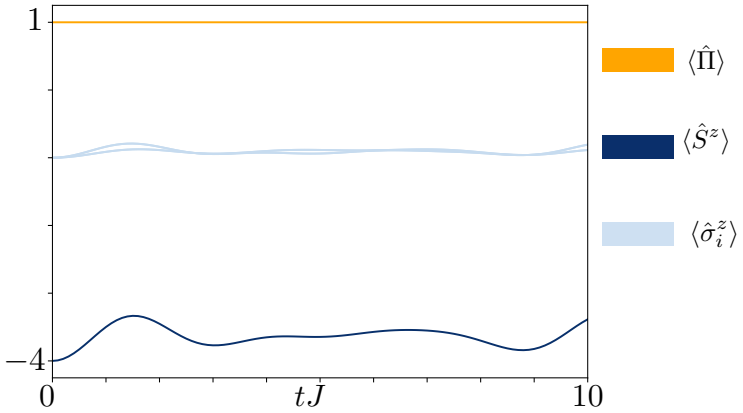

Figure 3.20: *Conserved Quantities in Transverse Ising Model* — (a) Time evolution for site magnetization, total magnetization, and the parity operator, using an all-down spin as initial state. Unlike the XXZ model, we notice that here the total magnetization is not preserved. Instead, it is the parity which preserves its value during the whole evolution. [$N = 4$, $dt = 0.1$, $\chi = 512$, $h_z = 1.0$].

particularly for the case of simulation with Matrix Product Operator.

In Fig. 3.20 using an all-down spin system as initial state, we see that in this case the total magnetization doesn't remain constant through the evolution. Instead is the parity, defined through operator $\hat{P}i = \prod_i \hat{\sigma}_i^z$ the quantity the quantity that remains constant throughout the evolution.

Bibliography

[1] Steven R. White. Density matrix formulation for quantum renormalization groups. *Phys. Rev. Lett.*, 69(19):2863–2866, November 1992.

[2] Steven R. White. Density-matrix algorithms for quantum renormalization groups. *Phys. Rev. B*, 48(14):10345–10356, October 1993.

[3] U. Schollwöck. The density-matrix renormalization group. *Rev. Mod. Phys.*, 77(1):259–315, April 2005.

[4] Karen A. Hallberg. New trends in density matrix renormalization. *Adv. Phys.*, 55(5-6):477–526, July 2006.

[5] Stellan Östlund and Stefan Rommer. Thermodynamic Limit of Density Matrix Renormalization. *Phys. Rev. Lett.*, 75(19):3537–3540, November 1995.

[6] J. Dukelsky, M. A. Martín-Delgado, T. Nishino, and G. Sierra. Equivalence of the variational matrix product method and the. *Europhys. Lett.*, 43(4):457, August 1998.

[7] Guifré Vidal. Efficient Classical Simulation of Slightly Entangled Quantum Computations. *Phys. Rev. Lett.*, 91(14):147902, October 2003.

[8] Guifré Vidal. Efficient Simulation of One-Dimensional Quantum Many-Body Systems. *Phys. Rev. Lett.*, 93(4):040502, July 2004.

[9] A. J. Daley, C. Kollath, U. Schollwock, and G. Vidal. Time-dependent density-matrix renormalization-group using adaptive effective Hilbert spaces. *J. Stat. Mech.: Theory Exp.*, 2004:P04005, 2004.

[10] Steven R. White and Adrian E. Feiguin. Real-Time Evolution Using the Density Matrix Renormalization Group. *Phys. Rev. Lett.*, 93(7):076401, August 2004.

[11] F. Verstraete, J. J. García-Ripoll, and J. I. Cirac. Matrix Product Density Operators: Simulation of Finite-Temperature and Dissipative Systems. *Phys. Rev. Lett.*, 93(20):207204, November 2004.

[12] Tomaž Prosen and Marko Žnidarič. Matrix product simulations of non-equilibrium steady states of quantum spin. *J. Stat. Mech.: Theory Exp.*, 2009(02):P02035, February 2009.

[13] Michael J. Hartmann, Javier Prior, Stephen R. Clark, and Martin B. Plenio. Density Matrix Renormalization Group in the Heisenberg Picture. *Phys. Rev. Lett.*, 102(5):057202, February 2009.

[14] M. C. Bañuls, M. B. Hastings, F. Verstraete, and J. I. Cirac. Matrix Product States for Dynamical Simulation of Infinite Chains. *Phys. Rev. Lett.*, 102(24):240603, June 2009.

[15] Luigi Amico, Rosario Fazio, Andreas Osterloh, and Vlatko Vedral. Entanglement in many-body systems. *Rev. Mod. Phys.*, 80(2):517–576, May 2008.

[16] Guifré Vidal. Efficient Simulation of One-Dimensional Quantum Many-Body Systems. *Phys. Rev. Lett.*, 93(4):040502, Jul 2004.

[17] Ulrich Schollwöck. The density-matrix renormalization group in the age of matrix product states. *Ann. Phys.*, 326(1):96–192, Jan 2011.

[18] Matthew Fishman, Steven White, and Edwin Stoudenmire. The ITensor Software Library for Tensor Network Calculations. *SciPost Phys. Codebases*, page 004, August 2022.

[19] A. T. Sornborger and E. D. Stewart. Higher-order methods for simulations on quantum computers. *Phys. Rev. A*, 60(3):1956–1965, Sep 1999.

[20] G. Vidal. Classical Simulation of Infinite-Size Quantum Lattice Systems in One Spatial Dimension. *Phys. Rev. Lett.*, 98(7):070201, February 2007.

[21] Pasquale Calabrese and John Cardy. Time Dependence of Correlation Functions Following a Quantum Quench. *Phys. Rev. Lett.*, 96(13):136801, April 2006.

[22] Pasquale Calabrese and John Cardy. Quantum quenches in extended systems. *J. Stat. Mech.: Theory Exp.*, 2007(06):P06008, June 2007.

[23] Anatoli Polkovnikov, Krishnendu Sengupta, Alessandro Silva, and Mukund Vengalattore. Colloquium: Nonequilibrium dynamics of closed interacting quantum systems. *Rev. Mod. Phys.*, 83(3):863–883, August 2011.

[24] Christian Gogolin and Jens Eisert. Equilibration, thermalisation, and the emergence of statistical mechanics in closed quantum systems. *Rep. Prog. Phys.*, 79(5):056001, April 2016.

[25] Pasquale Calabrese, Fabian H. L. Essler, and Giuseppe Mussardo. Introduction to 'Quantum Integrability in Out of Equilibrium Systems'. *J. Stat. Mech.: Theory Exp.*, 2016(6):064001, June 2016.

[26] Lev Vidmar and Marcos Rigol. Generalized Gibbs ensemble in integrable lattice models. *J. Stat. Mech.: Theory Exp.*, 2016(6):064007, June 2016.

[27] Fabian H. L. Essler and Maurizio Fagotti. Quench dynamics and relaxation in isolated integrable quantum spin chains. *J. Stat. Mech.: Theory Exp.*, 2016(6):064002, June 2016.

[28] Pasquale Calabrese and John Cardy. Quantum quenches in 1 + 1 dimensional conformal field theories. *J. Stat. Mech.: Theory Exp.*, 2016(6):064003, June 2016.

[29] CD Batista and Gerardo Ortiz. Generalized jordan-wigner transformations. *Physical review letters*, 86(6):1082, 2001.

[30] J Schachenmayer, BP Lanyon, CF Roos, and AJ Daley. Entanglement growth in quench dynamics with variable range interactions. *Physical Review X*, 3(3):031015, 2013.

[31] Pasquale Calabrese and John Cardy. Evolution of entanglement entropy in one-dimensional systems. *J. Stat. Mech.: Theory Exp.*, 2005(04):P04010, Apr 2005.

[32] J Dubail. Entanglement scaling of operators: a conformal field theory approach, with a glimpse of simulability of long-time dynamics in 1+1d. *Journal of Physics A: Mathematical and Theoretical*, 50(23):234001, may 2017.

[33] T. Barthel and U. Schollwöck. Dephasing and the Steady State in Quantum Many-Particle Systems. *Phys. Rev. Lett.*, 100(10):100601, March 2008.

[34] S. Bravyi, M. B. Hastings, and F. Verstraete. Lieb-Robinson Bounds and the Generation of Correlations and Topological Quantum Order. *Phys. Rev. Lett.*, 97(5):050401, July 2006.

Chapter 4

Entanglement Entropy

The study of entanglement in many-body models has undeniably been a long-standing focus in theoretical physics [1, 2]. It offers profound insights into a diverse range of phenomena, spanning from super-radiance [3] and superconductivity [4] to disordered systems [5] and the emergence of classicality [6]. Understanding the dynamics of entanglement growth in many-body systems not only sheds light on these phenomena but also plays a crucial role in refining simulation methods and revealing their limitations.

In particular, the evolution of entanglement entropy, which quantifies the entanglement between different regions of a quantum system, has been closely linked to the capabilities of classical computers in simulating non-equilibrium quantum dynamics, especially in one dimension, via MPS [7–11]. Based on early results from conformal field theory [12, 13] and on exact/numerical results for simple solvable models [12, 14], it is widely accepted [15] that the entanglement entropy grows linearly with time following a so-called quantum quench (i.e., starting with an initial state $|\psi_0\rangle$ at $t = 0$, typically the ground state of a quantum many-body Hamiltonian $\hat{H}_0$, the dynamics are abruptly changed to evolve the state with another Hamiltonian H, with $[\hat{H}, \hat{H}_0] \neq 0$). This observed linear increase in entanglement poses a significant challenge for simulating such systems, rendering the study of non-equilibrium dynamics in extended quantum systems one of the most daunting problems in contemporary theoretical physics.

An effective approach to understanding some of the primary qualitative features of entanglement in non-equilibrium dynamics has been provided through the so-called quasi-particle picture [12]. In this picture, the pre-quench initial state serves as a source of pairs of excitations with opposite momentum that propagate ballistically through the system. The central assumption of the quasiparticle picture is that excitations created far apart from each other are incoherent, whereas those emitted at the same point in space are entangled. As the quasiparticles propagate, larger regions of the system become entangled. At time t, the entanglement entropy of a subsystem A is proportional to the total number of quasiparticles that, after being emitted from the same point in space, are shared between subsystem A and its complement. A rigorous mathematical treatment of these arguments can be found in [16], but for our purposes, a qualitative understanding of the picture is sufficient as we proceed with the analysis of the topic from a numerical simulation

perspective.

Another essential feature of entanglement entropy is that it typically obeys the 'area law'. The area law states that the growth of entanglement entropy scales with the area of the boundary between the regions in a bipartition of the system, rather than their volume [17]. This property has significant implications across a range of physical phenomena, making it a key research focus in various disciplines.

In this chapter, we aim to delve deeper into the connection between entanglement and entropy in quantum systems. To accomplish this, we will introduce alternative measures of entanglement entropy, moving beyond the conventional Von Neumann entropy. Following that, we will further explore the implications and significance of the 'area law'. Finally, we will wrap up the chapter by presenting the concept of symmetry-resolved entanglement entropies.

4.1 Rényi Entropy

In section 3.1.1 we presented the Von Neumann entropy formula (Eq. (3.10) and we show how it can gives us information related to the entanglement of the system. However, Von Neumann entropy is not the only measure for entanglement entropy that exists. One of other that we consider worth mentioning is the Rényi entropy, which is given by

$$S_A^\alpha(t) = \frac{1}{1-\alpha}\log_2\left(\sum_i^r (\lambda_i^2)^\alpha\right), \tag{4.1}$$

where the λ_i are positive real coefficients of the Schmdit decomposition of some state $|\psi\rangle$. For $\alpha > 0$ and for $\alpha \neq 1$ will be known as Rényi Entropies of order α. In the limit $\alpha \to 1$ we recover the Von Neumann Entanglement Entropy equation (3.10)

$$S_{\text{vN}}(t) = \lim_{\alpha\to 1} S_A^\alpha(t) = -\sum_i^r (\lambda_i)^2 \log_2[(\lambda_i)^2]. \tag{4.2}$$

While we primarily use Eq. (4.2) to refer to entanglement entropy, it is valuable to also familiarize ourselves with Rényi entropies as they more precise insights into the possibilities of approximating one-dimensional quantum many-body systems through MPS, since, strictly speaking, the case $\alpha = 1$ is usually not sufficient to ensure that a state can be approximated by an MPS, see Ref. [7]. Another remarkable fact about Rényi entropies is that for integers $\alpha \geq 2$ it is possible to manipulate Eq. (4.1) and express it as the expectation value of an operator, dubbed swap operator by Zanardi, Zalka and Faoro [18], in a replicated system. Express it this way will make it amenable to experimental probing. To be more precise, taking α identical replicas of quantum state $|\psi\rangle$, creating a new state in a larger Hilbert space, $|\psi\rangle^{\otimes\alpha} = |\psi\rangle \otimes |\psi\rangle \otimes \cdots \otimes |\psi\rangle \in \mathcal{H}^\alpha$. The swap operator is the operator that cyclically permutes the α replicas of the subsystem A, leaving B untouched; we write it as $\mathcal{S}_A(1, 2, 3, ..., \alpha)$. The subscript $(1, 2, 3, \ldots, \alpha)$ indicates the permutation of α elements, written in cycle notation; notice that here the permutation σ has a single cycle $(1, \sigma(1), \sigma \circ \sigma(1)$, etc.) of total length α. The equation for Rényi entropies can then be expressed as

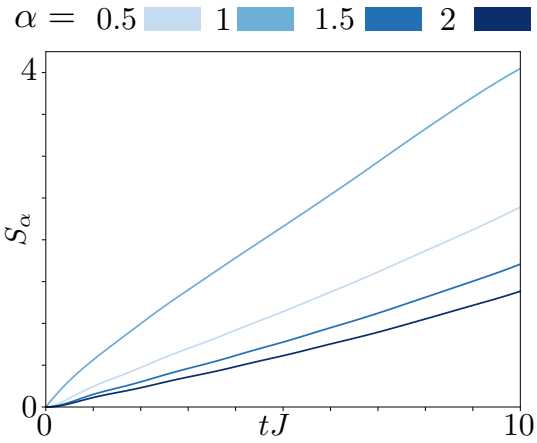

Figure 4.1: *Rényi entropies* — Rényi entropy dynamics in an XXZ model with a Néel state as an initial state, we calculate the rényi entropies for different values of $\alpha = 0.5, 1, 1.52.0$. In all cases, S_α displays a linear growth. $[N = 20, dt = 0.1, \chi = 256,\ J_z = 1]$.

$$(\alpha \text{ integer} > 2) \qquad S_\alpha(|\psi\rangle) = \frac{1}{1-\alpha}\log_2\Big(\langle\psi|^{\otimes\alpha}\,\mathcal{S}^A_{1,2,3,\ldots,\alpha}\,|\psi\rangle^{\otimes\alpha}\Big) \tag{4.3}$$

The main advantage of the latter expression over Eq. (4.1) is that it makes it clear that the quantity inside the logarithm is an observable [18]; it is the basic idea of various proposals to measure the entanglement entropy [19–21], and it is at heart of the recent groundbreaking experiment [22] that managed to measure S_2 in a cold atom setup.

Having mentioned this important facts concerning the role of the Rényi parameter α, it is fair to say that in most known situations, the behavior of S_α does not appear to depend dramatically on the precise value of α. This can be seen in Fig. 4.1, where despite the slight differences in the dynamics of S_α depending to the factor α, in all cases there is a linear scaling in the growth. and it is often the case in one-dimensional systems that the area law is either obeyed for all $\alpha > 0$, or violated for all $\alpha > 0$.

To have a better understanding about entanglement entropy let's look at a simple example where we compare the values of entanglement entropy for two different types of states: a Bell state (fully entangled) and a product state (no entanglement). Given that we have direct access to the Schmidt coefficient, we could use Eq. (4.2) which is what one does for extended systems, however for pedagogical purposes we consider convenient to do the longer procedure calculating the corresponding density matrices to gain insight and confirm that indeed Eq. (3.10) is a reliable measure for entanglement entropy.

We start by considering a Bell State

$$|\psi_1\rangle = \tfrac{1}{2}(|\uparrow_A\rangle|\downarrow_B\rangle + |\downarrow_A\rangle|\uparrow_B\rangle), \tag{4.4}$$

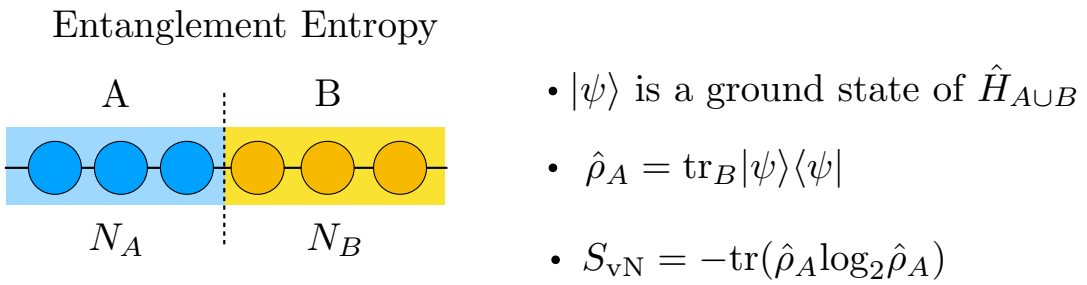

Figure 4.2: *Entanglement entropy* — By doing a bipartition of the system and calculating the Von Neumann entropy in one of the subsystems one obtains the entanglement entropy of the system.

The first step is to calculate the corresponing density matrix $\hat{\rho}_1 = |\psi_1\rangle\langle\psi_1|$. Then we proceed to calculate the reduced density matrix $\hat{\rho}_1^A = \mathrm{tr}_B(\rho_1) = \frac{1}{2}\hat{I}$ from one can simply use formula (3.10) obtaining the result

$$S_{\mathrm{vN}}(|\psi_1\rangle) = 1, \tag{4.5}$$

which is consistent with what we would expect from an entangled state.

On the other hand, when we consider a product state,

$$|\psi_2\rangle = |\uparrow_A\rangle\,|\downarrow_B\rangle\,, \tag{4.6}$$

and doing the same procudure, it's easy to see that

$$S_{\mathrm{vN}}(|\psi_2\rangle) = 0. \tag{4.7}$$

Let's look more closely about what this result implies, while in classical physics the concept of entropy quantifies the amount of information that is lacking to identify the microstate of a system from all possibilities compatible with the macrostate of the system. The entanglement entropy that we got in the first example did not arise due to a lack of information, since we considered a pure density matrix, instead its origin is because of a very fundamental property of quantum mechanics: entanglement.

4.2 Area Law

We will now provide a more rigorous analysis of what the area law says, by considering Hilbert space $\mathcal{H} = (\mathbb{C}^d)^{\otimes N}$ of a spin chain, as depicted in Fig 4.2, where d is the dimension of the local degree of freedom on each site, and N is the total number of sites. The subsystem A (resp. B) is made up of the first N_A sites (with $N_B = N - N_A$ sites). Then, one says that $|\psi\rangle$ obeys the area law (for a given α) if S_α remains bounded when $N_A, N_B \to \infty$. A famous theorem of Hastings [23]

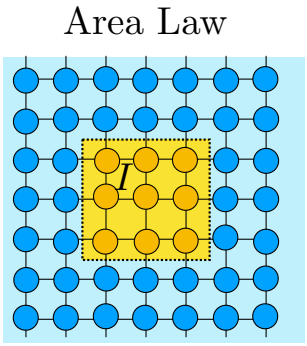

Figure 4.3: *Area law* — A lattice N with a distinguished set $I \subsetneq L$ (yellow area). Dotted lines depict the boundary ∂I of I with surface area $s(I) = |\partial I|$.

states that when $|\psi\rangle$ is the ground state of a gapped local Hamiltonian, it obeys the area law, with $\alpha = 1$.

In a more general case, when we are not necessarily dealing with a spin chain, but with a D dimensional lattice, what the area law says is that entanglement entropy often merely grows like the boundary area of the subregion, and not like its volume, in sharp contrast with an expected extensive behavior. To put it more precisely for a D-dimensional N-site lattice, one expects that the entanglement entropy grows as

$$S(N) = aN^{D-1} + \mathcal{O}(N^{D-1}). \tag{4.8}$$

From the MPS perspective, the area law can also be understood by noticing that in a MPS the entanglement between a block of sites and the rest of the system is primarily governed by the bonds connecting the block to the rest of the system. These bonds capture the correlations and entanglement between the block and its complement. Since the entanglement is mainly determined by the bonds, which are localized to the boundary of the subsystem, in a large number of cases the entanglement entropy obeys the area law.

Nevertheless, after seeing the entanglement entropy dynamics in cases, such as in Fig. 4.1, where we see a linear growth of entanglement entropy in 1D spin chains, this may seem contradictory with what the area law states, since one would expect a constant value. It is thus important to mention that the area law is more applicable when considering the steady-state or equilibrium properties of a quantum system. During the transient dynamics of a quantum quench, the system is out of equilibrium, and the growth of entanglement entropy can exceed the expectations of the area law.

Ultimately, while the growth of entanglement entropy during a quantum quench may not strictly follow the area law, the ultimate equilibrium state that the system reaches after the quench is expected to satisfy the area law. Once the system thermalizes or reaches a steady state, the entanglement entropy between regions will typically scale with the boundary size rather than the volume.

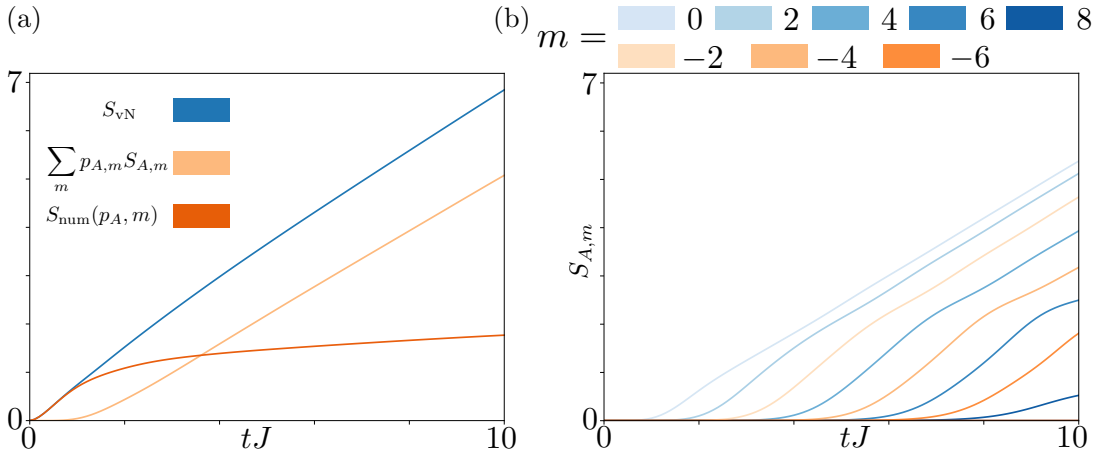

Figure 4.4: *Symmetry Resolved Entanglement Entropies* — We consider an infinite-site XXZ model with Néel state as an initial state. (a) Time-evolution for entanglement entropy and the contribution of the entropies for the magnetization symmetry sector and of the number fluctuations of the different symmetry sectors. We see that the contributions of the symmetry sectors and its fluctuations add up to give the entanglement entropy in accordance with Eq. (4.10). (b) Time-evolution for the entropies for magnetization symmetry sectors corresponding to eigenvalues of magnetization $m = 0, 2, 4, 6$ (blue lines) and $m = -2, -4, -6$ (orange lines). [N $= \infty$, $\chi = 512$, $dt = 0.1/J$, $J_z/J = 1.0$]

4.3 Symmetry Resolved Entanglement Entropies

Lastly we will introduce the Symmetry Resolved Entanglemenent Entropies. Such symmetry-resolved entropies have attracted attention recently [24–28] and will play a big role in Chapter 7 to study the dynamics of Operator Entanglement in the presence of conserved quantities.

The central idea about these symmetry-resolved entropies is to split the total entanglement into the contributions coming from disjoint symmetry sectors. To understand this more simply it can be convenient to look at a concrete example. We consider again a general quantum chain with N sites, whose Hamiltonian $\hat{H} = \sum_{i=1}^{N} \hat{h}_{i,i+1}$, commutes with the magnetization operator $\hat{S}^z = \sum_{i=1}^{N} \hat{\sigma}_i^z$. Let $|\psi\rangle$ be a common eigenstate of $\hat{H}$ and $\hat{S}_z$, with eigenvalues E and M respectively. We split the chain into disjoints blocks A ($i = 1, ..., l$) and B ($i = l+1, ..., N$), and compute the reduced density matrix $\hat{\rho}_A$. The magnetization operator also splits into the sum $\hat{S}^z = \hat{S}^z_A + \hat{S}^z_B$. Then, tracing over the Hilbert subspace of the block B in the equation$[\hat{S}^z, \hat{\rho}] = 0$ yields $[\hat{S}^z_A, \hat{\rho}_A] = 0$. This implies

$$\rho_A = \oplus_m \tilde{\rho}_{A,m} = \oplus_m p_{m,A} \rho_{A,m}, \tag{4.9}$$

where $\hat{\rho}_{A,m}$ is a density matrix with eigenvalue m of $\hat{S}^z_A$, and $p_{A,m} = \text{tr}\tilde{\rho}_{A,m} \geq 0$ is the probability of finding m in a measurement of $\hat{S}^z_A$. The decomposition (4.9), which has a block diagonal form is regurlarly implemented in DMRG, MPS, and MPDO simulations to reduce the memory resources needed for high precision

results. Particularly this decomposition will be implemented in several simulations shown in Chapters 8 and 7. The latter equation allows to express the entanglement entropy of the system as

$$S_{\text{vN}} = \sum_m p_{A,m} S_{A,m} + S_{\text{num}}(p_{A,m}), \tag{4.10}$$

where S_A are the entropies associated to each magnetization symmetry sector and are given by $S_{A,m} = -\text{tr}(\hat{\rho}_{A,m}\log_2\hat{\rho}_{A,m})$, and S_{num} is associated to number fluctuations in the different symmetry sectors is given by $S_{\text{num}} = -\sum_m p_{A,m}\log_2 p_{A,m}$. Eq. (4.10) means that the quantum entropy in the subsystem A is greater, in general, to the weighted sum of the entropies of the different magnetization sectors. There is also an additional contribution to the entanglement entropy due to the number fluctuations in each of the symmetry sectors of the bipartition.

To finalze the section, Fig. 4.4 displays simulations of an infinite-site XXZ model initialized with a Néel state. This figure provides insights into the dynamics of the entanglement entropy and the entropy corresponding to the symmetry sectors, along with their associated probabilities. Fig. 4.4 (a) demonstrates the anticipated linear increase of the entanglement entropy. However, the surprising elements lie within the contributions and interplay of the symmetry sectors. Initially, there is linear growth purely from the different blocks of the symmetry sectors. However, this contribution alone does not suffice to produce the total entanglement entropy; there is also a related contribution from the probabilities of measuring any of the various symmetry sectors in the bipartition. The entanglement created during evolution causes a loss of information concerning the measurement of different symmetry sectors of the bipartite system. Fig. 4.4 (b) reveals an initial visible contribution solely from the initial symmetry sector of $m = 0$, which corresponds to a Néel state. However, as the evolution progresses, there is an added contribution of more symmetry sectors, to the entanglement entropy.

The study of the dynamics of the symmetry resolved entanglement entropies and the distribution probability associated to the different symmetry sectors under dephasing will be a key process to understand the dynamics of what is known as Operator Entanglement, and will be the major subject of Chapter 7.

Bibliography

[1] Luigi Amico, Rosario Fazio, Andreas Osterloh, and Vlatko Vedral. Entanglement in many-body systems. *Rev. Mod. Phys.*, 80(2):517–576, May 2008.

[2] J. Eisert, M. Cramer, and M. B. Plenio. Colloquium: Area laws for the entanglement entropy. *Rev. Mod. Phys.*, 82(1):277–306, February 2010.

[3] Neill Lambert, Clive Emary, and Tobias Brandes. Entanglement and the Phase Transition in Single-Mode Superradiance. *Phys. Rev. Lett.*, 92(7):073602, February 2004.

[4] Vlatko Vedral. High-temperature macroscopic entanglement. *New J. Phys.*, 6(1):102, August 2004.

[5] W. Dür, L. Hartmann, M. Hein, M. Lewenstein, and H.-J. Briegel. Entanglement in Spin Chains and Lattices with Long-Range Ising-Type Interactions. *Phys. Rev. Lett.*, 94(9):097203, March 2005.

[6] Wojciech Hubert Zurek. Decoherence and the Transition from Quantum to Classical — Revisited. In *Quantum Decoherence*, pages 1–31. Birkhäuser, Basel, Switzerland, 2006.

[7] Norbert Schuch, Michael M. Wolf, Frank Verstraete, and J. Ignacio Cirac. Entropy Scaling and Simulability by Matrix Product States. *Phys. Rev. Lett.*, 100(3):030504, January 2008.

[8] N. Schuch, M. M. Wolf, K. G. H. Vollbrecht, and J. I. Cirac. On entropy growth and the hardness of simulating time evolution. *New J. Phys.*, 10(3):033032, March 2008.

[9] Álvaro Perales and Guifré Vidal. Entanglement growth and simulation efficiency in one-dimensional quantum lattice systems. *Phys. Rev. A*, 78(4):042337, October 2008.

[10] Philipp Hauke, Fernando M. Cucchietti, Luca Tagliacozzo, Ivan Deutsch, and Maciej Lewenstein. Can one trust quantum simulators? *Rep. Prog. Phys.*, 75(8):082401, July 2012.

[11] J. Dubail. Entanglement scaling of operators: a conformal field theory approach, with a glimpse of simulability of long-time dynamics in 1 + 1d. *J. Phys. A: Math. Theor.*, 50(23):234001, May 2017.

[12] Pasquale Calabrese and John Cardy. Evolution of entanglement entropy in one-dimensional systems. *J. Stat. Mech.: Theory Exp.*, 2005(04):P04010, April 2005.

[13] Pasquale Calabrese and John Cardy. Entanglement and correlation functions following a local quench: a conformal field theory. *J. Stat. Mech.: Theory Exp.*, 2007(10):P10004, October 2007.

[14] Gabriele De Chiara, Simone Montangero, Pasquale Calabrese, and Rosario Fazio. Entanglement entropy dynamics of Heisenberg chains. *J. Stat. Mech.: Theory Exp.*, 2006(03):P03001, March 2006.

[15] U. Schollwöck. The density-matrix renormalization group. *Rev. Mod. Phys.*, 77(1):259–315, April 2005.

[16] Vincenzo Alba and Pasquale Calabrese. Entanglement dynamics after quantum quenches in generic integrable systems. *SciPost Phys.*, 4(3):017, March 2018.

[17] J. Eisert, M. Cramer, and M. B. Plenio. Colloquium: Area laws for the entanglement entropy. *Rev. Mod. Phys.*, 82(1):277–306, Feb 2010.

[18] Paolo Zanardi, Christof Zalka, and Lara Faoro. Entangling power of quantum evolutions. *Phys. Rev. A*, 62(3):030301, August 2000.

[19] A. J. Daley, H. Pichler, J. Schachenmayer, and P. Zoller. Measuring Entanglement Growth in Quench Dynamics of Bosons in an Optical Lattice. *Phys. Rev. Lett.*, 109(2):020505, July 2012.

[20] John Cardy. Measuring Entanglement Using Quantum Quenches. *Phys. Rev. Lett.*, 106(15):150404, April 2011.

[21] Dmitry A. Abanin and Eugene Demler. Measuring Entanglement Entropy of a Generic Many-Body System with a Quantum Switch. *Phys. Rev. Lett.*, 109(2):020504, July 2012.

[22] Rajibul Islam, Ruichao Ma, Philipp M. Preiss, M. Eric Tai, Alexander Lukin, Matthew Rispoli, and Markus Greiner. Measuring entanglement entropy in a quantum many-body system. *Nature*, 528:77–83, December 2015.

[23] M. B. Hastings. An area law for one-dimensional quantum systems. *J. Stat. Mech.: Theory Exp.*, 2007(08):P08024, August 2007.

[24] Moshe Goldstein and Eran Sela. Symmetry-Resolved Entanglement in Many-Body Systems. *Phys. Rev. Lett.*, 120(20):200602, May 2018.

[25] J. C. Xavier, F. C. Alcaraz, and G. Sierra. Equipartition of the entanglement entropy. *Phys. Rev. B*, 98:041106(R), Jul 2018.

[26] Gilles Parez, Riccarda Bonsignori, and Pasquale Calabrese. Quasiparticle dynamics of symmetry-resolved entanglement after a quench: Examples of conformal field theories and free fermions. *Phys. Rev. B*, 103:L041104, Jan 2021.

[27] Hatem Barghathi, C. M. Herdman, and Adrian Del Maestro. Rényi Generalization of the Accessible Entanglement Entropy. *Phys. Rev. Lett.*, 121(15):150501, October 2018.

[28] Hatem Barghathi, Emanuel Casiano-Diaz, and Adrian Del Maestro. Operationally accessible entanglement of one-dimensional spinless fermions. *Phys. Rev. A*, 100(2):022324, August 2019.

Chapter 5

Quantum Trajectories in Many-Body Systems

The quantum trajectory method has proven extremely successful for studying individual or small quantum systems, yielding valuable insights into a variety of phenomena such as laser cooling [1], the behavior of cascaded quantum systems [2], the continuous quantum Zeno effect [3], and quantum non-demolition measurements [4]. These examples underscore the versatility and efficacy of quantum trajectory techniques for understanding and controlling quantum dynamics.

However, the quantum trajectory method's efficiency encounters substantial challenges when applied to quantum many-body systems. The increase in the number of particles in the system results in exponential scaling of the Hilbert space, posing significant computational difficulties. Despite the quantum trajectory method allowing for a smaller subset of the Hilbert space to be considered compared to the density matrix approach, the exponential growth of the space still limits its applicability for large-scale quantum many-body dynamics.

A promising approach that has emerged in recent years combines quantum trajectory methods with Matrix Product States (MPS). This hybrid approach, denoted as QT+MPS, formulates each pure state as an MPS and incorporates stochastic evolution with dissipation through quantum jumps. Given that the efficiency of the MPS representation is dictated by the bipartite entropy, the question of the scaling growth of the bipartite entropy dynamics and how it is influenced by dissipation becomes a crucial issue that determines the method's efficiency. Specifically, we will explore the average behavior of the bipartite entropies, which we will refer to as "trajectory entanglement" (TE). This approach has been successfully applied in many MPS simulations [5, 6]. The study and application of this method will be one of the primary topics in this chapter and a significant portion of the thesis.

Having already elucidated the basics of the quantum trajectory method in chapter 2, this chapter will shift focus towards its applications and constraints within the context of many-body systems. Furthermore, we will direct our attention towards the QT+MPS method. We will introduce the concept of trajectory entanglement (TE) and explore how trajectories can provide insight into the conserved quantities of a system.

5.1 Many-Body Wave Function Unravelling and the time-step problem

In the original formulation of the quantum trajectory method, presented in Chapter 2 there is an inherent issue known as the time-step problem. This arises from the fact that the equivalence of the master equation is based on a first-order Euler approximation [6], necessitating small time-step sizes Δt. To address this problem, several methods have been proposed to mitigate its impact. In this section, we will first present the many-body unravelling of the way function to identify in a more concrete way where exactly does the problem originates, and we present some alternative methods that offer partial solutions to the time-step problem, aiming to improve the efficiency and accuracy of the quantum trajectory method in the many-body setting.

5.1.1 Unravelling with one jump per-time step

This time we consider a N particles non-hermitian Hamiltonian expressed as

$$\hat{H} = \hat{H}_S - \tfrac{i\hbar}{2} \sum_{n,m}^{N,M} \gamma_{m,n} \hat{C}^\dagger_{m,n} \hat{C}_{m,n}. \tag{5.1}$$

Doing a trajectory unravelling with many-body Hamiltonian (5.1) it's easy to see that up to Eq. (2.28) the trajectory evolution through a time-step is the same. However the problem now relies at the moment of choosing a δt such that $\delta p \ll 1$. Assuming the dissipation rate is the same regardless of the site, one arrives to

$$\delta p \equiv \delta t \frac{i}{\hbar} \left\langle \psi_\tau(t) \right| \hat{H} - \hat{H} \left| \psi_\tau(t) \right\rangle \equiv \sum_{m,n} \delta p_{m,n} = N \sum_m \delta p_m. \tag{5.2}$$

Now, if one needs $\delta p \ll 1$, one can still adjust δt, however, given that in this case this is multiplied by a factor $N \sum_m \gamma_m$, this would become more inefficient the more sites one has and the higher the rate. Generally the time-step would scale as

$$\delta t \approx \frac{1}{\sum_m \gamma N}, \tag{5.3}$$

which becomes problematic if one attempts to do long-time many-body simulation. In any case, in order to select the site in which the jump will occur, one must simply selects accordingly to the jump probabilities

$$p_n \equiv \frac{\left\langle \phi(t) \right| \hat{C}^\dagger_n \hat{C}_n \left| \phi(t) \right\rangle}{\sum_{n'} p_{n'}}. \tag{5.4}$$

5.1.2 Possibility of several jumps per time-step

Here we present an alternative scheme developed by Vovke [7], in which the time-step problem can be partially improved by considering more than one jump per time-step. The method work as follows: If one considers jump operators which commute, $[\hat{C}_\eta, \hat{C}_\mu] = 0$ for $\nu \neq \mu$. Then, multiple quantum jumps can be applied within a single time-step. The way one do this is to first evolve $|\psi_\tau\rangle$ with only the hermitian Hamiltonian $\hat{H}_S$ and then conditionally apply quantum jumps after evolving with a trotterized non-unitary evolution operator, corresponding to the dynamics of individual decay channels η, $-i\hat{C}_\eta^\dagger \hat{C}_\eta/2$. While this scheme still leads to a first-order method, the method then only introduces time-step errors of order $\mathcal{O}(\Delta t\gamma)^2$ [instead of $\mathcal{O}(\Delta t N\gamma)^2$]. For higher order integration schemes one should resort to schemes as presented in [8], which are however cumbersome to implement in case of a large amount of decay channel.

If one considers again an unravel of the trajectories using Hamiltonian (5.1), one first evolves with the hermitian part, and in that case, since the probability is conserved no jumps will happen. However, one then considers an evolution with the non-hermitian part of Hamiltonian (5.1)

$$|\psi_\tau(t+\delta t)\rangle = e^{-i\hat{H}_{\rm nh}\delta t}\,|\psi_\tau(t)\rangle\,. \tag{5.5}$$

Given that we want to conditionally apply the quantum jump on each site, one does a trotter approximation on the Hamiltonian, which leads to an evolution of the form

$$|\psi_\tau(t+\delta t)\rangle = \prod_\eta e^{-i\hat{H}^\eta_{\rm nh}\delta t}\,|\psi_\tau(t)\rangle\,. \tag{5.6}$$

Doing a first-order expansion we get

$$|\psi_\tau(t+\delta t)\rangle \approx \prod_\eta (1 - \frac{i\hat{H}^\eta_{\rm nh}\delta t}{\hbar})\,|\psi_\tau(t)\rangle \tag{5.7}$$

Calculating the norm of the state we get

$$\langle\psi_\tau(t+\delta t)|\psi_\tau(t+\delta t)\rangle = \langle\psi(t)|\prod_\eta\prod_\eta (1 + \frac{i\hat{H}^{\eta\dagger}_{\rm nh}\delta t}{\hbar})(1 - \frac{i\hat{H}^\eta_{\rm nh}\delta t}{\hbar})\,|\psi_\tau(t)\rangle \tag{5.8}$$

$$\approx 1 - \sum_\eta \delta p_\eta \tag{5.9}$$

where

$$\delta p_\eta = \delta t\frac{i}{\hbar}\,\langle\phi(t)|\,\hat{H}^\eta_{n\rm nh} - \hat{H}^{\eta\dagger}_{\rm nh}\,|\psi_\tau(t)\rangle = \delta t\,\langle\psi_\tau(t)|\,\gamma_\eta\hat{C}^\dagger_\eta\hat{C}_\eta\,|\psi_\tau(t)\rangle \tag{5.10}$$

Here's where the main difference – and advantage – of the method can be more explicitly seen: rather than drawing one single random number ϵ, one draws a random number for every decay channel (i.e. if there is only one type of dissipation on every site, one would draw N random numbers) and after doing the evolution on each site, one compares the norm probability δp_η with a correspondent random number ϵ_η. This improves the time-step convergence, such that the scaling goes from $\delta t \approx 1/N\sum_m \gamma_m$ to just $\delta t \approx 1/\sum_m \gamma_m$. Allowing the possibility do reach larger time-scales in many-body simulations.

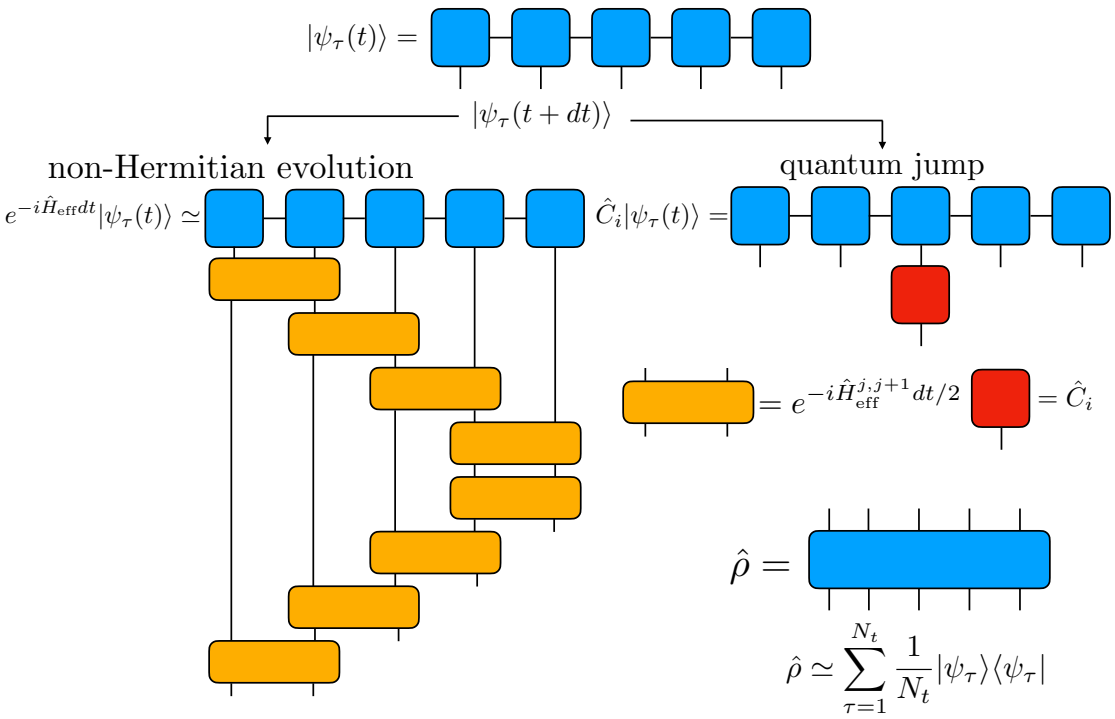

Figure 5.1: *Quantum Trajectories + Matrix Product States (QT+MPS)* — The QT+MPS method consists in decomposing the density operator into several trajectories, where each trajectory is represented as a MPS and follows a stochastic dynamics. For every time-step dt there will be two possible evolutions: i) Non-hermitian evolution: With probability $1-\delta p$ the system evolves according to $\hat{H}_{\text{eff}}$ in its trotterized form (left side). ii) Quantum jump: With the probability δp one acts with one of the jump operators. In this case, the jump occurs on site i (right side).

5.2 Quantum Trajectory + MPS

So far, we have discussed the Quantum Trajectory method for simulating the open system dynamics of individual or multiple particles, along with some approaches to address the time-step problem. However, even with improvements in the time-step size, the exponential growth of the Hilbert space with the number of particles presents significant challenges in simulating open quantum many-body systems. Having previously discussed MPS techniques, a tempting solution to this problem is to combine the quantum trajectory approach with MPS. We will denominate such method as QT+MPS, which has been studied previously in [5, 6]. In this method each trajectory is decomposed in a MPS form as presented in Fig. 5.1. The decomposition for each trajectory will be the same as the one presented in Chapter 3

$$|\psi_\tau\rangle = \sum_{\{i_n\}} \sum_{\{a_n\}}^{\chi} \prod_n \Gamma^{[n]i_n}_{a_n,a_{n+1}} \lambda^{[n]}_{a_n} \bigotimes_n |i_n\rangle \,. \tag{5.11}$$

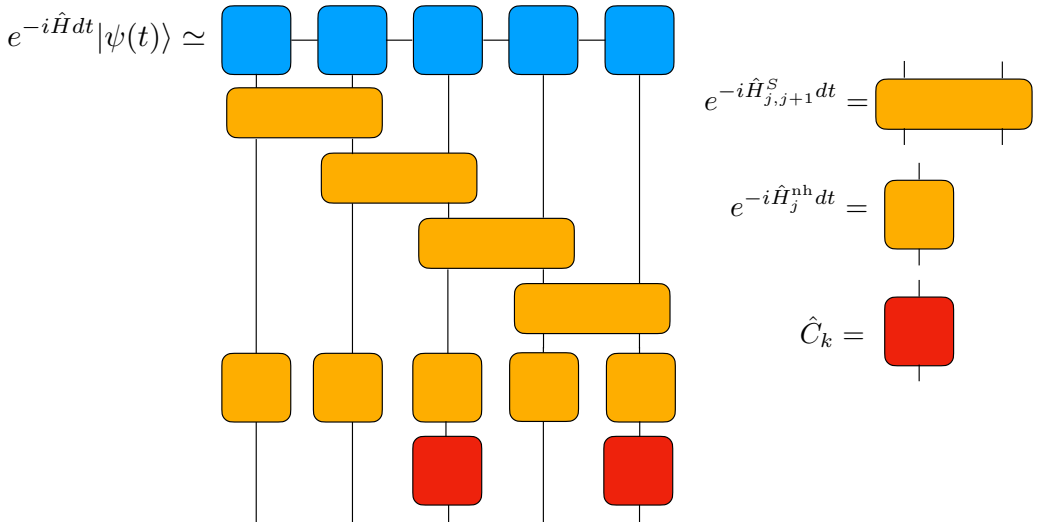

Figure 5.2: *Alternative implementation of QT+MPS* — Using as reference the article by Vovk and Pichler [9], we present the scheme for a different implementation of the QT+MPS method where it is possible to apply several quantum jumps per-time step. The main idea is to first evolve with the hermitian part of the Hamiltonian, and then after do a trotter-evolution with the non-hermitian part of the Hamiltonian, where after evolving through each site, one does a Monte-Carlo comparison to see whether one acts on the site with the correspondent jump operator. Second or higher orders are possible for the hermitian trotter evolution, but for simplicity we only present first order.

To evolve the state, there are two alternatives: either one applies the one jump per time-step as depicted in Fig. 5.1, or there is also the possibility to apply the Vovke method depicted in 5.2, in which more than one jump per time-step can be applied by separating the hermitian from the non-hermitian evolution.

In both approaches, and just like with regular MPS evolution, one will apply a trotter evolution and the application of the two-site gates which will generate an entanglement entropy increase in the bond dimension. However, and unlike the the traditional MPS there will be also be a destructive effect in the entanglement entropy growth via the application of the quantum jumps. Given the impact that the dynamics of entanglement entropy can have on the the efficiency of the simulation via the QT+MPS method, it is important to understand its behavior. Here we will just give a brief description but later, on 8, a greater in depth study of the entanglement entropy of quantum trajectories will be presented.

5.3 Trajectory Entanglement

Being a MPS decomposition the growth of the bipartite entropy will play a major role in its efficiency. However, since we consider multiple trajectories, in which the bipartite entropy can vary significantly, we will focus on the average value of the bipartite entropy. This average entropy, which we refer to as "trajectory entan-

glement" (TE), provides insights into the entanglement dynamics of the system.

To start explaining Trajectory Entanglement is important to remind that the amount of bipartite entanglement in each trajectory for a bond n is quantified by the Von Neumann entropy

$$S_{\mathrm{QT}}^{\tau(n)} = -\sum_{a_n} \left(\lambda_{a_n}^{[n],\tau}\right)^2 \log_2 \left(\lambda_{a_n}^{[n],\tau}\right)^2. \tag{5.12}$$

Trajectory entanglement (TE) is then defined as the average entanglement over all trajectories

$$\overline{S}_{\mathrm{QT}} = \lim_{N_t\to\infty} \frac{1}{N_t} \sum_{\tau=1}^{N_t} S_{\mathrm{QT}}^{\tau}. \tag{5.13}$$

Importantly, for mixed states TE is not necessarily a genuine measure of quantum entanglement, but it is still linked to the efficiency of the QT+MPS simulation. In addition to TE we will also analyze fluctuations of the TE, by computing TE sample standard deviations,

$$\sigma_{\overline{S}_{\mathrm{QT}}} = \sqrt{\frac{1}{N_t - 1} \sum_{\tau} \left(S_{\mathrm{QT}}^{\tau} - \overline{S}_{\mathrm{QT}}\right)^2}. \tag{5.14}$$

As error bars we use the sample standard error of the mean, $\epsilon = \sigma_{\overline{S}_{\mathrm{QT}}}/\sqrt{N_t}$. Note that the individual trajectories are not translation invariant, such that we cannot use an infinite MPS method to work in the thermodynamic limit.

5.4 Simulation Examples

In this section we present a series of simulations with the purpose of having a better understanding of the QT+MPS method. In particular we want to display how having access to the individual trajectories that comprise the density matrix ensemble can be helpful in terms of understanding concepts such as conservation laws.

5.4.1 XXZ with decay: QT+MPS Simulation Approach

We will consider again the XXZ model but this time we'll introduce some decay via the jump operator $\hat{C}_i = \sqrt{\gamma_i^-}\hat{\sigma}_i^-$. The Hamiltonian that describes such system is then

$$\hat{H}_{XXZ} = \frac{1}{4}\sum_{i}^{N-1} \left[-J(\hat{\sigma}_i^x\hat{\sigma}_{i+1}^x + \hat{\sigma}_i^y\hat{\sigma}_{i+1}^y) + J_z\hat{\sigma}_i^z\hat{\sigma}_{i+1}^z\right] - \sum_{j}^{N} \frac{i}{2}\gamma_j^-\hat{\sigma}_j^+\hat{\sigma}_j^-. \tag{5.15}$$

We previously mentioned how one of the main characteristics of the XXZ model is the conservation of magnetization. It is quite clear that by introducing some decay, this will no longer hold. The effect of the decay can be seen more clearly in

Fig. 5.3. Using the Néel state once again, in Fig. 5.3 (a) we plot the time evolution of the mean magnetization for each site. While normally we would expect that the magnetization goes to zero in this case it goes to -1. This is easy to understand by considering that after every quantum jump, there is going to be the possibility that there are going to be pairs of down-down spin. The XXZ Hamiltonian doesn't affect such states and eventually after many jumps there is going to be an all-down spin configuration, that is to say one in which each site has magnetization -1. Another way to see it, is in Fig. 5.3 (b), where before for all times tJ we had that the sum of the mean magnetization for every site was zero, here this is no longer the case. Instead we see an exponential decay on the average of the sum of the magnetization for all sites. It is worth to analyze the individual trajectories for the sum of the magnetization, and see how between jumps the magnetization is conserved, however every time a jump occurs the sum of the mean takes a lower value until arriving to -10, which corresponds to the all-down spin configuration.

Another of the key quantities that is worth analyzing is the TE. In Fig. 5.4 we plot the time evolution of the TE. While for short times ($tJ \approx 1/\gamma$) there is the linear growth, once the dissipation starts affecting the individual trajectories, there is clear decay in TE. From the individual trajectories one can perceive that a common scenario is that after a build-up once a quantum jump this normally has a destructive effect on the entanglement entropy, in most cases making it zero. Again, we have to consider that the quantum jump will eventually take the state to an all down-configuration, which can be expressed as a product state with zero entanglement entropy. Due to the random nature of the monte-carlo process, for some trajectories it will take some more time than from others, but eventually the steady state is an all-down spin configuration.

5.4.2 Trajectories in the case of weak and strong conservation of magnetization

Here we will consider two types of dissipation where one has a weak and the other a strong magnetization conservation. In both of these cases we will have $\mathrm{tr}(\hat{\rho}(t)\hat{S}^z) = \mathrm{tr}(\hat{\rho}(t=0)\hat{S}^z)$, i.e. the total mean magnetization remain constant. However, unlike the case of strong conservation, in the case of weak conservation the magnetization conservation will break for individual trajectories. Later on, in Chapter 8 we will focus on the entanglement entropy growth, for now we want to understand the behavior of magnetization in this setting and use the quantum trajectory approach to gain insight into weak and strong conservation.

a) *Spontaneous emission and absorption:* For the case of weak conservation of magnetization we will consider transition between states $|\uparrow\rangle \rightarrow |\downarrow\rangle$ which represent spontaneous emission and absorption as dissipation, and are given by the jump operators

$$\hat{L}_i^+ = \sqrt{\gamma_+}\hat{\sigma}_i^+ \qquad \hat{L}_i^- = \sqrt{\gamma_-}\hat{\sigma}_i^- . \tag{5.16}$$

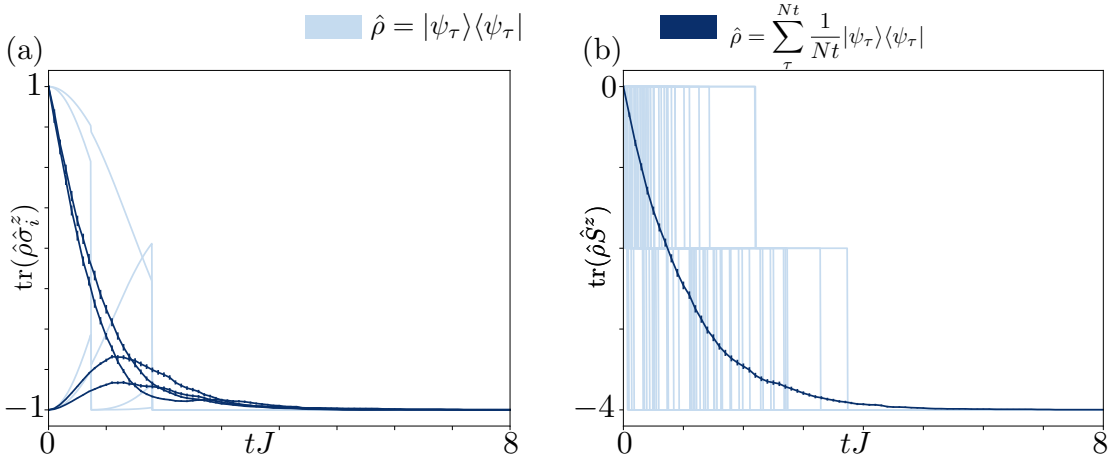

Figure 5.3: *Mean magnetization in XXZ model with decay* — (a) Time evolution of mean magnetization for each site. A few individual trajectories of each site is shown in light blue, while the average of all trajectories is shown in dark blue. (b) Time evolution of the sum of mean magnetization for every site. Light blue shows all the individual trajectories and dark blue the mean value. It is clear that the decay breaks the magnetization conservation of the XXZ model. $[N = 4, N_t = 800, \gamma_-/J = 1.0, dt = 0.01/J]$.

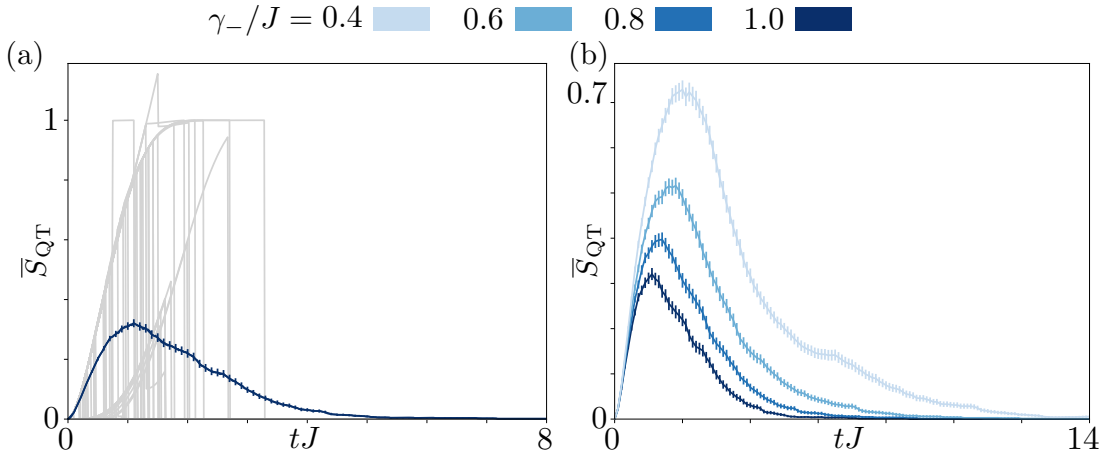

Figure 5.4: *Trajectory Entanglement in XXZ model with decay* — (a) Time evolution of TE at the center of the chain (dark blue). The entanglement entropy of individual trajectories are the grey lines. While at short times there is the linear increase, once the dissipation starts to affect at times $tJ \approx 1/\gamma$, it has a destructive effect on trajectory entanglement, creating a rise and fall pattern. (b) TE for different values of γ_-/J. As expected, the more dissipation implies a reduction on the value for TE. $[N = 4, N_t = 800, dt = 0.1/J]$.

b) *Dephasing:* The other type of dissipation that we will consider, which will be related to strong conservation of magnetization, is dephasing. Dephasing can be represented through jump operator

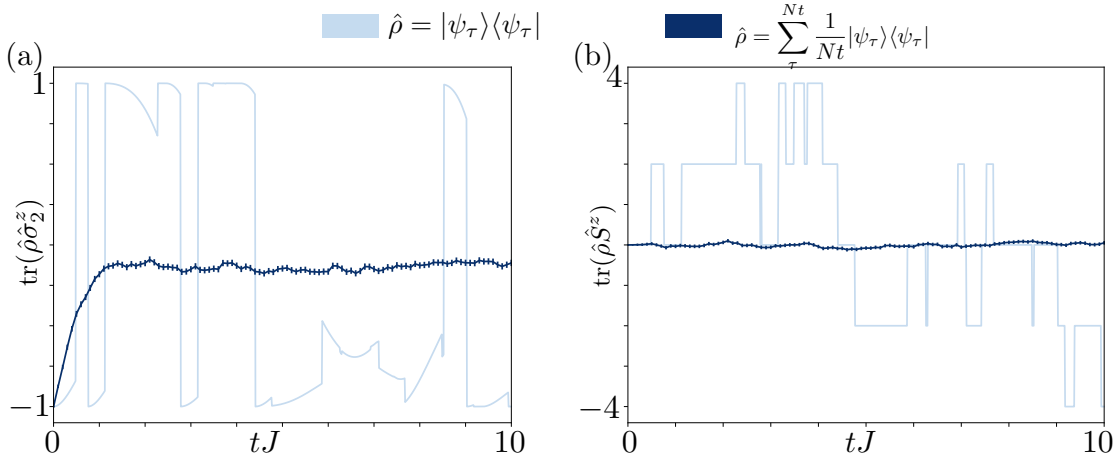

Figure 5.5: *Magnetization in the XXZ model with spontaneous emission and absorption* — (a) Time evolution of magnetization at site 2. As expected the application of the jump operator provokes abrupt changes in the value of magnetization taking it to $\pm$ 1, depended on the operator acted. Even though that with this dissipation (using equal rates) the mean value of total magnetization remains constant, the value of total magnetization for the individual trajectories can have different values from $-N$ to N. We associate this behavior with weak conservation of magnetization. $[N = 4, N_t = 800, dt = 0.01/J,\ \gamma_+ = \gamma_- = \gamma = 1.0]$.

$$\hat{L}_i^z = \sqrt{\gamma_z}\hat{\sigma}_i^z. \tag{5.17}$$

Dephasing will play a big role in Chapters 8 and 7, where it will be studied more in depth, particularly its effect on entanglement entropy dynamics. For now it's enough to mention that it's a type of dissipation that conserves magnetization and here will serve an example to explore weak and strong conservation laws.

For dephasing we also calculate the magnetization for individual sites in Fig. 5.6(a). If one looks at the individual trajectory, the effect of dephasing on the magnetization the change is less pronounced as with spontaneous emission/absorption. Remarkably, as depicted in Fig. 5.6(b), here the value of total magnetization, $\hat{S}^z$ always conserves even for individual trajectories. We associate this with a strong conservation of magnetization. This means that $\hat{\rho}$ stays an eigenoperator of S^z in the sense that $S^z\hat{\rho}(t) = M\hat{\rho}(t)$. This fact will be highly relevant when we study the effect of dissipation on entanglement entropy dynamics, given that whether the dissipation breaks or not a strong conservation of an observable on the system will affect the growth of the entanglement entropy.

Just as a last example to illustrate how can quantum trajectories can give insights into the dynamics of many-body systems, we consider the Transverse Field Ising Model of Eq. (3.45). This time we use a Néel state as an initial state, and we add dephasing as dissipation. While one could have the impression that the total magnetization is preserved by looking at the dynamics of the density operator in Fig. 5.7, by looking at the dynamics of the individual magnetization

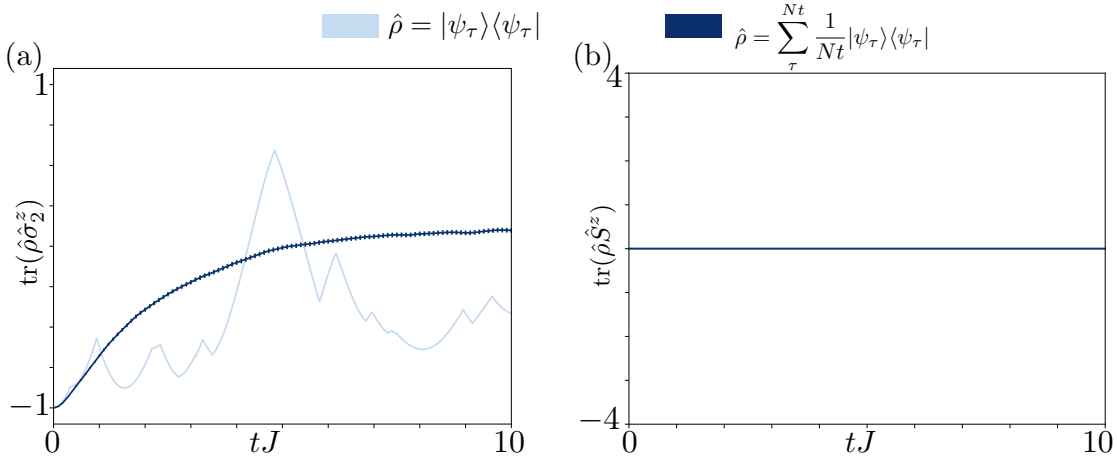

Figure 5.6: *Magnetization in the XXZ model with dephasing* — (a) Time evolution for magnetization at site 2. (b) Remarkably, for the case of dephasing, the total magnetization is preserved during the whole evolution not only for the density matrix but also for the the individual trajectories that compose the ensemble. We reefer to this as a display of strong conservation of magnetization.[$N = 4, N_t = 800, dt = 0.01/J$, $\gamma_z = 1.0$].

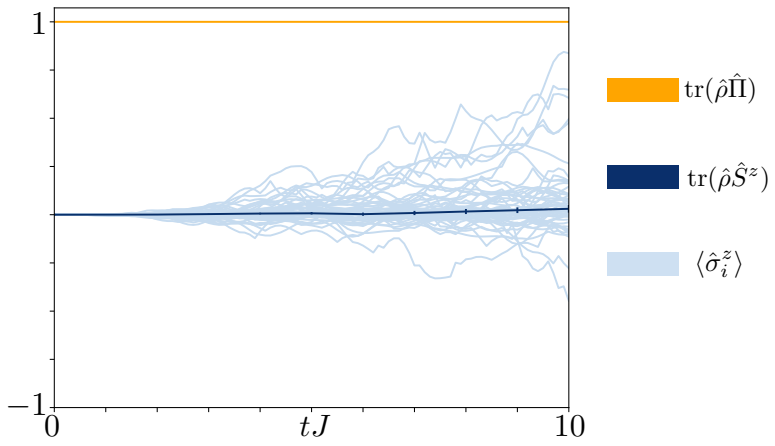

Figure 5.7: *Transverse Field Ising Model with dephasing* — We show the dynamics for parity, magnetization, and total magnetization. In the case of Parity the value of the density operator and the trajectories are superposed, since they have the same value, i.e. the density operator stays an eigenstate to the parity operator during the whole evolution. For the case of magnetization is different, while the mean value of the total magnetization remains constant for the density operator, this is not the case for the individual trajectories, and thus there is not a strong conservation of magnetization. [$N = 4, N_t = 800, dt = 0.01/J$, $\gamma_z = 1.0$].

we can tell it's rather a weak conservation of the mean value. In contrast the parity, which is a conserved quantity of the systems, preserved its value both for the density matrix and for individual trajectories that compose it.

Bibliography

[1] Klaus Mølmer, Yvan Castin, and Jean Dalibard. Monte Carlo wave-function method in quantum optics. *J. Opt. Soc. Am. B, JOSAB*, 10(3):524–538, March 1993.

[2] H. J. Carmichael. Quantum trajectory theory for cascaded open systems. *Phys. Rev. Lett.*, 70(15):2273–2276, April 1993.

[3] Wayne M. Itano, D. J. Heinzen, J. J. Bollinger, and D. J. Wineland. Quantum Zeno effect. *Phys. Rev. A*, 41(5):2295–2300, March 1990.

[4] A. Imamog¯lu. Quantum-nondemolition measurements using dissipative atom-field coupling: Monte Carlo wave-function approach. *Phys. Rev. A*, 48(1):770–781, July 1993.

[5] Hendrik Weimer, Augustine Kshetrimayum, and Román Orús. Simulation methods for open quantum many-body systems. *Rev. Mod. Phys.*, 93(1):015008, March 2021.

[6] Andrew J. Daley. Quantum trajectories and open many-body quantum systems. *Adv. Phys.*, 63(2):77–149, March 2014.

[7] Tatiana Vovk and Hannes Pichler. Entanglement-Optimal Trajectories of Many-Body Quantum Markov Processes. *Phys. Rev. Lett.*, 128(24):243601, June 2022.

[8] J. Steinbach, B. M. Garraway, and P. L. Knight. High-order unraveling of master equations for dissipative evolution. *Phys. Rev. A*, 51(4):3302–3308, April 1995.

[9] Tatiana Vovk and Hannes Pichler. Entanglement-Optimal Trajectories of Many-Body Quantum Markov Processes. *Phys. Rev. Lett.*, 128(24):243601, June 2022.

Chapter 6

Matrix Product Density Operator and Operator Entanglement

The significant success of tensor networks over the past three decades has fundamentally transformed our understanding of quantum many-body systems and the methods used to simulate them. Among these advancements, Matrix Product States (MPS) have emerged as a robust tool for simulating many-body quantum states in one dimension. The efficiency of MPS is largely due to the relatively low entanglement present in the physical states being simulated.

However, when considering the effects of the environment on quantum systems, described through a density operator $\hat{\rho}$, a critical question arises: How can we extend and adapt tensor network methods to depict the evolution of density operators? In the previous chapter, we introduced a method for simulating open quantum systems via a statistical mixture of MPS-decomposed quantum states, referred to as QT+MPS. Nonetheless, a potentially more efficient approach for simulating such systems could be through the use of Matrix Product Density Operator (MPDO). An MPDO format allows for the tensor product decomposition of an operator, as illustrated in Fig. 6.1. Algorithms that utilize MPDOs to represent and manipulate mixed states, i.e., density matrices, have been a subject of investigation since the early days of Tensor Networks [1, 2].

Importantly, a MPDO form allows to easily express the density matrix as a Schmidt decomposition between a left and a right block, given by

$$\hat{\rho} = \sum_a \lambda_a \hat{\tau}_a^{[L]} \hat{\tau}_a^{[R]}, \tag{6.1}$$

where $\mathrm{Tr}(\tau_a^{[L/R]} \tau_b^{[L/R]}) = \delta_{ab}$, and λ_a represents the Schmidt coefficients. The bipartite entropy of this decomposition is known as the 'operator space entanglement entropy' or simply 'operator entanglement' (OE) [3–12]. The OE quantifies how many Schmidt values are needed to approximate the decomposition (6.1), indicating the efficiency of an MPDO representation. This concept was first investigated by Zanardi in 2000 [4] and later reintroduced and termed Operator Space Entanglement Entropy (OSEE) by Prosen and Pižorn [7].

It's important to clarify that OE, unlike the entanglement entropy discussed in Chapter 4, does not directly measure genuine quantum entanglement between

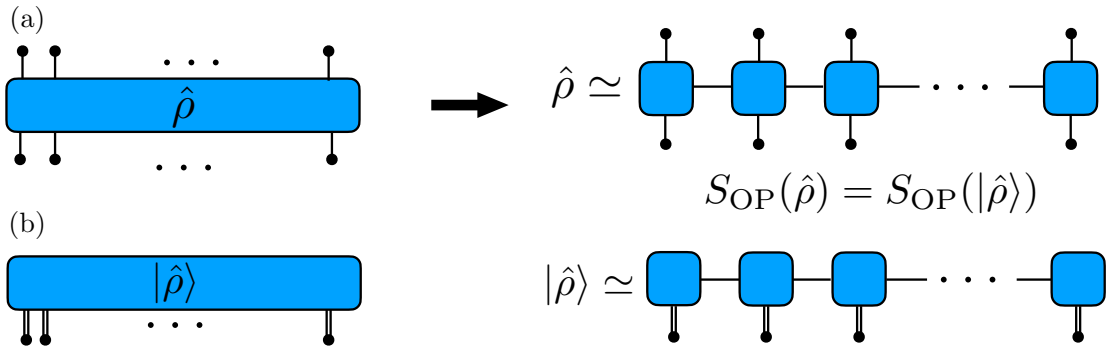

Figure 6.1: *Matrix Product Density Operator and Operator Entanglement* — (a) Scheme of the MPDO concept. We aim to achieve the equivalent of a MPS decomposition for an operator. (b) To achieve such decomposition one vectorizes the operator; it is then its possible to perform the MPS decomposition on the operator. S_{OP} will be an indicator of the efficiency of such decomposition.

distinct blocks of spins when $\hat{\rho}$ is a mixed state. This distinction mainly arises from the interaction with the environment, which obstructs a direct connection with the genuine amount of entanglement in the system. Nonetheless, the OE remains a critical quantity as it places stringent limitations on the feasibility of approximating $\hat{\rho}$ with an MPDO. Additionally, the OE can provide insights into quantum many-body effects such as quantum chaos and information [13–15].

In this chapter, we will explore the concept of Operator Entanglement and examine its dynamics under various scenarios, aiming to provide a comprehensive view of its behavior. We will also delve into the intricacies of the MPDO decomposition, with a particular focus on the connection between these concepts and the simulation of open quantum many-body systems.

6.1 Matrix Product Representation of Operators

Here we present two important concepts: Matrix Product Density Operator and Operator Entanglement. Particularly the study of Operator Entanglement is one of the essentials subjects of this thesis, which will be tackled again in Chapter **??**. Getting acquainted with these two subjects will facilitate the explanation of how to perform the evolution in infinite open systems via tensor network methods.

6.1.1 Matrix Product Density Operator

We want to apply some of the MPS ideas introduces in Chapter 3 to density operators. Having previously introduced the vectorized form of the density matrix in Chapter 2 this facilitates a great part of the task. Starting then from a general vectorized density matrix

$$\hat{\rho} = \sum_{i_1,i_2,\ldots,i_N} r_{i_1,i_2,\ldots,i_N} \hat{e}_{i_1} \otimes \hat{e}_{i_2} \otimes \cdots \otimes \hat{e}_{i_N} \tag{6.2}$$

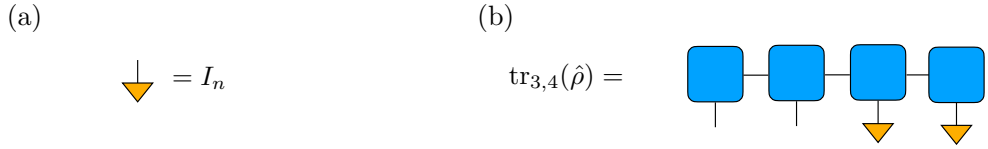

Figure 6.2: *Trace-ket* — (a) Each trace-ket is represented as a line with a triangle on one of the edges. Notice how unlike the application of other operators where there was a square connecting two lines in such a way that the site don't get 'trace-out'. (b) One can obtain a reduced density matrix, in this case $\hat{\rho}_{1,2}$, by applying a trace-ket on the other sites, here sites 3 and 4.

As previously mentioned in Chapter 2 the scalar product between operators is defined by the trace, i.e. $\langle\hat{\rho}_1|\hat{\rho}_2\rangle = \mathrm{tr}(\hat{\rho}_1\hat{\rho}_2)$. Here it is fundamental that the basis operators $\hat{e}_i$ be chosen orthonormal, $\mathrm{tr}(\hat{e}_i\hat{e}_j) = \delta_{ij}$. An efficient choice that maintains the tensors real, are the generalized Gell-Mann matrices [16]. The vectorization of the density matrix, can be represented by the tensor diagramatic notation as in Fig. 6.1. Where at the moment of vectorizing, the extra 'legs' get folded in such way that we keep the same number of N physical indices i_n with the difference that now each these indices for $1, 2, \cdots, d^2$ elements. One of the great advantages of this approach is that the previous techniques that we implemented for MPS are also applicable for the MPDO approach. In particular it is possible to arrive to the canonical form of MPDO through a series of SVD decompositions. This will allow to express our state as

$$\hat{\rho}(t) = \sum_{\{i_n\}} \sum_{a_n}^{\chi} \prod_n R^{[n]i_n}_{a_n a_{n+1}} \lambda^{[n]}_{a_n} \bigotimes_n \hat{e}_{i_n}, \tag{6.3}$$

where $R^{[n]}$ are three dimensional tensors and $\lambda^{[n]}$ the Schmidt vectors. Just like with MPS, tensors are truncated at a maximum bond dimension χ, where only the maximum χ values are retained to obtain an approximate representation of $\hat{\rho}$ [2, 17]. The dynamics will be computed analogously to the MPS case, with the difference that in this one will act during the trotter evolution with the evolution operator $\exp(\mathcal{L}dt)$ using the Lindbladian $\mathcal{L}$ instead of the hermitian Hamiltonian. A common question that arises using the vectorized form of the density matrix is how to obtain a reduced density matrix out of the full density matrix in this framework. Taking into account the definition of the scalar product and the orthogonal basis choice, in order to trace over one of the sites it's enough to apply it a vectorized density matrix correspondent to the site one wants to trace over. The vectorized density matrix will be refer to as a 'trace-ket'. This process is illustrated in Fig.6.2. Using the trace-kets it's trivial to obtain the expectation value for each of the pauli matrices of each site given that trace-ket's basis of the will also be given on the Gell-Mann basis, where each of coefficients it's simply the expected values of the Pauli matrices multiplied by a factor $1/\sqrt{2}$.

Having such representation it is important to study how efficient it actually is. For the case of MPS, the efficiency is strongly connected with the increase of the

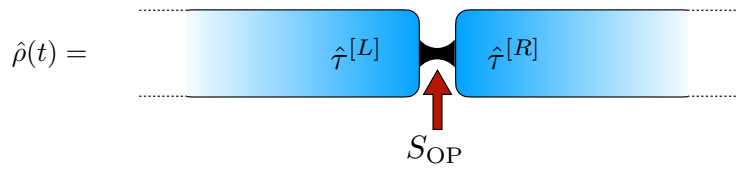

Figure 6.3: *Operator Entanglement* — Operator Entanglement gives us information about the number of Schmidt coefficients to efficiently do a MPDO representation of an operator $\hat{\rho}$.

entanglement entropy. For the case of MPDO, the measure we will use to study the complexity of such representation is Operator Entanglement.

6.1.2 Operator Entanglement

Having mentioned OE in the introduction, let's proceed to give a more detailed analysis about it. Starting from Eq. (6.1) we can start by mention that the λ_i are positive real coefficients, in decreasing order as with the case of entanglement entropy. The set of coefficients $\{\lambda_i\}$ is unique, and is invariant under changes of basis of $\mathcal{H}_L$ and $\mathcal{H}_R$. A general expression for the Operator Entanglement can be expressed as

$$S^{\alpha}_{\mathrm{OP}} = \frac{1}{1-\alpha}\log_2\left(\sum_i^r \lambda_i^{2\alpha}\right). \tag{6.4}$$

which for the limit $\alpha \to 1$ it becomes the Operator version for Von Neuman entropy

$$S_{\mathrm{OP}} = -\sum_i^r (\lambda_i)^2 \log_2(\lambda_i)^2. \tag{6.5}$$

This is the expression that we will refer to as OE and that will be used throughout this thesis. Following Ref. [8] one can rewrite the Eq. (6.4), for an integer $\alpha \geq 2$ in such a way that involves the swap operator over α identical copies. The operator expression involves α replicas of $\hat{\rho}, \hat{\rho}^{\otimes\alpha} = \hat{\rho}\otimes\cdots\otimes\hat{\rho}$, their complex conjugates, and the swap operator that cyclically permutes the replicas of subsystem A, $\mathcal{S}^A_(1,2,3,\ldots,\alpha)$, as well as its inverse SA $(1,\alpha,\alpha-1,...,2)$. The expression reads

$$(\alpha \text{ integer} \geq 2) \quad S^{\alpha}_{\mathrm{OP}} = \frac{1}{1-\alpha}\log_2\left(\frac{\mathrm{tr}[(\hat{\rho}^{\otimes\alpha})\cdot\mathcal{S}^A_{(1,\alpha,\alpha-1,\ldots,2)}\cdot\hat{\rho}^{\otimes\alpha}\cdot\mathcal{S}^A_{(1,2,3,\ldots,\alpha)}}{\mathrm{tr}[(\hat{\rho}^{\dagger})^{\otimes\alpha}\cdot\hat{\rho}^{\otimes\alpha}]}\right). \tag{6.6}$$

If one wants to relate the OE of a density matrix $\hat{\rho}$, to a physical observable, then Eq. (6.6) it's not enough since the traces involves expressions that are quadratic in the replicated density matrix $\hat{\rho}^{\otimes\alpha}$. There is, however, solution to this issue. Following Ref.[18], it is possible to write Eq. (6.6) in terms of expectation

values in a system with 2α replicas—instead of α replicas

$$S^{\alpha}_{\mathrm{OP}}(\hat{\rho}) = \frac{1}{1-\alpha}\log_2\left(\frac{\mathrm{tr}[(\hat{\rho}^{\otimes 2\alpha})\cdot \mathcal{S}^{A\cup B}_{(1,\alpha+1)(2,\alpha+2)\ldots(\alpha,2\alpha)}\cdot \mathcal{S}^{A}_{(1,2,3,\ldots,\alpha)(\alpha+1,2\alpha,2\alpha-1,\ldots,\alpha+2)}}{\mathrm{tr}[(\hat{\rho}^{\otimes 2\alpha}\cdot \mathcal{S}^{A\cup B}_{(1,\alpha+1)(2,\alpha+2)\ldots(\alpha,2\alpha)}]}\right). \tag{6.7}$$

While it's true that this expression may seem quite cumbersome, what is important to keep in mind is that $S^{\alpha}_{\mathrm{OP}}(\hat{\rho})$ is *measurable*, at least in principle, since both the numerator and the denominator in the logarithm are expectation values of observables.

To finish this section we will list some of what we consider are essential remarks about OE :

- **The OE of $|\psi\rangle\langle\psi|$ is exactly twice the entanglement entropy of $|\psi\rangle$.**

  Certainly, the OE and the entanglement entropy for states are not the same, and one cannot establish a general relation between them. Particularly, the OE is a measure of complexity for operators, which allows us to deal with open quantum systems represented by the density operator $\hat{\rho}$, which is not possible to do with a pure state $|\psi\rangle$. However, one case where a direct connection can be established is when the operator $\hat{\rho}$ is the density matrix of a pure state, $|\psi\rangle\langle\psi|$. In that case, the OE is exactly twice the entanglement entropy of $|\psi\rangle$:

  $$S^{\alpha}_{\mathrm{OP}}(|\psi\rangle\langle\psi|) = 2S_{\alpha}(|\psi\rangle). \tag{6.8}$$

  This simply follows from the fact that a Schmidt decomposition of the state $|\psi\rangle$ automatically induces a Schmidt decomposition for the operator $|\psi\rangle\langle\psi|$. Such increase on the value of entanglement entropy passing from state to operator $|\psi\rangle \to |\psi\rangle\langle\psi|$ implies an increase in dimension $\chi \to \chi^2$ for the system to be accurately simulated, since the bond dimension has to increase at least as $\chi \propto 2^{S(t)}$.

- **The OE is not a measure of entanglement in a mixed state**

  Although mentioned previously, we cannot stress enough the fact that for mixed states, despite its name, OE is not a genuine measure of entanglement. One counter example is presented in [7] by Prosen and Pižorn in which they present a state of the form $\frac{1}{2}(\hat{\rho}_{A,1}\otimes\hat{\rho}_{B,1} + \hat{\rho}_{A,2}\otimes\hat{\rho}_{B,2})$, which has non-zero OE, however it can be prepared by a fully classical protocol.

- **It is possible to experimentally measure OE**

  In recent years several schemes and experiments have been made to study entanglement entropy experimentally [19–21]. Many of these schemes rely on

6.2 Time Evolving Block Decimation for Infinite Open Systems

In this section we will present a method to simulate translationally invariant open infinite systems. This section is heavily based on the works of Orús and Vidal [22, 23].

6.2.1 Infinite Open Systems

Previously on Chapter 3 we show how to simulate closed 1D infinite translationally invariant systems. We now want do the analogous for open systems. This will imply dealing with a non-unitary evolution which prevents us for applying the same method as in Chapter 3. Therefore it will necessary to apply a re-orthogonalization scheme developed by Orus and Vidal [22, 23]. Instead of the previous left and right orthonormality conditions depicted in Fig. 3.5, the tensors will now yield $L = (\lambda^{[n]}\Gamma^{[n]})(\lambda^{[n]})(\Gamma^{[n]})^*$, and $R = (\Gamma^{[n]}\lambda^{[n]})(\Gamma^{[n]}\lambda^{[n]})^*$, where L and R are a set of eigenvectors. In order to restore the orthonormality we will begin by finding the dominant eigenvectors L and R to which the biggest eigenvalues, η_L and η_R, correspond and which we denominate V_R and V_R. On Fig.(a) 6.4 one can see a schematic representation of the dominant eigenvectors V_L and V_R introducing these eigenvectors parallelly into the MPS via the identity one can ultimately express the infinite MPS in the canonical form. The process is explained detailly in Fig. 6.4. To gain some intuition about how this works, it can be convenient to imagine it as an analogous of multiplying tensor L/R with an eigenvector from the left and its inverse from the right. It's easy to see that this new matrices will have the identity matrix as an eigenvector. Such process is done in parallel in Fig. 6.4.

In Fig. 6.5 we can see that indeed the new tensors $\{\lambda',\ \Gamma'\}$ fullfill the canonical form. Decomposing the new obtained tensors and re-acommodating we can arrive to the identity multiplied by the eigenvalue of the dominant eigenvector.

Knowing how to transform tensors $\{\lambda, \Gamma\}$ into canonical form, the process to perform the trotter evolution in infinite open systems becomes trivial. Having an infinite system with two-site translational invariance, we apply the two-site super-operator $\exp(\mathcal{L}_{1,2}dt)$ and we want to recover the canonical form after the evolution step, as depicted in Fig. 6.6. After applying the superoperator we will obtain tensor θ, for which we'll find the correspondent right and left dominant eigenvectors. Then from here we can follow the same process as in Fig. 6.5 up until (e). However, before obtaining the canonical form, we must apply a SVD in which the resulting tensors X and Y are not necessarily in the canonical form. The last step is equivalent to the one in Fig. 3.13, where introducing the tensors γ via the identity it's enough to recover the canonical form.

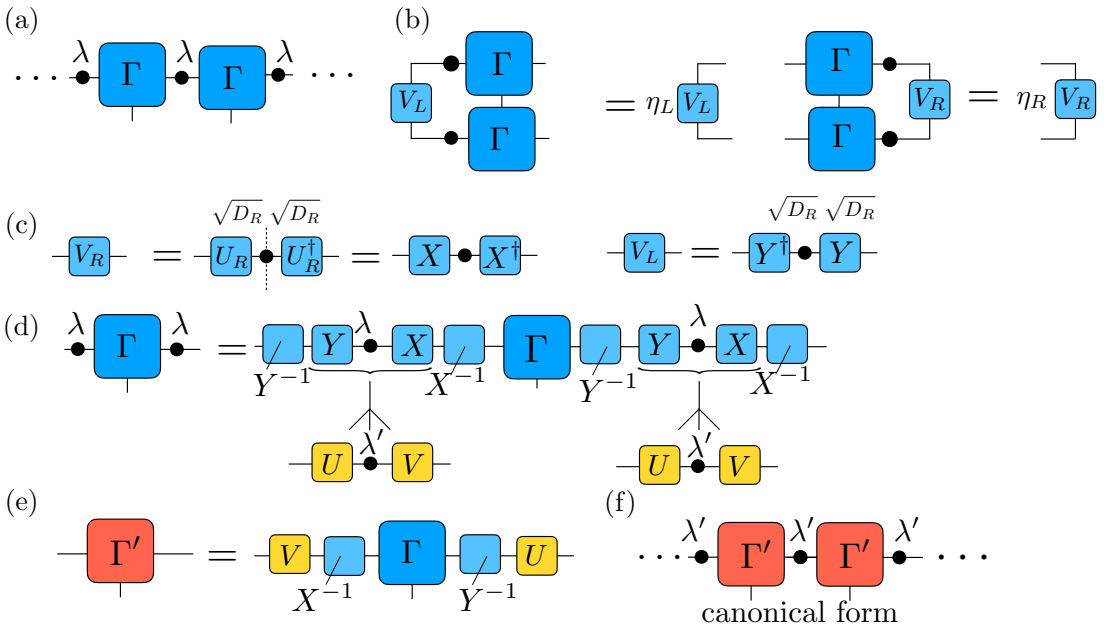

Figure 6.4: *Obtaining the canonical form* — (a) We want to re-orthonormalize an infinitely invariant system (b) In order to do that we need to find the dominant eigenvectors V_R and V_L. (c) We decompose the dominant eigenvectors, as squares $V_R = XX^\dagger$ and $V_L = Y^\dagger Y$. (d) We introduce the two resolutions of the identity matrix $I = (Y)^{-1}Y$ and $I = XX^{-1}$ in the bond indices of the infinite MPS. Then, compute the singular value decomposition of the product $Y\lambda X$, namely $Y\lambda X = U\lambda' V$, where U, V are unitary and the diagonal matrix λ contains the Schmidt coefficients of $|\psi_i\rangle$ (e) We arrange the remaining tensors $V, X^{-1}, \Gamma, (Y)^{-1}$ and U into a new tensor Γ'. (f) New tensors $\{\Gamma'\lambda'\}$ fulfill the canonical form.

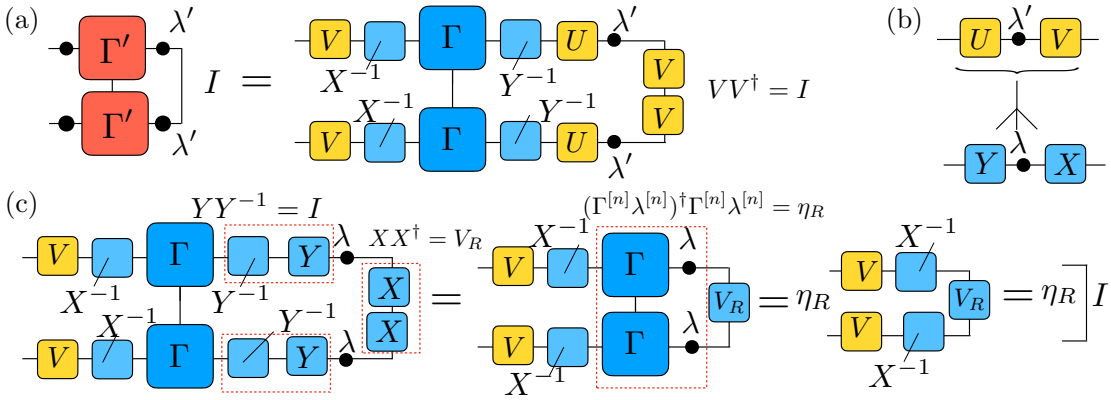

Figure 6.5: *Proof of canonical form* — Proof that $\{\Gamma'\lambda'\}$, the infinite MPS obtained from $\{\Gamma\lambda\}$ by re-orthonormalizing its bond indices following Fig. 6.4, is indeed in the canonical form. (a) We decompose tensors Γ'. (b) We the proceed to decompose tensor λ'.(c) Having plugged in tensors $\{\Gamma\lambda\}$ we obtain the right orthogonality. Here we applied the right orthogonalization, using eigenvector V_R. The procedure for left orthogonalization with eigenvector V_L is analogous.

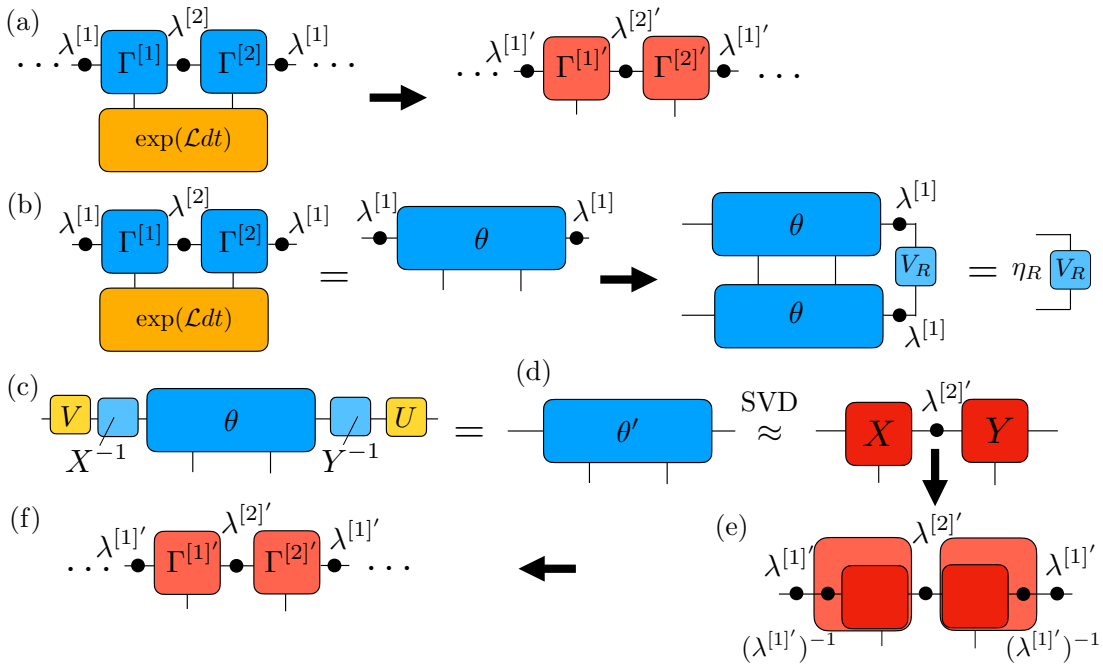

Figure 6.6: *Infinite open system evolution* — (a) We want to apply two-site non-hermitian evolution superoperator $\exp(\mathcal{L}dt)$ in such a way that the result can be expressed in canonical form. (b) At the moment of applying the superoperator the result doesn't obey the orthogonality conditions. (c) Following the same steps as in Fig.6.4 we can express operator θ in the canonical form. (d) We perform the SVD on $theta'$ which temporarily breaks the canonical form. (e) The canonical form can be recovered by applying multiplying the tensors X and Y with the identity $\lambda^{[1]}(\lambda^{[1]})^{-1}$. (f) Finally one obtains the canonical form.

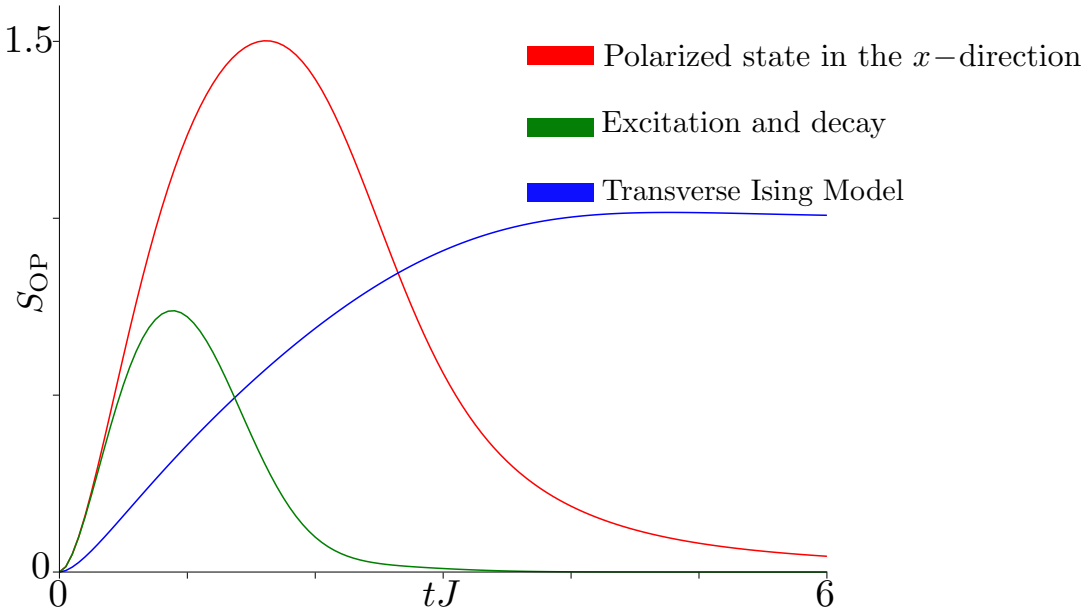

Figure 6.7: *Break of the 'rise and fall' behavior of OE* — Different scenarios to see under which conditions the 'rise fall' behavior prevails. In all cases we use the XXZ model with dephasing rate $\gamma_z/J = 0.5$, a Néel state polarized in the z direction as initial state $\hat{\rho}_0 = |\psi_0\rangle\langle\psi_0|$ with $|\psi_0\rangle = \bigotimes_i |\uparrow\rangle_{2i-1} |\downarrow\rangle_{2i}$ as default, and change one particular condition for every case. Color red (*Change of initial state*): We change the initial state to a Néel state polarized in the x-direction, $|\psi_0\rangle = \bigotimes_i |\rightarrow\rangle_{2i-1} |\leftarrow\rangle_{2i}$. Color green (*Change of dissipation*): We change dissipation from dephasing to decay/excitation, which is applied through the Lindblad jump operators $\hat{L}_i^+ = \sqrt{\gamma_+}\hat{\sigma}_i^+, \hat{L}_i^- = \sqrt{\gamma_-}\hat{\sigma}_i^-$ operators, with dissipation rate $\gamma_- = \gamma_+ = \gamma = 0.5J$. Color blue (*Change of Model*): We change from the XXZ model to a transverse Field Ising Field Model $\hat{H} = x$, and rather than 'rise and fall' the S_{OP} goes to value one.

6.3 Operator Entanglement dynamics and conserved quantities

Here we will provide some final examples of simulations which will serve as preparation for a better understanding of Chapters 7 and 8. The main focus of these simulations is to provide insights of the dynamics of OE in infinite open quantum systems and see how the presence of conserved quantities affect its behavior.

We will present the dynamics of OE under three different settings and see how, when there is the presence of conserved quantities, there will be a fundamental change in the behavior of OE. The three scenarios are:

i) *Spontaneous emission and absorption*: We consider the XXZ model with spontaneous emission and absorption using equal dissipation rates and a Néel state as initial state.

ii) *Dephasing with initial state polarised in the $\hat{x}$ direction*: We consider the

XXZ model with dephasing but this time with the Néel state polarized in the $\hat{x}$ direction, $|\psi_0\rangle = \bigotimes_i |{\rightarrow}\rangle_{2i-1} |{\leftarrow}\rangle_{2i}$.

iii) *Transverse Field Ising Model with dephasing*: We change to Transverse Ising model in which parity, defined by operator, $\hat{\Pi} = \bigotimes_i \hat{\sigma}_i^z$ is conserved, with dephasing as dissipation and a Néel state as initial state.

We first present a case where rather than only decay, which would simply lead to the trivial case of a product operator with all spins down, we also add excitations through Lindblad operator $\hat{L}_i^+ = \sqrt{\gamma^+}\hat{\sigma}_i^+$ and we consider equal decay rates for excitation and decay. In Fig. 6.7 (green line) we see that after the initial rise in OE, even though there is also dissipation exciting the spins, the overall effect is diminish in the value of OE, leading to a known 'rise and fall' effect [24, 25].

The second case that we analyze is the presence of dephasing with an initial density operator polarized in the $\hat{x}$ direction. Such initial configuration is not an eigenstate the total magnetization operator $\hat{S}^z$, and hence does not conserve magnetization. In this case, once more, the 'rise and fall' behavior appears in Fig. 6.7 (red line).

Lastly, given that Chapter 7 will cover the case of dephasing using an initial state where magnetization is conserved, we will instead look at another model which has a conserved quantity: the Transverse Field Ising Model. In Fig. 6.7 (blue line), we see that rather than a 'rise and fall' behavior, the OE increases until reaching a maximum value of $S_{\text{OP}} = 1$ and remains with that value. The explanation to such behavior is actually quite simple. We have to remember than the OE is basically a measure for the number of singular values that we need to express the system as a bipartition. As the system evolves by the master equation, the system is expected to relax to a simple stationary state characterized by the conserved quantities, or to the identity if there is no conservation quantities. In the case, of the Transverse Field Ising Model, the preserved quantity is the parity, the possible values being ± 1. By doing the bipartition, one will measure one of the possibles values in one of the partitions of the system. However, since the total parity must be preserved, the value in the other bipartition is defined instantly by knowing one of the halves. If initial parity in the system is -1, by measuring 1 in one of the halves we know that the other halves must be 1, or viceversa, in very close resemblance of the case one would have in a Bell State. This can be formally expressed through the use of the Symmetry Resolved Entanglement Entropies, presented in Chapter 4, in which we separating the total Operator Entanglement in terms of the contributions of each of the symmetry sectors. For the parity the different symmetry sectors will correspond to parity $\pm$ 1 as depicted in Fig. 6.8 (a).

In Chapter 7, we will explain the behavior of OE under dephasing. In this case, where magnetization is conserved, there will be a whole series of symmetry sectors corresponding to all the different right-side magnetization emerging throughout the evolution, as depicted in Fig. 6.8 (b). The evolution of the entanglement entropy in the different symmetry sectors and how they give rise to a logarithmic growth in OE is one of the major result of this thesis and will be explained thoroughly in Chapter 7.

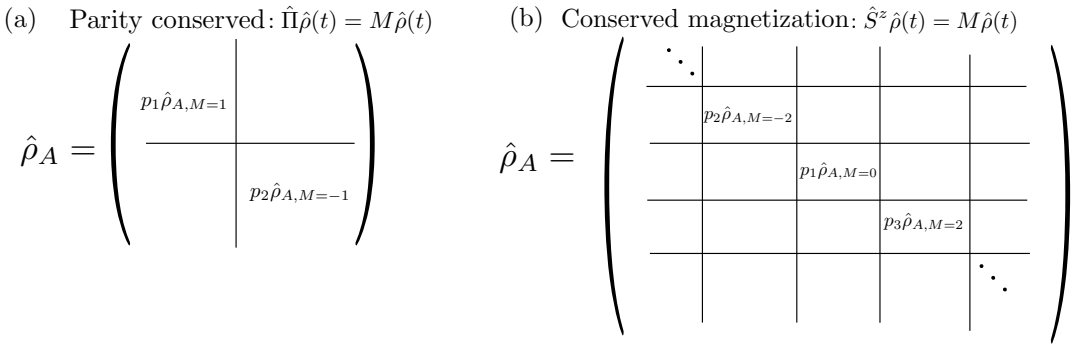

Figure 6.8: *Bipartition and preserved quantities* — By expressing the system in the basis of the operator whose value is preserved we can gain insight regarding the behavior of OE. (a) For parity the possible values in the bipartition are $\{1, -1\}$, and the value of the other bipartition will follow from that to ensure that the parity in the system is preserved at all times. (b) For magnetization conservation, there is a whole range of values of magnetization $\{..., -2, 0, 2, ...\}$. The likelihood for these different values will be spread in a diffusion process as the system evolves and will lead to a logarithmic increase in OE. This process will be explained in detail in Chapter 7.

Bibliography

[1] F. Verstraete, J. J. García-Ripoll, and J. I. Cirac. Matrix Product Density Operators: Simulation of Finite-Temperature and Dissipative Systems. *Phys. Rev. Lett.*, 93(20):207204, November 2004.

[2] Michael Zwolak and Guifré Vidal. Mixed-State Dynamics in One-Dimensional Quantum Lattice Systems: A Time-Dependent Superoperator Renormalization Algorithm. *Phys. Rev. Lett.*, 93(20):207205, November 2004.

[3] Cheryne Jonay, David A Huse, and Adam Nahum. Coarse-grained dynamics of operator and state entanglement. *arXiv:1803.00089*, 2018.

[4] Paolo Zanardi, Christof Zalka, and Lara Faoro. Entangling power of quantum evolutions. *Phys. Rev. A*, 62(3):030301(R), Aug 2000.

[5] Paolo Zanardi. Entanglement of quantum evolutions. *Phys. Rev. A*, 63(4):040304(R), Mar 2001.

[6] Xiaoguang Wang and Paolo Zanardi. Quantum entanglement of unitary operators on bipartite systems. *Phys. Rev. A*, 66(4):044303, Oct 2002.

[7] Tomaž Prosen and Iztok Pižorn. Operator space entanglement entropy in a transverse Ising chain. *Phys. Rev. A*, 76(3):032316, Sep 2007.

[8] J Dubail. Entanglement scaling of operators: a conformal field theory approach, with a glimpse of simulability of long-time dynamics in 1+1d. *Journal of Physics A: Mathematical and Theoretical*, 50(23):234001, may 2017.

[9] Tianci Zhou and David J. Luitz. Operator entanglement entropy of the time evolution operator in chaotic systems. *Phys. Rev. B*, 95(9):094206, Mar 2017.

[10] V. Alba, J. Dubail, and M. Medenjak. Operator entanglement in interacting integrable quantum systems: The case of the rule 54 chain. *Phys. Rev. Lett.*, 122:250603, Jun 2019.

[11] Huajia Wang and Tianci Zhou. Barrier from chaos: operator entanglement dynamics of the reduced density matrix. *J. High Energy Phys.*, 2019(12):1–44, Dec 2019.

[12] Georgios Styliaris, Namit Anand, and Paolo Zanardi. Information Scrambling over Bipartitions: Equilibration, Entropy Production, and Typicality. *Phys. Rev. Lett.*, 126(3):030601, Jan 2021.

[13] Tianci Zhou and David J. Luitz. Operator entanglement entropy of the time evolution operator in chaotic systems. *Phys. Rev. B*, 95(9):094206, March 2017.

[14] Huajia Wang and Tianci Zhou. Barrier from chaos: operator entanglement dynamics of the reduced density matrix. *J. High Energy Phys.*, 2019(12):1–44, December 2019.

[15] Georgios Styliaris, Namit Anand, and Paolo Zanardi. Information Scrambling over Bipartitions: Equilibration, Entropy Production, and Typicality. *Phys. Rev. Lett.*, 126(3):030601, January 2021.

[16] Reinhold A. Bertlmann and Philipp Krammer. Bloch vectors for qudits. *J. Phys. A: Math. Theor.*, 41(23):235303, May 2008.

[17] R. Orús and G. Vidal. Infinite time-evolving block decimation algorithm beyond unitary evolution. *Phys. Rev. B*, 78(15):155117, October 2008.

[18] J. Dubail. Entanglement scaling of operators: a conformal field theory approach, with a glimpse of simulability of long-time dynamics in 1 + 1d. *J. Phys. A: Math. Theor.*, 50(23):234001, May 2017.

[19] Adam M. Kaufman, M. Eric Tai, Alexander Lukin, Matthew Rispoli, Robert Schittko, Philipp M. Preiss, and Markus Greiner. Quantum thermalization through entanglement in an isolated many-body system. *Science*, 353(6301):794–800, August 2016.

[20] A. J. Daley, H. Pichler, J. Schachenmayer, and P. Zoller. Measuring Entanglement Growth in Quench Dynamics of Bosons in an Optical Lattice. *Phys. Rev. Lett.*, 109(2):020505, July 2012.

[21] Rajibul Islam, Ruichao Ma, Philipp M. Preiss, M. Eric Tai, Alexander Lukin, Matthew Rispoli, and Markus Greiner. Measuring entanglement entropy in a quantum many-body system. *Nature*, 528:77–83, December 2015.

[22] R. Orús and G. Vidal. Infinite time-evolving block decimation algorithm beyond unitary evolution. *Phys. Rev. B*, 78(15):155117, Oct 2008.

[23] G. Vidal. Classical Simulation of Infinite-Size Quantum Lattice Systems in One Spatial Dimension. *Phys. Rev. Lett.*, 98(7):070201, February 2007.

[24] Federico Carollo and Vincenzo Alba. Dissipative quasiparticle picture for quadratic Markovian open quantum systems. *Phys. Rev. B*, 105(14):144305, April 2022.

[25] Vincenzo Alba and Federico Carollo. Hydrodynamics of quantum entropies in Ising chains with linear dissipation. *J. Phys. A: Math. Theor.*, 55(7):074002, January 2022.

Chapter 7

Publication: The Rise and Fall, and Slow Rise Again, of Operator Entanglement under dephasing

The following chapter is a reprint of a work studying the growth of Operator Entanglement under dephasing, published in Phys. Rev. Lett. 129, 170401 [1]. In this work we have studied the OE of the density matrix of 1D many-body models undergoing dissipative evolution. It is expected that, after an initial linear growth reminiscent of unitary quench dynamics, the OE should be suppressed by dissipative processes as the system evolves to a simple stationary state. Surprisingly, we find that this scenario breaks down for one of the most fundamental dissipative mechanisms: dephasing. Under dephasing, after the initial 'rise and fall' the OE can rise again, increasing logarithmically at long times. Using a combination of MPO simulations for chains of infinite length and analytical arguments valid for strong dephasing, we demonstrate that this growth is inherent to a $U(1)$ conservation law. We argue that in an XXZ spin-model and a Bose-Hubbard model the OE grows universally as $\frac{1}{4}\log_2 t$ at long times, and as $\frac{1}{2}\log_2 t$ for a Fermi-Hubbard model. We trace this behavior back to anomalous classical diffusion processes.

This chapter is organized as follows: In Section 8.1 we introduce the main quantity of study in this paper: operator entanglement and we explain some of the motivations to study it in terms of its connection in the simulation of 1D systems though MPDS. In Section 8.2 we present the model that we use throughout this work. In Section 7.3 we present the MPDO decomposition and its connection with OE. In Section 7.4 we present the numerical results making emphasis on the logarithmic growth. In Section 7.5 we explain the mechanism of such logarithmic growth giving an analytical solution for long times. Section 7.6 is dedicated to explain symmetry-resolved entanglement entropies and its relation with OE. In Section 7.7 we explain how this mechanism also applies for both Fermi and Hubbard models. Finally Section 7.8 concludes the chapter.

7.1 Introduction

The study of quantum many-body systems through the prism of their quantum entanglement continues to prove extremely fruitful [2, 3]. In particular, the growth of entanglement in time-evolving quantum many-body systems is of fundamental interest [4–9]: not only is it useful to characterize the dynamics, but the amount of entanglement also indicates whether a quantum evolution can be efficiently simulated on a classical computer. In one dimension (1D) the connection can be made via the concept of matrix product states (MPS) [10–13]. An MPS is a decomposition of a many-body state vector into a product of $\chi \times \chi$ matrices (where the entries of the matrices are local kets). In such a representation, the bipartite von Neumann entanglement entropy S is bounded by $\max[S] = \log_2(\chi)$. Consequently, to represent a physical state $|\psi(t)\rangle$ with entanglement entropy $S(t)$ as an MPS, the matrix size (or 'bond dimension') has to grow at least as $\chi \propto 2^{S(t)}$ with time. For example, an evolution where S increases linear in time can therefore be considered computationally hard [14].

The past few years have seen the arrival of novel experiments capable of synthetically engineering quantum many-body models in controllable and clean environments, e.g. using optically trapped ultracold atoms [15–18], molecules [19], or ions [20]. Since such experiments are currently bringing the goal of analog quantum simulation into sight [21, 22], the question of entanglement growth, and thus classical simulability, has become very important.

Every experiment has small couplings to its environment, and should therefore be considered as an open quantum system described by a density matrix $\hat{\rho}$. Analogously to MPSs for pure states, also a matrix product operator (MPO) form of the density matrix $\hat{\rho}$ can be defined. An MPO form allows to easily express the density matrix as Schmidt decomposition between a left and a right block:

$$\hat{\rho} = \sum_a \lambda_a \hat{\tau}_a^{[L]} \hat{\tau}_a^{[R]}, \tag{7.1}$$

with $\mathrm{Tr}(\hat{\tau}_a^{[L/R]} \hat{\tau}_b^{[L/R]}) = \delta_{ab}$, and λ_a the Schmidt coefficients [schematically this is depicted in Fig. 7.1(b)]. The bipartite entropy of this decomposition is given by the 'operator space entanglement entropy' or simply 'operator entanglement' (OE) defined as [8, 23–31]

$$S_{\mathrm{OP}} = -\sum_a \lambda_a^2 \log_2\left(\lambda_a^2\right). \tag{7.2}$$

The OE quantifies how many Schmidt values are at least needed for faithfully approximating decomposition (7.1), and thus indicates the efficiency of an MPO representation [1]. It can be easily computed numerically [26, 28, 29, 32, 33] and is amenable to analytical treatment [27, 34, 35]. We stress that OE is not necessarily connected to genuine quantum entanglement between distinct blocks of spins

[1] Note that here this indicates approximability w.r.t. the two-norm of the vectorized density matrix.

when $\hat{\rho}$ is a mixed state. Still, it is a crucial quantity as it puts severe restrictions on the possibility to approximate $\hat{\rho}$ by an MPO. Furthermore, OE can give insights into quantum many body effects such as quantum chaos and information scrambling [28, 30, 31].

Here, we analyze the far-from-equilibrium dynamics of the OE, S_{OP}, in open many-body quantum systems. Our models include coherent nearest-neighbor Hamiltonian couplings that compete with incoherent single-particle dephasing [37–41] at rate γ [see sketch in Fig. 7.1(a)]. Under dephasing, fluctuations and coherences can decay towards equilibrium in a universal algebraic and sub-diffusive manor [42–45]. We treat dissipation in a Lindblad master equation. Dephasing arises due to a coupling with the environment in which local magnetization is preserved, e.g. for laser driven transitions due to laser-phase fluctuations [46, 47], or due to spontaneous photo-absorption of lattice photons in optical lattices [48]. We compute the evolution of S_{OP} for an infinite MPO representation of the full density matrix using an infinite time evolving block decimation algorithm (iTEBD) with re-orthogonalization [49].

Surprisingly, we find that for the magnetization conserving XXZ model and well-defined initial magnetization [see text below Eq. (7.3) for the definition of our models], the OE exhibits a universal logarithmic growth at long times [see Fig. 7.1(c/d)]. An identical universal behavior is also observed for particle number conserving Bose- and Fermi-Hubbard models [see discussion around Fig. 7.3 below]. Strikingly, as shown in Fig. 7.1(e), this logarithmic growth breaks down if the symmetry is broken by initial states, or for Liouvillians without magnetization conservation (see [36] for further initial states and non-conserving Lindblad operators). In the latter scenarios S_{OP} saturates, or even vanishes at long times. In this paper we explain this behavior by considering symmetry-resolved OE in combination with known results for classical models of interacting particles [50–52].

7.2 Model

We focus on infinite spin-1/2 chains, which evolve under the general Hamiltonian ($\hbar \equiv 1$):

$$\hat{H} = \frac{1}{4} \sum_i \left(J_x \hat{\sigma}_i^x \hat{\sigma}_{i+1}^x + J_y \hat{\sigma}_i^y \hat{\sigma}_{i+1}^y + J_z \hat{\sigma}_i^z \hat{\sigma}_{i+1}^z \right) + \frac{h_z}{2} \sum_i \hat{\sigma}_i^z. \tag{7.3}$$

Here, $\hat{\sigma}_i^{x,y,z}$ denote standard Pauli matrices defined in a local basis $|{\downarrow},{\uparrow}\rangle_i$, $J_{x,y,z}$ are the respective nearest-neighbor spin couplings, and h_z is a field strength along the z direction. Our Hamiltonian (7.3) includes: i) the *XXZ model*, with $J_x = J_y \equiv J$, $h_z = 0$; ii) an *XYZ model*, with $J_x \equiv J$, $J_x \neq J_y$, $h_z = 0$; and iii) a *transverse Ising model*, with $J_x \equiv J$, $J_y = J_z = 0$, $h_z \neq 0$. We are interested in the dynamics of highly-excited states. Here, we choose pure Néel product states polarized along the z direction, $\hat{\rho}_0 = |\psi_0\rangle\langle\psi_0|$ with $|\psi_0\rangle = \bigotimes_i |{\uparrow}\rangle_{2i-1} |{\downarrow}\rangle_{2i}$, or a tilted Néel state along the x direction, $|\psi_0\rangle = \bigotimes_i |{\rightarrow}\rangle_{2i-1} |{\leftarrow}\rangle_{2i}$ with $|{\leftrightarrows}\rangle_i = (|{\uparrow}\rangle_i \mp |{\downarrow}\rangle_i)/\sqrt{2}$. Dynamics

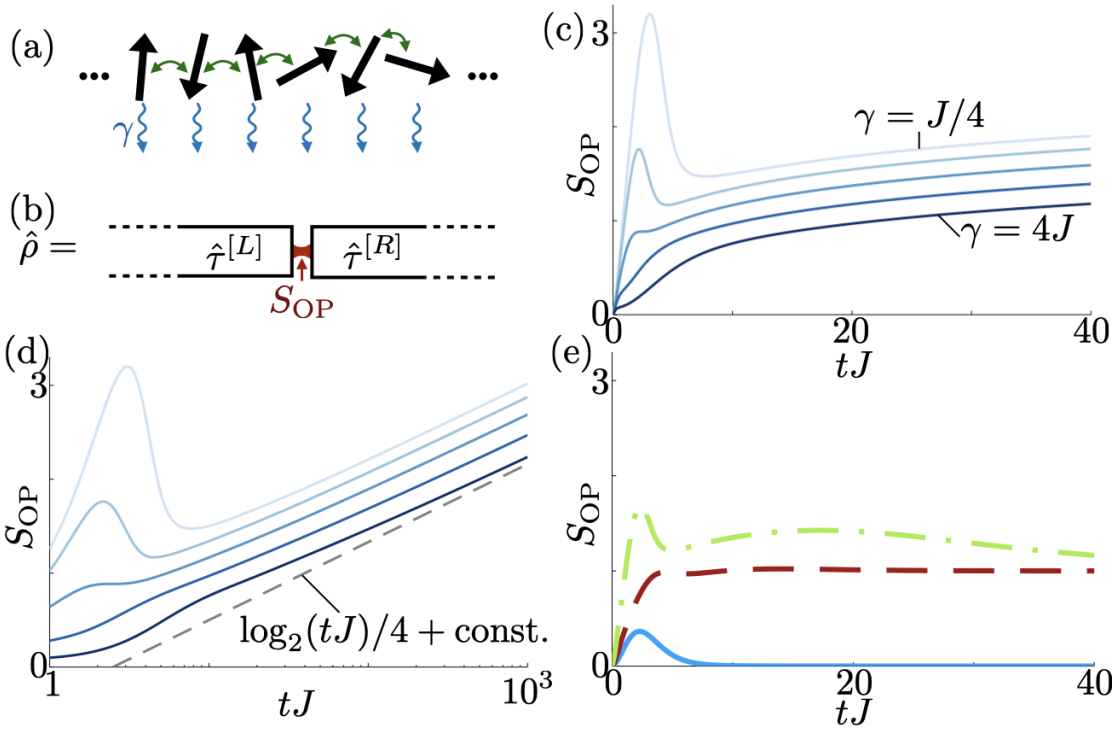

Figure 7.1: (a) We compute dynamics of spin chains with coherent nearest-neighbor couplings (double-arrows) and local dephasing at rate γ (wiggly arrows). (b) We analyze the growth of OE (S_{OP}) for a bipartition of an infinite chain into a left/right block [from a Schmidt decomposition of the density matrix $\hat{\rho}$, see Eq. (7.1)]. (c) Time evolution of S_{OP} for a Néel state in the XXZ model for different values of $\gamma = J/4, J/2, J, 2J, 4J$ in order of increasing darkness (anisotropy $J_z = -J$). (d) Same as (c), demonstrating logarithmic growth at long times (log-scale time axis). Grey dashed: Analytic long-time prediction: $S_{\mathrm{OP}} = \log_2(Jt)/4 + \mathrm{const.}$ (e) S_{OP} for dynamics in models breaking magnetization conservation. Green dash-dotted: XYZ model ($J_x = J, J_y = 0.8J, J_z = -J/2, \gamma = J/2$), Red dashed: transverse field Ising model ($h_z = J, \gamma = J/2$), blue solid: XXZ model with initial Néel state in x-direction ($J_z = -J/2, \gamma = J/2$). Results converged for time step $\Delta tJ = 0.2$ [$\Delta tJ = 0.5$ for panel (d) at long times] and different values for the bond dimension $\chi = 256, 512, 1024$ [36].

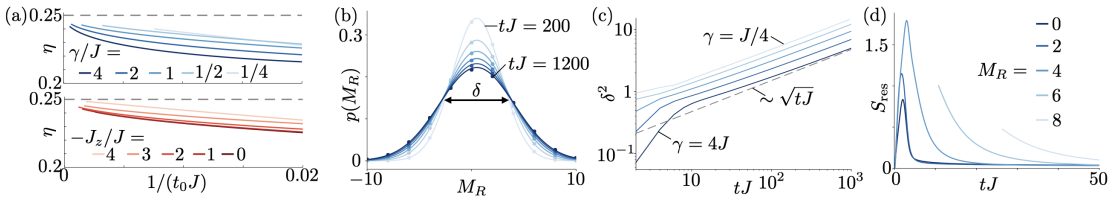

Figure 7.2: (a) Numerical determination of η for long times. η at time $t_0 J$ is obtained as the local tangent to $S_{\mathrm{OP}}(t) = S_0 + \eta \log(tJ)$ at $t_0 J$. We find $\eta \to 1/4$ (grey dashed line) for all parameters and $t_0 \to \infty$. Top (blue): Fixed $J_z = -J$ and various $\gamma/J = 1/4, 1/2, 1, 2, 4$. Bottom (red): Fixed $\gamma = J$ and various $-J_z/J = 0, 1, 2, 3, 4$. (b) Probabilities $p(M_R)$ for right-half magnetization M_R of the infinite chain (see text) at increasingly late times ($200 \leq tJ \leq 1200$ from light to dark, $J_z = -J$, $\gamma = J/2$. Lines are Gaussian fits. (c) Variance δ^2 of Gaussian fits [as in (b)] as a function of time for $J_z = -J$ and $\gamma/J = 1/4, 1/2, 1, 2, 4$ (light to dark). The grey dashed line indicates $\delta^2 \sim \sqrt{tJ}$ (double-log scale). (d) Symmetry-resolved operator entanglement entropies S_{res} as a function of time (see text). For short times and the larger $M_R = 6, 8$ the probabilities $p(M_R)$ are exponentially suppressed and no sub-machine-precision data could be extracted. Same parameters as panel (b). Results converged for $\Delta tJ = 0.5$ [(a)-(c)] and $\Delta tJ = 0.1$ [(d)] and different values of $\chi = 512, 1024, 2048$ [36].

is governed by a Lindblad master equation,

$$\frac{d}{dt}\hat{\rho} = -\mathrm{i}[\hat{H}, \hat{\rho}] + \sum_i \mathcal{D}^{[i]}\hat{\rho} \equiv \mathcal{L}\hat{\rho}\,, \tag{7.4}$$

where the local dephasing super-operators are defined as $\mathcal{D}^{[i]}\hat{\rho} = \gamma/2(\hat{\sigma}_i^z \hat{\rho} \hat{\sigma}_i^z - \hat{\rho})$ and $\mathcal{L}$ is the Liouvillian super-operator.

7.3 MPDO Decomposition and OE

For L spins, the full many-body density matrix $\hat{\rho}$ of a spin-1/2 system is a $2^L \times 2^L$ hermitian matrix with unit trace. The amount of information encoded in $\hat{\rho}$ can be effectively compressed using matrix product decompositions [12, 13]. This can be done in different ways [53]: For instance, by decomposing $\hat{\rho}$ into a particular (not unique) statistical mixture of pure states, while using an MPS for the latter. Then, the Lindblad dynamics can be computed using quantum trajectories [54]. Alternatively, one can use a direct MPO representation for $\hat{\rho}$, e.g. simply by effectively vectorizing local density matrices [55], or by constructing MPOs in a locally purified form which preserves positivity [56, 57].

Here, we decompose $\hat{\rho}$ into a canonical MPO form [55], which is formally achieved by an iterative application of the Schmidt decomposition from Eq. (7.1), until each spin n is described by a matrix of unique local operators $\hat{\gamma}^{[n]}_{a_n,a_{n+1}}$, i.e. $\hat{\rho} = \sum_{\{a_n\}} \prod_n \lambda_{a_n} \hat{\gamma}^{[n]}_{a_n,a_{n+1}}$. By choosing local basis operators, $\hat{e}_{i_n}$, for the density matrix

of spin n, we can then decompose:

$$\hat{\rho} = \sum_{\{i_n\}} \sum_{\{a_n\}}^{\chi} \prod_n \Gamma^{[n]\, i_n}_{a_n a_{n+1}} \lambda^{[n]}_{a_n} \bigotimes_n \hat{e}_{i_n}, \tag{7.5}$$

where $\Gamma^{[n]}$ are three-dimensional tensors and $\lambda^{[n]}$ the Schmidt vectors. Tensors are truncated at a maximum MPO bond dimension χ. All results shown are numerically converged in χ [36]. For $\hat{e}_i$ we choose local eigenoperators for the multiplication with $\hat{\sigma}^z$ from the left and right, to take advantage of the magnetization conservation (see below). Both the initial state and the Hamiltonian are invariant under translation by two lattice sites. As a consequence, in Eq. (7.5) one has $\Gamma^{[n+2]} = \Gamma^{[n]}$ and $\lambda^{[n+2]} = \lambda^{[n]}$ [49, 58], and only two Γ and λ tensors are needed to encode a density matrix. The time evolution is then computed with a fourth order Trotter decomposition of the matrix exponential of the Liouvillian $\exp(\mathcal{L}\Delta t)$ [49, 55, 59]. Importantly, since the dynamics is non-unitary, a naïve implementation of this algorithm destroys the orthogonality of the decomposition in Eq. (7.5), such that with time, the λs do not correspond to orthogonal Schmidt bases anymore. We fix this by re-orthogonalizing the tensors after updates [49].

When considering the XXZ model, the total magnetization $\hat{S}^z = \sum_n \hat{\sigma}^z_n$ is conserved. This means that $\hat{\rho}$ stays an eigenoperator of $\hat{S}^z$ in the sense that $\hat{S}^z\hat{\rho}(t) = M\hat{\rho}(t)$ at all times (for the Néel state, $M = 0$). Note that alternatively, one could also define a condition for multiplication from the right. Due to magnetization preservation, the $\hat{\tau}^{[R]}_a$ matrices in Eq. (7.1) can be chosen to be eigenoperators of the 'right-half magnetization' of the chain, $\hat{S}^z_R \equiv \sum_{n>0} \hat{\sigma}^z_n$ (w.l.o.g. we define the right half as $n > 0$), $\hat{S}^z_R \hat{\tau}^{[R]}_a = M_R \hat{\tau}^{[R]}_a$. Similarly, one can choose $\hat{\tau}^{[L]}_a$ to be eigenoperators of $\hat{S}^z_L \equiv \sum_{n\leq 0} \hat{\sigma}^z_n$ with $M_L = -M_R$. This means that the index a in Eq. (7.1) becomes a composite index $a \to (M_R, a')$, where a' distinguishes the Schmidt coefficients corresponding to the same M_R:

$$\hat{\rho} = \sum_{M_R} \sqrt{p_{M_R}} \sum_{a'} \widetilde{\lambda}_{M_R,a'} \hat{\tau}^{[L]}_{-M_R,a'} \hat{\tau}^{[R]}_{M_R,a'}\,. \tag{7.6}$$

Here we defined $\widetilde{\lambda}_{M_R,a} \equiv \lambda_{M_R,a}/\sqrt{p_{M_R}}$, with $p_{M_R} = \sum_a \lambda^2_{M_R,a}$ the probability of having magnetization M_R in the right half. The existence of the conservation law makes our simulations much more efficient, since the block-diagonal form of the tensors can be exploited.

7.4 Logarithmic increase of OE: Numerical results

In simulations in Fig. 7.1 we noticed a distinctive different behavior of OE growth at long times (log-growth) for the magnetization conserving XXZ model compared to other models breaking this conservation law. Quite generically, at times $t \ll \gamma^{-1}$, the dynamics is dominated by the Hamiltonian part in Eq. (8.3). Sufficiently pure states at such short times can be approximated by the state $|\psi_t\rangle = \mathrm{e}^{-\mathrm{i}\hat{H}t}|\psi_0\rangle$. In that case the OE is simply twice the entanglement entropy of $|\psi_t\rangle$ (see e.g. [27]),

and it is well established that the latter generically grows linearly in time (in the absence of disorder). At times $t \gtrsim \gamma^{-1}$, the initial coherence is destroyed by dephasing, and the OE decreases (see [36] for a more detailed discussion on the parameter dependence of the peak-heights). This 'rise and fall' is clearly visible in Fig. 7.1, and it is typical for OE dynamics, and also other quantities such as the mutual information [60, 61]. Typically, under the dynamics in Eq. (8.3) the system is expected to relax to a simple stationary state characterized by the conserved quantities of Eq. (8.3), or to the identity if there is no conservation law. The OE at late times converges towards the OE of that stationary state. This is visible in our simulations of the XYZ and Ising models, see Fig. 7.1(e). In this case only the parity $\hat{\Pi} = \bigotimes_i \hat{\sigma}_i^z$ is preserved by the dynamics. Since the initial Néel state is an eigenstate of $\hat{\Pi}$, the stationary density matrix is a projector on a fixed parity sector, $\frac{1}{2}(1 \pm \hat{\Pi})$, with the $\mathcal{O}(1)$ entropy $S_{\mathrm{OP}} = 1$ $(= \log_2 2)$. For the XXZ chain with the initial tilted Néel along the x direction, even parity conservation is broken, and the stationary density matrix becomes the identity, $S_{\mathrm{OP}} = 0$. In stark contrast, for the XXZ chain and initial Néel state, after the rise and fall dynamics, the OE increases again at long times, see Fig. 7.1(c), and this second increase is logarithmic in time, see Fig. 7.1(d). More precisely, we find the long-time behavior $S_{\mathrm{OP}}(t \to \infty) = \eta \log_2(tJ) + S_0$, which we will also understand analytically below. The prefactor η converges universally to $\eta = 1/4$ independent on the precise values of γ and J_z, as shown in Fig. 7.2(a), and has also been observed with additional disorder [62]. The offset S_0 depends on the characteristic time-scale of the long-time diffusive dynamics set by J, J_z and γ [36]. Note that we find the evolution of OE in the XXZ model to be independent of the signs of J and J_z.

7.5 Mechanism for logarithmic growth: Abelian symmetry and anomalous charge diffusion

To also analytically understand this behavior, we now consider the XXZ model evolution in the strong dephasing limit $\gamma \gg J$. The dissipators in the master equation (8.3) project the density matrix onto its diagonal part $\hat{\rho}_{\mathrm{diag}} = \sum_\sigma \rho_{\sigma\sigma} |\sigma\rangle \langle\sigma|$, where the σ denote all binary vectors of spin-z configurations. The dynamics then reduces to a classical master equation for the probability $p_\sigma = \rho_{\sigma\sigma}$, $dp_\sigma/dt = \sum_{\sigma'} \mathcal{M}_{\sigma\sigma'} p_{\sigma'}$. The stochastic matrix $\mathcal{M}$ was determined in Ref. [38] in second-order perturbation theory starting from Eq. (8.3). It takes the form of an effective ferromagnetic Heisenberg Hamiltonian, $\mathcal{M} = -J^2/(8\gamma) \sum_i \left[\hat{\sigma}_i^x \hat{\sigma}_{i+1}^x + \hat{\sigma}_i^y \hat{\sigma}_{i+1}^y + \hat{\sigma}_i^z \hat{\sigma}_{i+1}^z - 1\right]$. Importantly, $\mathcal{M}$ is the stochastic matrix of the Symmetric Simple Exclusion Process (SEP) [63, 64], a model of classical hard-core particles that perform random walks.

Crucially, in the SEP, the mean squared displacement of a tagged particle grows as $\langle X_t^2 \rangle \propto \sqrt{t}$ [51, 52, 65–68], as opposed to $\propto t$ for a usual random walk. This anomalous diffusion is universally found in problems of so-called 'single-file diffusion' [65, 69, 70], when classical particles diffuse in one-dimensional channels without bypassing each other. Here, it is now also tied to anomalous scaling

of the particle number fluctuations between the left and right half-systems. If $\Delta N(t) = M_R(t)/2$ is the excess number of particles (w.r.t. the initial Néel state) in the right half-system at time t, and if we tag the particle initially at the origin, then one can estimate $\Delta N(t) \simeq \rho_0 X_t$, where $\rho_0 = 1/2$ is the particle density in the Néel state. Consequently, $\langle \Delta N(t)^2 \rangle \simeq \rho_0^2 \langle X_t^2 \rangle \propto \sqrt{t}$. More generally, the probability distribution of $M_R(t)$ is found to obey a scaling form at long times [66]: $p(M_R(t) = m) \underset{t\to\infty}{\sim} \exp\left(\sqrt{t}\, G\left(\frac{m}{\sqrt{t}}\right)\right)$. Here, the large-deviation function G is non-positive, symmetric [$G(u) = G(-u)$], diverges when $|u| \to \infty$, and has a single minimum at $u = 0$ (see [66]). In particular, away from the tails the distribution is Gaussian with standard deviation $\delta = t^{1/4}/\sqrt{|G''(0)|}$. The Shannon entropy associated to number fluctuations is then

$$\begin{aligned} S_{\text{num}}(t) &= \sum_{m\in 2\mathbb{Z}} -p(m)\log_2 p(m) \\ &\simeq \int -\sqrt{\frac{2}{\pi\delta^2}}\mathrm{e}^{-\frac{m^2}{2\delta^2}} \log_2\left(\sqrt{\frac{2}{\pi\delta^2}}\mathrm{e}^{-\frac{m^2}{2\delta^2}}\right)\frac{dm}{2} \\ &= \log_2\delta + \log_2\left(\sqrt{\pi\mathrm{e}/2}\right) \underset{t\to\infty}{=} \frac{1}{4}\log_2 t + \mathcal{O}(1). \end{aligned} \tag{7.7}$$

It is no coincidence that S_{OP} grows in the same way as the number fluctuations S_{num} at long times (see below).

Away from the $\gamma/J \gg 1$ limit, the XXZ chain no longer reduces to the SEP. Nevertheless we find that the same type of anomalous scaling persists. This is confirmed in Fig. 7.2, where we show that, for times accessible numerically, $p(M_R = m)$ is approximately Gaussian [Fig. 7.2(b)] with width $\delta \propto t^{\frac{1}{4}}$ [Fig. 7.2(c)]. Thus, even though the exact correspondence with the SEP breaks down at finite γ/J, the scaling of S_{num} in Eq. (7.7) remains unchanged. This result is also consistent with previous studies of transport in the XXZ and related models [71–74].

7.6 Symmetry-resolved OE

We now show how the relation between S_{OP} and S_{num} can be revealed in so-called symmetry resolved operator entanglement. From Eq. (7.6) we can derive a decomposition of the OE into the form:

$$S_{\text{OP}} = \sum_{M_R} p_{M_R} S_{\text{res}}(M_R) + S_{\text{num}}(p_{M_R}), \tag{7.8}$$

where the 'symmetry-resolved entanglement entropies' are $S_{\text{res}}(M_R) = -\sum_a \widetilde{\lambda}^2_{M_R,a}\log_2(\widetilde{\lambda}^2_{M_R,a})$, and S_{num} is given in Eq. (7.7). Such symmetry-resolved entropies have attracted attention recently [9, 75–79]. In Fig. 7.2(d) we display $S_{\text{res}}(M_R)$ for different values of M_R. Also S_{res} exhibits the 'rise and fall' phenomenon discussed above, but independent of M_R they decrease to very small values at late times. This means that the logarithmic increase S_{OP} is solely due to the growth of S_{num}.

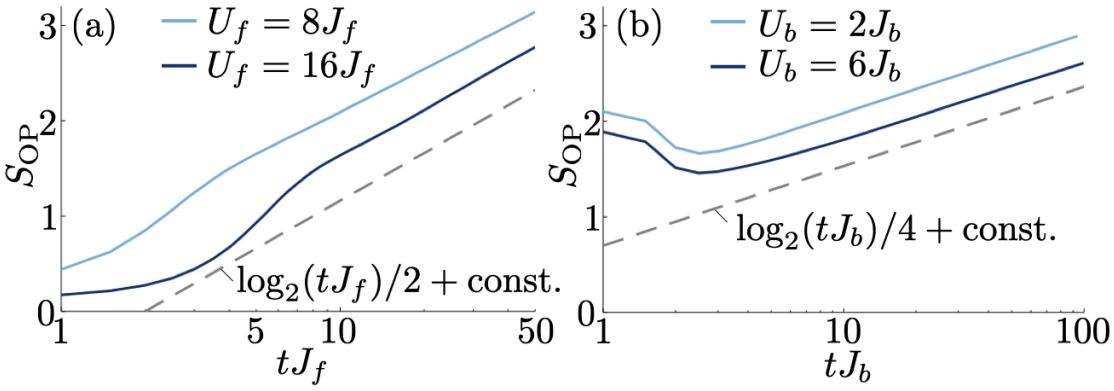

Figure 7.3: Logarithmic OE growth in the Fermi-Hubbard (a) and Bose-Hubbard (b) models with dephasing for different interaction strengths $U_{f/b}$. The grey dashed lines indicate the analytically expected long-time growth [36]. The initial states are: One fermion per site with alternating spins $|\cdots\uparrow\downarrow\uparrow\cdots\rangle$ (a) and alternating sites with 0 or 1 boson $|\cdots 101\cdots\rangle$ (b). Parameters: $\gamma_f = 8J_f$ (a) and $\gamma_b = 2J_b$ (b), $\chi = 512, 256$, $\Delta t J_{f/b} = 1/2$, maximum bosons per site $n_{\max} = 4$.

7.7 Fermi- and Bose-Hubbard model

To demonstrate the generality of the logarithmic OE growth, we discuss two additional paradigmatic many-body setups featuring number conservation: i) a Fermi-Hubbard (FH) model, $\hat{H}_{\mathrm{FH}} = -J_f \sum_{n,\sigma}(\hat{c}^\dagger_{\sigma,n}\hat{c}_{\sigma,n+1} + \mathrm{h.c.}) + U_f \sum_n \hat{c}^\dagger_{\uparrow,n}\hat{c}^\dagger_{\downarrow,n}\hat{c}_{\uparrow,n}\hat{c}_{\downarrow,n}$ with creation operators for spin-full fermions on site n, $\hat{c}^\dagger_{\sigma,n}$ ($\sigma = \uparrow,\downarrow$); and ii) a Bose-Hubbard (BH) model, $\hat{H}_{\mathrm{BH}} = -J_b \sum_n (\hat{b}^\dagger_n \hat{b}_{n+1} + \mathrm{h.c.}) + U_b/2 \sum_n \hat{b}^\dagger_n \hat{b}^\dagger_n \hat{b}_n \hat{b}_n$, for bosons created by $\hat{b}^\dagger_n$. In both cases we consider dephasing $\mathcal{D}^{[k]}\hat{\rho} = \gamma \hat{L}_k \rho \hat{L}^\dagger_k - \gamma(\hat{L}^\dagger_k \hat{L}_k \hat{\rho} + \hat{\rho}\hat{L}^\dagger_k \hat{L}_k)/2$, where $\hat{L}_{\sigma,n} = \hat{c}^\dagger_{\sigma,n}\hat{c}_{\sigma,n}$ and $\hat{L}_n = \hat{b}^\dagger_n \hat{b}_n$ in the FH and BH case, respectively. As demonstrated in Fig. 7.3, both models also exhibit a long-time logarithmic OE growth. In the FH model, we observe $S_{\mathrm{OP}} \sim \log_2(tJ_f)/2$. For $\gamma \gg J_f, U_f$, this can be understood analytically by considering the FH chain as the sum of two chains, one for each spin degree of freedom, both of which are described by the SEP and exhibit $S_{\mathrm{OP}} \sim \log_2(tJ_f)/4$. Here, interactions contribute only at higher orders [36]. The BH model exhibits $S_{\mathrm{OP}} \sim \log_2(tJ_b)/4$ analogous to the XXZ model. For large $U_b \gg \gamma \gg J_b$ the creation of doublons is energetically suppressed, leading back to the SEP. For finite interaction strength ($\gamma \gg J_b, U_b$), a different classical limit is reached, which also features logarithmic OE growth with a prefactor close to 1/4 stemming from a 'Symmetric Inclusion Process' [36, 64].

7.8 Conclusion

We showed that in a dissipative system possessing a $U(1)$ conservation law the operator entanglement grows logarithmically at long times. We pinpointed the mechanism that leads to this logarithmic growth, and identified its prefactor with the [possibly anomalous] exponent characterizing the fluctuations of the charge as-

sociated with the $U(1)$ symmetry. Our results and methods are of general interest to studies of imperfect quantum computation and quantum simulation platforms, currently pushing into a regime where they may offer a quantum advantage. The entanglement entropy dynamics we study here connects directly to similar results obtained for discrete quantum circuit models [28, 32, 80, 81], or to other dissipative simulation methods such as quantum trajectories [82, 83]. An understanding of the destructive processes of the environment on dynamics are essential, and the interplay between dissipation and coherent couplings can lead to interesting physics or state engineering (e.g. [84–87]). In the future, it will be interesting to investigate how the presence of more complex symmetries such as SU(N) impacts entanglement dynamics.

Acknowledgements

We thank P. Calabrese, O. Castro-Alvaredo, A. Grabsch, G. Misguich, S. Murciano, G. Pupillo and G. Schütz for helpful discussions. This work was supported by LabEx NIE under contract ANR-11-LABX0058 NIE, and the QUSTEC program, which has received funding from the European Union's Horizon 2020 research and innovation program under the Marie Skłodowska-Curie grant agreement number 847471. This work is part of the Interdisciplinary Thematic Institute QMat, as part of the ITI 2021-2028 program of the University of Strasbourg, CNRS and Inserm, and was supported by IdEx Unistra (ANR-10-IDEX-0002), SFRI STRAT'US project (ANR-20-SFRI-0012), and EUR QMAT ANR-17-EURE-0024 under the framework of the French Investments for the Future Program. Our MPO codes make use of the intelligent tensor library (ITensor) [88]. Computations were carried out using resources of the High Performance Computing Center of the University of Strasbourg, funded by Equip@Meso (as part of the Investments for the Future Program) and CPER Alsacalcul/Big Data.

Appendix

In Sec. 7.A, we provide details on the numerical convergence. In Sec. 7.B, we discuss a breaking of magnetization conservation on different levels. In Sec. 7.C we show numerical results on the parameter dependence of the short time peaks of the OE. In Sec. 7.D, we discuss the perturbative estimate for the offset of the operator entanglement. In Sec. 7.E, we identify the strong dephasing limits of the Fermi-Hubbard model, and of the Bose-Hubbard model, which are instrumental for explaining the prefactors of the logarithmic growth of the OE observed in the main text.

7.A Details on numerical convergence

For solving the time-evolution with the iTEBD algorithm [49, 58] we make use of a Trotter decomposition of the matrix exponential of the super-operator governing the full dissipative dynamics [55]. In order to reach long time-scales, we implement 4-th order decomposition [59], which allowed for time-step converged results even up to step sizes of $\Delta t = 1/(2J)$ [see Fig. 7.4(a)]. Δt signifies the full time step, which is composed of individual gates with time-steps of length $\Delta t/12$ and $\Delta t/6$. In particular, we use the method

$$(1)^T(1)(1)^T(-2)(1)^T(1)^T(1)^T(1)^T(1)(1)^T(1)(1)(1)(1)(-2)^T(1)(1)^T(1)\,. \tag{7.9}$$

Throughout the paper we only show simulations up to times until which the results are converged in the MPO bond dimension χ, defined in the truncated MPO

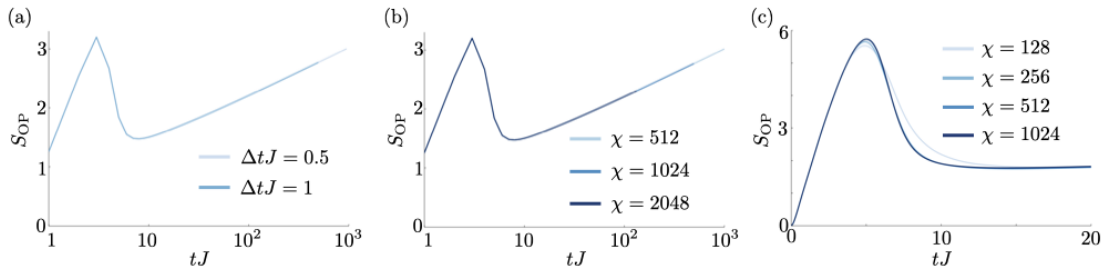

Figure 7.4: (a) Convergence in the time-step Δt (in units $1/J$) for $\gamma = J/4$, $J_z = -J$, $\chi = 1024$. (b) Convergence in χ for $\gamma = J/4$, $J_z = -J$, $\Delta tJ = 0.5$. (c) Convergence in χ for $\gamma = J/8$, $J_z = -J$, $\Delta tJ = 0.1$

decomposition in Eq. (5). In practice, we ran simulations repeatedly, doubling bond dimensions in the different runs until lines become visually indistinguishable. We varied the bond dimension in the range $\chi = 128, 256, 512, 1024, 2048$. Note that e.g. for $\chi = 1024$, a maximum possible entropy of $S_{\mathrm{OP}} \leq \log_2(\chi) = 10$ is theoretically supported. Naturally, the evolution producing the largest OE required the largest values of χ. The convergence plots in Fig. 7.4(b) and Fig. 7.4(c) demonstrate this procedure for "worst-case" scenarios (i.e. the data with the largest OE values and for long times). We choose the data from Fig. 1(d) with $\gamma = J/4$, simulated up to long times, and the data for Fig. 3(a) with $J_z/J = -1$ and $\gamma = J/8$, which reached the largest values in the short time peak $S_{\mathrm{OP}} \sim 6$.

In particular, the following parameters have been used for the figures in the main text:

Figure	$-J_z/J$	γ/J	χ	$\Delta t J$
Fig. 1(c)	1	0.25	512	0.2
Fig. 1(c)	1	≥ 0.5	256	0.1/0.2
Fig. 1(d)(short times)	1	≤ 1	1024	0.1/0.2
Fig. 1(d)(short times)	1	> 1	256	0.1/0.2
Fig. 1(d)(long times)	1	all	512	0.5
Fig. 1(e)	all	all	256	0.2
Fig. 2(a)/S3(b)	1	0.25	2048	0.5
Fig. 2(a)/S3(b)	1	0.5, 1	1024	0.5
Fig. 2(a)/S3(b)	1	2, 4	512	0.5
Fig. 2(a)/S3(b)	all	1	1024	0.5
Fig. 2(b)	1	0.5	512	0.5
Fig. 2(c)	1	all	512	0.5
Fig. 2(d)	1	0.5	1024	0.1
Fig. 3(a)	all	—	512	0.5
Fig. 3(b)	all	—	256	0.5
Fig. S3(a)	all	0.125	1024	0.1
Fig. S3(a)	all	≥ 0.25	512	0.1/0.2

Whenever two Δt values are given, different Δts were used for different parameters for historic reasons, but are clearly converged in either case.

7.B Breaking magnetization conservation

In this section, we give a few more examples without magnetization conservation. First, we discuss fully polarized states that are tilted at an angle θ, $\bigotimes_n \exp[\mathrm{i}\theta\hat{\sigma}_n^{(x)}]\,|{\downarrow}\rangle_n$. For $0 < \theta < \pi$, these states are not eigenstates of $\hat{S}_z$. We find that after the initial growth, the OE decays to zero, just like for the initial tilted Néel state. For the special cases $\theta = 0(\pi)$, the state $|\cdots{\downarrow\downarrow\downarrow}\cdots\rangle$ ($|\cdots{\uparrow\uparrow\uparrow}\cdots\rangle$) is an eigenstate of the Liouvillian, and thus the OE remains zero at all times.

If magnetization conservation is broken on the level of the Liouvillian, we find a similar rise and fall of OE, which remains zero at long times [see Fig. 7.5(b)].

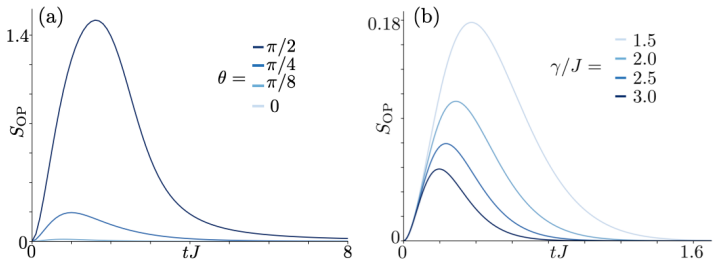

Figure 7.5: Rise and fall of operator entanglement without magnetization conservation. (a) We consider the XXZ model with dephasing, as in the main text, for $J_z = -J$, $\gamma = J/2$. The initial state is a fully polarized state $\bigotimes_n \exp[\mathrm{i}\theta\hat{\sigma}_n^{(x)}]\,|{\downarrow}\rangle_n$, which are not and eigenstate of $\hat{S}_z$ (except for $\theta = 0$). (b) We consider the XXZ model with $J_z = -J$ for a Néel initial state as in the main text. Instead of dephasing, we consider non-conserving dissipation $\mathcal{D}_n^{\pm}\hat{\rho} = \gamma/2(2\hat{\sigma}_n^{\pm}\hat{\rho}\sigma_n^{\mp} - \hat{\sigma}_n^{\mp}\hat{\sigma}_n^{\pm}\hat{\rho} - \hat{\rho}\hat{\sigma}_n^{\mp}\hat{\sigma}_n^{\pm})$, and for various rates γ. Simulations for $\chi = 128$, $\Delta tJ = 0.1$

For the case of both an incoherent pump and and decay at rate γ, after the initial rise and fall, we expect the steady state to be the (trivial) infinite temperature state with $S_{\mathrm{OP}} = 0$.

7.C Short-time peak heights

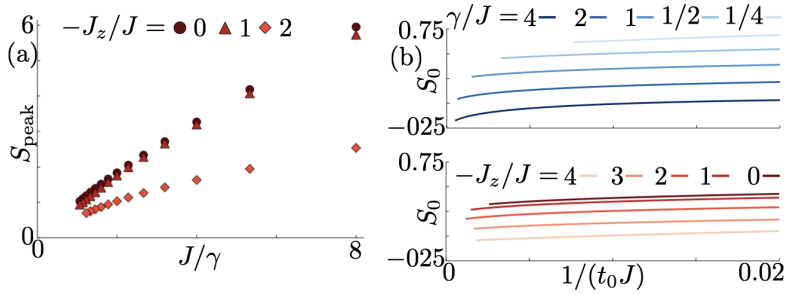

Figure 7.6: (a) Short-time peak-height of S_{OP} as a function of $1/\gamma$ for different J_z. (b) Offset S_0 (extracted from fits as in Fig. 2 in the main manuscript) as a function of the inverse tangent time $1/(t_0 J)$. Blue lines (top) indicate variable γ at fixed $J_z = -J$, red lines (bottom) indicate variable J_z at fixed γ. Results converged for (a) $\Delta tJ = 0.1$ and (b) $\Delta tJ = 0.5$, and different values of $\chi = 512, 1024, 2048$

Whether a state can be efficiently approximated by an MPO is determined by the OE of that state, which has a local maximum at short times. Thus, until not too long times, the approximability of the dynamics is determined by the value at this maximum S_{peak}. This value is shown in Fig. 7.6(a) as a function of the dephasing rate γ and the interaction strength J_z. We find that generally the peak-height grows as $S_{\mathrm{peak}} \sim 1/\gamma$ for small γ. Interestingly, S_{peak} decreases when increasing the spin interaction strength $|J_z|$. As a consequence, the dynamics

under strong dephasing can always be simulated, while for small dephasing the dynamics can only be simulated in the presence of strong interactions (large $|J_z|$).

7.D OE offset scaling

Whether a state can be efficiently approximated by an MPO is determined by the OE of that state, which is at long times dominated by the logarithmic growth $S_{\mathrm{OP}} = \log_2(tJ)/4 + S_0$. Since logarithmic growth is very slow, the offset is also important. We find that the offset S_0 decreases with increasing $|J_z|$ or γ [see Fig. 7.6(b)] when extrapolating to $t_0 \to \infty$. The approximately equal spacing of lines in a regime of large γ (when doubling γ) indicates a scaling of $S_0 \sim \log_2(1/\gamma)$ in this regime. This is confirmed by the perturbative argument given below, which leads to $S_0 = \log_2(J/2\sqrt{4\gamma^2 + J_z^2})/4 + \mathcal{O}(1)$.

In the analytical model, the offsets are given by the time scale of the transfer, as the multiplicative transfer rate under the logarithm becomes an additive constant (see below). Cai and Barthel have computed the transfer rates perturbatively for small $J \ll \gamma$, as discussed in the following [38].

We start by writing the evolution operator as a sum $\mathcal{L} = \mathcal{L}_0 + \mathcal{L}_1$ with $\mathcal{L}_0 = -\mathrm{i}[\hat{H}_0, \cdot] + \sum_i \mathcal{L}^{[i]}$ and $\mathcal{L}_1 = -\mathrm{i}[\hat{H}_1, \cdot]$. Here, the Hamiltonian is separated into interaction $\hat{H}_0 = J_z/4 \sum_i \hat{\sigma}_i^z \hat{\sigma}_{i+1}^z$ and $\hat{H}_1 = J/2 \sum_i \left(\hat{\sigma}_i^+ \hat{\sigma}_{i+1}^- + \hat{\sigma}_i^- \hat{\sigma}_{i+1}^+\right)$. In the limit of strong dissipation, we can then consider perturbation theory for small $\mathcal{L}_1$.

The eigenstates of $\mathcal{L}_0$ are product states in the z eigenbasis. Of these eigenstates, only those without off-diagonal correlations do not decay. Perturbative coupling between the states can be computed by [see also Eq. (7.22) in Sec. 7.E]

$$\mathcal{L}_{\mathrm{eff}} = \mathcal{L}_0 - \mathcal{P}\mathcal{L}_1(\mathcal{L}_0)^{-1}\mathcal{L}_1\mathcal{P}\,, \tag{7.10}$$

where $\mathcal{P}$ projects into the $\mathcal{L}_0$ eigenstates with zero decay rate.

According to Ref. [38], the transfer rate between sites i and $(i+1)$ depends on the state of the neighboring sites $(i-1)$ and $(i+2)$. Thus, focussing only on the two central spins, the transfer rates can be read from the prefactors of

$$\mathcal{L}_{\mathrm{eff}}^{i,(i+1)} \left|\cdots\uparrow\uparrow\downarrow\uparrow\cdots\right\rangle\left\langle\cdots\uparrow\uparrow\downarrow\uparrow\cdots\right| = \frac{J^2}{4\gamma}\big(\left|\cdots\uparrow\downarrow\uparrow\uparrow\cdots\right\rangle\left\langle\cdots\uparrow\downarrow\uparrow\uparrow\cdots\right| - \tag{7.11}$$

$$\left|\cdots\uparrow\uparrow\downarrow\uparrow\cdots\right\rangle\left\langle\cdots\uparrow\uparrow\downarrow\uparrow\cdots\right|\big)\,, \tag{7.12}$$

$$\mathcal{L}_{\mathrm{eff}}^{i,(i+1)} \left|\cdots\uparrow\uparrow\downarrow\downarrow\cdots\right\rangle\left\langle\cdots\uparrow\uparrow\downarrow\downarrow\cdots\right| = \frac{J^2\gamma}{4\gamma^2 + J_z^2}\big(\left|\cdots\uparrow\downarrow\uparrow\downarrow\cdots\right\rangle\left\langle\cdots\uparrow\downarrow\uparrow\downarrow\cdots\right| - \tag{7.13}$$

$$\left|\cdots\uparrow\uparrow\downarrow\downarrow\cdots\right\rangle\left\langle\cdots\uparrow\uparrow\downarrow\downarrow\cdots\right|\big)\,. \tag{7.14}$$

All other possibilities can be obtained by permuting bras and kets, up and down, and reading states from right to left. Here, $\mathcal{L}_{\mathrm{eff}}^{i,(i+1)}$ indicates that only the effective Liouvillian acting on site i and $i+1$ is given, i.e. $\mathcal{L}_{\mathrm{eff}} = \sum_i \mathcal{L}_{\mathrm{eff}}^{i,(i+1)}$.

Since both scenarios are combinatorically equally likely for randomly arranged spins, we compute an effective transfer rate r by taking the *geometric* average,

which yields

$$r = \frac{J^2}{2\sqrt{4\gamma^2 + J_z^2}}\,. \tag{7.15}$$

From this, we can compute the parameter scaling of S_0 using $S(t) = \log_2(rt)/4 + \mathcal{O}(1) = \log_2(Jt)/4 + \log_2(r/J)/4 + \mathcal{O}(1)$ as

$$S_0 = \frac{1}{4}\log_2\left[\frac{J}{2\sqrt{4\gamma^2 + J_z^2}}\right] + \mathcal{O}(1)\,. \tag{7.16}$$

7.E Strong dephasing limits of the Fermi-Hubbard model and of the Bose-Hubbard model

7.E.1 Strong dephasing limit of the Fermi-Hubbard model: two decoupled Symmetric Exclusion processes

We define the Fermi-Hubbard Hamiltonian as

$$\hat{H} = -J\sum_{j=1}^{N}[\hat{c}^\dagger_{\uparrow j+1}\hat{c}_{\uparrow j} + \text{h.c.} + \hat{c}^\dagger_{\downarrow j+1}\hat{c}_{\downarrow j} + \text{h.c.}] + U\sum_{j=1}^{N}\hat{c}^\dagger_{\uparrow j}\hat{c}_{\uparrow j}\hat{c}^\dagger_{\downarrow j}\hat{c}_{\downarrow j}, \tag{7.17}$$

where $\hat{c}^\dagger_{\uparrow j}$ (resp. $\hat{c}^\dagger_{\downarrow j}$) is the creation operator of a fermion with spin up (resp. down) on site j. We consider the strong dephasing limit of the Lindblad equation

$$\frac{d}{dt}\hat{\rho} = -\mathrm{i}[\hat{H},\hat{\rho}] + \gamma\sum_{j=1}^{N}\mathcal{D}[\hat{c}^\dagger_{\uparrow j}\hat{c}_{\uparrow j}](\hat{\rho}) + \gamma\sum_{j=1}^{N}\mathcal{D}[\hat{c}^\dagger_{\downarrow j}\hat{c}_{\downarrow j}](\hat{\rho}), \tag{7.18}$$

where $\mathcal{D}[\hat{A}](\rho) = \hat{A}\hat{\rho}\hat{A}^\dagger - \frac{1}{2}\{\hat{A}^\dagger\hat{A},\hat{\rho}\}$. For our purposes, it is more convenient to write this equation in vectorized form: we vectorize the density matrix $\hat{\rho} \to |\rho\rangle$ —we write the $4^N \times 4^N$ matrix $\hat{\rho}$ as a 4^{2N}-vector $|\rho\rangle$—, and write its evolution as

$$\frac{d}{dt}|\rho\rangle = \gamma\left(\mathcal{L}_0|\rho\rangle + \frac{1}{\gamma}\mathcal{L}_1|\rho\rangle\right) \tag{7.19}$$

where $\mathcal{L}_0$ contains the dissipative part of Eq. (7.18), and $\mathcal{L}_1$ contains the unitary part in (7.18). [Here, contrary to what is done in Ref. [38] and in Sec. 7.D, we do not treat the diagonal and non-diagonal parts of the Hamiltonian differently. Here $\mathcal{L}_1$ corresponds to $-\mathrm{i}[H,\cdot]$ where H is the whole Hamiltonian, including its diagonal part.] Let $\tau = \gamma t$, then

$$\frac{d}{d\tau}|\rho\rangle = \mathcal{L}_0|\rho\rangle + \frac{1}{\gamma}\mathcal{L}_1|\rho\rangle\,, \tag{7.20}$$

and the solution of that equation for some arbitrary initial condition $|\rho_0\rangle$ can be expanded to second order in $1/\gamma$,

$$\begin{aligned}|\rho(\tau)\rangle &= \exp\left(\tau\mathcal{L}_0+\frac{\tau}{\gamma}\mathcal{L}_1\right)|\rho_0\rangle \\ &= e^{\tau\mathcal{L}_0}|\rho_0\rangle+\frac{1}{\gamma}\int_0^\tau d\tau_1 e^{(\tau-\tau_1)\mathcal{L}_0}\mathcal{L}_1 e^{\tau_1\mathcal{L}_0}|\rho_0\rangle \\ &\quad+\frac{1}{\gamma^2}\int_0^\tau d\tau_1\int_0^{\tau_1}d\tau_2 e^{(\tau-\tau_1)\mathcal{L}_0}\mathcal{L}_1 e^{(\tau_1-\tau_2)\mathcal{L}_0}\mathcal{L}_1 e^{\tau_2\mathcal{L}_0}|\rho_0\rangle+\dots \quad (7.21)\end{aligned}$$

Importantly, the subspace of density matrices ρ that satisfy $\mathcal{L}_0|\rho\rangle=0$ is precisely the one of matrices that are diagonal in the computational basis. Let us call $\mathcal{P}$ the projector onto that subspace, and $\mathcal{P}^\perp=1-\mathcal{P}$ its orthogonal projector. Then for $\tau\gg 1$ we can replace $e^{\tau\mathcal{L}_0}$ with $\mathcal{P}$. This leads to

$$\begin{aligned}|\rho(\tau)\rangle &\simeq \mathcal{P}|\rho_0\rangle+\frac{\tau}{\gamma}\mathcal{P}\mathcal{L}_1\mathcal{P}|\rho_0\rangle+\frac{\tau^2}{2\gamma^2}\mathcal{P}\mathcal{L}_1\mathcal{P}\mathcal{L}_1\mathcal{P}|\rho_0\rangle \\ &\quad+\frac{1}{\gamma^2}\int_0^\tau d\tau_2(\tau-\tau_2)\mathcal{P}\mathcal{L}_1\mathcal{P}^\perp e^{\tau_2\mathcal{L}_0}\mathcal{P}^\perp\mathcal{L}_1\mathcal{P}|\rho_0\rangle+\dots \\ &\simeq \exp\left(\frac{\tau}{\gamma}\mathcal{P}\mathcal{L}_1\mathcal{P}\right)\mathcal{P}|\rho_0\rangle+\mathcal{P}\mathcal{L}_1\mathcal{P}^\perp\left(\frac{\tau}{\gamma^2}\int_0^\infty d\tau_2 e^{\tau_2\mathcal{L}_0}\right)\mathcal{P}^\perp\mathcal{L}_1\mathcal{P}|\rho_0\rangle+\dots \\ &\simeq \exp\left(\frac{\tau}{\gamma}\mathcal{P}\mathcal{L}_1\mathcal{P}\right)\mathcal{P}|\rho_0\rangle+\frac{\tau}{\gamma^2}\mathcal{P}\mathcal{L}_1\mathcal{P}^\perp\left(-\mathcal{L}_0^\perp\right)^{-1}\mathcal{P}^\perp\mathcal{L}_1\mathcal{P}|\rho_0\rangle+\dots,\end{aligned}$$

where $\mathcal{L}_0^\perp$ is the restriction of $\mathcal{L}_0$ to the subspace orthogonal to its kernel, and $\left(\mathcal{L}_0^\perp\right)^{-1}$ is its inverse on that subspace. Finally, one notes that $\mathcal{P}\mathcal{L}_1\mathcal{P}=0$, since $\mathcal{L}_1$ acts on the density matrix ρ as $-i[H,\rho]$. Thus, the result of second-order perturbation theory is that, in the strong dephasing limit, the density matrix remains diagonal on long times scales, $|\rho(t)\rangle\simeq\mathcal{P}|\rho(t)\rangle$. The slow evolution of the diagonal part $|\rho_{\text{diag}}(t)\rangle:=\mathcal{P}|\rho(t)\rangle$ is given by

$$\frac{d}{dt}|\rho_{\text{diag}}(t)\rangle = -\frac{1}{\gamma}\mathcal{P}\mathcal{L}_1\mathcal{P}^\perp\left(\mathcal{L}_0^\perp\right)^{-1}\mathcal{P}^\perp\mathcal{L}_1\mathcal{P}|\rho_{\text{diag}}(t)\rangle\,. \quad (7.22)$$

This equation has been obtained for the XXZ chain by Cai and Barthel [38] and also for other models, including models of bosons, by Bernard, Jin and Shpielberg [64]. Let us now apply it to the Fermi-Hubbard model (7.17). The key observation is that the interacting term $U\sum_{j=1}^N \hat{c}^\dagger_{\uparrow j}\hat{c}_{\uparrow j}\hat{c}^\dagger_{\downarrow j}\hat{c}_{\downarrow j}$ in the Hamiltonian (7.17) acts diagonally in the computational basis, so it does not contribute to the term $-\frac{1}{\gamma}\mathcal{P}\mathcal{L}_1\mathcal{P}^\perp\left(\mathcal{L}_0^\perp\right)^{-1}\mathcal{P}^\perp\mathcal{L}_1\mathcal{P}$ in Eq. (7.22). Therefore, in the strong dephasing limit, the spin components $\uparrow$ and $\downarrow$ simply decouple, and each spin component follows its own strong-dephasing dynamics. One can then simply set $U=0$ in the Hamiltonian (7.17) which splits into two independent models of non-interacting fermions, one for each spin component. Consequently, the strong-dephasing limit of the Fermi-Hubbard model consists of two decoupled Symmetric Exclusion Processes, one for the spins $\uparrow$, the other for the spins $\downarrow$, as claimed in the main text.

7.E.2 Strong dephasing limit of the Bose-Hubbard model: a Symmetric 'Inclusion' Process

We define the Bose-Hubbard Hamiltonian as

$$\hat{H} = -J\sum_{j=1}^{N}[\hat{b}_{j+1}^{\dagger}\hat{b}_j + \text{h.c.}] + \frac{U}{2}\sum_{j=1}^{N}\hat{b}_j^{\dagger}\hat{b}_j(\hat{b}_j^{\dagger}\hat{b}_j - 1) \tag{7.23}$$

and the Lindlblad equation with dephasing takes the form (see e.g. Ref. [48])

$$\frac{d}{dt}\rho = -\mathrm{i}[\hat{H},\hat{\rho}] + \gamma\sum_{j=1}^{N}\mathcal{D}[\hat{b}_j^{\dagger}\hat{b}_j](\hat{\rho}). \tag{7.24}$$

Like for the XXZ chain and for the Fermi-Hubbard model, the strong dephasing limit can be analyzed in second-order perturbation theory [38, 64]. The general formula (7.22), where $\gamma\mathcal{L}_0$ is the dissipative part of the Lindblad equation and $\mathcal{L}_1$ is the unitary part, applies also to the Bose-Hubbard model. As in the Fermi-Hubbard case, the interaction term $\frac{U}{2}\sum_{j=1}^{N}\hat{b}_j^{\dagger}\hat{b}_j(\hat{b}_j^{\dagger}\hat{b}_j - 1)$ in the Hamiltonian (7.23) acts diagonally in the single-site Fock basis. Consequently, it does not contribute to the term $-\frac{1}{\gamma}\mathcal{P}\mathcal{L}_1\mathcal{P}^{\perp}\left(\mathcal{L}_0^{\perp}\right)^{-1}\mathcal{P}^{\perp}\mathcal{L}_1\mathcal{P}$. At strong dephasing the Hubbard interaction is irrelevant, and the model can be analyzed simply by setting $U = 0$. The resulting model of non-interacting bosons with dephasing has been analyzed in Ref. [64]. For the convenience of the reader, here we briefly sketch a simple derivation of that strong-dephasing limit.

For notational simplicity, we focus on $N = 2$ two sites only, and label the basis states as $|n_1 n_2\rangle$ where $n_1, n_2 \in \mathbb{N}$ are the number of bosons on site 1 and 2. Diagonal density matrices are of the form

$$\rho_{\text{diag}} = \sum_{n_1,n_2} p(n_1,n_2)\,|n_1 n_2\rangle\langle n_1 n_2|\,. \tag{7.25}$$

Under strong dephasing, the effective dynamics within the space of diagonal density matrices must be a classical stochastic process for the probability distribution $p(n_1, n_2)$. The goal is to determine the rates that define the classical master equation of that process.

We proceed step by step to compute the r.h.s of Eq. (7.22). First, $\mathcal{L}_1\mathcal{P}\,|\rho_{\text{diag}}\rangle = \mathcal{L}_1\,|\rho_{\text{diag}}\rangle$ is the vectorized form of

$$\begin{aligned}
-\mathrm{i}\left[\hat{H},\rho_{\text{diag}}\right] &= -\mathrm{i}\left[H,\sum_{n_1,n_2}p(n_1,n_2)\,|n_1n_2\rangle\langle n_1n_2|\right] \\
&= \mathrm{i}J\sum_{n_1,n_2}p(n_1,n_2)\Big(\sqrt{(n_1+1)n_2}\,|n_1+1,n_2-1\rangle\langle n_1n_2| \\
&\quad + \sqrt{n_1(n_2+1)}\,|n_1-1,n_2+1\rangle\langle n_1n_2| \\
&\quad - \sqrt{(n_1+1)n_2}\,|n_1,n_2\rangle\langle n_1+1n_2-1| \\
&\quad + \sqrt{n_1(n_2+1)}\,|n_1,n_2\rangle\langle n_1-1,n_2+1|\Big)\,,
\end{aligned}$$

which we write as

$$\begin{aligned}\mathcal{L}_1 |\rho_{\rm diag}\rangle &= \mathrm{i}J \sum_{n_1,n_2} p(n_1,n_2) \Big(\sqrt{(n_1+1)n_2}\, |n_1+1, n_2-1\rangle \langle n_1 n_2| \\ &+ \sqrt{n_1(n_2+1)}\, |n_1-1, n_2+1\rangle |n_1 n_2\rangle \\ &- \sqrt{(n_1+1)n_2}\, |n_1, n_2\rangle \langle n_1+1 n_2-1| + \sqrt{n_1(n_2+1)}\, |n_1, n_2\rangle |n_1-1, n_2+1\rangle \Big) .\end{aligned}$$

Second, we observe that $\mathcal{L}[\hat{b}_1^\dagger \hat{b}_1]\, |n_1 \pm 1, n_2'\rangle\, |n_1, n_2\rangle = (n_1 \pm 1) n_1 - \frac{(n_1 \pm 1)^2 + n_1^2}{2} = -\frac{1}{2}$. Then

$$\begin{aligned}(\mathcal{L}_0^\perp)^{-1} \mathcal{P}^\perp \mathcal{L}_1 \mathcal{P} |\rho_{\rm diag}\rangle &= \frac{-iJ}{2\gamma} \sum_{n_1,n_2} p(n_1,n_2) \Big(\sqrt{(n_1+1)n_2}\, |n_1+1, n_2-1\rangle |n_1 n_2\rangle \\ &+ \sqrt{n_1(n_2+1)}\, |n_1-1, n_2+1\rangle |n_1 n_2\rangle \\ &- \sqrt{(n_1+1)n_2}\, |n_1, n_2\rangle |n_1+1 n_2-1\rangle \\ &+ \sqrt{n_1(n_2+1)}\, |n_1, n_2\rangle |n_1-1, n_2+1\rangle \Big) .\end{aligned}$$

Applying again the vectorized form of $-\mathrm{i}[\hat{H}, .]$, and projecting onto diagonal configurations, one arrives at

$$\begin{aligned}-\mathcal{P}\mathcal{L}_1 \mathcal{P}^\perp (\mathcal{L}_0^\perp)^{-1} \mathcal{P}^\perp \mathcal{L}_1 \mathcal{P} \qquad |\rho_{\rm diag}\rangle &= \frac{J^2}{2\gamma} \sum_{n_1,n_2} p(n_1,n_2) \\ &\Big(\sqrt{(n_1+1)n_2}^2 (|n_1+1, n_2-1\rangle |n_1+1 n_2-1\rangle - |n_1, n_2\rangle |n_1 n_2\rangle) \\ &+ \sqrt{n_1(n_2+1)}^2 (|n_1-1, n_2+1\rangle |n_1-1 n_2+1\rangle - |n_1, n_2\rangle |n_1 n_2\rangle) \\ &+ \sqrt{(n_1+1)n_2}^2 (|n_1+1, n_2-1\rangle |n_1+1 n_2-1\rangle - |n_1, n_2\rangle |n_1 n_2\rangle) \\ &+ \sqrt{n_1(n_2+1)}^2 (|n_1-1, n_2+1\rangle |n_1-1, n_2+1\rangle - |n_1, n_2\rangle |n_1, n_2\rangle) \Big) .\end{aligned}$$

In conclusion, the classical master equation obeyed by the probability distribution $p(n_1, n_2)$ is

$$\begin{aligned}\frac{d}{dt} p(n_1,n_2) &= \frac{J^2}{\gamma} n_1 (n_2+1) [p(n_1-1, n_2+1) - p(n_1,n_2)] \\ &+ \frac{J^2}{\gamma} (n_1+1) n_2 [p(n_1+1, n_2-1) - p(n_1,n_2)]. \qquad (7.26)\end{aligned}$$

This result generalizes straightforwardly to the case with more sites, $N > 2$, i.e.

$$\begin{aligned}\frac{d}{dt} p(n_1, n_2, \ldots, n_N) = \frac{J^2}{\gamma} \sum_i n_i [&(n_{i-1}+1) p(\ldots, n_{i-1}+1, n_i - 1, \ldots) \qquad (7.27) \\ &+ (n_{i+1}+1) p(\ldots, n_i - 1, n_{i+1}+1, \ldots) \\ &- (n_{i-1} + n_{i+1} + 2) p(\ldots, n_i, n_{i+1}, \ldots)]. \qquad (7.28)\end{aligned}$$

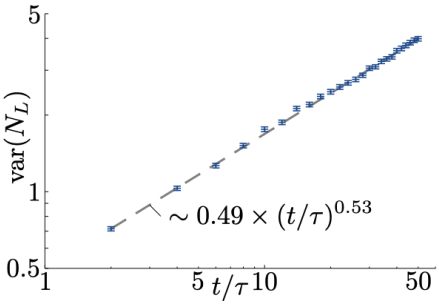

Figure 7.7: Fit for the variance growth for the Symmetric Inclusion Process. The blue crosses are determined by a Monte Carlo simulation of Eq. (7.27) with 5000 trajectories. The grey dashed line is a power law fit to the numerical data.

What is interesting about the master equation (7.27) is that it is very different from the one of non-interacting particles undergoing a random walk, which would rather be of the form

$$\frac{d}{dt}p(n_1, n_2, \ldots, n_N) \propto \sum_i n_i[p(\ldots, n_i - 1, n_{i+1} + 1, \ldots) + p(\ldots, n_{i-1} + 1, n_i - 1, \ldots) - 2p(\ldots, n_{i-1}, n_i, n_{i+1}, \ldots)].$$

Interestingly, the resulting classical dynamics exhibits a signature of bosonic bunching in the original quantum model. The classical stochastic process defined by Eq. (7.27) belongs to a class of models known as 'Symmetric Inclusion Processes' in the statistical physics literature, see e.g. Refs. [89, 90].

In order to determine the dynamics of number fluctuations in the model described by Eq. (7.27), we numerically compute $n_{\text{samples}} = 5000$ different sample trajectories for a chain of length $L = 100$. Fig. 7.7 shows the time trace of the variance of the number of particles in the left half of the chain $\text{var}(N_L)$ [corrected by $n_{\text{samples}}/(n_{\text{samples}}-1)$]. We compute the error of the variance using the jackknife method [91] by separating the data into $M = 500$ bins with 10 trajectories each. Then, we compute the variances v_m for all possible subsets of $M-1$ different bins (i.e. deleting 1 bin for each subset). Finally, we compute the error from these variances as

$$\text{error}[\text{var}(N_L)] = \sqrt{\frac{M-1}{M}\sum_m [v_m - \text{var}(N_L)]^2}\,. \tag{7.29}$$

We use `LsqFit.jl` to fit the numerical data with a power law of the form $\text{var}(N_L) = a \times (t/\tau)^b$, and find $a \approx 0.49$ and $b = 0.53$, close to $b = 1/2$. We find that this fit describes the data well, as shown in Fig. 7.7. Here, $\tau = \gamma/J^2$ is the characteristic time scale of the dynamics.

If we thus assume that N_L is Gaussian distributed with standard deviation $\delta \sim (t/\tau)^{b/2}$, we can use Eq. (7) of the main text to compute $S_{\text{num}}(t) = \log_2[(t/\tau)^{b/2}] + \mathcal{O}(1)$, close to $\log_2(t/\tau)/4 + \text{const.}$ used in the main text.

Bibliography

[1] D. Wellnitz, G. Preisser, V. Alba, J. Dubail, and J. Schachenmayer. Rise and Fall, and Slow Rise Again, of Operator Entanglement under Dephasing. *Phys. Rev. Lett.*, 129(17):170401, October 2022.

[2] Luigi Amico, Rosario Fazio, Andreas Osterloh, and Vlatko Vedral. Entanglement in many-body systems. *Rev. Mod. Phys.*, 80(2):517, May 2008.

[3] J. Eisert, M. Cramer, and M. B. Plenio. Colloquium: Area laws for the entanglement entropy. *Rev. Mod. Phys.*, 82(1):277–306, Feb 2010.

[4] Pasquale Calabrese and John Cardy. Evolution of entanglement entropy in one-dimensional systems. *J. Stat. Mech.: Theory Exp.*, 2005(04):P04010, Apr 2005.

[5] Maurizio Fagotti and Pasquale Calabrese. Evolution of entanglement entropy following a quantum quench: Analytic results for the xy chain in a transverse magnetic field. *Phys. Rev. A*, 78:010306(R), Jul 2008.

[6] Marko Žnidarič, Tomaž Prosen, and Peter Prelovšek. Many-body localization in the Heisenberg XXZ magnet in a random field. *Phys. Rev. B*, 77(6):064426, Feb 2008.

[7] V. Alba and P. Calabrese. Entanglement and thermodynamics after a quantum quench in integrable systems. *Proc. Natl. Acad. Sci. U. S. A.*, 114(30):7947–7951, 2017.

[8] Cheryne Jonay, David A Huse, and Adam Nahum. Coarse-grained dynamics of operator and state entanglement. *arXiv:1803.00089*, 2018.

[9] Alexander Lukin, Matthew Rispoli, Robert Schittko, M. Eric Tai, Adam M. Kaufman, Soonwon Choi, Vedika Khemani, Julian Léonard, and Markus Greiner. Probing entanglement in a many-body–localized system. *Science*, 364(6437):256, Apr 2019.

[10] Guifré Vidal. Efficient Simulation of One-Dimensional Quantum Many-Body Systems. *Phys. Rev. Lett.*, 93(4):040502, Jul 2004.

[11] F. Verstraete, V. Murg, and J. I. Cirac. Matrix product states, projected entangled pair states, and variational renormalization group methods for quantum spin systems. *Adv. Phys.*, 57(2):143–224, Mar 2008.

[12] Ulrich Schollwöck. The density-matrix renormalization group in the age of matrix product states. *Ann. Phys.*, 326(1):96–192, Jan 2011.

[13] Sebastian Paeckel, Thomas Köhler, Andreas Swoboda, Salvatore R. Manmana, Ulrich Schollwöck, and Claudius Hubig. Time-evolution methods for matrix-product states. *Ann. Phys.*, 411:167998, Dec 2019.

[14] Norbert Schuch, Michael M. Wolf, Frank Verstraete, and J. Ignacio Cirac. Entropy Scaling and Simulability by Matrix Product States. *Phys. Rev. Lett.*, 100(3):030504, Jan 2008.

[15] Immanuel Bloch, Jean Dalibard, and Sylvain Nascimbène. Quantum simulations with ultracold quantum gases. *Nat. Phys.*, 8(4):267–276, Apr 2012.

[16] C. S. Adams, J. D. Pritchard, and J. P. Shaffer. Rydberg atom quantum technologies. *J. Phys. B: At. Mol. Opt. Phys.*, 53(1):012002, Dec 2019.

[17] Antoine Browaeys and Thierry Lahaye. Many-body physics with individually controlled Rydberg atoms. *Nat. Phys.*, 16(2):132–142, Feb 2020.

[18] M. Morgado and S. Whitlock. Quantum simulation and computing with Rydberg-interacting qubits. *AVS Quantum Sci.*, 3(2):023501, May 2021.

[19] Bryce Gadway and Bo Yan. Strongly interacting ultracold polar molecules. *J. Phys. B: At. Mol. Opt. Phys.*, 49(15):152002, Jun 2016.

[20] R. Blatt and C. F. Roos. Quantum simulations with trapped ions. *Nat. Phys.*, 8(4):277–284, Apr 2012.

[21] J. Ignacio Cirac and Peter Zoller. Goals and opportunities in quantum simulation. *Nat. Phys.*, 8(4):264–266, Apr 2012.

[22] I. M. Georgescu, S. Ashhab, and Franco Nori. Quantum simulation. *Rev. Mod. Phys.*, 86(1):153–185, Mar 2014.

[23] Paolo Zanardi, Christof Zalka, and Lara Faoro. Entangling power of quantum evolutions. *Phys. Rev. A*, 62(3):030301(R), Aug 2000.

[24] Paolo Zanardi. Entanglement of quantum evolutions. *Phys. Rev. A*, 63(4):040304(R), Mar 2001.

[25] Xiaoguang Wang and Paolo Zanardi. Quantum entanglement of unitary operators on bipartite systems. *Phys. Rev. A*, 66(4):044303, Oct 2002.

[26] Tomaž Prosen and Iztok Pižorn. Operator space entanglement entropy in a transverse Ising chain. *Phys. Rev. A*, 76(3):032316, Sep 2007.

[27] J Dubail. Entanglement scaling of operators: a conformal field theory approach, with a glimpse of simulability of long-time dynamics in 1+1d. *Journal of Physics A: Mathematical and Theoretical*, 50(23):234001, may 2017.

[28] Tianci Zhou and David J. Luitz. Operator entanglement entropy of the time evolution operator in chaotic systems. *Phys. Rev. B*, 95(9):094206, Mar 2017.

[29] V. Alba, J. Dubail, and M. Medenjak. Operator entanglement in interacting integrable quantum systems: The case of the rule 54 chain. *Phys. Rev. Lett.*, 122:250603, Jun 2019.

[30] Huajia Wang and Tianci Zhou. Barrier from chaos: operator entanglement dynamics of the reduced density matrix. *J. High Energy Phys.*, 2019(12):1–44, Dec 2019.

[31] Georgios Styliaris, Namit Anand, and Paolo Zanardi. Information Scrambling over Bipartitions: Equilibration, Entropy Production, and Typicality. *Phys. Rev. Lett.*, 126(3):030601, Jan 2021.

[32] Kyungjoo Noh, Liang Jiang, and Bill Fefferman. Efficient classical simulation of noisy random quantum circuits in one dimension. *Quantum*, 4:318, Sep 2020.

[33] Tibor Rakovszky, C. W. von Keyserlingk, and Frank Pollmann. Dissipation-assisted operator evolution method for capturing hydrodynamic transport. *arXiv:2004.05177*, Apr 2020.

[34] Bruno Bertini, Pavel Kos, and Tomaz Prosen. Operator Entanglement in Local Quantum Circuits I: Chaotic Dual-Unitary Circuits. *SciPost Phys.*, 8(4):067, Apr 2020.

[35] Bruno Bertini, Pavel Kos, and Tomaz Prosen. Operator Entanglement in Local Quantum Circuits II: Solitons in Chains of Qubits. *SciPost Phys.*, 8(4):068, Apr 2020.

[36] see Supplemental Material details on the MPO simulations, non-conserving models, the perturbative OE offset, for numerical results on the parameter dependence of the short-time peaks, and for analytical results for the Hubbard models, including Refs. [38, 48, 49, 55, 58, 59, 64, 89–91].

[37] Davide Rossini and Ettore Vicari. Coherent and dissipative dynamics at quantum phase transitions. *Physics Reports*, 936:1–110, 2021.

[38] Zi Cai and Thomas Barthel. Algebraic versus Exponential Decoherence in Dissipative Many-Particle Systems. *Phys. Rev. Lett.*, 111(15):150403, Oct 2013.

[39] Mariya V. Medvedyeva, Fabian H. L. Essler, and Tomaž Prosen. Exact Bethe Ansatz Spectrum of a Tight-Binding Chain with Dephasing Noise. *Phys. Rev. Lett.*, 117(13):137202, Sep 2016.

[40] Michael Foss-Feig, Jeremy T. Young, Victor V. Albert, Alexey V. Gorshkov, and Mohammad F. Maghrebi. Solvable Family of Driven-Dissipative Many-Body Systems. *Phys. Rev. Lett.*, 119(19):190402, Nov 2017.

[41] Marko Žnidarič. Relaxation times of dissipative many-body quantum systems. *Phys. Rev. E*, 92(4):042143, October 2015.

[42] Dario Poletti, Jean-Sébastien Bernier, Antoine Georges, and Corinna Kollath. Interaction-Induced Impeding of Decoherence and Anomalous Diffusion. *Phys. Rev. Lett.*, 109(4):045302, July 2012.

[43] Dario Poletti, Peter Barmettler, Antoine Georges, and Corinna Kollath. Emergence of Glasslike Dynamics for Dissipative and Strongly Interacting Bosons. *Phys. Rev. Lett.*, 111(19):195301, November 2013.

[44] Jie Ren, Qiaoyi Li, Wei Li, Zi Cai, and Xiaoqun Wang. Noise-Driven Universal Dynamics towards an Infinite Temperature State. *Phys. Rev. Lett.*, 124(13):130602, March 2020.

[45] Raphaël Bouganne, Manel Bosch Aguilera, Alexis Ghermaoui, Jérôme Beugnon, and Fabrice Gerbier. Anomalous decay of coherence in a dissipative many-body system. *Nat. Phys.*, 16:21–25, January 2020.

[46] D. Plankensteiner, J. Schachenmayer, H. Ritsch, and C. Genes. Laser noise imposed limitations of ensemble quantum metrology. *J. Phys. B: At. Mol. Opt. Phys.*, 49(24):245501, Nov 2016.

[47] C. W. Gardiner and P. Zoller. *Quantum noise.* Springer, 1991.

[48] H. Pichler, A. J. Daley, and P. Zoller. Nonequilibrium dynamics of bosonic atoms in optical lattices: Decoherence of many-body states due to spontaneous emission. *Phys. Rev. A*, 82(6):063605, Dec 2010.

[49] R. Orús and G. Vidal. Infinite time-evolving block decimation algorithm beyond unitary evolution. *Phys. Rev. B*, 78(15):155117, Oct 2008.

[50] T. E. Harris. Diffusion with "Collisions" between Particles. *J. Appl. Probab.*, 2(2):323–338, Dec 1965.

[51] David G. Levitt. Dynamics of a Single-File Pore: Non-Fickian Behavior. *Phys. Rev. A*, 8(6):3050–3054, Dec 1973.

[52] Richard Arratia. The Motion of a Tagged Particle in the Simple Symmetric Exclusion System on Z. *aop*, 11(2):362–373, May 1983.

[53] Hendrik Weimer, Augustine Kshetrimayum, and Román Orús. Simulation methods for open quantum many-body systems. *Rev. Mod. Phys.*, 93(1):015008, Mar 2021.

[54] Andrew J. Daley. Quantum trajectories and open many-body quantum systems. *Adv. Phys.*, 63(2):77–149, Mar 2014.

[55] Michael Zwolak and Guifré Vidal. Mixed-State Dynamics in One-Dimensional Quantum Lattice Systems: A Time-Dependent Superoperator Renormalization Algorithm. *Phys. Rev. Lett.*, 93(20):207205, Nov 2004.

[56] F. Verstraete, J. J. García-Ripoll, and J. I. Cirac. Matrix Product Density Operators: Simulation of Finite-Temperature and Dissipative Systems. *Phys. Rev. Lett.*, 93(20):207204, Nov 2004.

[57] A. H. Werner, D. Jaschke, P. Silvi, M. Kliesch, T. Calarco, J. Eisert, and S. Montangero. Positive Tensor Network Approach for Simulating Open Quantum Many-Body Systems. *Phys. Rev. Lett.*, 116(23):237201, Jun 2016.

[58] G. Vidal. Classical Simulation of Infinite-Size Quantum Lattice Systems in One Spatial Dimension. *Phys. Rev. Lett.*, 98(7):070201, February 2007.

[59] A. T. Sornborger and E. D. Stewart. Higher-order methods for simulations on quantum computers. *Phys. Rev. A*, 60(3):1956–1965, Sep 1999.

[60] Federico Carollo and Vincenzo Alba. Emergent dissipative quasi-particle picture in noninteracting Markovian open quantum systems. *arXiv:2106.11997*, Jun 2021.

[61] Vincenzo Alba and Federico Carollo. Hydrodynamics of quantum entropies in Ising chains with linear dissipation. *arXiv:2109.01836*, Sep 2021.

[62] Mariya V. Medvedyeva, Tomaž Prosen, and Marko Žnidarič. Influence of dephasing on many-body localization. *Phys. Rev. B*, 93(9):094205, Mar 2016.

[63] Kirone Mallick. The exclusion process: A paradigm for non-equilibrium behaviour. *Physica A*, 418:17–48, Jan 2015.

[64] Denis Bernard, T Jin, and O Shpielberg. Transport in quantum chains under strong monitoring. *EPL (Europhysics Letters)*, 121(6):60006, 2018.

[65] Binhua Lin, Mati Meron, Bianxiao Cui, Stuart A. Rice, and Haim Diamant. From Random Walk to Single-File Diffusion. *Phys. Rev. Lett.*, 94(21):216001, Jun 2005.

[66] Bernard Derrida and Antoine Gerschenfeld. Current Fluctuations of the One Dimensional Symmetric Simple Exclusion Process with Step Initial Condition. *J. Stat. Phys.*, 136(1):1–15, Jul 2009.

[67] Takashi Imamura, Kirone Mallick, and Tomohiro Sasamoto. Large Deviations of a Tracer in the Symmetric Exclusion Process. *Phys. Rev. Lett.*, 118(16):160601, Apr 2017.

[68] Aurélien Grabsch, Alexis Poncet, Pierre Rizkallah, Pierre Illien, and Olivier Bénichou. Closing and solving the hierarchy for large deviations and spatial correlations in single-file diffusion. *arXiv:2110.09269*, 2021.

[69] K. Hahn, J. Kärger, and V. Kukla. Single-File Diffusion Observation. *Phys. Rev. Lett.*, 76(15):2762–2765, Apr 1996.

[70] Q.-H. Wei, C. Bechinger, and P. Leiderer. Single-File Diffusion of Colloids in One-Dimensional Channels. *Science*, 287(5453):625, Jan 2000.

[71] Marko Žnidarič. Dephasing-induced diffusive transport in the anisotropic Heisenberg model. *New J. Phys.*, 12(4):043001, Apr 2010.

[72] Marko Žnidarič. Exact solution for a diffusive nonequilibrium steady state of an open quantum. *J. Stat. Mech.: Theory Exp.*, 2010(05):L05002, May 2010.

[73] Viktor Eisler. Crossover between ballistic and diffusive transport: the quantum exclusion process. *J. Stat. Mech.: Theory Exp.*, 2011(06):P06007, Jun 2011.

[74] Jacopo De Nardis, Sarang Gopalakrishnan, Romain Vasseur, and Brayden Ware. Subdiffusive hydrodynamics of nearly-integrable anisotropic spin chains. *arXiv:2109.13251*, Sep 2021.

[75] Moshe Goldstein and Eran Sela. Symmetry-resolved entanglement in many-body systems. *Phys. Rev. Lett.*, 120:200602, May 2018.

[76] J. C. Xavier, F. C. Alcaraz, and G. Sierra. Equipartition of the entanglement entropy. *Phys. Rev. B*, 98:041106(R), Jul 2018.

[77] Gilles Parez, Riccarda Bonsignori, and Pasquale Calabrese. Quasiparticle dynamics of symmetry-resolved entanglement after a quench: Examples of conformal field theories and free fermions. *Phys. Rev. B*, 103:L041104, Jan 2021.

[78] Hatem Barghathi, C. M. Herdman, and Adrian Del Maestro. Rényi Generalization of the Accessible Entanglement Entropy. *Phys. Rev. Lett.*, 121(15):150501, October 2018.

[79] Hatem Barghathi, Emanuel Casiano-Diaz, and Adrian Del Maestro. Operationally accessible entanglement of one-dimensional spinless fermions. *Phys. Rev. A*, 100(2):022324, August 2019.

[80] Yaodong Li, Xiao Chen, and Matthew P. A. Fisher. Quantum Zeno effect and the many-body entanglement transition. *Phys. Rev. B*, 98(20):205136, Nov 2018.

[81] Amos Chan, Rahul M. Nandkishore, Michael Pretko, and Graeme Smith. Unitary-projective entanglement dynamics. *Phys. Rev. B*, 99(22):224307, Jun 2019.

[82] Michele Coppola, Emanuele Tirrito, Dragi Karevski, and Mario Collura. Growth of entanglement entropy under local projective measurements. *arXiv:2109.10837*, Sep 2021.

[83] T. Botzung, S. Diehl, and M. Müller. Engineered dissipation induced entanglement transition in quantum spin chains: From logarithmic growth to area law. *Phys. Rev. B*, 104(18):184422, Nov 2021.

[84] M. J. Mark, S. Flannigan, F. Meinert, J. P. D'Incao, A. J. Daley, and H.-C. Nägerl. Interplay between coherent and dissipative dynamics of bosonic doublons in an optical lattice. *Phys. Rev. Res.*, 2(4):043050, Oct 2020.

[85] B. Zhu, B. Gadway, M. Foss-Feig, J. Schachenmayer, M. L. Wall, K. R. A. Hazzard, B. Yan, S. A. Moses, J. P. Covey, D. S. Jin, J. Ye, M. Holland, and A. M. Rey. Suppressing the Loss of Ultracold Molecules Via the Continuous Quantum Zeno Effect. *Phys. Rev. Lett.*, 112(7):070404, Feb 2014.

[86] V. S. Shchesnovich and V. V. Konotop. Control of a Bose-Einstein condensate by dissipation: Nonlinear Zeno effect. *Phys. Rev. A*, 81(5):053611, May 2010.

[87] T. Müller, S. Diehl, and M. Buchhold. Measurement-Induced Dark State Phase Transitions in Long-Ranged Fermion Systems. *Phys. Rev. Lett.*, 128(1):010605, Jan 2022.

[88] Matthew Fishman, Steven White, and Edwin Stoudenmire. The ITensor Software Library for Tensor Network Calculations. *SciPost Phys. Codebases*, page 004, August 2022.

[89] Cristian Giardina, Frank Redig, and Kiamars Vafayi. Correlation inequalities for interacting particle systems with duality. *Journal of Statistical Physics*, 141(2):242–263, 2010.

[90] Stefan Grosskinsky, Frank Redig, and Kiamars Vafayi. Dynamics of condensation in the symmetric inclusion process. *Electronic Journal of Probability*, 18:1–23, 2013.

[91] Rupert G Miller. The jackknife-a review. *Biometrika*, 61(1):1–15, 1974.

Chapter 8

Publication: Comparing bipartite entropy growth in open-system matrix product simulation methods

The following chapter is a reprint of a work comparing the bipartite entropy growth in open-system using matrix product simulation methods, which was published in *Phys. Rev. A* ***108****, 012616* [1]. In this work we have done a thorough comparison of bipartite entropy growth in open-systems using two different methods: MPDO and QT+MPS. Under the types of dissipation that we considered, we give a thorough comparison of bipartite entropy growth, using the XXZ model. In general we found significant advantages of the MPDO approach over the QT+MPS method such as a better growth scaling of bipartite entropy growth at long times, and also an easier exploitation of higher order Trotter decompositions and translational invariance, allowing for larger time steps and system sizes.

This chapter is organised as follows: In Section 8.1 we introduce some of the motivations to study bipartite entropy growth in the context of many-body quantum systems and the two approaches that we use to study it. In Section 8.2 we introduce the XXZ model, which is the Hamiltonian that we use throughout this paper, as well as the initial state and the two different types of dissipation that we use: spontaneous emission/absorption and dephasing. In Section 8.3 we explain the two measures for bipartite entropy that we use: Operator Entanglement and Trajectory Entanglement, along with the correspondent matrix product decompositions that they are associated with. In Section 8.4 we present numerical comparison of bipartite entropy growth between MPDO and QT+MPS under spontaneous emission/absorption and under dephasing. In Section 8.5 we present some details regarding the numerical methods that we employ along with analytical results for the case of spontaneous emission/absorption. Finally in Section 8.6 we give some outlooks and a conclusion.

8.1 Introduction

In recent years, experimental developments have made it possible to analyze and control almost fully coherent quantum many-body dynamics [2], in particular for effective spin-1/2 models, e.g. with trapped ultracold atoms or molecules in optical lattices [3, 4], Rydberg excitations [5–8], or ion traps [9]. The possibility of controlled quantum simulations on such platforms promises various practical applications that may lead to a quantum advantage compared to classical simulations [10].

The study of entanglement in many-body models has been a long-standing theory quest [11, 12], especially its growth dynamics (e.g. [13–15]). The study of entanglement is of practical interest in one dimension (1D), where the growth of the bipartite entanglement entropy S (see Sec. 8.3 for definitions) is directly connected to the question whether dynamics can be efficiently simulated on a classical computer. This connection is made via the concept of matrix product states (MPS) [16–20]. An MPS is a numerical decomposition of a many-body state vector into a product of $\chi \times \chi$ matrices, where the entries of the matrices are local kets. For such a representation, the bipartite entanglement entropy is limited to $\max[S] = \log_2(\chi)$. Consequently, to represent a physical state $|\psi(t)\rangle$ with entanglement entropy $S(t)$ as MPS over time, the matrix size (or "bond dimension") has to grow at least as $\chi \propto 2^{S(t)}$. An evolution where S increases faster than logarithmic can therefore be considered computationally inefficient.

Every experiment features at least small couplings to the environment, and should therefore be treated as an open quantum system described by a density matrix $\hat{\rho}$. Then, the definition of entanglement needs to be adapted: A bipartition of the open system is effectively a tripartition of a larger (closed) system, with the environment acting as third party, and bipartite entropies do not necessarily indicate entanglement. However, analogously to MPSs for pure states, also a matrix product decomposition of the density matrix can be defined, known as density matrix product density operator (MPDO) [21–25]. Equivalently to the pure state case, the so-called operator space entanglement entropy, or simply "operator entanglement" (OE) [26–37] is linked to the efficiency of this MPDO representation.

Alternatively, the density matrix can be non-uniquely decomposed as a statistical mixture of pure states [see Fig. 8.1(a) for a sketch]. Each pure state can then be expressed as an MPS, and the efficiency of such a representation is determined by the bipartite entanglement entropies in the individual states. In order to compute time evolution, pure state trajectories can be stochastically evolved with a technique known as quantum Monte-Carlo wavefunction method or quantum trajectories (QT) [38–40]. This approach has been successfully applied in many simulations with MPS [25, 41]. We denote it as QT+MPS, and the average bipartite entropy of the trajectories as "trajectory entanglement" (TE). In general, due to the smaller local state space, a QT+MPS approach seems favorable compared to an MPDO, in particular for computations where only small numbers of trajectories are required for statistical convergence (e.g. for computing evolution of simple local observables). However, a decreased entropy scaling could make the

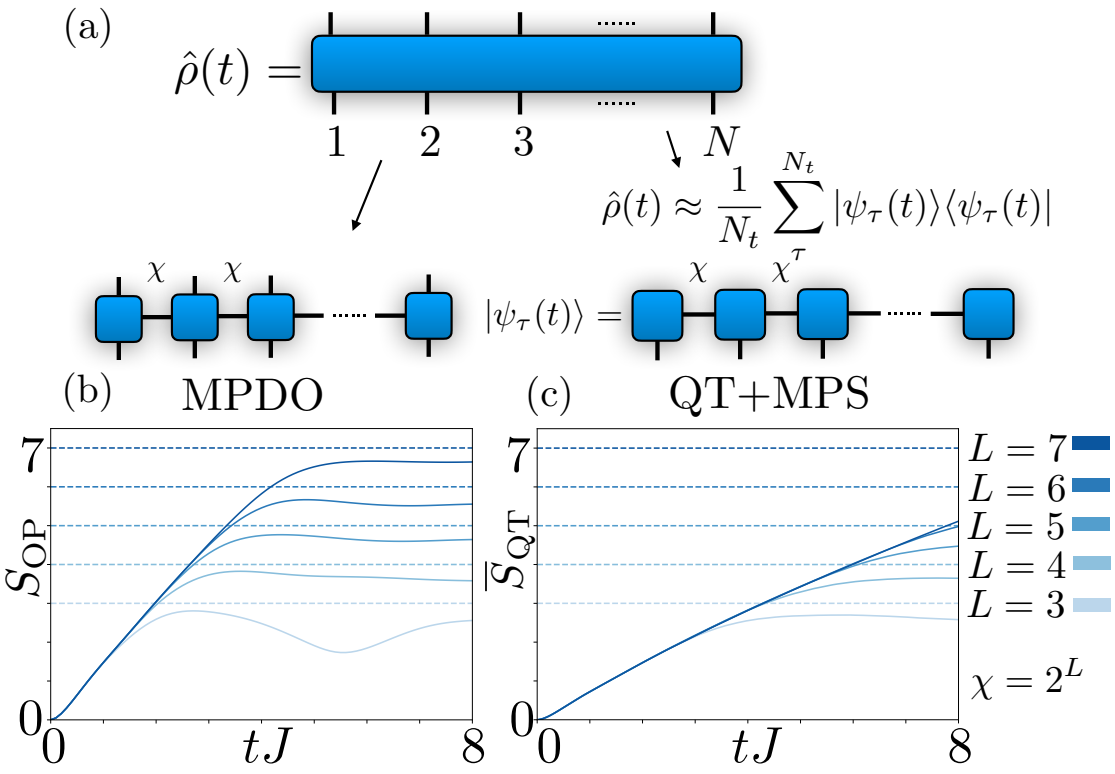

Figure 8.1: *Overview* — (a) Schematics of different numerical approaches for simulating master equation dynamics: i) decomposition of the density matrix into a matrix product density operator (MPDO); ii) unravelling of the density matrix into matrix product state (MPS) quantum trajectories. MPDO and MPS bond dimensions, χ, limit operator entanglement (OE, S_{OP}) and trajectory entanglement (TE, $\overline{S}_{\mathrm{QT}}$), respectively (see text). (b/c) Evolution of OE and TE for a simulation of the master equation (8.3) with an initial Néel state. Results are shown in a small dissipation limit ($\gamma_\pm = 0.01J$, $\gamma_z = 0$), and entropies are computed for a splitting at the center (averaged over 11 center bonds for QT+MPS). Different lines correspond to simulations with increasingly large bond dimensions $\chi = 2^L$ and $L = 3, \ldots, 7$, horizontal dashed lines indicate the entropy limits $\log_2(\chi)$. Statistical error bars are within the linewidths [$N = 40$, for QT+MPS: $N_t = 400$].

MPDO approach fundamentally more efficient since it can significantly relax the requirements on bond dimensions χ [42].

The answer to the question about the relative performance of the two different approaches depends on the model Hamiltonian, the initial state, the nature of dissipation, and the observable of interest. Which of the two approaches is preferable was analyzed for several specific setups in previous works, e.g.: for a Bose-Hubbard model subjected to dephasing [43]; for disordered fermionic hopping models with particle loss and dephasing [44], and for computations of two-time correlations in an XXZ model with spontaneous emission or dephasing [45]. For the Bose-Hubbard model discussed in [43] calculations were limited to relatively small systems up to 20 sites, which led to a saturation of both OE and TE to relatively small constant values quickly, with the averaged TE staying below the OE. For such scenarios it was argued that the QT+MPS approach is favorable, except for limits of large dephasing rates. In the latter case QT suffers from extremely small time-step requirements. In contrast, for the disordered fermionic model in Ref. [44], the disorder leads to a strong suppression of both TE and OE. In this setup it was then argued that an MPDO approach is more efficient. In Ref. [45] a thorough comparison led to the conclusion that for the computation of two-time correlations the magnitude of the dephasing rates is the crucial factor that determines which approach is favorable, related to the small time-step problem in the QT method. It was furthermore pointed out that the initial state plays a very important role, since already the compression of an initially entangled state into the MPDO form can be very costly, rendering the approach impractical.

In addition to the previous works, here we now perform a systematic comparison of OE and TE scaling behavior at long times in sufficiently large systems. We focus on the generic XXZ model with spontaneous emission/absorption and dephasing for a simple initial product Néel state. Our simulations reveal that OE and TE exhibit a strikingly different scaling. Recent work in Ref. [46] compared the TE scaling for different master equation unravelling strategies. It was found that when using a homodyne measurement unravelling [47], the TE scaling can fundamentally change (from volume to area law), depending on homodyne measurement parameters. Consequently an entanglement optimized trajectory method can exploit this [46]. It was shown that entanglement can thereby be reduced compared to the commonly used number measurement method (exhibiting also area law behavior). It is now also important to compare TE scaling laws with those of OE, which is the main objective of this work.

In this paper we consider a generic XXZ model with different types of noise, and compare MPDO simulations with QT+MPS (number measurement scheme). While for small noise rates and sufficiently short times TE seems to be generally smaller than OE [see Fig. 8.1(b) and (c)], ultimately, we find that for larger rates and sufficiently long times, the MPDO approach has fundamental advantages compared to the QT+MPS ansatz in terms of the entropy scaling: The OE growth is significantly reduced (at times longer than the inverse rate of dissipation). In the case of spontaneous emission and absorption the OE vanishes, while the TE exhibits a growth and approaches a constant for large dissipation rates and long

times. This implies that here QT+MPS produces fundamentally inefficient representations with entangled trajectory states. We derive an analytical value for the constant TE in a large dissipation limit. We find a similar scenario for dephasing: Here, OE scales logarithmically with time (as long as magnetization conservation is not broken) [48, 49], while TE increases as a power law. In addition to the fundamentally different entropy scaling, we also point out several practical differences in the implementation of both methods that make the MPDO approach more attractive. The latter allows e.g. to implement higher-order Trotter decomposition and to exploit translational invariance easily. We also point out that for the correct choice of basis, MPDO elements can be made real.

This paper is organized as follows: In Sec. 8.2 we introduce our XXZ and noise models. In Sec. 8.3 we review the bipartite entropies associated to MPDO and QT+MPS, respectively. We compare the two approaches for the different noise models in Sec. 8.4.1 for spontaneous emission an absorption and in Sec. 8.4.2 for dephasing, respectively. In Sec. 8.5 we provide technical details on our numerical methods and analytical calculations. Finally, we provide a conclusion and an outlook in Section 8.6.

8.2 Model

In this work we consider a 1D spin-1/2 XXZ chain with Hamiltonian ($\hbar \equiv 1$ throughout this paper)

$$\hat{H}_{\mathrm{XXZ}} = \sum_{i=1}^{N-1} \frac{J}{4}\Big[-(\hat{\sigma}_i^x \hat{\sigma}_{i+1}^x + \hat{\sigma}_i^y \hat{\sigma}_{i+1}^y) + \hat{\sigma}_i^z \hat{\sigma}_{i+1}^z \Big]. \tag{8.1}$$

Here, N is the number of spins, $\hat{\sigma}_i^{x,y,z}$ denote standard Pauli matrices defined in a local basis $|{\downarrow},{\uparrow}\rangle_i$, and J is the nearest neighbor spin-coupling strength. For finite system size calculations we consider open boundary conditions. Note that in the main text we consider a fixed anisotropy in the XXZ model. However, we point out that the OE and TE exhibits interesting opposite behavior as function of the ZZ interaction, see Appendix 8.B.

Starting in a pure Néel product state,

$$\hat{\rho}(t=0) = \bigotimes_{i=1}^{N/2} |{\uparrow}\rangle_{2i-1} |{\downarrow}\rangle_{2i} \langle{\uparrow}|_{2i-1} \langle{\downarrow}|_{2i}\,, \tag{8.2}$$

we will consider open system dynamics under a Lindblad master equation, i.e. for a chain being coupled to a Markovian environment [40]

$$\frac{d}{dt}\hat{\rho} = -\mathrm{i}[\hat{H}_{\mathrm{XXZ}}, \hat{\rho}] + \sum_{\eta} \mathcal{D}[\hat{L}_\eta]\hat{\rho}. \tag{8.3}$$

Here, our dissipative channels are given by super-operators

$$\mathcal{D}[\hat{L}_\eta]\hat{\rho} = \hat{L}_\eta \hat{\rho} \hat{L}_\eta^\dagger - \frac{1}{2}\{\hat{L}_\eta^\dagger \hat{L}_\eta, \hat{\rho}\}, \tag{8.4}$$

which are defined by the Lindblad jump operators $\hat{L}_\eta$. The curly bracket denotes the anti-commutator. Alternatively the master equation can be written in the form

$$\frac{d}{dt}\hat{\rho} = -\mathrm{i}\left(\hat{H}_{\mathrm{eff}}\hat{\rho} - \hat{\rho}\hat{H}_{\mathrm{eff}}^{\dagger}\right) + \sum_{\eta}\hat{L}_\eta\hat{\rho}\hat{L}_\eta^{\dagger} \tag{8.5}$$

with the effective Hamiltonian $\hat{H}_{\mathrm{eff}} = \hat{H}_{\mathrm{XXZ}} + \hat{H}_{\mathrm{nh}}$ with non-hermitian part $\hat{H}_{\mathrm{nh}} = -\mathrm{i}\sum_\eta \hat{L}_\eta^{\dagger}\hat{L}_\eta/2$. In the following we will consider two noise models:

Spontaneous emission and absorption – In the first scenario we consider local incoherent transitions between the two states $|{\uparrow}\rangle_i \leftrightarrow |{\downarrow}\rangle_i$, defined respectively by the two jump operators for spin i:

$$\hat{L}_i^{+} = \sqrt{\gamma_+}\hat{\sigma}_i^{+} \tag{8.6a}$$
$$\hat{L}_i^{-} = \sqrt{\gamma_-}\hat{\sigma}_i^{-}. \tag{8.6b}$$

Spontaneous emission $|{\uparrow}\rangle_i \to |{\downarrow}\rangle_i$ occurs for example naturally for atomic two-level systems coupled the electron-magnetic vacuum. For optical transition frequencies, spontaneous absorption $|{\downarrow}\rangle_i \to |{\uparrow}\rangle_i$ is typically negligible, can however be engineered e.g. by using a laser drive to a highly excited state that quickly relaxes to $|{\uparrow}\rangle_i$ [50]. Here, we will mostly focus on the scenario where $\gamma_+ = \gamma_-$. This scenario conserves the mean magnetization of the initial Néel state, i.e. at all times $\mathrm{Tr}\left(\hat{S}^z\hat{\rho}\right) = 0$ with $\hat{S}^z = \sum_i \hat{\sigma}_i^z$, which implies that the state explores a large Hilbert space throughout the evolution. Note that, in contrast, for the maximally imbalanced cases $\gamma_+ = 0 < \gamma_-$ or $\gamma_- = 0 < \gamma_+$, the system relaxes to trivial steady states $\bigotimes_i |{\downarrow}\rangle_i$ or $\bigotimes_i |{\uparrow}\rangle_i$, respectively.

Dephasing – As a second noise model we consider an interaction with the environment that leads to dephasing, a loss of a definite phase relation between the two spin-states. Such a mechanism occurs when the environment effectively measures the spin-states without changing them. For example, for a spin-model realized with hard-core bosons in an optical lattice, such a process can be the dominant dissipative mechanism, due to atoms spontaneously absorbing and re-emitting light from the lattice lasers [51]. In XXZ models, dephasing noise has been shown to be important [52], with further connections to Tomonaga-Luttinger liquids [53, 54]. In the master equation, we describe dephasing by the local jump operators

$$\hat{L}_i^z = \sqrt{\gamma_z}\hat{\sigma}_i^z. \tag{8.7}$$

Note that for dephasing, the magnetization is associated with a strong symmetry, i.e. it commutes with the Hamiltonian and all Lindblad operators $[\hat{H}, \hat{S}^z] = [\hat{L}_\eta, \hat{S}^z] = 0$. As a consequence, the state remains restricted to a single symmetry sector, here given by magnetization $S^z = 0$. This can be exploited to make

numerical (MPS) simulations more efficient, and can lead to fundamentally interesting many-body physics [55–60]. A direct consequence of the magnetization conservation is a long-time logarithmic growth of OE [48].

8.3 Matrix Product Decomposition and bipartite entropy

In order to exactly represent the $2^N \times 2^N$-dimensional density matrix of our system, in principle $(4^N - 1)$ real numbers are needed. Because of the exponential dependence on N, exact diagonalization approaches become thus intractable even for moderately large $N \gtrsim 15$. However, if the entanglement between different subsystems is not too large, the density matrix may be efficiently represented as a matrix product decomposition. For pure states, this decomposition is well known as a matrix product state (MPS). The MPS concept can be generalized to mixed states in several ways, and the appropriate measure of entanglement depends on the choice of decomposition. Below, we introduce two different decompositions and the respective relevant bipartite entropies [for a sketch, see Fig. 8.1(a)].

8.3.1 Operator entanglement (OE)

First we consider a direct matrix product form of $\hat{\rho}$ written as an MPDO as illustrated on the left hand side of Fig. 8.1(a) [21–25]. For a concise description, we further combine the two physical indices on each site into a joint index to "vectorize" $\hat{\rho}$ and write

$$\hat{\rho} = \sum_{\{i_n\}} \sum_{\{a_n\}}^{\chi} \prod_n R^{[n]\, i_n}_{a_n a_{n+1}} \lambda^{[n],\rho}_{a_n} \bigotimes_n \hat{e}_{i_n}. \tag{8.8}$$

The $R^{[n]\, i_n}_{a_n a_{n+1}}$ are three-dimensional tensors and the $\lambda^{[n],\rho}_{a_n}$ are vectors of normalized Schmidt values $[\sum_{a_n} (\lambda^{[n],\rho}_{a_n})^2 = 1]$. As common in matrix product decompositions, only the χ largest Schmidt values are retained to obtain an approximate representation of $\hat{\rho}$ [21, 22]. The basis operators $\hat{e}_{i_n}$ need to be chosen orthonormal, $\mathrm{Tr}(\hat{e}_i \hat{e}_j) = \delta_{ij}$. A commonly used choice is a straightforward linearization with $\hat{e}_1 = |0\rangle\langle 0|$, $\hat{e}_2 = |0\rangle\langle 1|$, $\hat{e}_3 = |1\rangle\langle 0|$, and $\hat{e}_4 = |1\rangle\langle 1|$. This choice has the disadvantage that the basis operators are not Hermitian, and as a consequence the entries of the R tensors are generally complex. We point out that instead one can also keep the tensors real by choosing e.g. the hermitian generalized Gell-Mann matrices [61] as basis operators, which for local physical dimension 2 are related to the Pauli matrices as

$$\begin{aligned} \hat{e}_1 &= \frac{1}{\sqrt{2}} \mathbb{1} \quad \hat{e}_2 = \frac{1}{\sqrt{2}} \hat{\sigma}^x \\ \hat{e}_3 &= \frac{1}{\sqrt{2}} \hat{\sigma}^y \quad \hat{e}_4 = \frac{1}{\sqrt{2}} \hat{\sigma}^z. \end{aligned} \tag{8.9}$$

Having to deal with only real numbers can be a practical advantage in terms of memory and run time. However, this basis may prevent implementations of algorithms that exploit conservation of magnetization in the XXZ model. The Pauli matrix basis has e.g. also been employed in tensor network simulations in [62]. Alternatively a density matrix product operator matrix can also be defined in a locally purified form [23], which has the advantage of retaining the positivity of the density matrix after bond dimension truncation.

Analogous to pure state MPS decompositions, the required bond dimension χ necessary to faithfully represent a state can be connected to the entropy in a bipartition of the chain [17, 24]. In the case of density matrices, this leads to the definition of OE

$$S_{\mathrm{OP}}^{(n)} = -\sum_{a_n} \left(\lambda_{a_n}^{[n],\rho}\right)^2 \log_2 \left(\lambda_{a_n}^{[n],\rho}\right)^2 . \tag{8.10}$$

Since the OE can be generally largest in the center of the chain, we only consider $S_{\mathrm{OP}} \equiv S_{\mathrm{OP}}^{(N/2)}$. It is important to point out that for mixed states, S_{OP} is not necessarily a genuine measure of entanglement. However, it remains a crucial quantity linked to the efficiency of the decomposition (8.8), since for a truncation to bond dimension χ, the OE is limited to values $S_{\mathrm{OP}} \leq \log_2(\chi)$.

For our model in the thermodynamic limit $N \to \infty$, the density matrix remains invariant with respect to translations by two lattice sites. Numerical simulations can exploit this symmetry to effectively simulate infinite chains using an iTEBD algorithm with proper re-orthogonalization [22, 48]. Except for Fig. 8.1, in this paper we make use of this and all MPDO simulations will be for $N = \infty$.

In Fig. 8.1(b) we show an example evolution of the OE dynamics in a weak-dissipation limit ($N = 40$, $\gamma_\pm = 0.01J$, $\gamma_z = 0$). For times at which Hamiltonian dynamics dominates ($tJ \ll 1/\gamma_\pm$) the OE initially exhibits a quick linear growth, such that the simulation quickly saturates to the maximum possible OE imposed by the finite bond dimension, $S_{\mathrm{OP}} \leq \log_2(\chi)$ (horizontal dashed lines). For example, for $\chi = 128$, a faithful simulation of the dynamics with the representation of Eq. (8.8) is only possible up to times of $tJ \sim 3$. For small dissipation, MPDO simulations thus become numerically inefficient quickly.

8.3.2 Trajectory entanglement (TE)

Alternatively, the density matrix $\hat{\rho}$ can be decomposed into a statistical mixture of pure states as sketched on the right hand side of Fig. 8.1(a). For example, a quantum trajectory evolution algorithm (see Sec. 8.5.2) produces an approximation of $\hat{\rho}$ of the form:

$$\hat{\rho} \approx \frac{1}{N_t} \sum_{\tau=1}^{N_t} |\psi_\tau\rangle \langle\psi_\tau| . \tag{8.11}$$

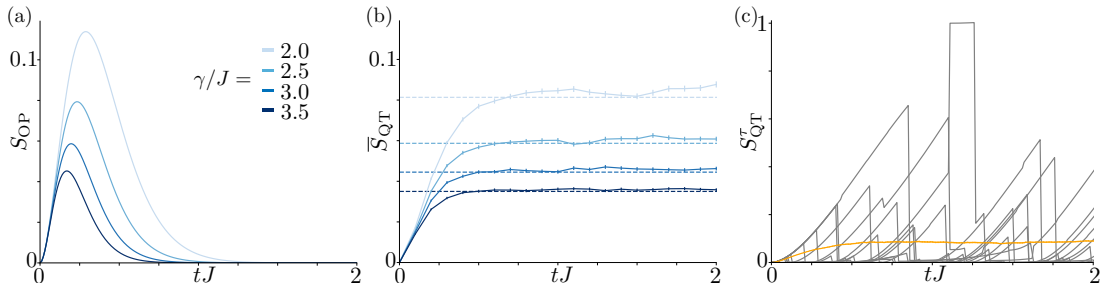

Figure 8.2: *Strong spontaneous emission/absorption*— (a/b) Time-evolution of S_{OP} (a) and $\overline{S}_{\mathrm{QT}}$ (b) for various rates of $\gamma/J = 2, 2.5, 3, 3.5$ (blue solid lines, color from light to dark). S_{OP} exhibits a clear rise and fall behavior, whereas $\overline{S}_{\mathrm{QT}}$ quickly reaches a constant plateau value. Statistical error bars are barely visible in (b). Horizontal dashed lines in (b) correspond to the analytical estimate from Eq. (8.33). (c) Dynamics of S^{τ}_{QT} for several individual trajectories. Here, $\gamma/J = 2$, and $\overline{S}_{\mathrm{QT}}$ is shown as solid yellow line. [For MPDO: $N = \infty$, $\chi = 512$; for QT+MPS: $N = 40$, $\chi = 32$, $N_t = 2000$].

Each of the N_t states $|\psi_\tau\rangle$ can then be decomposed as an ordinary MPS in canonical form [16]:

$$|\psi_\tau\rangle = \sum_{\{i_n\}} \sum_{\{a_n\}}^{\chi} \prod_n \Gamma^{[n]\, i_n}_{a_n a_{n+1}} \lambda^{[n],\tau}_{a_n} \bigotimes_n |i_n\rangle \ . \tag{8.12}$$

As in Eq. (8.8), the $\Gamma^{[n]\, i_n}_{a_n a_{n+1}}$ are three-dimensional tensors and the $\lambda^{[n],\tau}$ are real-valued Schmidt vectors, which are truncated at a maximum bond dimension χ. $|i_n = 1, 2\rangle = |\downarrow, \uparrow\rangle_n$ describes the local physical basis of spin n.

Analogous to pure state MPS, the amount of bipartite entanglement in each trajectory for a bond n is quantified by von Neumann entropy

$$S^{\tau(n)}_{\mathrm{QT}} = -\sum_{a_n} \left(\lambda^{[n],\tau}_{a_n}\right)^2 \log_2 \left(\lambda^{[n],\tau}_{a_n}\right)^2, \tag{8.13}$$

and we will compute it around the center of the chain, averaging over 11 center sites to reduce the standard deviation (see Appendix Fig. 8.9). The MPS decomposition of Eq. (8.12) implies that $S^{\tau}_{\mathrm{QT}} \leq \log_2(\chi)$. We now define trajectory entanglement (TE) as the average entanglement over all trajectories

$$\overline{S}_{\mathrm{QT}} = \lim_{N_t \to \infty} \frac{1}{N_t} \sum_{\tau=1}^{N_t} S^{\tau}_{\mathrm{QT}}. \tag{8.14}$$

Importantly, just like OE, for mixed states TE is not necessarily a genuine measure of quantum entanglement, but it is still linked to the efficiency of the QT+MPS simulation. In addition to TE we will also analyze fluctuations of the TE, by computing TE sample standard deviations,

$$\sigma_{\overline{S}_{\mathrm{QT}}} = \sqrt{\frac{1}{N_t - 1} \sum_{\tau} \left(S^{\tau}_{\mathrm{QT}} - \overline{S}_{\mathrm{QT}}\right)^2}. \tag{8.15}$$

As error bars we use the sample standard error of the mean, $\epsilon = \sigma_{\overline{S}_{\mathrm{QT}}}/\sqrt{N_t}$. Note that the individual trajectories are not translation invariant, such that we cannot use an infinite MPS method to work in the thermodynamic limit.

In Fig. 8.1(c) we show an example evolution of the TE for the same setup as in in Fig. 8.1(b), i.e. in the weak-dissipation limit [$N = 40$, $\gamma_\pm = 0.01J$, $\gamma_z = 0$]. Here we used $N_t = 400$, and the entropy is averaged over 11 bonds in the center (see Appendix 8.A for a discussion on this bond-averaging). Like the OE, the TE increases approximately linearly at short times, and then saturates to a plateau value (horizontal dashed line) imposed by χ. However, the TE increases only half as fast as the OE in Fig. 8.1(b) due to the local dimension only being half the size. Therefore, with QT+MPS we can faithfully simulate dynamics up to twice the simulation time, $tJ \sim 6$. Thus, for small dissipation rates it seems evident that QT+MPS is preferable over MPDO. Not only is the local state space smaller, but also the bipartite entropy growth is reduced. However, below we will see that the situation changes drastically for larger dissipation rates.

8.4 Comparing MPDO and QT+MPS

We now systematically compare entropy growth in MPDO and QT+MPS simulations also for larger-noise cases. We start by pointing out some practical advantages of the MPDO approach. As discussed in previous work [43], quantum trajectory approaches are best suited for small dissipation rates, since the most common implementation is first order in the time step $\gamma\Delta t$, where only one jump can happen per time step per decay channel. Extensions to higher orders [63] are cumbersome to implement for many-body systems with many decay channels. As a consequence, for large dissipation rates, time steps get prohibitively small. In contrast, the MPDO approach relies on a Trotter expansion for which well established higher order methods exist [64] (e.g. here we use a 4th order method, see Appendix 8.A). In addition, individual trajectories can break symmetries that are present in the full density matrix, such as translation invariance in the case considered here. The latter can be used to significantly boost the efficiency of the MPDO simulations [22, 48]. Finally, the stochastic nature of trajectories only allows to resolve observables with some noise for a fixed number of trajectories N_t. Thus, to accurately determine the absolute magnitude of an observable $\overline{A}$ requires a large number of trajectories $N_t \gg \sigma_A^2/\overline{A}^2$ [65], where $\overline{A}$ and σ_A^2 are the average and variance of the observable A.

Besides those practical considerations, the most important difference between both methods is the growth of the corresponding bipartite entropy, OE for MPDO and TE for QT+MPS, since the simulation complexity scales exponentially with entropy. In Sec. 8.4.1 and Sec. 8.4.2 we analyze the entropy dynamics in the presence of spontaneous emission/absorption and dephasing, respectively. For QT+MPS not only the averaged entanglement of trajectories, but also the variations of entanglement are important, which we discuss in Sec. 8.4.3.

8.4.1 Spontaneous emission/absorption

In this section we consider spontaneous emission and absorption, i.e. dynamics with Lindblad operators of Eqs. (8.6a) and (8.6b) for $\gamma_- = \gamma_+ \equiv \gamma$. In Fig. 8.2 we start by considering a large dissipation scenario with $\gamma > J$.

In Fig. 8.2(a), we observe that the OE dynamics is initially (at times $t \ll \gamma^{-1}$) exhibiting a quick build-up, which can be attributed to dominating Hamiltonian dynamics in this short-time limit. Approximating the state at short times as a pure state, $\hat{\rho}(t) \approx |\psi_t\rangle\langle\psi_t|$ with $|\psi_t\rangle = e^{-i\hat{H}t}|\psi_0\rangle$, it becomes obvious that the OE growth is twice as fast as the entanglement entropy growth in $|\psi_t\rangle$ (see e.g. [30]). The latter dominates the short-time dynamics of the TE in Fig. 8.2(b). At times $t \gtrsim \gamma^{-1}$, however, the initial coherence is quickly destroyed by the dissipation, and the OE decreases creating a well-known "rise and fall" behavior [66, 67]. The long-time value of $S_{\mathrm{OP}} = 0$ can be understood, as the overall entropy increase with time pushes the system towards a trivial maximum entropy state $\hat{\rho} \propto \mathbb{1}$ with $S_{\mathrm{OP}} = 0$.

Fig. 8.2(b) shows the evolution of $\overline{S}_{\mathrm{QT}}$ for the same parameters. Again, at times $t \ll \gamma^{-1}$ there is an initial rise, but at longer times, in contrast to S_{OP}, rather than going to zero, $\overline{S}_{\mathrm{QT}}$ reaches a plateau with a value depending on γ. This implies that at sufficiently long times $S_{\mathrm{OP}} < \overline{S}_{\mathrm{QT}}$. This means that the density matrix is then decomposed as statistical mixture (8.11) of trajectories with (on average) finite entanglement. QT+MPS therefore produces an inefficient state representation of the trivial density matrix $\hat{\rho} \propto \mathbb{1}$ and therefore requires bond dimensions $\chi > 1$, in contrast to the MPDO approach.

To better understand the origin of the plateau value of $\overline{S}_{\mathrm{QT}}$ in the large dissipation case, in Fig. 8.2(c) we show S^{τ}_{QT} for a few individual trajectories. It is striking that in this regime, nearly every quantum jumps leads to a reset of the entanglement to zero. More precisely, there are three dominating scenarios that can be identified in the evolution of S^{τ}_{QT}. After an initial rise: i) S^{τ}_{QT} drops to zero followed by a rise; ii) S^{τ}_{QT} drops to zero and remains at zero; iii) S^{τ}_{QT} jumps to one. All of these scenarios can be understood analytically from a simple model:

Consider a system of just two neighboring spins initially in the state $|{\downarrow\uparrow}\rangle$. At sufficiently short times, Hamiltonian dynamics evolves the system into a state $\propto (|{\downarrow\uparrow}\rangle + \delta\,|{\uparrow\downarrow}\rangle)$ with some small amplitude $|\delta| \ll 1$. This state features finite $S^{\tau}_{\mathrm{QT}} > 0$, which however will be immediately destroyed by a quantum jump of the form (8.6a) or (8.6b). Post-jump states are then either $|{\downarrow\uparrow}\rangle$ or $|{\uparrow\downarrow}\rangle$ [rare cases with probability of order $\mathcal{O}(\delta^2)$], which both will start to build-up entanglement again [scenario i)], or more likely [with probability of $\mathcal{O}(1)$] they will be $|{\downarrow\downarrow}\rangle$ or $|{\uparrow\uparrow}\rangle$, for which Hamiltonian (8.1) does not induce entanglement [scenario ii)] until the next quantum jump. Note that although for the two-spin case discussed here technically only scenario ii) is relevant, other relevant cases enter when more than two sites are involved. For example, to understand scenario iii), it is crucial to consider an effective block of four neighboring spins (see Sec. 8.5.3). Taking this into account allows us to derive an analytical result including terms up to order $\mathcal{O}(J^2/\gamma^2)$ for the plateau value, which is given in Eq. (8.33). These analytical estimates are shown as horizontal dashed lines in Fig. 8.2(b), and fit the numerical

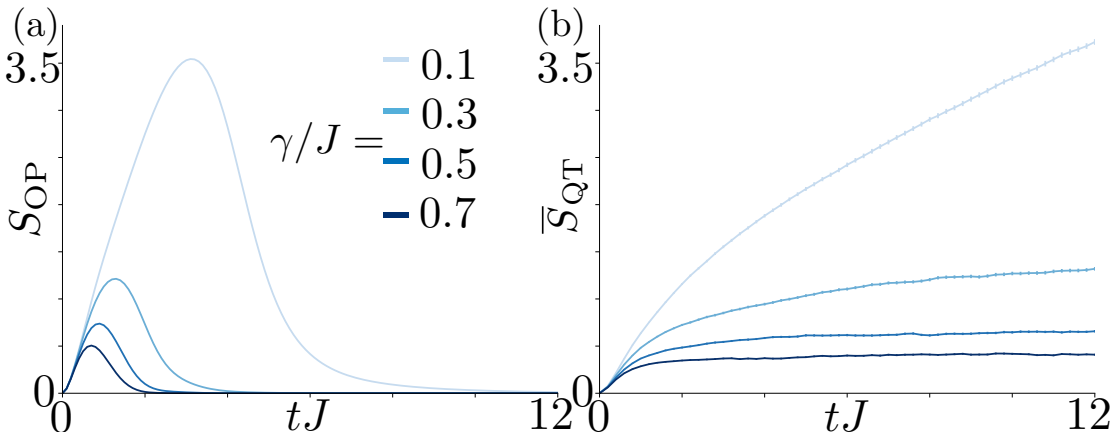

Figure 8.3: *Intermediate spontaneous emission/absorption rates* — (a/b) Time-evolution of S_{OP} (a) and $\overline{S}_{\mathrm{QT}}$ (b) for various rates of $\gamma/J = 0.1, 0.3, 0.5, 0.7$ (blue solid lines, color from light to dark). S_{OP} exhibits a clear rise and fall behavior, whereas, for the smallest values of γ, $\overline{S}_{\mathrm{QT}}$ follows a continuous increase that decreases with the increase of γ until reaching a plateau around values of $\gamma/J \geq 0.5$. Statistical error bars are barely visible in (b). [$\chi = 256$; for MPDO: $N = \infty$, for QT+MPS: $N = 40$, $N_t = 500$].

result especially especially well for large γ. The fact that S^{τ}_{QT} can also jump to one emphasizes again the importance of also considering the strong fluctuations of TE in QT+MPS, which we will analyze in more detail in Sec. 8.4.3.

For intermediate dissipation rates $\gamma \lesssim J$, the relevant physics cannot be described by simple few-spin arguments anymore. In this case we find that $\overline{S}_{\mathrm{QT}}$ in QT+MPS simulations starts to exhibit a steady growth on the time-scale of multiple spin-exchange interactions $tJ \sim 10$ for $\gamma \lesssim 0.3J$ [see Fig. 8.3(b)]. Importantly, as expected, the evolution of S_{OP} still exhibits the usual rise and fall behavior [see Fig. 8.3(b)]. Taking the example of $\gamma = 0.1J$ in Fig. 8.3, this implies that $\overline{S}_{\mathrm{QT}}$ overcomes the equivalent S_{OP} (after the fall) already for $tJ \sim 6$, and $\overline{S}_{\mathrm{QT}}$ continues to grow. It eventually also surpasses the peak value of S_{OP}. Here, for $\gamma = 0.1J$ we observe a continuous growth of $\overline{S}_{\mathrm{QT}}$ on our whole simulation time-scale. While from our simulations there is no definite proof that this growth would continue for $\chi \to \infty$ and $N \to \infty$, the results are e.g. in line with recent predictions for entanglement transitions in measured systems for similar fermionic hopping and spin models [68, 69]. However, in this context it is interesting to emphasize that also in a case where $\overline{S}_{\mathrm{QT}}$ keeps growing (e.g. for $\gamma = 0.1$ and the range $4 \lesssim tJ \leq 12$), the OE is already decaying towards zero.

Finally, in Fig. 8.4 we also show the effect of the experimentally more relevant scenario of imbalanced emission and absorption rates, $\gamma_- \neq \gamma_+$. In MPDO simulations we generally find that dynamics exhibits a robust rise and fall behavior with the maximum OE simply depending on the overall amount of dissipation, $\gamma_- + \gamma_+$ [Fig. 8.4(a)]. Similarly, the plateau value found for $\overline{S}_{\mathrm{QT}}$ decreases with increasing γ_+ when $\gamma_- = J$ fixed [Fig. 8.4(b)]. Only for values very close to $\gamma_+ \approx 0$, the quantum jumps start to remove almost all excitations from the system. Therefore,

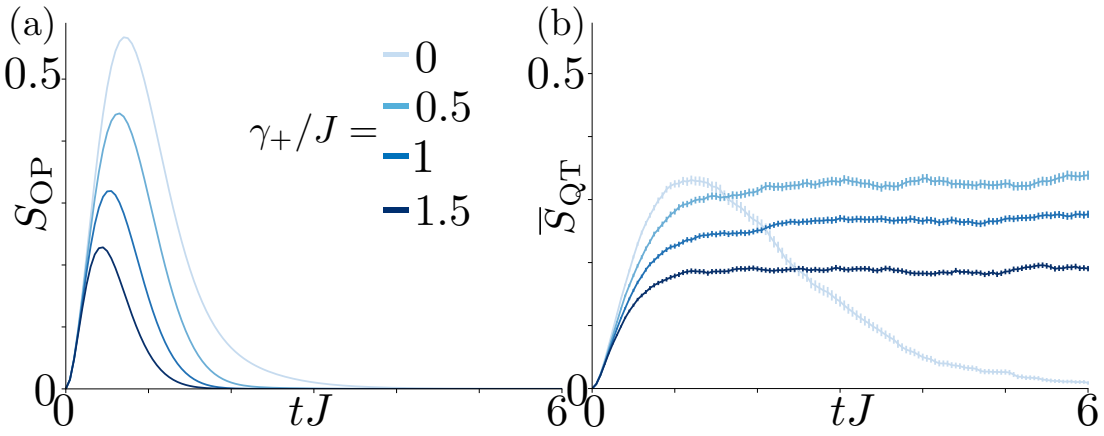

Figure 8.4: *Imbalanced* $\gamma_- \neq \gamma_+$— Time-evolution of entropies with fixed $\gamma_- = J$ and $\gamma_+/J = 0, 0.5, 1, 1.5$ (blue solid lines, color from light to dark). (a) For S_{OP} the rise and fall behaviour persists and the peak OE only decreases with γ_+. (b) For $\overline{S}_{\mathrm{QT}}$ the plateau height generally decreases with γ_+. Only for $\gamma_+/J = 0$, $\overline{S}_{\mathrm{QT}} \to 0$. [For MPDO: $N = \infty$, $\chi = 256$; for QT+MPS: $\chi = 64, N_t = 800$].

$\overline{S}_{\mathrm{QT}}$ only vanishes in the long time limit for $\gamma_+ = 0$, when the system evolves into the trivial product steady state $\bigotimes_i |{\downarrow}\rangle_i$.

8.4.2 Dephasing

In this section we consider dephasing as noise model, i.e. dynamics with Lindblad operators of the form (8.7). Fig. 8.5 summarizes our findings.

Fig. 8.5(a) reproduces the evolution of S_{OP} from Ref. [48]. It is shown that, after the rise and fall the OE exhibits a slow universal logarithmic increase as $\log_2(tJ)/4$ (see inset for the long-time evolution on a lin-log scale). In Ref. [48] it is shown that this growth can be traced back to a classical stochastic sub-diffusion process of symmetry blocks in the density matrix, and is inherent to the master equation and the initial state being $U(1)$ symmetric.

In contrast, in Fig. 8.5(b) we now also analyze the corresponding evolution of $\overline{S}_{\mathrm{QT}}$ in a QT+MPS simulation for identical parameters as in panel (a). It is striking that no rise and fall behavior is present, instead $\overline{S}_{\mathrm{QT}}$ grows continuously while the absolute values are decreased with increasing dephasing rate γ_z.

The inset in Fig. 8.5(b) shows a small number of individual trajectories. In contrast to Fig. 8.2(c), here quantum jumps do not lead to discontinuous dynamics, i.e. they do not reset S^{τ}_{QT} to zero. This can be again rationalized from a simple two-spin argument in the short-time limit. Considering the short-time approximation to the state, being $\propto (|{\downarrow\uparrow}\rangle + \delta\,|{\uparrow\downarrow}\rangle)$, it is clear that a unitary quantum jump of the form (8.7) leads to a state with flipped relative phase $\propto (|{\downarrow\uparrow}\rangle \pm \delta\,|{\uparrow\downarrow}\rangle)$, but cannot quench entanglement. Here, entanglement growth must be explained by a more complex interplay between Hamiltonian and Lindbladian dynamics, reflected in the continuous variation of individual trajectories in the inset.

Comparing OE evolution in Fig. 8.5(a) with TE evolution in Fig. 8.5(b), an

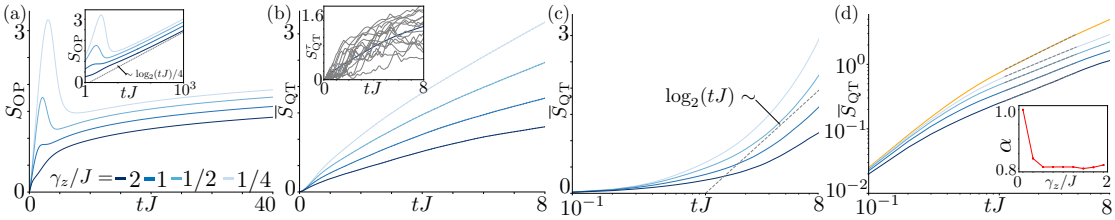

Figure 8.5: *Dephasing*— Time-evolution of entropies for $\gamma_z/J = 0.25, 0.5, 1, 2$ (blue solid lines, color from light to dark). (a) Rise and fall of the OE, and universal logarithmic long-time growth, $S_{\mathrm{OP}} = \frac{1}{4}\log_2(tJ) + \text{const.}$ (inset: log-lin scale). Reproducing results in Ref. [48]. (b) In contrast, $\overline{S}_{\mathrm{QT}}$ growth steadily in QT+MPS simulations. The inset shows S^{τ}_{QT} for several trajectories and $\gamma_z = 2J$. (c) S^{τ}_{QT} on a lin-log scale, demonstrating super-logarithmic growth in contrast to S_{OP} in panel (a). (d) $\overline{S}_{\mathrm{QT}}$ on a log-log scale. Solid yellow line: $\gamma_z = 0$. Thin dashed lines show power law fits $\overline{S}_{\mathrm{QT}} \propto t^{\alpha}$. Fitting range is chosen to best fit $\alpha = 0$ (linear increase) for $\gamma_z = 0$, $1.1 < tJ < 3.9$. Inset: Fitted power-law exponent as function of γ_z. [For MPDO: $N = \infty$, $\chi = 512$; for QT+MPS: $N = 40$, $\chi = 256$, $N_t = 400$].

important fact to point out is that TE growth is significantly faster for time-scales $t \gtrsim 1/\gamma_z$. In Fig. 8.5(c) we plot $\overline{S}_{\mathrm{QT}}$ on a log-lin scale, to clearly demonstrate a super-logarithmic increase. This implies that for $tJ \gtrsim 1/\gamma_z$, TE quickly becomes larger than OE in MPDO simulations.

In Fig. 8.5(d) we plot $\overline{S}_{\mathrm{QT}}$ on a log-log scale and find that the growth of TE at intermediate time scales (of a few tunneling processes J^{-1}) resembles a power law $\overline{S}_{\mathrm{QT}} \propto ct^{\alpha}$ with α barely depending on γ_z. To obtain an estimate of α we perform a power-law fit in the window $1.1 < tJ < 3.9$ (dashed lines). This time window is chosen to avoid on the one hand short-time physics, and on the other hand finite size effects at long times. As criterion for a good fitting range we chose the range where the fit reproduces the expected exponent $\alpha = 1$ (linear increase) with the smallest possible error in the case of $\gamma_z = 0$. The $\gamma_z = 0$ simulation is shown as solid yellow line in Fig. 8.5(d). The inset in Fig. 8.5(d) shows the fitted values for α as function of γ_z. Remarkably, for $\gamma_z \gtrsim 0.5J$ we observe a quite robust value of $\alpha \approx 0.8$. It has to be emphasized, however, that this finding is restricted to a transient time-range due to the relatively small system size ($N = 40$) accessible in our simulation. We therefore do not draw conclusions about whether this effect persists universally over extended time scales. It would be an interesting prospect to investigate this closer in the future in larger systems and for longer times.

8.4.3 Trajectory entanglement fluctuations in QT+MPS

In this section we finally also show results on the variations of the entanglement entropy in individual trajectories of our QT+MPS simulations. In Fig. 8.6(a) and Fig. 8.6(b) we plot the sample standard deviation, $\sigma_{\overline{S}_{\mathrm{QT}}}$, for the data of our previous simulations with spontaneous emission/absorption and for dephasing, re-

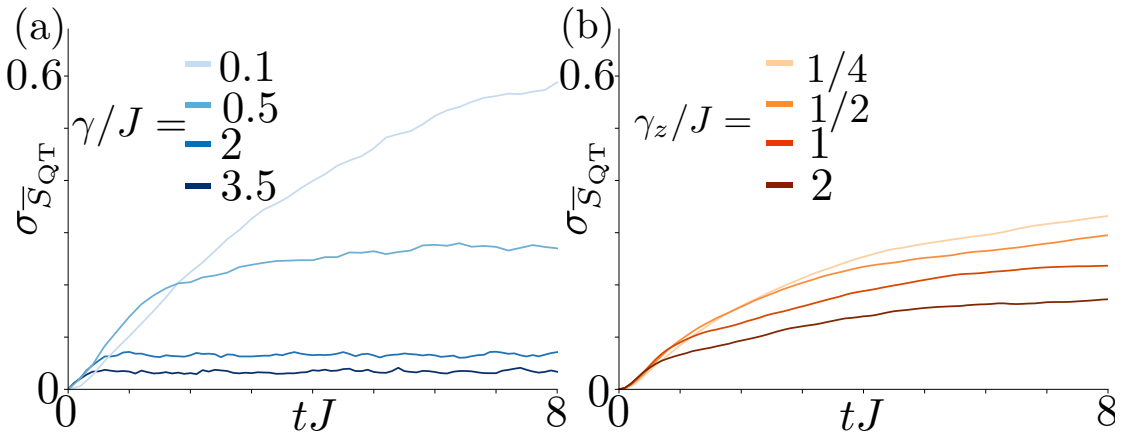

Figure 8.6: *Standard deviation of TE* — Time-evolution of sample standard deviations of the TE. (a) With spontaneous emission and absorption for both strong and weak dissipation rates $\gamma/J = 3.5, 2.0, 0.5, 0.1$ (blue solid lines, color from light to dark) [$\chi = 32$ and $N_t = 2000$]. (b) With dephasing for various rates $\gamma_z/J = 0.25, 0.5, 1, 2$ (orange solid lines, color from light to dark) [$\chi = 256$ and $N_t = 400$]. In both cases, the growth of $\overline{S}_{\mathrm{QT}}$ is correlated with a growth of its standard deviation $\sigma_{\overline{S}_{\mathrm{QT}}}$ over time [in comparison with Figs. 8.2(b), 8.3(a), 8.5(b)].

spectively. There, an important insight is that the growth of $\overline{S}_{\mathrm{QT}}$ is also correlated with the growth of its standard deviation $\sigma_{\overline{S}_{\mathrm{QT}}}$. In cases where $\overline{S}_{\mathrm{QT}}$ reaches a constant value quickly, e.g. for $\gamma \gtrsim 2.0$ [see Fig. 8.2(b)], also $\sigma_{\overline{S}_{\mathrm{QT}}}$ saturates quickly in Fig. 8.6(a). In contrast, in all other cases where $\overline{S}_{\mathrm{QT}}$ shows a persistent growth on our simulation time-scales, i.e. for $\gamma/J \lesssim 0.3$ [see Fig. 8.3(b)] and for all considered values of $0.25 \leq \gamma_z/J \leq 2$ [see Fig. 8.5(b)], also the standard deviation $\sigma_{\overline{S}_{\mathrm{QT}}}$ increases over time. Since the bond dimensions need to be chosen large enough to include "worst-case" trajectories with entropies $\sim S^{\tau}_{\mathrm{QT}} + \sigma_{\overline{S}_{\mathrm{QT}}}$, the presence of an increasing standard deviation implies that bond dimensions should be much larger than expected from the averaged entropy $\overline{S}_{\mathrm{QT}}$ only.

8.5 Details on numerical and analytical calculations

In this section we provide and discuss some technical details of our MPDO and QT+MPS algorithms and provide the analytical calculation for the plateau values observed in Fig. 8.2.

8.5.1 MPDO Simulations

Equations of motion for our MPDO decomposition in (8.8) can be easily derived and depend on the choice of the basis matrices $\hat{e}_{i_n}$. Inserting a general many-body

density matrix expansion in the chosen basis,

$$\hat{\rho} = \sum_{i_1,i_2,\ldots,i_N} r_{i_1,i_2,\ldots,i_N} \hat{e}_{i_1} \hat{e}_{i_2} \ldots \hat{e}_{i_N}, \tag{8.16}$$

into the master equation (8.3), leads to an evolution equation which only depends on nearest neighbor terms for the vectorized density matrix elements, i.e.

$$\frac{d}{dt} r_{i_1,i_2,\ldots,i_N} = \sum_{k_n,k_{n+1}} \left(A^{k_n,k_{n+1}}_{i_n,i_{n+1}} \right) r_{i_1,\ldots,k_n,k_{n+1}\ldots,i_N}, \tag{8.17}$$

for sites n and $n+1$.

The relevant super-operator two-site gates $A^{k_n,k_{n+1}}_{i_n,i_{n+1}}$ include Hamiltonian and Lindblad terms. Explicitly, in the bulk of the chain,

$$A^{k_n,k_{n+1}}_{i_n,i_{n+1}} = H^{k_n,k_{n+1}}_{i_n,i_{n+1}} + \frac{1}{2} \left(L^{k_n}_{i_n} \delta^{k_{n+1}}_{i_{n+1}} + \delta^{k_n}_{i_n} L^{k_{n+1}}_{i_{n+1}} \right), \tag{8.18}$$

with, $\delta^{k_n}_{i_n}$ being Kronecker deltas. The Hamiltonian/Lindblad super-operator expansions $H^{k_n,k_{n+1}}_{i_n,i_{n+1}}$ and $L^{k_n}_{i_n}$ can be easily computed numerically: From the XXZ Hamiltonian (8.1), $\hat{H}_{\mathrm{XXZ}} \equiv \sum_{n=1}^{N-1} \hat{H}_{i_n,i_{n+1}}$ via

$$H^{k_n,k_{n+1}}_{i_n,i_{n+1}} = \mathrm{tr} \left[\hat{e}_{i_n} \hat{e}_{i_{n+1}} \left(-\mathrm{i}[\hat{H}_{i_n,i_{n+1}}, \hat{e}_{k_n} \hat{e}_{k_{n+1}}] \right) \right], \tag{8.19}$$

and for the Lindblad terms via

$$\begin{aligned} L^{k_n}_{i_n} = {} & 2\,\mathrm{tr}\Big\{ \hat{e}_{i_n} \hat{L}_\eta \hat{e}_{k_n} \hat{L}^\dagger_\eta \Big\} \\ & - \mathrm{tr}\Big\{ \hat{e}_{i_n} \hat{L}_\eta \hat{e}_{k_n} \Big\} - \mathrm{tr}\Big\{ \hat{e}_{i_n} \hat{e}_{k_n} \hat{L}_\eta \Big\} \end{aligned} \tag{8.20}$$

with the corresponding jump operators $\hat{L}_\eta$ from Eqs. (8.6b), (8.6a), or (8.7).

We compute the two-site superoperator gates (8.18) and apply them to the MPDO decomposition (8.8) using a standard TEBD [16] algorithm. As common, we can use conservation laws to significantly speed up gate applications by exploiting the block-diagonal form of the super-operator gates $A^{k_n,k_{n+1}}_{i_n,i_{n+1}}$. For dephasing this is enabled by the fact that the gates commute with the expansion of the super-operator for the total magnetization, $\hat{S}_z \hat{\rho}$. It is interesting to point-out that even for spontaneous emission/absorption the gates commute with a super-operator of the form $[\hat{\rho}, \hat{S}_z]$, which can be exploited.

We also exploit translational invariance of our model to simulate dynamics using an iTEBD algorithm, in which case due to the non-hermitian nature of the super-operator gates we resort to the re-orthogonalization scheme presented in [22]. We also emphasize again that numerical truncation errors in the TEBD step lead to a loss of positivity of the density matrix. This can in principle be avoided by using a locally purified representation of the density matrix as proposed in [23]. In practice however, since we always operate in a regime of negligible truncation (results are converged in χ, see Appendix 8.A), we do not find the loss of positivity to be a numerical problem.

8.5.2 Quantum Trajectories

For our QT+MPS simulations we use a variation of a standard quantum trajectory (QT) method [38–40], also known as quantum Monte-Carlo wavefunction method, quantum jump approach, or simulated number measurement unravelling [25, 41, 46]. In its original formulation a trajectory $|\psi_\tau(\Delta t)\rangle$ is evolved with the non-hermitian effective Hamiltonian, $\hat{H}_{\text{eff}}$, over a time Δt, and a Lindblad jump operator is randomly applied with a probability proportional to $1 - \| \, |\psi_\tau(\Delta t)\rangle \, \|^2$, followed by a renormalization. The specific Lindblad operator $\hat{L}_{\eta_0}$ for a decay channel η_0 is chosen with probability $\propto \langle\psi_\tau(t)| \, \hat{L}^\dagger_{\eta_0}\hat{L}_{\eta_0} \, |\psi_\tau(t)\rangle$.

In this original formulation, the method suffers from the inherent problem that the equivalence of the master equation relies on a first-order Euler argument [41] and thus requires small time-step sizes Δt. This problem can be partly ameliorated by an alternative formulation of QT, in which quantum jump times are numerically pre-calculated from the decay-dynamics of the norm, such that the system can be evolved to the quantum jump time with an arbitrarily high order method [39, 41].

We make use of this idea, but in our case also exploit the fact that the non-hermitian part of our effective Hamiltonian has a particularly simple form:

$$\hat{H}_{\text{nh}} = -\frac{\mathrm{i}}{2}\sum_\eta \hat{L}^\dagger_\eta \hat{L}_\eta = -\frac{\mathrm{i}N\gamma}{2}\mathbb{1} \tag{8.21}$$

for both spontaneous emission/absorption with equal rate, $\gamma = \gamma_\pm$, and for dephasing with $\gamma = \gamma_z$. Trivially, this also implies $[\hat{H}_{\text{XXZ}}, \hat{H}_{\text{nh}}] = 0$. The time-dependent decay of squared norm thus follows

$$\begin{aligned} \| \, |\psi_\tau(t)\rangle \, \|^2 &= \langle\psi_\tau(t=0)| \, e^{-2i\hat{H}_{\text{nh}}t} \, |\psi_\tau(t=0)\rangle \, , \\ &= e^{-N\gamma t}. \end{aligned} \tag{8.22}$$

This implies that the time for a jump $j+1$, t_{j+1}, can be easily pre-calculated [45], e.g. for a random threshold value $0 \leq r_{j+1} \leq 1$ with: $t_{j+1} = t_j - \ln(r_{j+1})/N\gamma$.

It is important to point out, however, that also this approach fundamentally suffers from the issue that the difference between two consecutive jumps is $(t_{j+1} - t_j) \propto 1/N\gamma$. Thus the selected time-step for the time-evolution is on average limited by $\Delta t \sim 1/N\gamma$ and has to decrease with system size N. This strongly limits the applicability of the method for large N.

For large N, a way around this problem can be found in cases where jump operators commute, $[\hat{L}_\eta, \hat{L}_\mu] = 0$ for $\eta \neq \mu$. Then, multiple quantum jumps can be applied within a single time-step. Therefore one can first evolve $|\psi_\tau\rangle$ with only the hermitian Hamiltonian $\hat{H}_{\text{XXZ}}$, and then conditionally apply quantum jumps after non-hermitian Hamiltonian dynamics for individual decay channels η, $-\mathrm{i}\hat{L}^\dagger_\eta\hat{L}_\eta/2$, as e.g. described in [46]. While this scheme still leads to a first-order method, the method then only introduces time-step errors of order $\mathcal{O}((\Delta t\gamma)^2)$ [instead of $\mathcal{O}((\Delta t N\gamma)^2)$]. For higher order integration schemes one should resort to schemes as presented in [63], which are however cumbersome to implement in case of a large amount of decay channels.

8.5.3 Analytical Formula for plateau

In this section, we develop a further understanding of the plateau value of $\overline{S}_{\mathrm{QT}}$ observed in quantum trajectory simulations with spontaneous emission/absorption at sufficiently long times. Our reasoning is based on simple analytical arguments using blocks of just a few spins.

We start by considering only two spins, $N = 2$. In a many-body system, these two spins may represent the spins adjacent to the bipartite splitting in the center of the chain. In a regime of sufficiently large dissipation (such that entanglement cannot build up over distances larger than two spins), the overall entanglement will thus be dominated by the entanglement entropy of one of the two single spins. For two spins, there are four distinct possible initial states $\{|\uparrow\uparrow\rangle, |\downarrow\downarrow\rangle, |\uparrow\downarrow\rangle, |\downarrow\uparrow\rangle\}$. The states $\{|\uparrow\uparrow\rangle, |\downarrow\downarrow\rangle\}$ are left unchanged by the dynamics under Hamiltonian (8.1), which implies that the entanglement entropy remains strictly zero in this case. In contrast, the initial "Néel states", $|\phi_1\rangle \equiv |\uparrow\downarrow\rangle$ and $|\phi_2\rangle \equiv |\downarrow\uparrow\rangle$ evolve under Hamiltonian (8.1). Starting e.g. $|\phi_1\rangle$ the state at time t is:

$$|\psi(t)\rangle = \frac{1}{\sqrt{2}}\left(\mathrm{e}^{-\mathrm{i}E_- t}\,|E_-\rangle + \mathrm{e}^{-\mathrm{i}E_+ t}\,|E_+\rangle\right), \tag{8.23}$$

with $E_\pm = -J/4 \pm J/2$ two eigenvalues of (8.1) for $N = 2$ and the corresponding two eigenstates are $|E_\pm\rangle = (|\phi_1\rangle \mp |\phi_2\rangle)/\sqrt{2}$. Then, the reduced density matrix for the single spin of state (8.23) evolves according to

$$\rho_1(t) = \cos^2(tJ/2)\,|\uparrow\rangle\langle\uparrow| + \sin^2(tJ/2)\,|\downarrow\rangle\langle\downarrow|, \tag{8.24}$$

which leads to the single-spin entanglement entropy evolution

$$\begin{aligned} S_1(t) = &-\cos^2(tJ/2)\log_2(\cos^2(tJ/2)) \\ &-\sin^2(tJ/2)\log_2(\sin^2(tJ/2)). \end{aligned} \tag{8.25}$$

A quantum jump event can happen after a certain time t with a probability given by Eq. (8.22). Hence, the probability distribution function for a jump occurring on any of the two sites is given by an exponential distribution of the form

$$f_2(t) = 2\gamma \mathrm{e}^{-2t\gamma}, \tag{8.26}$$

with $\gamma = \gamma_+ = \gamma_-$, and a mean time between jumps of $\bar{\tau} = 1/2\gamma$. Importantly, from the jump operators (8.6), we readily see that for $N = 2$ a quantum jump will systematically collapse $|\psi(t)\rangle$ into one of the initial product states $\{|\uparrow\uparrow\rangle, |\downarrow\downarrow\rangle, |\uparrow\downarrow\rangle, |\downarrow\uparrow\rangle\}$, resetting the entanglement entropy to zero. As argued already in Sec. 8.4.1, starting in a state $|\phi_1\rangle$ or $|\phi_2\rangle$, for jumps at a short time of $\sim 1/2\gamma$, the collapsed state will almost always be $|\downarrow\downarrow\rangle$ or $|\uparrow\uparrow\rangle$. Vice versa, on average after a time of $1/2\gamma$ the states $|\downarrow\downarrow\rangle$ and $|\uparrow\uparrow\rangle$ will collapse into $|\phi_1\rangle$ or $|\phi_2\rangle$. Thus on average we can assume that in a steady-state situation and large γ, all four states are equally probable. Therefore, using a short-time expansion of (8.25)

and keeping terms of order $\mathcal{O}(J^2/\gamma^2)$, we can derive

$$\overline{S}_{\mathrm{QT}}^{2-\mathrm{site}} = \frac{1}{2}\int_0^\infty S(t) f_J(t)\,\mathrm{d}t \tag{8.27}$$

$$\approx \frac{1}{2}\frac{\gamma J^2}{2\ln(2)}\int_0^\infty t^2 e^{-2\gamma t}\big[1-\ln((Jt/2)^2)\big]\mathrm{d}t \tag{8.28}$$

$$= \frac{J^2}{16\gamma^2\ln(2)}\big[2(E-1)+\ln\big((\gamma^2 16)/J^2\big)\big], \tag{8.29}$$

where E is the Euler-Mascheroni constant. The $1/2$ in (8.27) stems from the fact that only half of the states contribute to the entropy growth.

While this result gets close to the long-time TE in Fig. 8.2(b), we did not find a perfect match with the numerical solution in the large γ limit. We attribute this to the fact that there are additional contributions of order $\mathcal{O}(J^2/\gamma^2)$ coming from rare jump events in a 4-spin block that collapse to states with TE one, as seen e.g. in Fig. 8.2(c). To illustrate how such a scenario can arise: Consider an initial state of the form $|{\downarrow}\rangle\,|\phi_1\rangle\,|{\uparrow}\rangle$. At short times $t \ll 1/J$ the state is approximated by

$$|\phi'\rangle \approx |{\downarrow}{\uparrow}{\downarrow}{\uparrow}\rangle - \mathrm{i}\frac{tJ}{2}(|{\uparrow}{\downarrow}{\downarrow}{\uparrow}\rangle + |{\downarrow}{\downarrow}{\uparrow}{\uparrow}\rangle + |{\downarrow}{\uparrow}{\uparrow}{\downarrow}\rangle). \tag{8.30}$$

Denoting the probability for a jump on spin i by $p_{i,\pm} \propto \langle\phi'|\,\hat{\sigma}_i^{\mp}\hat{\sigma}_i^{\pm}\,|\phi'\rangle$, the probability for a jump with $\hat{\sigma}_2^+$ (on the second spin) is $p_{2,+} \propto J^2/\gamma^2$. However, the state after this jump will be given by:

$$\hat{\sigma}_2^+\,|\phi'\rangle \propto (|{\uparrow}{\uparrow}{\downarrow}{\uparrow}\rangle + |{\downarrow}{\uparrow}{\uparrow}{\uparrow}\rangle). \tag{8.31}$$

This is an entangled state between blocks of sites $(1,2)$ and $(3,4)$ with entropy one. Since such a state will remain robust on a $1/\gamma$ time-scale, overall such a processes will give another contribution to the plateau value of the TE of order $\mathcal{O}(J^2/\gamma^2)$. Note that the identical argument holds for a jump with $\hat{\sigma}_3^-$, and for jumps with $\hat{\sigma}_2^-$ and $\hat{\sigma}_3^+$ if we would consider the initial Néel state $|{\uparrow}\rangle\,|\phi_2\rangle\,|{\downarrow}\rangle$.

Using this, we can now roughly estimate the correction due to such processes in steady state. We consider again jumps on the two central spins and focus on the initial state $|{\downarrow}\rangle\,|\phi_1\rangle\,|{\uparrow}\rangle$. Up to quadratic order in t, $p_{2,+}(t) \approx t^2J^2/4$ [after using state (8.30) and normalizing with four possible jump probabilities $p_{2,3,\pm}$]. This then leads to a correction term of

$$\overline{S}_{\mathrm{QT}}^{\mathrm{corr}} = \frac{1}{4}\int_0^\infty \frac{t^2J^2}{4} f_2(t)\,\mathrm{d}t = \frac{J^2}{32\gamma^2} \tag{8.32}$$

Here, the factor $1/4$ comes from the fact that we assume that in steady-state a Néel state configuration in the 4-site block has the probability of $1/8$, and the fact that we have two possible "entangling jumps" per Néel state. Summing the contributions from Eq. (8.29) and (8.32) we arrive at our final estimate for the plateau value of

$$\overline{S}_{\mathrm{QT}} = \frac{J^2}{16\gamma^2\ln(2)}\big[2(E-1)+\ln\big((\gamma^2 16)/J^2\big)\big] + \frac{J^2}{32\gamma^2}. \tag{8.33}$$

This estimate provides an excellent estimation for the numerical results in the large γ limit as shown in Fig. 8.2(b).

8.6 Conclusion and Outlook

Here, we made a systematic comparison between two approaches to numerical simulations of open quantum many-body dynamics with matrix product decompositions. We denote them: i) MPDO (evolving full matrix product density operators); and ii) QT+MPS ("number measurement unravelling" of the density matrix into MPS trajectories). In our study we focused on a comparison of bipartite entropy growth dynamics in the two methods: operator entanglement (OE) for the MPDO approach, and trajectory entanglement (TE) for QT+MPS. For both methods these entropies are fundamentally linked to the respective numerical efficiency of the state representation. We compared the entropy growth behavior for two types of single-spin dissipative mechanisms: spontaneous emission/absorption and dephasing.

On a technical level, we discussed several details of both numerical approaches and highlight several advantages of the MPDO method compared to QT+MPS. It allows for: i) Easier implementation of high-order Trotter decompositions (thus larger time-steps); ii) easier exploitation of translational invariance; and iii) a real-valued representation of the tensors in the matrix product decomposition.

On a fundamental level, our most important insight is that for time-scales $\gtrsim 1/\gamma$ (with dissipative rates γ), the growth of OE is generally slower than that of TE. For spontaneous emission/absorption OE generally vanishes at long times. In contrast, we find that TE grows on our simulable time-scales for small γ, and approaches a constant value quickly for large γ (for which we found an analytical estimate). For dephasing, OE grows only logarithmically [48], while TE (and also its sample standard deviation) grows as a power-law. For our (number measurement) unravelling, we found a robust growth exponent of ~ 0.8 for sufficiently large dephasing rates. In both cases our results imply that at sufficiently long times, MPDO matrices become a numerically significantly more efficient state representation compared to the ones obtained from QT+MPS. In other words, the standard QT approach produces a statistical mixture of entangled trajectories that can classically be less inefficiently represented than the whole density matrix.

Our simulations make use of a simple initial product state. In the future it would be interesting to also include more complex entangled initial states for systematic studies, which have e.g. led to a clearly decreased efficiency of the MPDO approach in [45].

Furthermore, another interesting prospect would be to study in depth the variations of TE growth under different types of environmental measurement schemes (e.g. homodyne measurement unravelings [46]). The dynamics of trajectory resolved entanglement in continuously monitored open systems has been a very recent topic of study in the context of "measurement-induced phase transitions" [68–73]. It is an interesting future prospect to investigate whether the scaling behavior that we observed here (e.g. the robust power-law behavior for dephasing) is a feature of the most commonly used number measurement unraveling, or if it also holds for different unravelling schemes.

Acknowledgments

We thank Vincenzo Alba and Jérôme Dubail for very helpful input on operator entanglement, as well as Guido Pupillo, Shannon Whitlock, Tomaž Prosen, Marko Žnidaric and Enej Ilievski for valuable discussions. This work was supported by LabEx NIE under contract ANR-11-LABX0058 NIE, and the QUSTEC program, which has received funding from the European Union's Horizon 2020 research and innovation program under the Marie Skłodowska-Curie grant agreement number 847471. This work is part of the Interdisciplinary Thematic Institute QMat, as part of the ITI 2021-2028 program of the University of Strasbourg, CNRS and Inserm, and was supported by IdEx Unistra (ANR-10-IDEX-0002), SFRI STRAT'US project (ANR-20-SFRI-0012), and EUR QMAT ANR-17-EURE-0024 under the framework of the French Investments for the Future Program. D.W. acknowledges funding by NIST. Our codes make use of the intelligent tensor library (ITensor) [74]. Computations were carried out using resources of the High Performance Computing Center of the University of Strasbourg, funded by Equip@Meso (as part of the Investments for the Future Program) and CPER Alsacalcul/Big Data.

Appendix

8.A Details on numerical convergence

In this appendix we present details on the numerical convergence for the results presented in the main text. We discuss: Convergence in the matrix product bond dimension χ, convergence in the time-step sizes, and our bond-averaging procedure that we use in QT+MPS. Throughout the main text we only show results that are converged in both χ and times-step sizes.

8.A.1 Bond dimension convergence

In order to make sure that our simulations are converged in the bond dimension χ for both representations [MPDO and QT+MPS defined in Eqs. (8.8) and (8.12), respectively], we repeat our simulations while doubling χ for each run until lines become visually indistinguishable. All parameters used for the figures in the main text are summarized in Tables 8.1 and 8.2 below. For spontaneous emission/absorption we varied the bond dimension in the range $\chi = 32, 64, 128, 256$ and for dephasing in the range $\chi = 64, 128, 256, 512$. The convergence plots in Fig. 8.7 demonstrate this procedure for the scenario where OE and TE grow largest (i.e. for cases where the largest χ values are necessary). We choose the parameters from Fig. 8.3 (a) and (b) for MPDO and QT+MPS with $\gamma = 0.1$ simulated up to times $tJ = 12$. In the case of MPDO, the OE reaches a peak of value $S_{\mathrm{OP}} \approx 3.5$, while in the case of QT+MPS, as explained in section 8.4.1, the dissipation γ shows a continuous increase reaching a value of $\overline{S}_{\mathrm{QT}} \approx 3.5$ around times $tJ = 12$. Note that for $\chi = 256$, fundamentally an entropy of $\log_2(256) = 8$ could be supported, and in practice we observe convergence for $\chi \gtrsim 128$ in both cases. For dephasing, to reach convergence of χ we choose parameters from Fig. 8.5 (a) and (b), for MPDO and QT+MPS respectively, with $\gamma_z/J = 0.25$. In the case of MPDO the OE reaches its highest value in the short-time peak $S_{\mathrm{OP}} \approx 3.0$, and convergence is clearly reached for $\chi \gtrsim 256$. For QT+MPS, just as in the case of weak spontaneous emission/absorption the TE shows a continuous growth reaching a value of $\overline{S}_{\mathrm{QT}} \approx 3.0$ around $tJ = 8$, and convergence is already reached for $\chi \gtrsim 64$.

8.A.2 Time-step convergence

To check convergence in time-step size Δt, we also run simulations repeatedly, decreasing Δt until lines become visually indistinguishable. To demonstrate this,

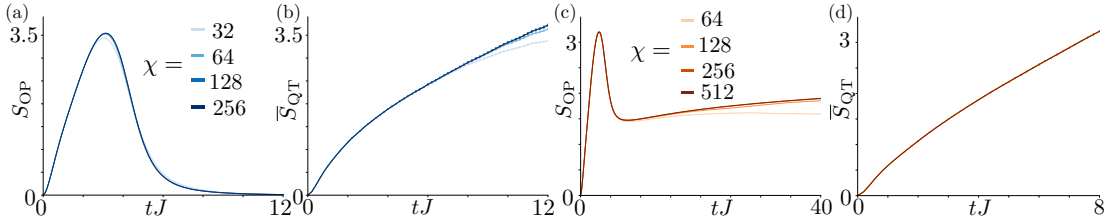

Figure 8.7: *Convergence in* χ — For (a/b) we consider spontaneous emission/absorption with a rate $\gamma/J = 0.1$ for different values of $\chi = 32, 64, 128, 256$. We notice that a value of $\chi = 128$ suffices for convergence at all times for $S_{\rm OP}$ and for $\overline{S}_{\rm QT}$ it suffices until $tJ \approx 12$. For (c/d) we consider dephasing with a rate $\gamma_z/J = 0.25$ for different values of $\chi = 64, 128, 256, 512$. In this case a value of $\chi = 256$ suffices at least until $tJ = 40$ for the case of $S_{\rm OP}$. For the case of $\overline{S}_{\rm QT}$, at least until $tJ = 8$, a value of $\chi = 64$ is enough to reach convergence [for MPDO: $N = \infty$, for QT+MPS: $N = 40$, $N_t = 500$ (a/b), $N_t = 400$ (c/d)].

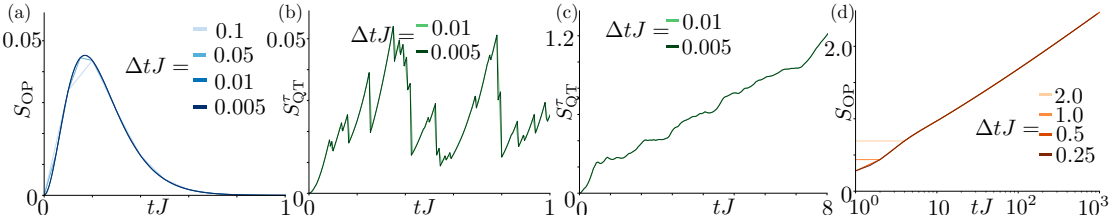

Figure 8.8: *Time-step convergence* — For (a/b) we consider spontaneous emission/absorption with a large rate $\gamma/J = 3.5$. In the case of $S_{\rm OP}$ a value of $\Delta t = 0.1/J$ already clearly suffices. In our QT+MPS methods Trotter time-steps (h) are adaptive with $h \leq \Delta t$ to resolve jumps. However results also agree when Δt becomes smaller than the inter-jump times (see text). For (c/d) we consider dephasing with a rate γ_z/J =2. In the case of $S_{\rm OP}$ a time-step $\Delta tJ = 2$ is already clearly enough due to a 4-th order Trotter decomposition used in our code [$\chi = 512$; for MPDO $N = \infty$; for QT+MPS $N = 40$].

in Fig. 8.8 we consider again "worst-case" scenarios with simulations for the largest rates γ and γ_z used in the main text (which generally require the smallest Δt). For all simulations in Fig. 8.8 we use $\chi = 512$ such that the results are clearly converged in χ. For the case of spontaneous emission/absorption we use parameters from Fig 8.2 (a) and (b) with $\gamma = 3.5J$ for MPDO and QT+MPS, respectively. Here, for QT+MPS we show results for a single trajectory, but averaged over the 11 center bonds such that rapid jumps are still visible. For dephasing we use parameters from Fig. 8.5 (a) and (b) with $\gamma_z = 2J$. In our QT+MPS algorithm we pre-calculate quantum jump times analytically and therefore the true time-step used in the Trotter decomposition gates, h is adaptive and therefore $h \leq \Delta t$. For spontaneous emission/absorption (MPDO and QT+MPS) as well as for dephasing in QT+MPS [i.e. in all panels Fig. 8.8(a-c)] we vary Δt in the range $\Delta tJ = 0.1, 0.05, 0.01, 0.005$, and only for dephasing and MPDO simulations [Fig. 8.8(d)] we also demonstrate convergence for very large steps in the range

Figure	γ_+/J	γ_-/J	γ_z/J
Fig. 1(b)	0.01	0.01	0
Fig. 1(c)	0.01	0.01	0
Fig. 2(a)	2, 2.5, 3, 3.5	γ_+/J	0
Fig. 2(b)	2, 2.5, 3, 3.5	γ_+/J	0
Fig. 2(c)	2	2	0
Fig. 3(a)	0.1, 0.3, 0.5, 0.7	γ_+/J	0
Fig. 3(b)	0.1, 0.3, 0.5, 0.7	γ_+/J	0
Fig. 4(a)	0, 0.5, 1, 1.5	1	0
Fig. 4(b)	0, 0.5, 1, 1.5	1	0
Fig. 5(a)	0	0	0.25, 0.5, 1,2
Fig. 5(a) (inset)	0	0	0.25, 0.5, 1,2
Fig. 5(b)	0	0	0.25, 0.5, 1,2
Fig. 5(c)	0	0	0.25, 0.5, 1,2
Fig. 5(d)	0	0	0.25, 0.5, 1,2
Fig. 5(d) (inset)	0	0	[0.25 : 0.25 : 2]
Fig. 6(a)	0.1, 0.5, 2, 3.5	γ_+/J	0
Fig. 6(b)	0	0	0.25, 0.5, 1,2
Fig. S1(a)	0.1	0.1	0
Fig. S1(b)	0.1	0.1	0
Fig. S1(c)	0	0	0.25
Fig. S1(d)	0	0	0.25
Fig. S2(a)	3.5	3.5	0
Fig. S2(b)	3.5	3.5	0
Fig. S2(c)	0	0	2
Fig. S2(d)	0	0	2
Fig. S3(a)/(c)	0	0	2.0
Fig. S3(b)/(d)	3.5	3.5	0

Table 8.1: The numerical values for the dissipations γ_+/J, γ_-/J, and γ_z used for all figures in this paper.

$\Delta tJ = 2.0, 1.0, 0.5, 0.25$. The very large values of Δt in MPDO are enabled by the fact that here we can easily incorporate a 4-th order Trotter decomposition for the matrix exponential of the master-equation super-operator. In particular, we use the following decomposition from [64]:

$$(1)^T(1)(1)^T(-2)(1)^T(1)^T(1)^T(1)^T(1)(1)^T(1)(1)(1)(1)(-2)^T(1)(1)^T(1), \qquad (8.34)$$

where the notation "$(n)^{(T)}$" denotes a (transposed) sweep of two-spin super-operator gates with time-step $n\Delta t/12$. This allows us to observe convergence even for $\Delta t = 2J$ in Fig. 8.8(d). Also in Fig. 8.8(a) the time-step size $\Delta t \approx 0.1$ is already clearly sufficient. For QT+MPS in Fig. 8.8(b) and (c) the mean times between jumps are on the order of $1/N\gamma \sim 0.007/J$ and $\sim 0.01/J$, respectively. Because of our adaptive time-step algorithm, the Trotter time-step h is on the order of those small values, and therefore a 2nd order decomposition is sufficient. Here

Figure	χ	ΔtJ	N_t
Fig. 1(b)	8,16,32,64,128	0.1	—
Fig. 1(c)	8,16,32,64,128	0.01	400
Fig. 2(a)	512	0.01	—
Fig. 2(b)	32	0.01	2000
Fig. 2(c)	32	0.01	10
Fig. 3(a)	256	0.1	—
Fig. 3(b)	256	0.2	500
Fig. 4(a)	256	0.05	—
Fig. 4(b)	64	0.005	800
Fig. 5(a)	512	0.1	—
Fig. 5(a) (inset)	1024	0.1, 1.0	—
Fig. 5(b)	256	0.1	400
Fig. 5(c)	256	0.1	400
Fig. 5(d)	256	0.1	400
Fig. 5(d) (inset)	256	0.1	400
Fig. 6(a)	32	0.01	2000
Fig. 6(b)	256	0.1	400
Fig. S1(a)	32, 64, 128, 256	0.1	—
Fig. S1(b)	32, 64, 128, 256	0.2	500
Fig. S1(c)	64, 128, 256, 512	0.2	—
Fig. S1(d)	64, 128, 256, 512	0.2	400
Fig. S2(a)	256	$0.1, 0.05, 0.01, 0.005$	—
Fig. S2(b)	256	$0.1, 0.05, 0.01, 0.005$	1
Fig. S2(c)	256	$0.1, 0.05, 0.01, 0.005$	—
Fig. S2(d)	256	$0.1, 0.05, 0.01, 0.005$	1
Fig. S3(a)/(c)	256	0.1	400
Fig. S3(b)/(d)	64	0.1	2000

Table 8.2: The numerical values of χ, Δt, and N_t used for all figures in this paper. Whenever two Δt values are given, different Δts were used for different parameters for historic reasons, but are clearly converged in either case.

we use the decomposition $(1)(1)^T$, where $(1)^{(T)}$ [64] denotes a (transposed) sweep with time-step of $h/2$ in the non-hermitian two site gates. To show that this is sufficient we demonstrate that results are indistinguishable for $\Delta tJ = 0.01$ and $\Delta tJ = 0.005$, where the latter is smaller than the mean inter-jump times in both cases. All time-step sizes used for the figures in the main text are also summarized in Table 8.2 below.

8.A.3 Bond averaging

In Fig. 8.9, we verify that we can use bond averaging to reduce the sample standard error of the mean in the TE of QT+MPS simulations. In our system with $N = 40$ we generally average the entropies over the 5 bonds neighboring the center

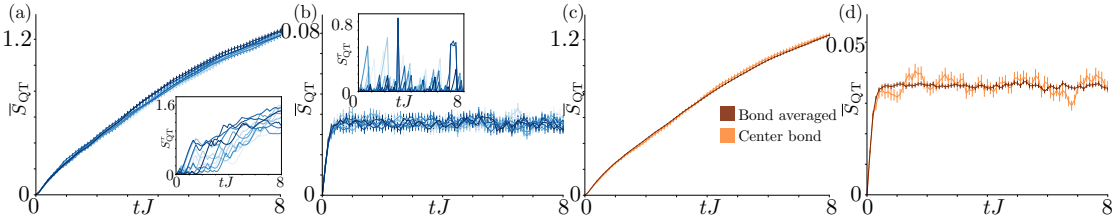

Figure 8.9: *Reduction of standard error of the mean through bond averaging* — (a/b) Trajectory averaged entropies $\overline{S}_{\mathrm{QT}}$ for the 11 central bonds (bond 16 to 26 from light to dark) for dephasing (a) and for spontaneous emission/absorption (b). The insets also show the entropy for the 11 bonds for a single trajectory. (c/d) Comparing the trajectory averaged entropy $\overline{S}_{\mathrm{QT}}$ for the center bond with the one averaged over the 11 center bonds. [for dephasing: $\gamma_z/J = 2.0$, $\chi = 256$, and $N_t = 400$; for spontaneous emission/absorption: $\gamma/J = 3.5$, $\chi = 64$, and $N_t = 2000$].

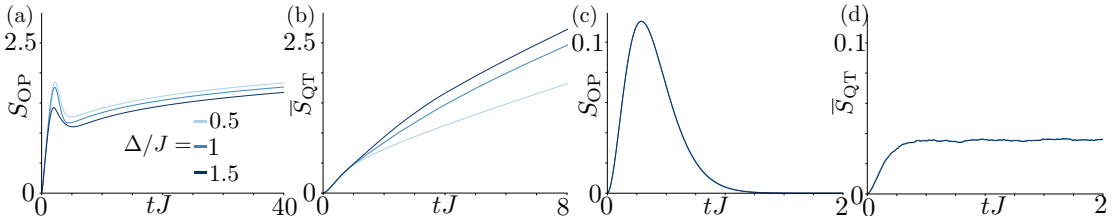

Figure 8.10: *Effects of ZZ spin-spin interaction* Δ — For (a/b) we consider dephasing with a rate $\gamma_z/J = 0.5$. For (c/d) we consider spontaneous emission/absorption with a rate $\gamma/J = 3.5$. In both cases we consider different values of $\Delta/J = 0.5, 1, 1.5$. [for MPDO: $N = \infty$, for dephasing we use $\chi = 1024$, for spontaneous emission/absoption we use $\chi = 512$; for QT+MPS: $N = 40$, for dephasing $N_t = 500$, $\chi = 1024$, for spontaneous emission/absortion $N_t = 2000$, $\chi = 256$]

bond, i.e., denoting the center bond as bond 21, we average over all bonds from 16 to 26. In Fig. 8.9(a) and (b) we show the trajectory averaged entropy $\overline{S}_{\mathrm{QT}}$ for dephasing (a) and spontaneous emission/absorption (b) for each of these bonds. Within statistical fluctuations given by the error bars (sample standard error of the mean) all entropies show similar behavior (the insets show variations for a single trajectory S^{τ}_{QT}, naturally exhibiting large fluctuations). This implies that the bond averaged entropy also agrees with the one of the center site, only with reduced error bars despite using the same number of trajectories. This is demonstrated in Fig. 8.9(c) and (d) for dephasing and spontaneous emission/absorption, respectively.

8.B Effects of ZZ spin-spin interaction

Here we consider an XXZ Hamiltonian, but with variable ZZ spin-spin interactions, Δ, in the Hamiltonian:

$$\hat{H}_{\mathrm{XXZ}} = \sum_{i=1}^{N-1} \left[-\frac{J}{4}(\hat{\sigma}_i^x \hat{\sigma}_{i+1}^x + \hat{\sigma}_i^y \hat{\sigma}_{i+1}^y) + \frac{\Delta}{4}\hat{\sigma}_i^z \hat{\sigma}_{i+1}^z \right]. \tag{8.35}$$

We confirmed that a change of the sign $\Delta = +J \leftrightarrow \Delta = -J$ does not have any effect on the TE/OE evolution. Simulation results for different magnitudes $|\Delta|$ are shown in Fig. 8.10. We point out the interesting fact that with increasing Δ the OE and the TE depend on Δ in opposite ways. While the OE decreases with increasing interaction strength [Fig. 8.10(a)] (as also pointed out in the supplementary material of [48]), the TE increases with Δ. For the cases of large spontaneous/emission absorption, in contrast, the TE and OE remains essentially unchanged [Fig. 8.10(c/d)].

Bibliography

[1] Guillermo Preisser, David Wellnitz, Thomas Botzung, and Johannes Schachenmayer. Comparing bipartite entropy growth in open-system matrix product simulation methods, March 2023. [Online; accessed 6. Jun. 2023].

[2] J. Ignacio Cirac and Peter Zoller. Goals and opportunities in quantum simulation. *Nat. Phys.*, 8(4):264–266, Apr 2012.

[3] Immanuel Bloch, Jean Dalibard, and Sylvain Nascimbène. Quantum simulations with ultracold quantum gases. *Nat. Phys.*, 8(4):267–276, Apr 2012.

[4] Bryce Gadway and Bo Yan. Strongly interacting ultracold polar molecules. *J. Phys. B: At. Mol. Opt. Phys.*, 49(15):152002, Jun 2016.

[5] Robert Löw, Hendrik Weimer, Johannes Nipper, Jonathan B. Balewski, Björn Butscher, Hans Peter Büchler, and Tilman Pfau. An experimental and theoretical guide to strongly interacting Rydberg gases. *J. Phys. B: At. Mol. Opt. Phys.*, 45(11):113001, May 2012.

[6] C. S. Adams, J. D. Pritchard, and J. P. Shaffer. Rydberg atom quantum technologies. *J. Phys. B: At. Mol. Opt. Phys.*, 53(1):012002, Dec 2019.

[7] Antoine Browaeys and Thierry Lahaye. Many-body physics with individually controlled Rydberg atoms. *Nat. Phys.*, 16(2):132–142, Feb 2020.

[8] M. Morgado and S. Whitlock. Quantum simulation and computing with Rydberg-interacting qubits. *AVS Quantum Sci.*, 3(2):023501, May 2021.

[9] R. Blatt and C. F. Roos. Quantum simulations with trapped ions. *Nat. Phys.*, 8(4):277–284, Apr 2012.

[10] Andrew J. Daley, Immanuel Bloch, Christian Kokail, Stuart Flannigan, Natalie Pearson, Matthias Troyer, and Peter Zoller. Practical quantum advantage in quantum simulation. *Nature*, 607(7920):667–676, July 2022.

[11] Luigi Amico, Rosario Fazio, Andreas Osterloh, and Vlatko Vedral. Entanglement in many-body systems. *Rev. Mod. Phys.*, 80(2):517, May 2008.

[12] J. Eisert, M. Cramer, and M. B. Plenio. Colloquium: Area laws for the entanglement entropy. *Rev. Mod. Phys.*, 82(1):277–306, Feb 2010.

[13] Pasquale Calabrese and John Cardy. Evolution of entanglement entropy in one-dimensional systems. *J. Stat. Mech.: Theory Exp.*, 2005(04):P04010, Apr 2005.

[14] Maurizio Fagotti and Pasquale Calabrese. Evolution of entanglement entropy following a quantum quench: Analytic results for the xy chain in a transverse magnetic field. *Phys. Rev. A*, 78:010306(R), Jul 2008.

[15] Vincenzo Alba and Pasquale Calabrese. Entanglement dynamics after quantum quenches in generic integrable systems. *SciPost Phys.*, 4(3):017, Mar 2018.

[16] Guifré Vidal. Efficient Simulation of One-Dimensional Quantum Many-Body Systems. *Phys. Rev. Lett.*, 93(4):040502, Jul 2004.

[17] Norbert Schuch, Michael M. Wolf, Frank Verstraete, and J. Ignacio Cirac. Entropy Scaling and Simulability by Matrix Product States. *Phys. Rev. Lett.*, 100(3):030504, Jan 2008.

[18] F. Verstraete, V. Murg, and J. I. Cirac. Matrix product states, projected entangled pair states, and variational renormalization group methods for quantum spin systems. *Adv. Phys.*, 57(2):143–224, Mar 2008.

[19] Ulrich Schollwöck. The density-matrix renormalization group in the age of matrix product states. *Ann. Phys.*, 326(1):96–192, Jan 2011.

[20] Sebastian Paeckel, Thomas Köhler, Andreas Swoboda, Salvatore R. Manmana, Ulrich Schollwöck, and Claudius Hubig. Time-evolution methods for matrix-product states. *Ann. Phys.*, 411:167998, Dec 2019.

[21] Michael Zwolak and Guifré Vidal. Mixed-State Dynamics in One-Dimensional Quantum Lattice Systems: A Time-Dependent Superoperator Renormalization Algorithm. *Phys. Rev. Lett.*, 93(20):207205, Nov 2004.

[22] R. Orús and G. Vidal. Infinite time-evolving block decimation algorithm beyond unitary evolution. *Phys. Rev. B*, 78(15):155117, Oct 2008.

[23] A. H. Werner, D. Jaschke, P. Silvi, M. Kliesch, T. Calarco, J. Eisert, and S. Montangero. Positive Tensor Network Approach for Simulating Open Quantum Many-Body Systems. *Phys. Rev. Lett.*, 116(23):237201, Jun 2016.

[24] Jiří Guth Jarkovský, András Molnár, Norbert Schuch, and J. Ignacio Cirac. Efficient Description of Many-Body Systems with Matrix Product Density Operators. *PRX Quantum*, 1(1):010304, Sep 2020.

[25] Hendrik Weimer, Augustine Kshetrimayum, and Román Orús. Simulation methods for open quantum many-body systems. *Rev. Mod. Phys.*, 93(1):015008, Mar 2021.

[26] Paolo Zanardi, Christof Zalka, and Lara Faoro. Entangling power of quantum evolutions. *Phys. Rev. A*, 62(3):030301(R), Aug 2000.

[27] Paolo Zanardi. Entanglement of quantum evolutions. *Phys. Rev. A*, 63(4):040304(R), Mar 2001.

[28] Xiaoguang Wang and Paolo Zanardi. Quantum entanglement of unitary operators on bipartite systems. *Phys. Rev. A*, 66(4):044303, Oct 2002.

[29] Tomaž Prosen and Iztok Pižorn. Operator space entanglement entropy in a transverse Ising chain. *Phys. Rev. A*, 76(3):032316, Sep 2007.

[30] J Dubail. Entanglement scaling of operators: a conformal field theory approach, with a glimpse of simulability of long-time dynamics in 1+1d. *Journal of Physics A: Mathematical and Theoretical*, 50(23):234001, may 2017.

[31] Tianci Zhou and David J. Luitz. Operator entanglement entropy of the time evolution operator in chaotic systems. *Phys. Rev. B*, 95(9):094206, Mar 2017.

[32] Cheryne Jonay, David A Huse, and Adam Nahum. Coarse-grained dynamics of operator and state entanglement. *arXiv:1803.00089*, 2018.

[33] V. Alba, J. Dubail, and M. Medenjak. Operator entanglement in interacting integrable quantum systems: The case of the rule 54 chain. *Phys. Rev. Lett.*, 122:250603, Jun 2019.

[34] Huajia Wang and Tianci Zhou. Barrier from chaos: operator entanglement dynamics of the reduced density matrix. *J. High Energy Phys.*, 2019(12):1–44, Dec 2019.

[35] Georgios Styliaris, Namit Anand, and Paolo Zanardi. Information Scrambling over Bipartitions: Equilibration, Entropy Production, and Typicality. *Phys. Rev. Lett.*, 126(3):030601, Jan 2021.

[36] Kyungjoo Noh, Liang Jiang, and Bill Fefferman. Efficient classical simulation of noisy random quantum circuits in one dimension. *Quantum*, 4:318, September 2020.

[37] H. Landa and G. Misguich. Nonlocal correlations in noisy multiqubit systems simulated using matrix product operators. *arXiv: 2203.05871*, March 2022.

[38] Jean Dalibard, Yvan Castin, and Klaus Mølmer. Wave-function approach to dissipative processes in quantum optics. *Phys. Rev. Lett.*, 68(5):580–583, February 1992.

[39] R. Dum, P. Zoller, and H. Ritsch. Monte Carlo simulation of the atomic master equation for spontaneous emission. *Phys. Rev. A*, 45(7):4879–4887, April 1992.

[40] Howard Carmichael. *An open systems approach to quantum optics: lectures presented at the Université Libre de Bruxelles, October 28 to November 4, 1991*, volume 18. Springer Science & Business Media, 2009.

[41] Andrew J. Daley. Quantum trajectories and open many-body quantum systems. *Adv. Phys.*, 63(2):77–149, Mar 2014.

[42] Tomaž Prosen and Marko Žnidarič. Is the efficiency of classical simulations of quantum dynamics related to integrability? *Phys. Rev. E*, 75(1):015202(R), January 2007.

[43] Lars Bonnes and Andreas M Läuchli. Superoperators vs. trajectories for matrix product state simulations of open quantum system: a case study. *arXiv preprint arXiv:1411.4831*, 2014.

[44] Epl van Nieuwenburg, J. Yago Malo, A. J. Daley, and M. H. Fischer. Dynamics of many-body localization in the presence of particle loss. *Quantum Sci. Technol.*, 3(1):01LT02, Dec 2017.

[45] Stefan Wolff, Ameneh Sheikhan, and Corinna Kollath. Numerical evaluation of two-time correlation functions in open quantum systems with matrix product state methods: a comparison. *arXiv*, Apr 2020.

[46] Tatiana Vovk and Hannes Pichler. Entanglement-Optimal Trajectories of Many-Body Quantum Markov Processes. *Phys. Rev. Lett.*, 128(24):243601, June 2022.

[47] L. Tian and H. J. Carmichael. Quantum trajectory simulations of two-state behavior in an optical cavity containing one atom. *Phys. Rev. A*, 46(11):R6801–R6804(R), December 1992.

[48] D. Wellnitz, G. Preisser, V. Alba, J. Dubail, and J. Schachenmayer. Rise and Fall, and Slow Rise Again, of Operator Entanglement under Dephasing. *Phys. Rev. Lett.*, 129(17):170401, October 2022.

[49] Mariya V. Medvedyeva, Tomaž Prosen, and Marko Žnidarič. Influence of dephasing on many-body localization. *Phys. Rev. B*, 93(9):094205, Mar 2016.

[50] B. Zhu, J. Schachenmayer, M. Xu, F. Herrera, J. G. Restrepo, M. J. Holland, and A. M. Rey. Synchronization of interacting quantum dipoles. *New J. Phys.*, 17(8):083063, Sep 2015.

[51] H. Pichler, A. J. Daley, and P. Zoller. Nonequilibrium dynamics of bosonic atoms in optical lattices: Decoherence of many-body states due to spontaneous emission. *Phys. Rev. A*, 82(6):063605, Dec 2010.

[52] Stefan Wolff, Jean-Sébastien Bernier, Dario Poletti, Ameneh Sheikhan, and Corinna Kollath. Evolution of two-time correlations in dissipative quantum spin systems: Aging and hierarchical dynamics. *Phys. Rev. B*, 100(16):165144, October 2019.

[53] Jean-Sébastien Bernier, Ryan Tan, Chu Guo, Corinna Kollath, and Dario Poletti. Melting of the critical behavior of a Tomonaga-Luttinger liquid under dephasing. *Phys. Rev. B*, 102(11):115156, September 2020.

[54] Michael Buchhold and Sebastian Diehl. Nonequilibrium universality in the heating dynamics of interacting Luttinger liquids. *Phys. Rev. A*, 92(1):013603, July 2015.

[55] Katarzyna Macieszczak, Emanuele Levi, Tommaso Macrì, Igor Lesanovsky, and Juan P. Garrahan. Coherence, entanglement, and quantumness in closed and open systems with conserved charge, with an application to many-body localization. *Phys. Rev. A*, 99(5):052354, May 2019.

[56] Davide Rossini and Ettore Vicari. Coherent and dissipative dynamics at quantum phase transitions. *Physics Reports*, 936:1–110, 2021.

[57] Zi Cai and Thomas Barthel. Algebraic versus Exponential Decoherence in Dissipative Many-Particle Systems. *Phys. Rev. Lett.*, 111(15):150403, Oct 2013.

[58] Mariya V. Medvedyeva, Fabian H. L. Essler, and Tomaž Prosen. Exact Bethe Ansatz Spectrum of a Tight-Binding Chain with Dephasing Noise. *Phys. Rev. Lett.*, 117(13):137202, Sep 2016.

[59] Michael Foss-Feig, Jeremy T. Young, Victor V. Albert, Alexey V. Gorshkov, and Mohammad F. Maghrebi. Solvable Family of Driven-Dissipative Many-Body Systems. *Phys. Rev. Lett.*, 119(19):190402, Nov 2017.

[60] Marko Žnidarič. Relaxation times of dissipative many-body quantum systems. *Phys. Rev. E*, 92(4):042143, October 2015.

[61] Reinhold A Bertlmann and Philipp Krammer. Bloch vectors for qudits. *Journal of Physics A: Mathematical and Theoretical*, 41(23):235303, 2008.

[62] Gabriela Wójtowicz, Justin E. Elenewski, Marek M. Rams, and Michael Zwolak. Open-system tensor networks and Kramers' crossover for quantum transport. *Phys. Rev. A*, 101(5):050301, May 2020.

[63] J. Steinbach, B. M. Garraway, and P. L. Knight. High-order unraveling of master equations for dissipative evolution. *Phys. Rev. A*, 51(4):3302–3308, April 1995.

[64] A. T. Sornborger and E. D. Stewart. Higher-order methods for simulations on quantum computers. *Phys. Rev. A*, 60(3):1956–1965, Sep 1999.

[65] William H Press, Saul A Teukolsky, William T Vetterling, and Brian P Flannery. *The Art of Scientific Computing*. Cambridge University Press, 1992.

[66] Federico Carollo and Vincenzo Alba. Emergent dissipative quasi-particle picture in noninteracting Markovian open quantum systems. *arXiv:2106.11997*, Jun 2021.

[67] Vincenzo Alba and Federico Carollo. Hydrodynamics of quantum entropies in Ising chains with linear dissipation. *arXiv:2109.01836*, Sep 2021.

[68] O. Alberton, M. Buchhold, and S. Diehl. Entanglement Transition in a Monitored Free-Fermion Chain: From Extended Criticality to Area Law. *Phys. Rev. Lett.*, 126(17):170602, April 2021.

[69] F. Azad, A. Hallam, J. Morley, and A. G. Green. Phase Transitions in the Classical Simulability of Open Quantum Systems. *arXiv:2111.06408*, November 2021.

[70] Brian Skinner, Jonathan Ruhman, and Adam Nahum. Measurement-Induced Phase Transitions in the Dynamics of Entanglement. *Phys. Rev. X*, 9(3):031009, July 2019.

[71] Xiangyu Cao, Antoine Tilloy, and Andrea De Luca. Entanglement in a fermion chain under continuous monitoring. *SciPost Phys.*, 7(2):024, August 2019.

[72] Yohei Fuji and Yuto Ashida. Measurement-induced quantum criticality under continuous monitoring. *Phys. Rev. B*, 102(5):054302, August 2020.

[73] Xhek Turkeshi, Alberto Biella, Rosario Fazio, Marcello Dalmonte, and Marco Schiró. Measurement-induced entanglement transitions in the quantum Ising chain: From infinite to zero clicks. *Phys. Rev. B*, 103(22):224210, June 2021.

[74] Matthew Fishman, Steven White, and Edwin Stoudenmire. The ITensor Software Library for Tensor Network Calculations. *SciPost Phys. Codebases*, page 004, August 2022.

Chapter 9

Conclusion

In this thesis, I have explored the dynamics of entanglement entropy in open spin systems using two distinct approaches: Quantum Trajectories +Matrix Product States (QT+MPS) and Matrix Product Density Operator (MPDO). Our focus centered on studying two different quantities: Operator Entanglement (OE) and Trajectory Entanglement (TE). By investigating both of these quantities, we gained valuable insights into the computational complexity of simulating many-body open quantum systems with matrix-product methods. In the case of the MPDO approach, we demonstrated that in a dissipative system possessing a $U(1)$ conservation law, the OE grows logarithmically over extended periods. We identified the prefactor and provided a comprehensive analytical description of the effect, which stems from the interplay of number conservation. For QT+MPS, we studied the dynamics under various dissipation cases and, by conducting a thorough comparison with the MPDO method, we discovered that the OE generally scales more favorably with time, making the MPDO approach fundamentally more efficient than QT+MPS.

Despite QT+MPS generally displaying poorer scaling in entanglement entropy than MPDO, it's worth noting that it remains a method capable of revealing interesting insights into open many-body dynamics by treating the interaction with the environment as a continuous measurement process. Furthermore, recent advances in the implementation of the method have made it possible to minimize the expected entanglement in the many-body quantum state, thereby reducing the computational cost of the matrix product state representation of each trajectory [1]. This enables simulations with larger systems over extended periods, making further exploration of this method promising. In the future, it would be intriguing to conduct an in-depth study of the variations in Trajectory Entanglement growth under different types of environmental measurement schemes. As for the OE, an interesting prospect would be to investigate how the presence of more complex symmetries such as $SU(N)$ impacts its dynamics.

Given the crucial role that entanglement entropy plays in simulating quantum systems through tensor network methods, the study of its dynamics is broadly relevant to studies of imperfect quantum computation and quantum simulation platforms. These platforms are currently advancing into a regime where they may offer a quantum advantage. Another significant incentive for studying the

dynamics of open quantum many-body systems, and particularly understanding the destructive processes of the environment on dynamics, is that the interplay between dissipation and coherent couplings can lead to intriguing physics or state engineering [2–5].

A natural extension of the work presented in this thesis is to simulate the dynamics of 2D models. While tensor networks are generally less efficient in 2D settings, recent advancements have yielded promising results, approaching the limits of state-of-the-art quantum simulators' capabilities [6, 7]. It is clear that the performance and capabilities of quantum simulators will continue to improve, making it crucial to evaluate the point at which classical methods can still compete. This competition is vital as it could drive advancements in simulating quantum systems and offer new insights into the nature of entanglement and quantum many-body systems.

Without a doubt, quantum science is advancing rapidly, and its results could bring about disruptive technologies. However, the development of classical methods is equally crucial for gaining clarity regarding the current limits of simulation and identifying which physical scenarios offer a more likely path to achieve a quantum advantage. In the meantime, as new claims for quantum supremacy emerge [8, 9], careful analysis will be required to determine when this point has indeed been achieved.

Bibliography

[1] Tatiana Vovk and Hannes Pichler. Entanglement-Optimal Trajectories of Many-Body Quantum Markov Processes. *Phys. Rev. Lett.*, 128(24):243601, June 2022.

[2] B. Zhu, B. Gadway, M. Foss-Feig, J. Schachenmayer, M. L. Wall, K. R. A. Hazzard, B. Yan, S. A. Moses, J. P. Covey, D. S. Jin, J. Ye, M. Holland, and A. M. Rey. Suppressing the Loss of Ultracold Molecules Via the Continuous Quantum Zeno Effect. *Phys. Rev. Lett.*, 112(7):070404, Feb 2014.

[3] M. J. Mark, S. Flannigan, F. Meinert, J. P. D'Incao, A. J. Daley, and H.-C. Nägerl. Interplay between coherent and dissipative dynamics of bosonic doublons in an optical lattice. *Phys. Rev. Res.*, 2(4):043050, Oct 2020.

[4] V. S. Shchesnovich and V. V. Konotop. Control of a Bose-Einstein condensate by dissipation: Nonlinear Zeno effect. *Phys. Rev. A*, 81(5):053611, May 2010.

[5] T. Müller, S. Diehl, and M. Buchhold. Measurement-Induced Dark State Phase Transitions in Long-Ranged Fermion Systems. *Phys. Rev. Lett.*, 128(1):010605, Jan 2022.

[6] Joseph Tindall, Matt Fishman, Miles Stoudenmire, and Dries Sels. Efficient tensor network simulation of IBM's kicked Ising experiment. *arXiv*, June 2023.

[7] Timo Felser, Simone Notarnicola, and Simone Montangero. Efficient Tensor Network Ansatz for High-Dimensional Quantum Many-Body Problems. *Phys. Rev. Lett.*, 126(17):170603, April 2021.

[8] Frank Arute, Kunal Arya, Ryan Babbush, Dave Bacon, Joseph C. Bardin, Rami Barends, Rupak Biswas, Sergio Boixo, Fernando G. S. L. Brandao, David A. Buell, Brian Burkett, Yu Chen, Zijun Chen, Ben Chiaro, Roberto Collins, William Courtney, Andrew Dunsworth, Edward Farhi, Brooks Foxen, Austin Fowler, Craig Gidney, Marissa Giustina, Rob Graff, Keith Guerin, Steve Habegger, Matthew P. Harrigan, Michael J. Hartmann, Alan Ho, Markus Hoffmann, Trent Huang, Travis S. Humble, Sergei V. Isakov, Evan Jeffrey, Zhang Jiang, Dvir Kafri, Kostyantyn Kechedzhi, Julian Kelly, Paul V. Klimov, Sergey Knysh, Alexander Korotkov, Fedor Kostritsa, David Landhuis, Mike Lindmark, Erik Lucero, Dmitry Lyakh, Salvatore Mandrà, Jarrod R. McClean, Matthew McEwen, Anthony Megrant, Xiao Mi, Kristel Michielsen, Masoud Mohseni, Josh Mutus, Ofer Naaman, Matthew Neeley, Charles Neill, Murphy Yuezhen Niu, Eric Ostby, Andre Petukhov, John C. Platt, Chris Quintana, Eleanor G. Rieffel, Pedram Roushan, Nicholas C. Rubin, Daniel Sank, Kevin J. Satzinger, Vadim Smelyanskiy, Kevin J. Sung, Matthew D. Trevithick, Amit Vainsencher, Benjamin Villalonga, Theodore White, Z. Jamie Yao, Ping Yeh, Adam Zalcman, Hartmut Neven, and John M. Martinis. Quantum supremacy using a programmable superconducting processor. *Nature*, 574:505–510, October 2019.

[9] Youngseok Kim, Andrew Eddins, Sajant Anand, Ken Xuan Wei, Ewout van den Berg, Sami Rosenblatt, Hasan Nayfeh, Yantao Wu, Michael Zaletel, Kristan Temme, and Abhinav Kandala. Evidence for the utility of quantum computing before fault tolerance. *Nature*, 618:500–505, June 2023.

Université de Strasbourg

GUILLERMO PREISSER

Numerical Studies of Entanglement Dynamics in Open Spin Systems

EDSC École Doctorale des Sciences Chimiques

Résumé : Cette thèse vise à développer une compréhension théorique plus approfondie de la dynamique de l'entropie d'intrication dans les systèmes de spins ouverts, et d'étudier les implications en termes de simulation classique de systèmes de spins ouverts à plusieurs corps par des méthodes de réseaux de tenseurs. Deux résultats principaux sont présentés dans cette thèse. L'une est une étude de la dynamique de croissance de l'intrication de l'opérateur dans une chaîne de spin ouverte avec déphasage, qui présente une croissance logarithmique à long terme. Une telle croissance logarithmique permet une simulation pendant de longues périodes avec la méthode Matrix Product Density Operator, et une compréhension analytique complète de l'effet en est dérivée. La seconde est une comparaison approfondie entre l'enchevêtrement d'opérateur et l'enchevêtrement de trajectoire où nous avons constaté que, dans la plupart des cas, l'enchevêtrement de trajectoire présente une croissance plus rapide pendant de longues périodes, ce qui rend l'approche de l'opérateur de densité de produit matriciel fondamentalement plus efficace qu'un dénouement de trajectoire quantique où chaque trajectoire est représentée comme un état de produit matriciel.

Mots-clés : Intrication quantique, Systèmes Quantiques Ouverts, Etats de Produits Matrices, Dynamique Quantique à Plusieurs Corps, Trajectoires Quantiques.

Abstract: This thesis aims to develop a deeper theoretical understanding of entanglement entropy dynamics in open spin systems, and study the implications in terms of the classical simulation of many-body open spin systems through tensor network methods. There are two main results presented in this thesis. One is a study of Operator Entanglement growth dynamics in an open spin-chain with dephasing, which is found to exhibit a logarithmic growth at long times. Such logarithmic growth enables simulation for long times with the Matrix Product Density Operator method, and a full analytical understanding of the effect is derived. The second one is a thorough comparison between Operator Entanglement and Trajectory Entanglement where we found that, in most cases, Trajectory Entanglement exhibits a faster growth for long times, making the Matrix Product Density Operator approach fundamentally more efficient than a quantum trajectory unravel where each trajectory is represented as a Matrix Product State.

Keywords: Entanglement, Open Quantum Systems, Matrix Product States, Many-body quantum dynamics, Quantum Trajectories.